The Modelling of a Squirrel-Cage Induction Generator in an Oscillating-Water-Column Wave-Energy Converter

Ronaldo Jorge Pestana

A dissertation submitted to the Faculty of Engineering and the Built Environment, University of the Witwatersrand, Johannesburg, in fulfilment of the requirements for the degree of Master of Science in Engineering.

Johannesburg, October 2014

The financial assistance of the National Research Foundation (NRF) towards this research is hereby acknowledged. Opinions expressed and conclusions arrived at, are those of the author and are not necessarily to be attributed to the NRF.

Declaration

I declare that this dissertation is my own unaided work. It is being submitted for the degree of Master of Science in Engineering at the University of the Witwatersrand, Johannesburg. It has not been submitted before for any degree or examination at any other university.

Signed on_____day of_____2014

_____

Ronaldo Jorge Pestana

Abstract

The research is focused on the modelling of a squirrel-cage induction generator in dynamic generation involving ocean-wave energy. The chosen application includes an oscillating water column fitted with a Wells turbine.

The modelling approach is based on the evaluation of existing generator models. These include the equivalent steady-state and dynamic models which are considered from a time-domain (differential equation) perspective. Since generation is dynamic in nature, model stability is an important component of model evaluation.

The evaluated models provide information regarding the electrical and mechanical operational variables of the generator. Power flow and energy loss between the mechanical and electrical subsystems are easily calculated from these variables.

The wave-energy converter excluding the induction generator is not explicitly considered. The generator models are evaluated by considering typical generator inputs which are representative of the given application. These dynamics are reproduced experimentally and in simulations with a comparison of generator response allowing for a conclusion on model performance. Generator inputs include the stator voltage excitation and turbine torque with the generator response given by the stator currents and rotor velocity. Electrical and mechanical power are also considered.

Dynamic generation is broken down into two modes of operation: the first mode involves generation for a constant sea state and the second mode involves generator operation for a change in sea state. The dynamics for the first mode involve a set generator speed (set voltage supply) and a sinusoidal prime-mover torque. Dynamics for the second operating mode are not well-defined owing to system variations. Since only the generator model is considered, an informative dynamic is tested providing an indication of possible model performance. The tested dynamic involves a sinusoidally-varying stator frequency and prime-mover torque.

The steady-state model considered from a time-domain perspective is found to be unstable for all generating slip values and is, therefore, unsuitable for the given generation application.

The dynamic model shows good agreement between experimental and simulated generator response for the two operating modes identified. In conclusion, the model is applicable for a constant sea state with a wave period of up to $0.2\,\mathrm{s}$. Furthermore, it is suspected that the dynamic model is applicable in the case of a change in sea state. Cases involving magnetic saturation and parameter variation are left for future development.

The dynamic-model evaluation assumes a balanced stator-voltage excitation – strange electrical transients including electrical faults are not considered.

An important simulation consideration involves the quantification of state-variable initial conditions. Initial rotor currents are problematic as these are not easily measured or defined in a practical squirrel-cage rotor construction. The initial rotor currents are approximated by a phasor analysis of the steady-state circuit model at zero time.

The use of an inverter-based generator excitation for the experimental work poses an analysis problem owing to the pulse-width-modulation-based voltage supply (not truly sinusoidal). This is solved by considering only the fundamental component of the stator voltage and current. Second-order low-pass filters are used to facilitate such measurements.

Acknowledgement

I would like to thank:

- My family, for their continuous support and encouragement – I love you all very much.
- My supervisor, Professor Ivan Hofsajer, for his invaluable guidance, insight and time spent.
- Professor Willie Cronje for the procurement of the experimental equipment.
- Jacques Naude for his critique of my final work.

The financial assistance of the National Research Foundation (NRF) towards this research is hereby acknowledged. Opinions expressed and conclusions arrived at, are those of the author and are not necessarily to be attributed to the NRF.

CONTENTS

CHAPTERS:

APPENDIX:

Nomenclature

- UPPER CASE is used for constant quantities.
- lower case is used for instantaneous (time-varying) quantities.
- $\tilde{}$ denotes a phasor quantity.
- $\bar{}$ denotes a time-average quantity.
- Vector quantities and matrices are written in **bold.**
- Where angles are given in mechanical radians, the subscript m will be included. Otherwise the angle is expressed in electrical radians. The same applies to angular velocities in $\mathrm{rad.\,s^{-1}}$.

Abbreviations

- SCIG = Squirrel-Cage Induction Generator
- OWC = Oscillating Water Column
- WEC = Wave-Energy Converter
- DFIG = Doubly-Fed Induction Generator
- FWSG = Field-Wound Synchronous Generator
- PMSG = Permanent-Magnet Synchronous Generator
- DC = Direct Current
- PWM = Pulse-Width-Modulation
- CMC = Common-Mode-Current
- CT = Current Transformer
- DVP = Differential Voltage Probe
- LPF = Low-Pass Filter
- VT = Voltage Transformer
- MOI = Moment Of Inertia
- EMI = ElectroMagnetic Interference
- IC = Integrated Circuit

1 Introduction

1.1 Introduction

The purpose of this work involves the modelling of a three-phase Squirrel-Cage Induction Generator (SCIG) driven by a Wells turbine in an Oscillating-Water-Column (OWC) Wave-Energy Converter (WEC). Since the focus is on the generator model, the turbine and WEC models are not considered. SCIG models are evaluated for the given application by reproducing typical operating conditions.

The modelling of induction machines for both steady-state as well as dynamic operating conditions is well established [**1**,**2**]. Therefore, the purpose of the work is to evaluate these models considering the given generation application. This is of interest owing to the nature of the anticipated generator dynamics.

The SCIG model can be broken down into equivalent electrical and mechanical models. The mechanical model reduces to a typical rotating system involving applied torque, friction/windage and moment of inertia [**1**,**3**]. The electrical model comprises an equivalent circuit model of which two possibilities are considered. These are the equivalent steady-state and dynamic electrical models presented in [**1**,**2**]. Therefore, two complete SCIG models are evaluated by combining the above-mentioned electrical and mechanical model components.

The steady-state circuit model as presented in [**2**] is considered from a phasor perspective. As its name suggests, it is applicable under steady-state operation. The chosen generation application is dynamic in nature which challenges the application of such a model. However, the dynamics involved are slowly-varying in nature such that the generator operation may be considered as quasi-steady-state. Under these conditions, the steady-state circuit model may provide a good approximation of the generator electrical behaviour. The work presented in [**4**] supports the possible use of the steady-state circuit model for this application and is discussed in more detail later in this chapter. More literature that supports the possible use of the steady-state circuit model in slowly-varying dynamic operation is [**2**]. In this case, the generator electrical sub-system is considered to be in quasi-steady-state when the rotor speed varies slowly over a given electrical excitation cycle since the generator electrical response occurs quickly. This is stated in the context of a voltage supply which is constant in amplitude and frequency. Under such conditions, the steady-state torque-speed curve may approximate induction-machine behaviour [**2**].

In the proposed research, the steady-state model is considered from a time-domain perspective and not from a frequency-domain (phasor) perspective. The steady-state circuit model is relatively simple when compared to the equivalent dynamic electrical model which involves various reference-frame transformations [**1**,**2**]. The dynamic model does, as its name suggests, cater for dynamic operation. Both these models are evaluated for the given dynamic

generation condition through a comparison of simulated and experimental results where possible. Model stability is also considered in the evaluation process.

This chapter provides some background information regarding existing WEC technology including basic turbine functionality. Considering the wave-energy application, the feasibility of a SCIG is also considered. The research problem is then formalised. This includes:

- The SCIG models being considered
- The means of model evaluation
- The dynamics to be accommodated by the models
- Existing model solutions in the application of OWC WECs

The chapter concludes with a breakdown of the remaining chapters/appendices.

1.2 Problem Contextualisation

1.2.1 Why is this research important?

There is an increasing demand for reliable and sustainable (renewable) sources of energy. This is a result of increasing pressure on non-renewable energy sources owing to increasing energy demand, environmental degradation and non-renewable energy depletion. Electricity generation from wave energy is a possible solution.

WEC modelling is an important part of developing wave-energy technology as it represents the level of understanding of such systems. Theoretical models facilitate the design and control of the systems which are modelled. Modelling helps to reduce system uncertainty which is often a cause of an iterative design/implementation process.

The need for developing wave-energy technology together with the usefulness of modelling gives relevance to task of modelling a SCIG as used in WEC systems.

1.2.2 The Nature of Ocean-Wave Energy

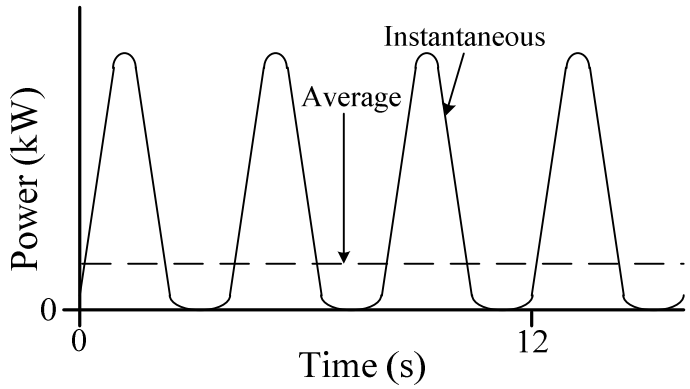

Figure 1.1: Example Wave-Energy Power Profile – adapted from [**5**]

Figure 1.1 gives an example of the power input to WEC converter devices [**5**]. The wave power has a serious oscillating nature and drops periodically to 0 kW. As a result, there is a large peak-to-average power ratio.

The oscillating nature of wave power implies the need for some sort of energy storage in order to achieve power smoothing [**5**,**6**,**7**]. This may be achieved mechanically through the various inertias of the WEC as well as electrically through the use of capacitors.

Another important characteristic of wave energy is the variation in power, even at a fixed location [**6**]. Apart from long-term seasonal variation, and short-term daily (tidal) variation, the power of the incident waves even varies from wave to wave. The variation as a result of weather conditions also needs to be mentioned. These variations are considered by designing for a particular wave climate [**5**]. Variability in wave power requires certain flexibility in WECs in order to allow for maximum power output. This involves variable speed operation as discussed later [**5**,**8**].

1.2.3 Existing WEC Technologies

In [**6**], WECs are classified according to principle of operation grouping WECs as OWCs, oscillating bodies and overtopping devices.

The WEC used is dependent, to a large extent, on the location of the proposed device. Regarding location, WECs may be further classified as shoreline, near-shore and offshore devices [**6**]. Owing to practical and cost considerations, fixed structures are usually near-shore and shoreline devices. The use of breakwater formations and the coastline for structural support is often used to reduce structural costs.

A drawback of near-shore and shoreline WECs is that the wave power is generally reduced compared with offshore devices [**6**]. The benefit of this is that the WEC structural demands may be reduced as a result of a calmer wave climate. A setback of offshore devices is that maintenance is less practical owing to structural layout and sometimes not even possible due to sea conditions [**5**]. As a result, offshore WECs require a low-maintenance and high-durability implementation.

A brief summary of the various WEC types as described in [**6**] is now presented.

1.2.3.1 OWCs

OWCs may be further subdivided into fixed versus floating structures where fixed structures may be isolated or attached to a breakwater [**6**]. Figure 1.2 illustrates example fixed/isolated and floating variations of OWCs [**6**].

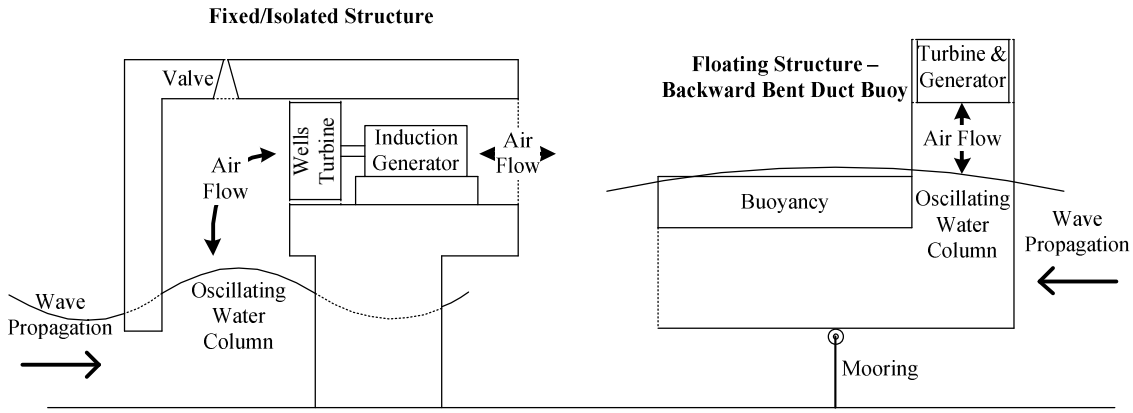

Figure 1.2: Two Possible Variations in OWCs (cross-section) – adapted from [**6**]

The OWC may be considered as some chamber-forming structure which is open at both ends. The lower end of the chamber is submerged in the ocean with the upper end open to the air. An intermediate air chamber is thus formed. The varying water level at the lower chamber end forms the oscillating water column which develops a varying air pressure gradient between the air chamber and the atmosphere outside. The resulting air flow is used to drive an air turbine. It is important to note that the air flow is reciprocating in nature and, therefore, a self-rectifying turbine is required [**6**]. Relief valves may be present in the OWC structure for protection against excessive excitation (storm conditions) as well as to facilitate turbine air-flow control.

Demonstrated power ratings of standard fixed/isolated OWCs lie in the range of 60 – 500 kW [**6**].

1.2.3.2 Oscillating Bodies

Oscillating bodies may be further classified as floating or submerged devices generating electrical energy either through translational or rotational motion [**6**]. Floating variations of oscillating-body WECs are given in figure 1.3 which illustrates the translational and rotational actions of wave-energy conversion [**6**].

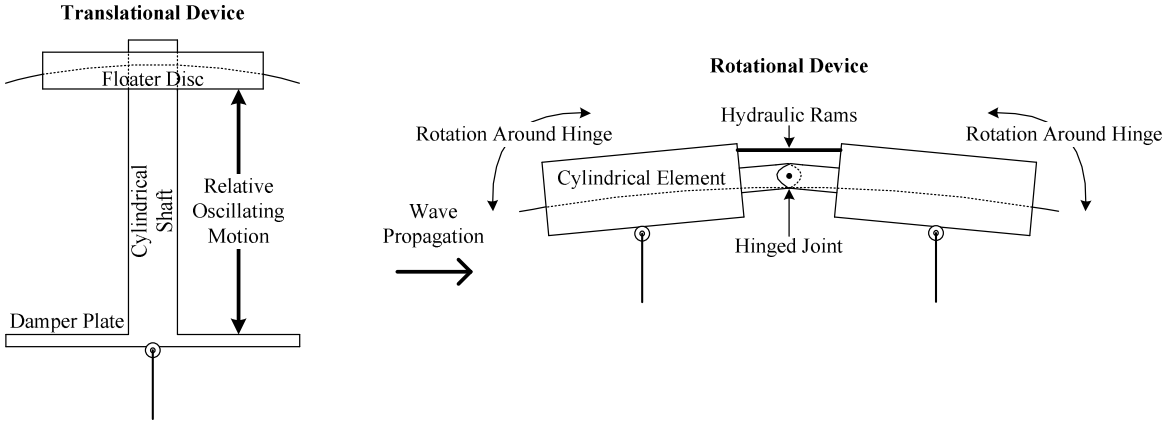

Figure 1.3: Floating Variation of Oscillating-Body WECs –Translational and Rotational Devices (side-view)

Translational devices are typically vertically orientated. The structure depicted on the left of figure 1.3 is known as the PowerBuoy [**6**]. A disc-shaped floater moves in heave with the incident waves relative to a stationary cylindrical shaft. The shaft is held stationary by a large damper plate at its bottom-most end which increases the effective inertia of the shaft through the inclusion of the mass of the water above the damper plate. The relative floater-shaft motion activates a hydraulic system which, in turn, drives an electrical generator.

The rotational device depicted on the right of figure 1.3 is known as the Pelamis [**6**]. Figure 1.3 shows two of the four cylindrical elements arranged in a linear fashion to form the complete structure. The Pelamis is orientated perpendicular to the crest of the incoming waves which induces a vertical rotational motion of the elements about the hinged joints. The relative motion between adjacent elements activates hydraulic rams which force oil through hydraulic motors. The motors, in turn, drive electrical generators.

Achieved power ratings of the PowerBuoy and Pelamis are 150 kW and 750 kW respectively [**6**]. Oscillating bodies typically activate hydraulic systems which run hydraulic motors or hydraulic turbines [**6**]. These, in turn, drive rotational electrical generators. The use of hydraulic systems allows for a certain amount of energy storage and, thus, power smoothing [**6**]. Some translational devices also directly drive linear generators [**6**].

1.2.3.3 Overtopping Devices

Overtopping devices may also be categorised as fixed versus floating structures [**6**]. The principle of operation is practically the same for both classifications. The basic components of a floating overtopping device are given in figure 1.4 [**6**].

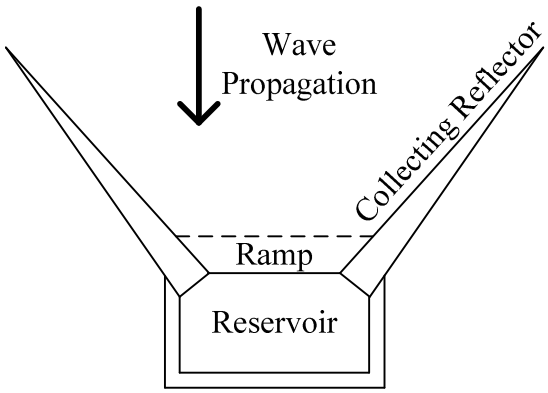

Figure 1.4: Layout of Floating Overtopping Devices (top view) – adapted from [**6**]

Overtopping devices make use of the potential energy stored in ocean waves to generate electrical energy [**6**]. Collecting reflectors "catch" incident waves and direct them towards a central ramp. The waves progress over the ramp and into a reservoir which stores water at a level higher than the surrounding ocean water. The reservoir water has potential energy relative to the surrounding water. This potential energy is eventually converted to electrical energy as the reservoir is emptied into the surrounding ocean through a hydraulic turbine.

The purpose of the reflectors is also to concentrate the wave potential energy as a certain wave height is required in order to fill the reservoir. In this way, the energy of smaller waves can be "summed" to produce a sufficiently large wave as opposed to "losing" smaller wave energies.

A particularly attractive feature of overtopping devices is the power smoothing that may be achieved through the use of large reservoirs with large energy storage [**6**].

1.2.3.4 Final Remarks

The WEC of choice is the OWC since it is one of the more promising WECs [**8**,**9**,**10**]. Therefore, the generator input dynamics associated with this WEC (which is likely to be different compared with the other WECs) are considered. This is discussed in more detail when the research question is formalised. Based on this choice of WEC, possible turbine technologies are now briefly reviewed together with the feasibility of a SCIG.

1.2.4 Turbine Solutions for an OWC WEC

It has already been mentioned that a self-rectifying air turbine is required to accommodate the reciprocating air flow of the OWC WEC [**6**]. Possible solutions include the Wells turbine and impulse turbine as illustrated in figure 1.5 [**6**,**11**].

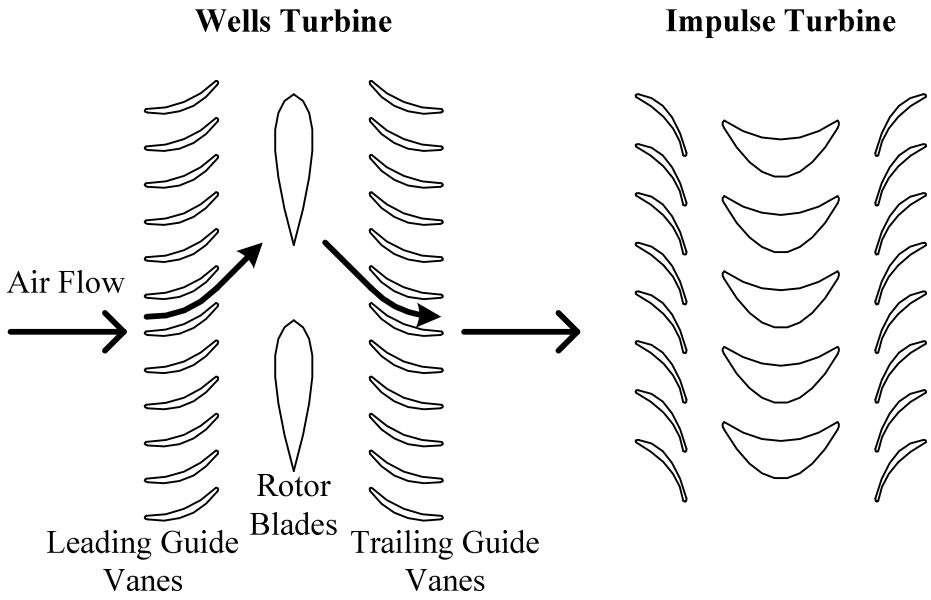

Figure 1.5: Side View of Wells and Impulse Turbines showing Blade/Vane Configuration – adapted from [**6**,**11**]

The Wells turbine functions with the air flow along the rotor axis and consists of zero-pitch rotor blades as well as leading and trailing rotor guide vanes. The leading vanes are included to improve turbine efficiency and stalling characteristic whereas the trailing vanes allow for turbine self-starting [**11**]. The Wells turbine, as shown in figure 1.5, is symmetrical about the vertical axis as required by the reciprocating air flow [**10**].

Fixed-pitch turbines should be considered for the OWC WEC in order to satisfy the need for a low-maintenance implementation [**6**,**12**]. Variable pitch turbines have increased mechanical (frictional) wearing and, therefore, increased maintenance and associated costs. A basic comparison between the fixed-pitch Wells and the impulse turbines is presented in [**12**] where these turbines (with similar specifications) are tested under similar conditions of unidirectional steady flow. Turbine efficiency as a function of flow coefficient modified from [**12**] is given in figure 1.6. Typical maximum Wells turbine efficiencies are in the range of $50 - 65$ % [**5**].

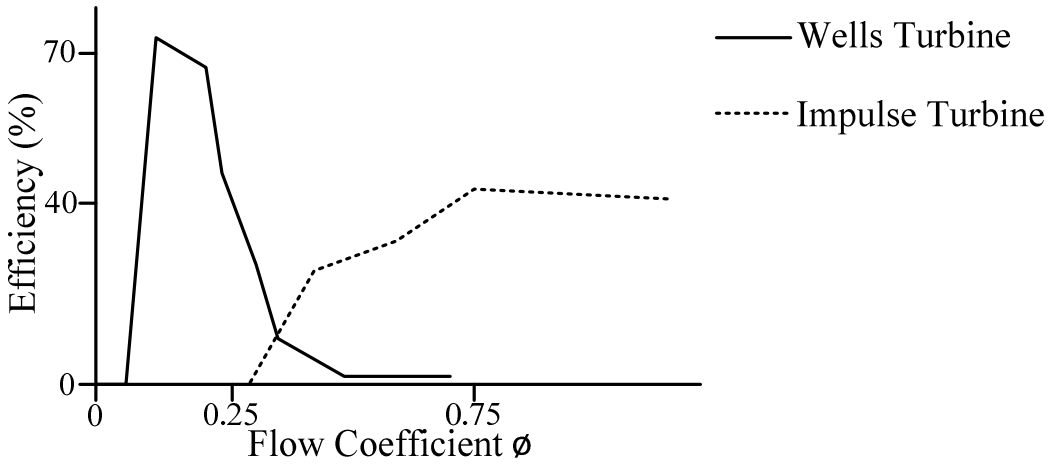

Figure 1.6: Wells Turbine and Impulse Turbine Efficiency versus Flow Coefficient – adapted from [**12**]

Flow coefficient is the ratio of the air speed through the turbine over the turbine tip speed [**5**]. Figure 1.6 shows that the Wells turbine has a higher maximum efficiency but for a relatively small range of flow coefficient ϕ. High flow coefficients results from a large air flow rate and a relatively low turbine tip speed. In such cases, the Wells turbine stalls resulting in poor turbine efficiency [**5**]. The impulse turbine, on the other hand, has a lower maximum turbine efficiency but for a larger range of flow coefficient values. The impulse turbine achieves this consistency owing to the absence of aerodynamic stalling.

Turbines used in OWC WECs have speeds in the range of $400 - 1500$ rpm with Wells turbines operating at the higher end of the speed range and impulse turbines operating at the lower end [**5**,**6**,**12**]. This means that Wells turbines can be directly coupled to their corresponding electrical generator (of similar speed rating) whereas impulse turbines will require the use of a gearbox [**12**]. Therefore, Wells turbines have a distinct advantage in terms of simplicity, maintenance and cost. A possible alternative for the impulse turbine is to use a generator with a lower operating speed. However, these generators are more expensive owing to the increased pole count [**6**]. The higher operating speed of the Wells turbine also allows for a certain amount of power smoothing through the flywheel effect [**6**].

As previously stated, the Wells turbine is the turbine considered for use in an OWC WEC owing to its popularity [**10**]. It is important for the rotational speed of the Wells turbine to be controlled in some way so as to achieve a flow coefficient associated with better efficiency [**5**,**8**]. This will make the Wells turbine useful over a larger range of sea states.

1.2.4.1 System Control Considerations

An important system requirement is the need to avoid turbine aerodynamic stalling and the corresponding poor turbine efficiency at high flow coefficient values. This is achieved by allowing for increased turbine speed during very excited sea states [**5**,**8**]. For a given sea state, the turbine speed is kept at a certain value such that the fluctuating flow coefficient (which varies with the fluctuating air flow) avoids aerodynamic stalling. In other words, the flow co-efficient fluctuates between zero and some maximum value where maximum turbine efficiency is achieved just before stalling occurs. In this way, the turbine speed should change as the sea-state changes. For sea states with a lower energy content the same principle applies except the operating speed should be decreased so as to prevent the turbine from continuously operating with a low flow coefficient [**5**].

This paradigm of system control is important when considering the generator dynamics to be tested.

1.2.5 The SCIG as a Generator Solution for an OWC WEC

A comparative analysis regarding the selection of an appropriate generator in the case of an offshore OWC WEC is presented in [**5**]. Four possible generators are considered and include the SCIG, the Doubly-Fed Induction Generator (DFIG), the Field-Wound Synchronous Generator (FWSG) and the Permanent-Magnet Synchronous Generator (PMSG). The generators are compared on the basis of offshore durability, electrical grid requirements, cost and energy efficiency. Important factors in the selection of an appropriate generator are now highlighted based on the analysis presented in [**5**]. This is done with the intention of showing the feasibility of the SCIG for the given application.

1.2.5.1 Offshore Durability

Owing to the isolated nature of offshore OWC WECs as well as the difficulty associated with their maintenance, it is desired that as little maintenance be required as possible [**5**]. This is where brushed generators suffer a serious disadvantage. Furthermore, brush durability is compromised by factors such as varying power profile and high humidity levels [**5**]. Brushed generators require operation close to their rated current level to avoid poor brush performance. However, the power profile given in figure 1.1 indicates that this requirement is not generally met in OWC WECs. The generator of an OWC WEC is also likely to be ventilated by air with high humidity levels. This results in further complications.

Another important consideration is the mechanical vibration and shock resulting from the heaving motion of the OWC structure (which may be quite severe in storm conditions) [**5**].

Benefits are observed in generators with higher power-to-mass ratios from both an initial structural-cost perspective as well as a maintenance perspective. Here, the synchronous generators have an advantage [**5**]. However, PMSGs require special consideration owing to the brittle nature of their permanent magnets.

The corrosive nature of sea air poses a problem particularly for permanent-magnet-based generators [**5**]. Permanent-magnet contact with corrosive air is likely to occur through the ventilation process. Therefore, corrosion-resistant permanent-magnets or protective coatings are required [**5**].

Owing to the absence of conducting brushes and permanent magnets, the squirrel-cage induction machine is well suited for generation in an OWC WEC.

1.2.5.2 Electrical Grid Requirements

Important grid specifications from a generator perspective include flicker (the presence of low-frequency voltage components), voltage distortion (non-sinusoidal voltage), voltage limits (requirements on the voltage amplitude), reactive power requirements (the ability to supply reactive power), fault ride-through (the ability of the generator to continue operation through grid-side faults) and power ramp rates (limitations on the rate of change of active power supplied by the generator) [**5**].

The above-mentioned grid requirements are easily met if power converters are used to interface the generator with the grid [**5**]. Such devices separate the generator and grid such that each may operate at a different voltage amplitude and frequency. The intermediate Direct Current (DC) bus capacitors also allow for limited energy storage. The "separation" of the generator and electrical grid together with the capacitor energy storage helps to meet the grid requirements. The capacitive energy storage is particularly important for reactive power supply, fault-ride through and steady power supply.

In the case of a DFIG, the rotor windings are separated from the grid by a power converter; however, the stator windings are grid-tied [**8**]. Owing to the nature of wave energy (figure 1.1) and the absence or reduced use of power electronics between the generator and the grid, a DFIG may perform poorly as a generator in OWC WECs. The SCIG, FWSG and PMSG are all completely interfaced with the grid through power converters and may be better solutions for use in OWC WECs [**5**].

Owing to the power-converter interface of the SCIG with the electrical grid, the SCIG is able to meet the above-mentioned grid requirements. As a result, a SCIG implementation is well suited for use in an OWC WEC.

1.2.5.3 Cost

The variable power of ocean waves for different sea states coupled with the need to avoid turbine aerodynamic stalling for improved turbine efficiency results in a requirement for

variable-speed operation [**5**,**8**]. This, together with the above-mentioned grid requirements implies the use of power electronics in interfacing the generator with the grid [**5**]. Therefore, the cost associated with power converters is considered as unavoidable. WEC costs are broken down into capital and running costs [**5**].

In [**5**], capital costs in 2009 for a generator device rated at 500 kW are given. These figures state the machine cost associated with the SCIG and the FWSG as being approximately equal and the PMSG and DFIG being approximately 1.7 and 2 times as expensive respectively. The cost of the power electronics for the SCIG, FWSG and PMSG are the same (rated at 100 % of rated plant power) whereas the DFIG power electronics cost is reduced by approximately 70 % as a result of the reduced power rating (rated at approximately 30 % of rated plant power). Total generator capital costs are listed below relative to the cost of a DFIG implementation [**5**]:

DFIG 100 %

SCIG 112 %

FWSG 113 %

PMSG 121 %

Running costs associated with maintenance are significantly higher for generators with brushes. Other mechanical maintenance including bearing replacement as well as electrical maintenance of complicated power electronic devices should be considered [**5**]. Electrical maintenance is required as the various electronic components also have limited lifespan which may be determined by such things as continuous operating point, continuous operating temperature, overloading incidents and switching frequency [**7**].

From the above cost-based perspective, there is no obvious advantage or disadvantage regarding a SCIG-based implementation.

1.2.5.4 Energy Efficiency

In order to allow for good energy harvesting over a range of sea states, variable generator speed operation is desired [**5**,**8**]. As previously mentioned, this is made possible through the use of power converters which interface the generators with the electrical grid while satisfying the grid requirements [**5**].

General conclusions can be made regarding complete OWC WEC system efficiency based on the use of different generator technologies and their power converters [**5**]. Firstly, a fixed-speed SCIG connected directly to the grid can achieve good system efficiency if the desired system speed is close to the generator synchronous speed. A contributing factor is the elimination of power-converter-associated losses. However, the system performance is

reduced as the desired system speed varies with changing sea state. At higher system excitation, the DFIG has the best efficiency owing to the lower losses in the power electronics with reduced power rating. The generator technologies (with power electronics) may be generally listed as the DFIG, PMSG, FWSG and SCIG in order of decreasing efficiency.

From an efficiency perspective, a SCIG-based implementation is at a disadvantage.

1.2.5.5 Final Remarks

There appears to be no outright optimal generator solution in generating electricity in an OWC WEC. This is not the purpose of the above analysis; the idea is to show the possible feasibility of the SCIG in an OWC WEC. From the above analysis, there is no serious contradiction to the application of the SCIG. The SCIG is actually well suited to given generation environment:

- An important generator requirement in an OWC WEC is low maintenance and, therefore, good reliability and durability. In this regard the SCIG is suitable as its construction does not include conducting brushes or permanent magnets.
- From a grid-requirement perspective, the SCIG is able to meet the various grid specifications provided it is connected to the grid via a power converter.
- The use of a power converter to control the SCIG allows for a variable-speed operation. In this way, the generator set is able to cater for a range of sea states.

1.3 Research Problem

The fundamental research problem involves the modelling of a SCIG. The operating dynamics to be accommodated by the model(s) are based on electrical and mechanical input dynamics that may be expected in electricity generation from ocean-wave energy. More specifically, an OWC WEC fitted with a Wells turbine which drives the electrical generator is assumed. This is illustrated in figure 1.7 which also shows the system power flow.

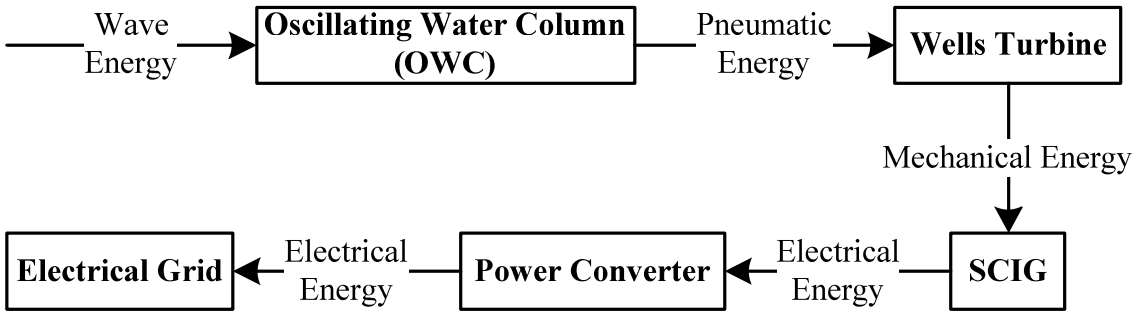

Figure 1.7: WEC Power Flow

The research question is stated as: *What existing models are applicable considering the dynamic nature of the generation application?*

Only the SCIG model is considered in this work. The other system components are implied through the inclusion of particular generation dynamics for the chosen application. As stated in the research question, the generator modelling approach is based on evaluating existing squirrel-cage induction machine models.

1.3.1 What models are considered?

As previously mentioned, the generator model is broken down into equivalent electrical and mechanical components. The mechanical model reduces to a rotating system involving applied torque, friction/windage and rotor moment of inertia [**1**,**3**]. For the electrical component, two models are considered.

The first electrical model is the per-phase steady-state equivalent circuit model expressed in terms of machine variables [**1**,**2**]. This model assumes balanced steady-state operation. As such it is typically analysed from a phasor/frequency-based approach [**2**]. Regarding the research problem which involves dynamic generation, the given model is evaluated from a differential-equation/time-based perspective. This is discussed further in the context of existing work in generator modelling for the given application. Included in this discussion is the applicability of a steady-state model to dynamic generation.

The other electrical model is the equivalent dynamic model referred to the arbitrary reference frame with the variables expressed in terms of "qd0" components [**1**]. This model is a differential-equation/time-based model and is analysed as such. In this model, steady-state simplifying assumptions are not made. Therefore, it is referred to as the dynamic model.

1.3.2 How are the models evaluated?

Model evaluation is a two-step process. The first step involves evaluating model stability which is important for dynamic operation. The second step involves a comparison of experimental and simulation results. If a model is found to be unsuitable based on model stability, the second step is not required.

The comparison of experimental and simulation results is based on expected generator operation for the given application. Particular input dynamics are considered which include the stator voltage (amplitude and frequency) as well as prime-mover (Wells turbine) torque. Model suitability is based on a comparison of experimental and simulated generator response as given by the stator currents. The rotor speed response is also used where possible; however, a comparison of stator currents is sufficient to determine model suitability. A detailed discussion regarding this sufficiency condition is given in chapter 5. Generator electrical and mechanical power provides a different perspective in model evaluation. A suitable SCIG model would produce a generator response that is comparable with the practical response.

1.3.3 Typical Generator Operation

As previously mentioned, poor turbine efficiency associated with very low and very high (aerodynamic stalling) flow coefficients should be avoided [**5**,**8**]. This can be achieved in two ways [**8**]:

- Regulation of air flow through the use of an airflow valve.
- Decrease/increase in turbine speed.

As presented in [**8**], the variable-speed approach has a faster response with regards to avoiding aerodynamic stall, allows for a higher power output for a given sea state and may also result in power smoothing. However, the use of an airflow valve (for example, the relief valve in figure 1.2) allows for the control of the average power output. Therefore, a combination of the two approaches may produce the best result.

Based on the need to maximise turbine efficiency, generation can be broken down into two modes of operation:

1. The first mode involves normal operation where the system has already adjusted to the given sea state. In this mode, any valve function and speed change will have already been completed. The pulsating wave power drives the SCIG via the air-chamber and Wells turbine.
2. The second mode of operation involves the WEC response in an attempt to avoid poor turbine efficiency as a consequence of a transition to a different sea state. As previously mentioned, this may include some combination of valve and speed control. This mode is a transition mode between two consecutive operating conditions (for two different sea states) as defined by mode 1 above.

The above-mentioned modes of operation are used to define the dynamics for generator model evaluation. These modes are now discussed in more detail together with their consideration in model evaluation. For simplicity, linear wave theory is assumed which approximates ocean waves as sinusoids with a particular wave amplitude and wave period [**8**].

1.3.3.1 SCIG Operation for a Constant Sea State

In this case, valve position and generator speed has been set and the pulsating wave power is absorbed by the WEC without turbine stalling [**5**,**8**,**9**]. A set generator speed implies a stator voltage supply that is constant in amplitude and frequency [**2**,**5**]. The turbine torque and mechanical power output is approximately sinusoidal in nature [**5**,**8**,**9**]. Owing to turbine rectification, two turbine torque/power oscillations occur for each wave period [**8**,**9**].

The pulsating turbine torque produces a pulsating turbine/generator speed as a result of the generator slip required to produce an opposing electromagnetic torque. The turbine attempts to drive the generator faster than the set synchronous velocity while the generator applies a

reactive torque so as to bring the rotor speed back down towards synchronous velocity. Since induction machines usually operate at low slip values, any speed variation is not expected to be very large [**2**]. This is a consequence of a steep machine torque-speed curve near synchronous velocity [**1**].

The generator speed and torque oscillations as a result of the pulsating turbine mechanical power will depend on the corresponding torque-speed curve for the given voltage amplitude and frequency [**2**]. These oscillations may be reduced by a large system inertia as a result of the flywheel effect which would function in reducing the oscillations in generator power [**4**].

The worst fluctuation in generator power for a given sea state would be an oscillating power ranging from light generation to rated generation [**5**,**9**]. This would be typical of systems with small inertias where the generator electromagnetic torque and system speed would be synchronised with the input prime-mover torque as shown in [**9**]. In some cases, the SCIG may even operate as a motor during the cyclic intervals of low turbine power output [**5**].

Typical sinusoidal wave periods range from $8\ \mathrm{s} - 10\ \mathrm{s}$ [**5**,**9**,**13**]. As previously mentioned, two turbine torque/power oscillations occur for each wave period. Therefore, expected power/torque dynamics would be sinusoidal with a period of $4\ \mathrm{s} - 5\ \mathrm{s}$.

1.3.3.2 SCIG Operation for a Change in Sea State

Generator input dynamics should also be considered for the WEC response to a change in sea state as the system moves to a new operating point for maximum turbine efficiency. This would include decreasing/increasing generator speed for low/high-excitation sea states as previously described [**5**,**8**]. Characterising the dynamic generator inputs for the purposes of this research is more difficult than in the previous case. This is because the WEC response to a change in system speed is not exactly known without explicitly considering all system components. Different dynamic generator inputs could be a consequence of:

- Different combinations of valve-position and generator-speed control.
- Different system transition times in combination with different system inertias. Transition times may also be a function of limiting conditions such as limits on stator current [**13**].
- The presence/absence of turbine stalling together with the point in time during which the transition is initiated.

Therefore, SCIG model evaluation will not consider actual dynamic inputs in response to a change in sea state. Instead, an informative yet simple dynamic case is considered which may form the basis for future development.

1.3.3.2.1 Input Dynamics Considered

A desired change in system speed would be initiated by the corresponding change in generator electrical excitation (voltage amplitude and frequency). Constant volts-per-hertz

generator control is assumed where a change in rotor speed is brought about by a change in stator electrical frequency [**2**]. The magnitude of stator supply voltage is also regulated so as to avoid magnetic saturation.

A change in system speed is not required to be effective very quickly. This is because a change in sea state is not likely to occur very frequently – certainly not at the wave frequency. For the purpose of model evaluation, a sinusoidally-varying rotor speed (excitation frequency) is assumed where the sea-states vary between low- and highly-excited conditions continuously.

The resulting turbine torque as observed by the generator is assumed to be sinusoidal for simplicity.

1.3.3.3 Final Remarks

SCIG operation for a constant sea state involves a steady-state voltage supply and a dynamic prime-mover mechanical torque. In the case of a change in sea state, both electrical and mechanical generator inputs are dynamic in nature.

Only these two cases are considered in the evaluation of SCIG modelling. Generator operation involving system start-up/shutdown is not considered and is left for future development. Inclusion of the complete WEC system would facilitate this investigation as well as a conclusive investigation into WEC response to a change in sea state. This is also left for future development.

1.3.4 Existing SCIG Model Solutions for an OWC WEC

In order to place this research into context with respect to existing work in the field OWC WECs, the use of existing induction generator models is now considered. The focus here is on electrical-component modelling.

1.3.4.1 Per-Phase Steady-State Equivalent Circuit Model

The work presented in [**4**] is concerned with reducing the fluctuation in generated power which is typical of the wave-energy problem as illustrated in figure 1.1. The work assumes an OWC WEC fitted with an impulse turbine which drives an induction generator. The effect of increasing system inertia together with different generator parameters is observed.

In this analysis, the per-phase steady-state equivalent circuit model is assumed for the induction generator. This is because the wave period and the period at which the sea state varies are both large compared with the generator electrical response [**4**]. As presented in [**2**], the model is used from a phasor (frequency-domain) perspective. At any given point in time, voltage and current signals are represented by their corresponding RMS equivalents which allows for the calculation of a "varying" average power. The chosen mechanical model is the typical model used for a rotational system as previously described.

Based on this approach, the only system dynamics that are considered are the mechanical dynamics as given by the mechanical system differential equation. The electrical system is evaluated by a simple phasor calculation (no differential equations) based on the variables for the given time-step.

The approach of the proposed research involves implementing the given steady-state circuit model from a time-based/differential-equation perspective so as to consider the electrical dynamics of the corresponding circuit model. The simulation of instantaneous-time voltage and current waveforms is desirable for dynamic generation conditions so that generator transients may be observed – this is not possible with a phasor approach. The time-based approach would also allow for the calculation of instantaneous per-phase power as opposed to just an average power which is the case for the phasor approach. Knowledge of instantaneous per-phase powers allows for the calculation of instantaneous total power and instantaneous electromagnetic torque as opposed to average quantities using the phasor approach.

1.3.4.2 Equivalent Dynamic Circuit Model

The purpose of the research in [**8**] is to establish the improvement in WEC output power as a result of avoiding Wells turbine stalling in the case of an OWC WEC. The research considers the effect of turbine speed control as well as airflow control achieved through valve action. The work assumes a DFIG.

In generating the various simulation results, the equivalent dynamic model expressed in terms of "qd0" components is assumed. This is the same electrical model to be evaluated in the proposed research. In [**8**], the electrical model is used in simulating the electrical power output of the WEC. In the proposed research, the model suitability is not assumed and is evaluated by considering generator response as previously described.

The analysis in [**8**] also assumes a typical mechanical model for rotating systems.

1.3.4.3 Final Remarks

An important difference between the proposed research problem and the work presented in [**4**,**8**] is that the research problem does not assume the use of the generator models adopted in [**4**,**8**]. Instead, experimental and simulated generator responses are compared for model evaluation so as to allow for a conclusion regarding model applicability considering the given generation application. Furthermore, a comparison of model performance is desirable if possible.

It is desired for time-instantaneous generator variables (such as stator voltage and current) to be modelled. An instantaneous-time approach allows for a direct comparison of model/simulation results with experimental results.

The steady-state circuit model is tested for a case of dynamic generation. In order to model dynamic operation, the model is considered from a time-based/differential-equation perspective. As presented in [**4**], the model may be implemented from a phasor perspective and evaluated at each point in time; however, the model dynamics are not considered in such an analysis. Therefore, the model is not evaluated with this approach together with the reasons given in section 1.3.4.1 – the phasor approach of [**4**] is not a true instantaneous-time approach.

1.4 Dissertation Breakdown

The remainder of the dissertation is broken down as follows:

- Chapter 2 presents the SCIG electrical and mechanical models to be evaluated together with the means of approximating the various initial conditions for simulation purposes.
- Chapter 3 reveals the experimental and measurement setup used in establishing the experimental generator response – the use of inverter-based generator excitation as well as the effect of experimental scaling is discussed.
- Chapter 4 documents the parameters of the experimental SCIG to be used in the model simulations while highlighting the parameterisation process.
- Chapter 5 presents an evaluation of the given SCIG models for dynamic generation. This evaluation is based on model stability and a comparison of experimental and simulation test results. The effect of an inverter-based generator supply as opposed to a truly sinusoidal supply is also observed.
- Chapter 6 concludes on the work presented in this dissertation with a focus on the modelling of a SCIG given the dynamics of an OWC WEC.
- Appendix A highlights basic induction-machine construction and operation.
- Appendix B is a summary of the development of the equivalent dynamic circuit model.
- Appendix C details the measurement system design and implementation including the measurement circuit layout and equipment list.
- Appendix D details the measurement system calibration.

1.5 References

[1] Krause P. C., Wasynczuk O., and Sudhoff S. D., *Analysis of Electric Machinery and Drive Systems*, 2nd ed., El-Hawary M. E., Ed. Hoboken, United States of America: John Wiley & Sons, Inc., 2002.

[2] Sen P. C., *Principles of Electric Machines and Power Electronics*, 2nd ed. Hoboken, United States of America: John Wiley & Sons, Inc., 1997.

[3] Burns R. S., *Advanced Control Engineering*. Oxford, United Kingdom: Butterworth-Heinemann, 2001.

[4] Muthukumar S. et al., "On Minimizing the Fluctuations in the Power Generated from a Wave Energy Plant," in *2005 IEEE International Conference on Electric Machines and Drives*, San Antonio, 2005, pp. 178-185.

[5] O'Sullivan D. L. and Lewis A.W., "Generator Selection and Comparative Performance in Offshore Oscillating Water Column Ocean Wave Energy Converters," *IEEE Transactions on Energy Conversion*, vol. 26, no. 2, pp. 603-614, June 2011.

[6] de O. Falcão A. F., "Wave energy utilization: A review of the technologies," *Renewable and Sustainable Energy Reviews*, vol. 14, no. 3, pp. 899-918, April 2010.

[7] Murray D. B., Hayes J. G., Egan M. G., and O'Sullivan D. L., "Supercapacitor Testing for Power Smoothing in a Variable Speed Offshore Wave Energy Converter," in *Twenty-Sixth Annual IEEE Applied Power Electronics Conference and Exposition*, Fort Worth, 2011, pp. 1933-1939.

[8] Amundarain M., Alberdi M., Garrido A. J., and Garrido I., "Modeling and Simulation of Wave Energy Generation Plants: Output Power Control," *IEEE Transactions on Industrial Electronics*, vol. 58, no. 1, pp. 105-117, January 2011.

[9] Darabi A. and Poriavali P., "Guide Vanes Effect of Wells Turbine on OWC Wave Power Plant Operation," in *The World Congress on Engineering 2007*, London, 2007, pp. 465-469.

[10] Cashman D. P., O'Sullivan D. L., Egan M. G., and Hayes J. G., "Modelling and Analysis of an Offshore Oscillating Water Column Wave Energy Converter," in *8th European Wave and Tidal Energy Conference*, Uppsala, 2009, pp. 924-933.

[11] Suzuki M., "Design Method of Guide Vane for Wells Turbine," *Journal of Thermal Science*, vol. 15, no. 2, pp. 126-131, June 2006.

[12] Thakker A., Frawley P., Khaleeq H. B., and Bajeet E. S., "Comparison of 0.6 m Impulse and Wells Turbines for Wave Energy Conversion Under Similar Conditions," in *Eleventh International Offshore and Polar Engineering Conference*, Stavanger, 2001, pp. 630-633.

[13] "Islay LIMPET Wave Power Plant," The Queen's University of Belfast, Report (1 November 1998 - 30 April 2002). Available at: http://cordis.europa.eu/documents/documentlibrary/66628981EN6.pdf, Last accessed: 16 May 2014,.

2 The Modelling of a SCIG

2.1 Introduction

The purpose of this chapter is to present the models considered for modelling a squirrel-cage induction machine operating in quasi-steady-state generation. To facilitate understanding, basic induction machine construction and operation is highlighted in appendix A. This includes important concepts such as the rotating air-gap magnetic field, electrical versus mechanical units of space and time, basic winding arrangement, rotor slip and the steady-state torque-speed curve.

The electrical-component models considered in this chapter include the per-phase steady-state equivalent circuit model as well as the equivalent dynamic circuit model [**1**,**2**]. The steady-state model is presented first as it is the simpler more-intuitive of the two models. The dynamic model generalised to the arbitrary reference frame is then presented. Modelling assumptions/simplifications are identified for both models as appropriate. An important consideration is the quantification of magnetic core loss.

The development of dynamic circuit model including its reference-frame transformations is summarised in appendix B [**2**].

Once the mechanical model is presented, the overall models are discussed with consideration given to model simulation. Model non-linearity and possible time variability is revealed; these are also important characteristics for model stability evaluation presented in chapter 5. Important initial conditions are identified together with their quantification. Of particular importance are the rotor currents which are not easily defined/measured in a squirrel-cage rotor construction.

2.2 Electrical Component Models

2.2.1 Model Assumptions

The dynamic circuit model is a generic induction machine model whereas the steady-state circuit model assumes short-circuited rotor windings and, therefore, directly models a squirrel-cage induction machine [**1**,**2**]. Both models are based on the assumption of sinusoidally-distributed rotor and stator windings as well as a magnetically linear machine where no magnetic saturation occurs [**2**]. For simplicity and circuit model symmetry, the dynamic model and its steady-state equivalent assume a symmetrical induction machine where the corresponding parameters of all three phases (such as stator winding resistance) are identical [**2**].

For ideal machine operation, it is desired that the three-phase excitation is balanced [**1**]. However, this is only an assumption of the steady-state circuit model derivation [**2**].

2.2.2 Per-Phase Steady-State Equivalent Circuit Model

The per-phase steady-state equivalent circuit model of a three-phase squirrel-cage induction machine is now presented as a summary of [**1**]. Steady-state operation is such that the stator voltage excitation is balanced and constant in amplitude and frequency; the mechanical torque applied to the rotor by a prime-mover/load is also constant [**2**]. As a result, the stator current is balanced and constant in amplitude and frequency and the rotor speed is also constant. From a machine operation perspective one point in time is simply a time-shifted representation of any other point in time.

The circuit model is given in figure 2.1 [**1**]:

- v_s is the per-phase stator excitation voltage
- i_s is the per-phase stator current
- R_s is the per-phase stator winding resistance
- L_{ls} is the per-phase stator-winding leakage inductance
- i_m is the per-phase stator magnetising current
- L_M is the per-phase stator magnetising inductance
- e_s is the per-phase stator winding induced voltage
- e'_r is the per-phase rotor induced voltage e_r but referred to the stator
- i'_r is the per-phase rotor current i_r but referred to the stator
- L'_{lr} is the per-phase rotor leakage inductance L_{lr} but referred to the stator
- R'_r is the per-phase rotor resistance R_r but referred to the stator

s is the rotor slip as defined in equation A.2 of appendix A. The rotor equivalent circuit model is arranged so as to operate at stator frequency f_s, thus, allowing for connection with the stator equivalent circuit model [**1**]. The rotor quantities are also transformed to stator-equivalent quantities (regarding magnitude) through the stator-rotor turns ratio a.

The rotor effective resistance $\frac{R'_r}{s}$ can be broken down into two parts: R'_r and $\frac{R'_r(1-s)}{s}$ as shown in figure 2.1. The first resistance component, as mentioned above, represents the actual per-phase rotor resistance. The second resistance component is dependent on the operating slip of the induction machine and, therefore, accounts for the energy transferred to (positive resistance value for motoring) or received from (negative resistance value for generating) the mechanical system. The magnetic core loss is not included in the circuit model of figure 2.1. A discussion on modelling magnetic core loss is given in section 2.2.5.

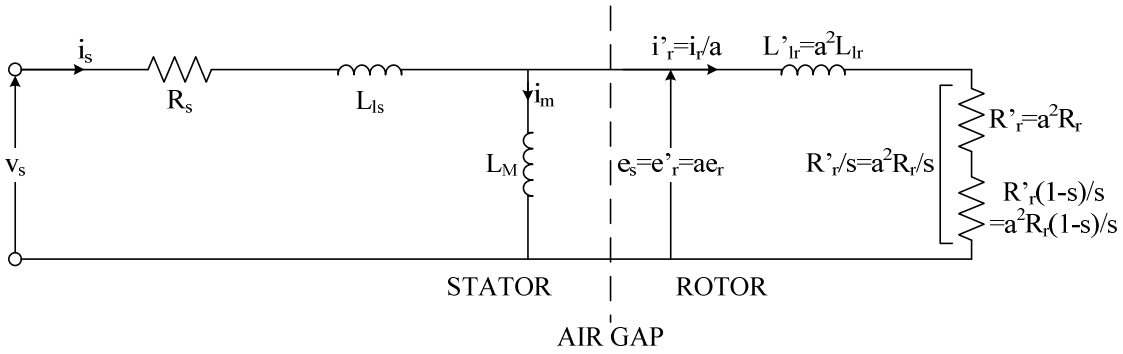

Figure 2.1: Per-Phase Steady-State Equivalent Circuit Model of a Squirrel-Cage Induction Machine – adapted from [**1**,**2**]

2.2.2.1 Power Flow in a Squirrel-Cage Induction Machine

For steady-state motor operation, the relationship between the power transferred across the air gap (from the stator to the rotor) $\overline{p_{ag}}$, the power dissipated in the rotor resistance $\overline{p_{R'_r}}$ and the mechanical power developed $\overline{p_{mech}}$ is given by the ratio [**1**]

$$\overline{p_{ag}}:\overline{p_{R'_r}}:\overline{p_{mech}} = 1:s:1-s \tag{2.1}$$

For motoring action, friction and windage losses are still to be subtracted from $\overline{p_{mech}}$, whereas, in generation, $\overline{p_{mech}}$ is the mechanical input to the generator already considering these losses. Noting that $\overline{p_{mech}}$ and s are negative for generation, equation 2.1 may be re-written as

$$\overline{p_{mech}}:\overline{p_{R'_r}}:\overline{p_{ag}} = 1:\frac{s}{1-s}:\frac{1}{1-s} \tag{2.2}$$

From equation 2.2, $\overline{p_{ag}}$ is negative and $\overline{p_{R'_r}}$ is positive during generating as expected. It is observed from equation 2.1 and equation 2.2 that the induction machine operates more efficiently (in terms of rotor resistive loss) as a motor/generator at lower values of slip [**1**]. However, maximum efficiency does not imply maximum generated power. The relationship of equation 2.2 is illustrated in figure 2.2 where the SCIG is more efficient for lower values of rotor slip.

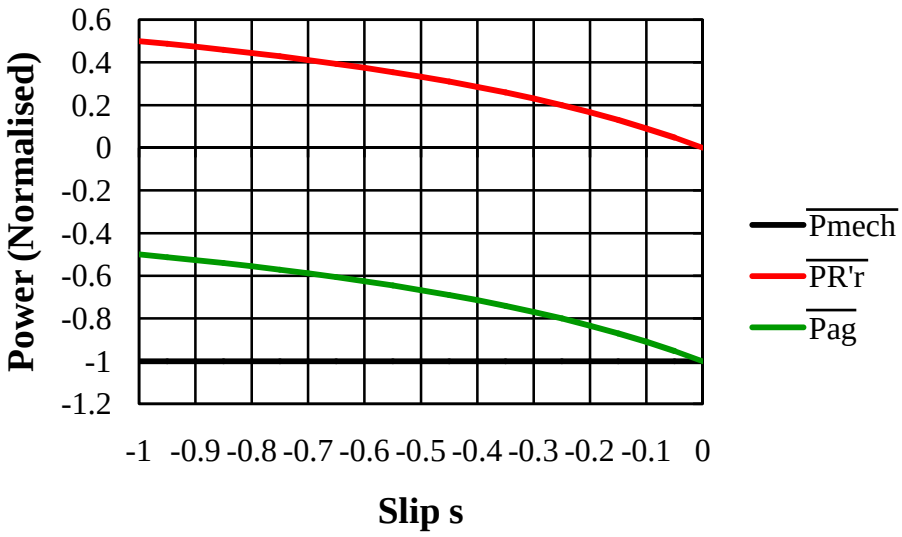

Figure 2.2: Power Flow across the Air-Gap of a SCIG

Steady-state power flow in a SCIG is presented in figure 2.3 [**1**]. The only difference that applies for motoring action is that power flows from the electrical system ($\overline{p_{elec}}$) to the mechanical system ($\overline{p_{shaft}}$).

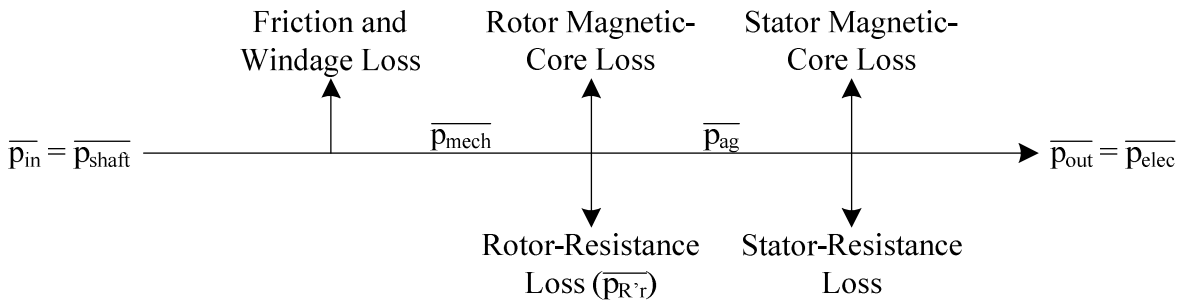

Figure 2.3: Steady-State Power Flow in a SCIG – adapted from [**1**]

2.2.2.2 Electromagnetic Torque

Variables linking the electrical and mechanical components include the electromagnetic torque applied to the rotor by the rotating magnetic field τ_e as well as the associated transferred power p_{mech}. The model convention adopted assumes a driving torque with electro-mechanical power flow to the rotor as positive (motoring action). The per-phase electromagnetic torque exerted on the rotor is given as [**1**]

$$\tau_{epp} = \frac{R'_r {i'_r}^2}{\omega_{synm} s} \tag{2.3}$$

where ω_{synm} $(\mathrm{rad.\,s^{-1}})$ is the mechanical synchronous velocity (velocity of the rotating magnetic field) relative to the stator expressed as [**1**]

$$\omega_{synm} = \frac{2\pi n_{syn}}{60} = \frac{4\pi f_s}{P} \tag{2.4}$$

n_{syn} is the synchronous velocity expressed in rpm and P is the machine magnetic-pole count.

The total electromagnetic torque τ_e is found by adding all of the per-phase torque components. The corresponding power flow between the electrical and mechanical subsystems is [**1**]

$$p_{mech} = \tau_e \omega_{rsm} \tag{2.5}$$

ω_{rsm} (rad.s^{-1}) is the mechanical rotor velocity relative to the stator where the positive direction of rotation is given by the rotating air-gap magnetic field.

In a balanced three-phase system at steady-state the total instantaneous electrical power is constant and equal to the sum of the per-phase average powers (which are equal) [**1**]. As a result, the total instantaneous mechanical torque and power developed by the magnetic field is also constant [**1**].

2.2.2.3 State-Space Representation

The steady-state circuit model is used in the context of dynamic (quasi-steady-state) generation and is considered from a state-space perspective. The per-phase steady-state model of figure 2.1 may be written in state-space form as

$$\begin{bmatrix} \frac{di_s}{dt} \\ \frac{di_m}{dt} \\ \frac{di'_r}{dt} \end{bmatrix} = \begin{bmatrix} -\frac{R_s L'_{lr} + L_M R_s}{D_1} & 0 & -\frac{L_M R'_r}{D_1 s} \\ -\frac{R_s L'_{lr}}{D_1} & 0 & \frac{L_{ls} R'_r}{D_1 s} \\ -\frac{L_M R_s}{D_1} & 0 & -\frac{L_{ls} R'_r + L_M R'_r}{D_1 s} \end{bmatrix} \begin{bmatrix} i_s \\ i_m \\ i'_r \end{bmatrix} + \begin{bmatrix} \frac{L'_{lr} + L_M}{D_1} \\ \frac{L'_{lr}}{D_1} \\ \frac{L_M}{D_1} \end{bmatrix} v_s \tag{2.6}$$

where

$$D_1 = L_{ls} L'_{lr} + L_M L'_{lr} + L_M L_{ls} \tag{2.7}$$

and t is time. It is observed that none of the derivatives of the state variables are dependent on the magnetising current state variable i_m. Therefore, the third-order state-space model of equation 2.7 may be reduced to a second model:

$$\begin{bmatrix} \frac{di_s}{dt} \\ \frac{di'_r}{dt} \end{bmatrix} = \begin{bmatrix} -\frac{R_s L'_{lr} + L_M R_s}{D_1} & -\frac{L_M R'_r}{D_1 s} \\ -\frac{L_M R_s}{D_1} & -\frac{L_{ls} R'_r + L_M R'_r}{D_1 s} \end{bmatrix} \begin{bmatrix} i_s \\ i'_r \end{bmatrix} + \begin{bmatrix} \frac{L'_{lr} + L_M}{D_1} \\ \frac{L_M}{D_1} \end{bmatrix} v_s \tag{2.8}$$

with

$$i_m = i_s - i'_r \tag{2.9}$$

From figure 2.1, it is observed that the circuit model has three currents with each current flowing in a modelled inductor. Since each inductor represents an energy storage element, a

third-order state-space model such as that given by equation 2.6 might be expected. However, the three currents are related by Kirchhoff's Current Law shown in equation 2.9 which implies that if two currents are known, the third one is automatically known. Therefore, the third-order state-space model may be reduced to a second-order one with the third current found by Kirchhoff's Current Law. This is supported in [**3**] (page 232) where the system state variables are defined as *the smallest number of states that are required to describe the dynamic nature of the system*.

The concept of rotor slip and synchronous velocity implies a three-phase sinusoidal electrical excitation with a common excitation frequency. Furthermore, the model assumes a non-zero rotor slip s.

2.2.3 Equivalent Dynamic Circuit Model

The equivalent dynamic circuit model is now presented [**2**]. The model is expressed in terms of the arbitrary reference-frame where substitution of the corresponding angular velocity determines the chosen reference frame.

Development of the arbitrary-reference-frame-based model using general reference-frame theory is detailed in [**2**]. A summary of this development is given in appendix B for convenience.

The dynamic model is significantly more complicated than the steady-state model given in figure 2.1. However, it does not assume steady-state operation. Derivation of the steady-state model as a special case of the dynamic model is given in [**2**].

2.2.3.1 Arbitrary Reference Frame in Relation to the Stator and Rotor Circuits

The dynamic model involves a transformation of the induction-machine phase variables to an arbitrary reference frame such that [**2**]

$$g_{as}, g_{bs}, g_{cs} \rightarrow g_{qs}, g_{ds}, g_{0s}$$

and

$$g'_{ar}, g'_{br}, g'_{cr} \rightarrow g'_{qr}, g'_{dr}, g'_{0r}$$

for the stator and rotor circuits respectively. g is a placeholder for the machine terminal voltages v, terminal currents i and flux linkages λ (Wb.turns). The subscripts a, b and c refer to the three phases of the induction machine while q, d and 0 refer to the arbitrary-reference-frame components. Subscripts s and r refer to stator and rotor quantities respectively. The rotor circuit variables have been referred to the stator circuit via the effective winding ratio.

The relationship between the arbitrary reference frame and the stator and rotor circuits is illustrated in figure 2.4 where [**2**]:

- θ_{rs} is the rotor circuit angular displacement relative to the stator circuit and ω_{rs} is the corresponding angular velocity
- θ_{refs} is the reference frame angular displacement relative to the stator circuit and ω_{refs} is the corresponding angular velocity
- θ_{refr} is the reference frame angular displacement relative to the rotor circuit

As shown in figure 2.4, the q and d arbitrary-reference-frame components are trigonometrically related to the corresponding machine variables [**2**]. The "zero" reference-frame components (g_{0s} and g'_{0r}) are not shown in figure 2.4 since the corresponding transformations do not depend on the relative reference-frame displacements (θ_{refs} and θ_{refr}).

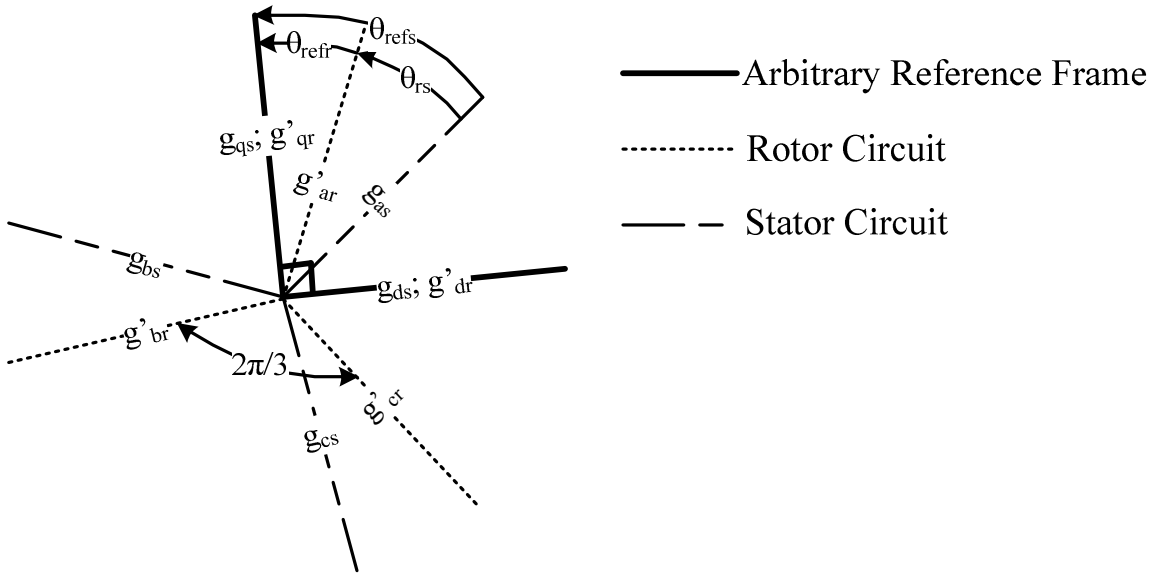

Figure 2.4: Transformation of Machine Variables to the Arbitrary Reference Frame (angles are in electrical radians) – adapted from [**2**]

2.2.3.2 Dynamic Circuit Model in the Arbitrary Reference Frame

The equivalent circuit model expressed in terms of the arbitrary reference frame is illustrated in figure 2.5 [**2**]. The model is a generic induction machine model accommodating both wound-rotor and squirrel-cage induction machines.

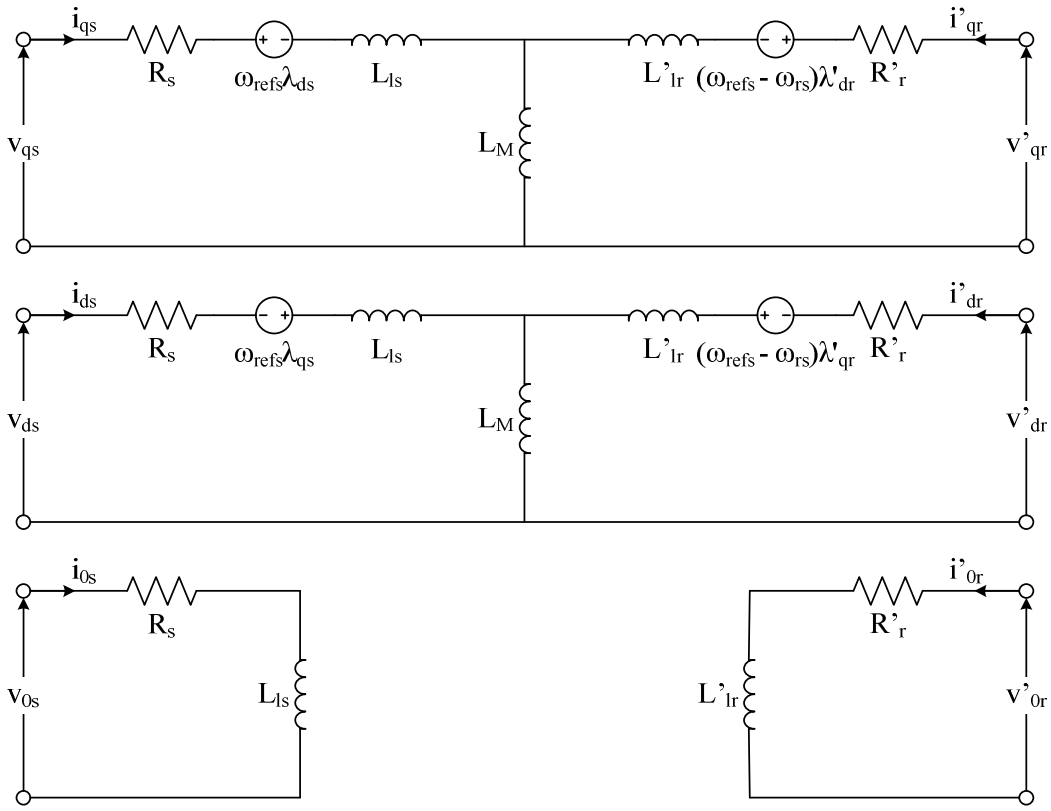

Figure 2.5: Induction Machine Dynamic Circuit Model expressed in terms of an Arbitrary Reference Frame – adapted from [**2**]

The voltage equations corresponding to the model in figure 2.5 are [**2**]

$$\boldsymbol{v}_{qd0s} = \boldsymbol{R}_s \boldsymbol{i}_{qd0s} + \omega_{refs} \boldsymbol{\lambda}_{dqs} + \frac{d}{dt} \boldsymbol{\lambda}_{qd0s} \tag{2.10}$$

$$\boldsymbol{v'}_{qd0r} = \boldsymbol{R'}_r \boldsymbol{i'}_{qd0r} + \left(\omega_{refs} - \omega_{rs}\right) \boldsymbol{\lambda'}_{dqr} + \frac{d}{dt} \boldsymbol{\lambda'}_{qd0r} \tag{2.11}$$

where

$$\left(\boldsymbol{g}_{qd0s}\right)^T = [g_{qs} \quad g_{ds} \quad g_{0s}] \tag{2.12}$$

$$\left(\boldsymbol{g'}_{qd0r}\right)^T = [g'_{qr} \quad g'_{dr} \quad g'_{0r}] \tag{2.13}$$

$$\left(\boldsymbol{\lambda}_{dqs}\right)^T = [\lambda_{ds} \quad -\lambda_{qs} \quad 0] \tag{2.14}$$

$$\left(\boldsymbol{\lambda'}_{dqr}\right)^T = [\lambda'_{dr} \quad -\lambda'_{qr} \quad 0] \tag{2.15}$$

T refers to the transpose of a matrix/vector. $\boldsymbol{R}_s$ and $\boldsymbol{R'}_r$ are diagonal matrices accounting for the stator and rotor phase-winding resistances respectively. A symmetrical induction machine implies equal diagonal values. As shown in figure 2.5, $\boldsymbol{v'}_{qd0r}$ represents the terminal voltages applied to the rotor windings. In the case of a SCIG, these voltages are short-circuited such that

$$v'_{ar} = v'_{br} = v'_{cr} = 0\ \text{V} \rightarrow v'_{qr} = v'_{dr} = v'_{0r} = 0\ \text{V} \tag{2.16}$$

This is discussed in more detail in section B.3.4. In order to complete the circuit model of figure 2.5 from equations 2.10-2.11, the stator and rotor flux linkages are given in terms of stator and rotor terminal currents from [**2**]

$$\begin{bmatrix} \boldsymbol{\lambda}_{qd0s} \\ \boldsymbol{\lambda}'_{qd0r} \end{bmatrix} = \begin{bmatrix} \begin{bmatrix} L_{ls}+L_M & 0 & 0 \\ 0 & L_{ls}+L_M & 0 \\ 0 & 0 & L_{ls} \end{bmatrix} & \begin{bmatrix} L_M & 0 & 0 \\ 0 & L_M & 0 \\ 0 & 0 & 0 \end{bmatrix} \\ \begin{bmatrix} L_M & 0 & 0 \\ 0 & L_M & 0 \\ 0 & 0 & 0 \end{bmatrix} & \begin{bmatrix} L'_{lr}+L_M & 0 & 0 \\ 0 & L'_{lr}+L_M & 0 \\ 0 & 0 & L'_{lr} \end{bmatrix} \end{bmatrix} \begin{bmatrix} \boldsymbol{i}_{qd0s} \\ \boldsymbol{i}'_{qd0r} \end{bmatrix} \tag{2.17}$$

The parameters $R_s, L_{ls}, L_M, L'_{lr}$ and R'_r are as defined for the steady-state circuit model of figure 2.1.

The electromagnetic torque (positive for motoring) expressed in terms of current components is given as [**2**]

$$\tau_e = \frac{3PL_M}{4}\left(i_{qs}i'_{dr} - i_{ds}i'_{qr}\right) \tag{2.18}$$

2.2.3.3 Simulation of the Dynamic Circuit Model

The voltage equations 2.10-2.11 expressed only in terms of current variables and not flux-linkage variables have more than one current derivative with respect to time [**2**]. Therefore, for simplicity, the dynamic circuit model of figure 2.5 will be considered with flux linkages as state variables giving a state equation [**2**]

$$\begin{bmatrix} \frac{d}{dt}\lambda_{qs} \\ \frac{d}{dt}\lambda_{ds} \\ \frac{d}{dt}\lambda_{0s} \\ \frac{d}{dt}\lambda'_{qr} \\ \frac{d}{dt}\lambda'_{dr} \\ \frac{d}{dt}\lambda'_{0r} \end{bmatrix} = \begin{bmatrix} -\frac{R_s L'_{RR}}{D_2} & -\omega_{refs} & 0 & \frac{R_s L_M}{D_2} & 0 & 0 \\ \omega_{refs} & -\frac{R_s L'_{RR}}{D_2} & 0 & 0 & \frac{R_s L_M}{D_2} & 0 \\ 0 & 0 & -\frac{R_s}{L_{ls}} & 0 & 0 & 0 \\ \frac{R'_r L_M}{D_2} & 0 & 0 & -\frac{R'_r L_{SS}}{D_2} & -\left(\omega_{refs}-\omega_{rs}\right) & 0 \\ 0 & \frac{R'_r L_M}{D_2} & 0 & \left(\omega_{refs}-\omega_{rs}\right) & -\frac{R'_r L_{SS}}{D_2} & 0 \\ 0 & 0 & 0 & 0 & 0 & -\frac{R'_r}{L'_{lr}} \end{bmatrix} \begin{bmatrix} \lambda_{qs} \\ \lambda_{ds} \\ \lambda_{0s} \\ \lambda'_{qr} \\ \lambda'_{dr} \\ \lambda'_{0r} \end{bmatrix} + \begin{bmatrix} 1 & 0 & 0 & 0 & 0 & 0 \\ 0 & 1 & 0 & 0 & 0 & 0 \\ 0 & 0 & 1 & 0 & 0 & 0 \\ 0 & 0 & 0 & 1 & 0 & 0 \\ 0 & 0 & 0 & 0 & 1 & 0 \\ 0 & 0 & 0 & 0 & 0 & 1 \end{bmatrix} \begin{bmatrix} v_{qs} \\ v_{ds} \\ v_{0s} \\ v'_{qr} \\ v'_{dr} \\ v'_{0r} \end{bmatrix} \tag{2.19}$$

where

$$L_{SS} = L_{ls} + L_M \tag{2.20}$$

$$L'_{RR} = L'_{lr} + L_M \tag{2.21}$$

$$D_2 = L_{SS}L'_{RR} - {L_M}^2 \tag{2.22}$$

The current variables are related to the flux linkages by [**2**]

$$\begin{bmatrix} i_{qs} \\ i_{ds} \\ i_{0s} \\ i'_{qr} \\ i'_{dr} \\ i'_{0r} \end{bmatrix} = \frac{1}{D_2}\begin{bmatrix} L'_{RR} & 0 & 0 & -L_M & 0 & 0 \\ 0 & L'_{RR} & 0 & 0 & -L_M & 0 \\ 0 & 0 & \frac{D_2}{L_{ls}} & 0 & 0 & 0 \\ -L_M & 0 & 0 & L_{SS} & 0 & 0 \\ 0 & -L_M & 0 & 0 & L_{SS} & 0 \\ 0 & 0 & 0 & 0 & 0 & \frac{D_2}{L'_{lr}} \end{bmatrix}\begin{bmatrix} \lambda_{qs} \\ \lambda_{ds} \\ \lambda_{0s} \\ \lambda'_{qr} \\ \lambda'_{dr} \\ \lambda'_{0r} \end{bmatrix} \tag{2.23}$$

The electromagnetic torque may also be expressed in terms of flux linkage components using [**2**]

$$\tau_e = \frac{3PL_M}{4D_2}\left(\lambda_{qs}\lambda'_{dr} - \lambda_{ds}\lambda'_{qr}\right) \tag{2.24}$$

In order to use the model, terminal voltages expressed as machine variables need to be transformed to the arbitrary reference frame as model inputs and terminal currents need to be transformed from the arbitrary reference frame back to machine-variable form as model outputs. This allows for a comparison with practical/experimental measurements which are in machine-variable form. The appropriate transformation of stator variables to the arbitrary reference frame is given by [**2**]

$$\boldsymbol{g}_{qd0s} = \boldsymbol{K}_s\boldsymbol{g}_{abcs} \tag{2.25}$$

where

$$(\boldsymbol{g}_{abcs})^T = [g_{as} \quad g_{bs} \quad g_{cs}] \tag{2.26}$$

$$\boldsymbol{K}_s = \frac{2}{3}\begin{bmatrix} \cos(\theta_{refs}) & \cos\left(\theta_{refs} - \frac{2\pi}{3}\right) & \cos\left(\theta_{refs} + \frac{2\pi}{3}\right) \\ \sin(\theta_{refs}) & \sin\left(\theta_{refs} - \frac{2\pi}{3}\right) & \sin\left(\theta_{refs} + \frac{2\pi}{3}\right) \\ \frac{1}{2} & \frac{1}{2} & \frac{1}{2} \end{bmatrix} \tag{2.27}$$

A similar transformation exists for the rotor variables where the transformation matrix $\boldsymbol{K_r}$ is $\boldsymbol{K}_s$ but with θ_{refs} replaced by θ_{refr} [**2**]. As shown in figure 2.4, θ_{refr} is given as

$$\theta_{refr} = \theta_{refs} - \theta_{rs} \tag{2.28}$$

Stator variables in the arbitrary reference frame can be transformed back to machine-variable form using the inverse transformation [**2**]

$$\boldsymbol{g}_{abcs} = (\boldsymbol{K}_s)^{-\mathbf{1}}\boldsymbol{g}_{qd0s} \tag{2.29}$$

where

$$(\boldsymbol{K}_s)^{-1} = \begin{bmatrix} \cos(\theta_{refs}) & \sin(\theta_{refs}) & 1 \\ \cos\left(\theta_{refs} - \frac{2\pi}{3}\right) & \sin\left(\theta_{refs} - \frac{2\pi}{3}\right) & 1 \\ \cos\left(\theta_{refs} + \frac{2\pi}{3}\right) & \sin\left(\theta_{refs} + \frac{2\pi}{3}\right) & 1 \end{bmatrix} \tag{2.30}$$

Again, a similar relationship and inverse matrix exists for the rotor variables with θ_{refs} replaced by θ_{refr} [**2**].

2.2.3.4 Reference-Frame Selection

As previously mentioned, the model presented in figure 2.5 is expressed relative to an arbitrary reference frame. The reference frame is specified by the selection of a particular angular velocity ω_{refs}.

Reference frame selection is a considered one if work/analysis is being done in the "qd0" reference frame [**2**]. However, model verification in chapter 5 is achieved through a comparison of simulation and experimental results. In light of this, the simulation outputs will be in machine-variable form and the selection of a particular reference frame is arbitrary in this case.

2.2.4 Electrical Parameter Variability

It is assumed, for the purpose of this research, that the machine electrical parameters are constant. Cases involving variable parameters are left for future consideration. These include, for example, squirrel-cage induction machines with deep-bar and double-cage rotors where the rotor leakage inductance and rotor resistance varies with rotor frequency f_r [**1**].

2.2.5 Magnetic Core Loss

The steady-state and dynamic electrical models in question do not include magnetic core loss. According to [**2**] the magnetic core loss is often negligibly small. As such it is neglected in this research. The inclusion of magnetic core loss in the model of a SCIG is left for future development.

2.3 Induction Machine Mechanical Model

The SCIG mechanical subsystem reduces to a simple free-body diagram of the rotor as illustrated in figure 2.6.The air-gap magnetic field rotation defines the convention for positive rotation [**1**]. The rotor is assumed to be rigid with no hysteresis in any mechanical coupling. The corresponding differential equation is expressed as [**2**,**3**]

$$\tau_e + \tau_{pm} - \tau_{f,w} = J_g \frac{d\omega_{rsm}}{dt} = J_g \dot{\omega_{rsm}} \tag{2.31}$$

τ_e is the total electromagnetic torque (positive for motoring action) as calculated from equations 2.3, 2.18 or 2.24. The prime-mover torque driving the generator rotor is given by τ_{pm}. The opposing friction and windage torque is given as

$$\tau_{f,w} = C_{f,w}\text{sign}(\omega_{rsm})\sqrt[4]{|\omega_{rsm}|} \tag{2.32}$$

This expression is derived in the parameterisation process outlined in chapter 4. $C_{f,w}$ is the friction/windage co-efficient and the function sign() returns the sign (positive/negative) of the rotor angular velocity ω_{rsm}. ω_{rsm} is ω_{rs} but expressed in mechanical radians as discussed in section A.3. The same applies to θ_{rsm} and θ_{rs}. Equation 2.32 is not proposed as a generic friction/windage torque equation but is the most appropriate expression for the experimental setup of chapter 3 as determined through measurement. According to [**2**], losses associated with rotor friction and windage are often small but are still included in the mechanical model.

J_g is the effective rotor moment of inertia. For the experimental setup of chapter 3, this includes inertia associated with the rotor, shaft-encoder, torque transducer and coupling between the rotor and torque transducer. This is considered further in the generator parameterisation of chapter 4.

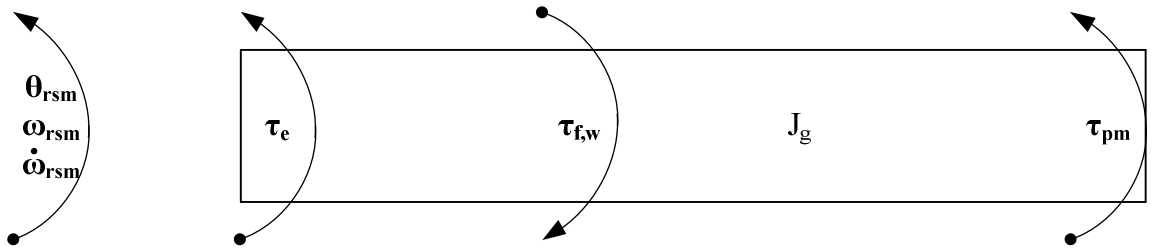

Figure 2.6: Free-Body Diagram of Generator Rotor

2.4 Complete SCIG Model

A discussion on the complete SCIG model is now presented with consideration given to model simulation. This includes the specification of state-variable initial conditions. Model non-linearity and time-variability is also discussed. Non-linearity is important for the stability analysis presented in chapter 5 where the SCIG models are evaluated for dynamic generation.

2.4.1 Equivalent Steady-State Model

The electrical component requires equations 2.8-2.9 to be repeated for each of the three electrical phases. The mechanical component involves equations 2.31-2.32 where the generator electromagnetic torque is given by equation 2.3 repeated for each electrical phase. The machine operating slip is given by equation A.2 where [**1**]

$$\omega_{rsm} = \frac{2\pi n_{rs}}{60} \tag{2.33}$$

n_{rs} is simply the rotor velocity relative to the stator expressed in rpm. As discussed in section 1.3.2, the stator terminal voltages and prime-mover torque are model inputs.

2.4.1.1 Model Non-Linearity and Time-Variability

From equations 2.8, 2.33, A.2 and A.3, the electrical subsystem differential equations may be expressed as

$$\begin{bmatrix} \frac{di_s}{dt} \\ \frac{di'_r}{dt} \end{bmatrix} = \begin{bmatrix} -\frac{R_s L'_{lr} + L_M R_s}{D_1} & -\frac{L_M R'_r}{D_1\left(1-\frac{P}{4\pi f_s}\omega_{rsm}\right)} \\ -\frac{L_M R_s}{D_1} & -\frac{L_{ls} R'_r + L_M R'_r}{D_1\left(1-\frac{P}{4\pi f_s}\omega_{rsm}\right)} \end{bmatrix} \begin{bmatrix} i_s \\ i'_r \end{bmatrix} + \begin{bmatrix} \frac{L'_{lr}+L_M}{D_1} \\ \frac{L_M}{D_1} \end{bmatrix} v_s \tag{2.34}$$

Considering the electromagnetic torque (equation 2.3) and friction/windage torque (equation 2.32), the mechanical subsystem (equation 2.31) is

$$\frac{d\omega_{rsm}}{dt} = \frac{R'_r}{J_g\left(\frac{4\pi f_s}{P} - \omega_{rsm}\right)}\left(i'_{ar}{}^2 + i'_{br}{}^2 + i'_{cr}{}^2\right) + \frac{1}{J_g}\tau_{pm} - \frac{C_{f,w}}{J_g}\,\mathrm{sign}(\omega_{rsm})\sqrt[4]{|\omega_{rsm}|} \tag{2.35}$$

The complete SCIG model is a seventh-order model with the per-phase stator and rotor currents and rotor angular velocity forming the system state variables.

The electrical model component includes the rotor angular velocity in the system matrix and is, therefore, non-linear. Furthermore, the dependence of the system matrix on the stator frequency implies a time-varying model should this be variable.

The mechanical model is also a non-linear expression of system state variables. Again, a variable stator frequency results in a time-varying mechanical model.

Therefore, it is concluded that the complete equivalent steady-state model is non-linear and possibly time-varying.

2.4.1.2 Simulation Considerations

If simulation results are to be compared with practical results, the correct state-variable initial conditions are required. Rotor angular velocity and stator currents at $t = 0$ are easily determined through measurement. However, the rotor construction of a SCIG makes defining and measuring the rotor currents difficult. Therefore, an alternative means of approximating the initial rotor currents is required.

Perhaps the initial rotor currents may be approximated from a phasor analysis of the steady-state circuit model at $t = 0$ for a given stator voltage supply and initial rotor velocity. This is discussed further in section 2.4.2.2 where the dynamic model initial conditions are considered.

2.4.2 Equivalent Dynamic Model

While the equations used may be different, the paradigm adopted in simulating the SCIG dynamic model is as presented in [**2**]:

- The electrical model is evaluated in terms of flux linkages referred to the arbitrary reference frame
- Electrical inputs expressed as machine variables are transformed to this reference frame
- The solved flux linkages are expressed as currents before being transformed back to machine-variable from
- Electromagnetic torque is calculated from the electrical state variables
- The rotor velocity is solved by evaluating the mechanical model

The fundamental difference in the model equations is that in [**2**], the electrical-component equations are arranged so as to accommodate magnetic saturation effects more conveniently. Since saturation is not considered here, this extension is not included for simplicity.

2.4.2.1 Model Non-Linearity and Time-Variability

In order to comment on model non-linearity and time-variability, the system first-order differential equations are considered. The electrical-component differential equations are given by equation 2.19. If the electromagnetic and friction/windage torques are considered in the mechanical model then the mechanical system may be expressed as

$$\frac{d\omega_{rsm}}{dt} = \frac{3PL_M}{4D_2J_g}\left(\lambda_{qs}\lambda'_{dr} - \lambda_{ds}\lambda'_{qr}\right) + \frac{1}{J_g}\tau_{pm} - \frac{C_{f,w}}{J_g}\,\mathrm{sign}(\omega_{rsm})\sqrt[4]{|\omega_{rsm}|} \tag{2.36}$$

From equations 2.19 and 2.36, the SCIG state variables include $\lambda_{qs}, \lambda_{ds}, \lambda_{0s}, \lambda'_{qr}, \lambda'_{dr}, \lambda'_{0r}$ and ω_{rsm} where $\omega_{rs} = \frac{P}{2}\omega_{rsm}$ (equation A.1). Inspection of the electrical subsystem reveals a non-linear model owing to the presence of the rotor angular velocity (state variable) in the system matrix. Furthermore, the model may or may not be time-invariant depending on whether the reference-frame angular velocity is constant or not. Inspection of the mechanical subsystem also reveals a non-linear model as a result of flux-linkage multiplication as well as the fourth root of the rotor angular velocity.

In conclusion, the complete SCIG model is non-linear and possibly time-varying.

2.4.2.2 Simulation Considerations

As previously mentioned, matching initial conditions is required in order for simulation and experimental results to be compared. This includes the initial model state variables and initial reference-frame and rotor angular positions relative to the stator.

The reference-frame transformations depend on θ_{refs} and θ_{refr} where θ_{refr} requires knowledge of θ_{rs} as given by equation 2.28. θ_{refs} and θ_{rs} are easily found through integration of their corresponding angular velocities: ω_{refs} is a model/simulation input

whereas ω_{rs} is a system state variable. The integration process implies that $\theta_{refs}(0)$ and $\theta_{rs}(0)$ are required.

As previously mentioned, the model evaluation presented in chapter 5 is based on machine variables and not quantities referred to the reference frame. Therefore, reference-frame selection is arbitrary as the reference frame does not affect the induction-machine's operating condition. In light of this, the initial reference-frame position ($\theta_{refs}(0)$) is also arbitrary.

However, the same does not apply to the initial rotor position ($\theta_{rs}(0)$). This is because the rotor position determines the instantaneous machine variables for a given operating point. This is shown in equation B.11 where the mutual inductance between the stator and rotor windings is dependent on rotor position [**2**].

The initial rotor angular velocity (state variable) may be quantified through measurement. What remains is to establish the initial machine flux linkages as well as the initial rotor position.

2.4.2.2.1 Initial Flux Linkages

As shown by equations 2.17 and 2.25, the initial flux-linkage state variables ($\lambda_{qs}(0), \lambda_{ds}(0), \lambda_{0s}(0), \lambda'_{qr}(0), \lambda'_{dr}(0)$ and $\lambda'_{0r}(0)$) are derived from the initial stator and rotor currents ($i_{as}(0), i_{bs}(0), i_{cs}(0), i'_{ar}(0), i'_{br}(0)$ and $i'_{cr}(0)$). In the case of a SCIG, measurement of the initial rotor currents is difficult to achieve. Therefore, a means of approximating the initial machine currents (rotor currents in particular) is desired.

If it may be assumed that the initial machine operation approximates some sort of balanced steady-state condition then perhaps a phasor analysis of the steady-state circuit model may be used to approximate the initial stator and rotor currents [**1**,**4**]. A variable steady-state condition may involve a combination including:

- A balanced three-phase voltage supply variable/constant in amplitude and/or frequency
- A varying/constant prime-mover torque

where input variations are slow in nature. The above-mentioned phasor analysis requires knowledge of the stator terminal voltage and rotor velocity. A single phase is evaluated at $t = 0$ – variables of the other phases are merely phase-shifted by $\frac{2\pi}{3}$ and $\frac{4\pi}{3}$ electrical radians respectively.

It is important to note that the rotor-current transformation for the rotor equivalent of equation 2.25 assumes rotor currents referred to the stator regarding magnitude but remaining at rotor frequency. Rotor currents derived from the steady-state circuit model are referred to the stator and are also at stator frequency. This is not a problem because only the initial

($t = 0$) rotor currents are required making frequency irrelevant. Furthermore, there is no phase difference between these rotor currents at stator frequency and rotor frequency [**1**].

The method of approximating the initial generator currents as described above is evaluated for the tests considered in chapter 5 – this method is not proposed as a generic means of deriving initial generator currents.

2.4.2.2.2 Initial Rotor Angular Displacement

As previously mentioned, rotor angular displacement is indirectly involved in all rotor-variable transformations to and from the arbitrary reference frame. This includes the transformation of rotor terminal voltages to the arbitrary reference frame as well as recovery of simulated rotor currents from the arbitrary reference frame.

Since the induction machine is of squirrel-cage construction, the rotor terminal voltages are zero. Therefore, their qd0-equivalents are zero regardless of rotor position. In this regard, $\theta_{rs}(0)$ does not need to be known.

$\theta_{rs}(0)$ is also required in recovering the rotor machine currents from their qd0-equivalents. However, rotor currents are not easily measured/defined for a squirrel-cage rotor construction. Therefore, there is no need for simulated machine-variable rotor currents to correspond with their equivalent experimental currents as these are not measured for comparison. Furthermore, the rotor currents expressed as machine variables do not feature in the electromagnetic torque equations 2.18 and 2.24 so that incorrect rotor currents will not affect simulated generator behaviour.

As mentioned in the previous section, the initial rotor currents (in machine-variable form) are approximated using the steady-state circuit model. These currents still need to be transformed to the chosen reference frame before they can be expressed as flux linkages. It is this transformation that requires $\theta_{rs}(0)$ to be known. Since rotor position is difficult to define owing to its squirrel-cage construction, the initial rotor position is guessed for simulation purposes.

2.4.3 Simulation Implementation

Model implementation involves a time-based SIMULINK implementation where the first-order differential equations are executed by integrators [**5**]. This implementation is convenient considering the non-linear (and possibly time-varying) nature of the complete SCIG model as previously described. The various transformations and other calculations (power etc.) are also easily accommodated on an instantaneous-time basis.

2.5 Conclusion

Two SCIG models are identified by combining two different electrical component models with the equivalent mechanical model. The first electrical model is the per-phase steady-state equivalent circuit model; the other being the equivalent dynamic circuit model.

A symmetrical induction machine with constant parameters is assumed. Magnetic core loss is neglected and magnetic saturation is not modelled. Parameter variability, core loss and magnetic saturation are left for further development.

The SCIG models are found to be non-linear and possibly time-varying. These are important considerations regarding model stability evaluation and model simulation.

Important simulation considerations are identified which include various initial conditions. Of particular importance is the establishment of initial rotor currents which are not easily defined/measured for a squirrel-cage rotor construction. A possible means of approximating initial rotor currents is based on applying a phasor analysis to the steady-state circuit model at $t = 0$ s. This is not proposed as a generic means of identifying initial machine currents but may be useful for conditions of "varying steady-state operation". This approach to approximating initial rotor currents is considered and evaluated together with SCIG model evaluation in chapter 5.

2.6 References

[1] Sen P. C., *Principles of Electric Machines and Power Electronics*, 2nd ed. Hoboken, United States of America: John Wiley & Sons, Inc., 1997.

[2] Krause P. C., Wasynczuk O., and Sudhoff S. D., *Analysis of Electric Machinery and Drive Systems*, 2nd ed., El-Hawary M. E., Ed. Hoboken, United States of America: John Wiley & Sons, Inc., 2002.

[3] Burns R. S., *Advanced Control Engineering*. Oxford, United Kingdom: Butterworth-Heinemann, 2001.

[4] Muthukumar S. et al., "On Minimizing the Fluctuations in the Power Generated from a Wave Energy Plant," in *2005 IEEE International Conference on Electric Machines and Drives*, San Antonio, 2005, pp. 178-185.

[5] Rowell D. (2002, October) State-Space Representation of LTI Systems. [Online]. Available at: http://web.mit.edu/2.14/www/Handouts/StateSpace.pdf, Last accessed: 13 April 2014

3 Experimental Setup and Measurement System for SCIG Model Evaluation

3.1 Introduction

In order to evaluate the applicability of the equivalent steady-state and dynamic SCIG models, simulation results produced by such models need to be compared with experimental measurements. The purpose of this chapter is to describe the experimental setup and measurement system adopted for the experimental testing of a SCIG. This includes:

- The basic experimental setup
- The measurements required
- How these measurements are achieved (measurement system configuration)

Pictures of the complete experimental setup are shown. The use/interpretation of measurement outputs as well as possible improvements is then discussed. Before concluding, the effect of experimental scaling is considered.

Measurement system design and implementation including interference mitigation is presented in appendix C with the corresponding unit testing and calibration given in appendix D.

3.2 Basic Experimental Setup

The basic experimental setup is shown in figure 3.1. A four-pole SCIG is coupled to another identical squirrel-cage induction motor which is controlled so as to reproduce the required torque dynamics. Both squirrel-cage induction machines are interfaced with a typical balanced three-phase sinusoidal supply using Pulse-Width-Modulation-based (PWM) variable speed drives which, in turn, drive the machines. The converter on the generator side is capable of transferring generated electrical energy back to the electrical grid such that braking resistors are not required.

The power converter driving the SCIG allows for generation to be tested under different electrical supply conditions (steady-state as well as dynamic). The prime mover variable speed drive allows for a variable mechanical input to the SCIG (also steady-state or dynamic).

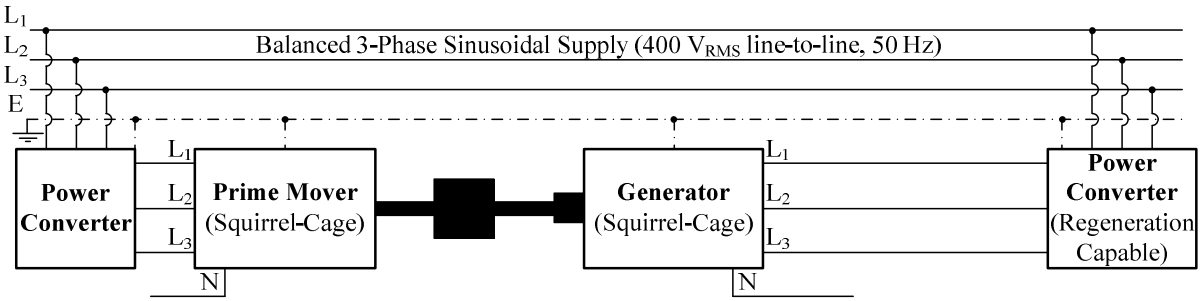

Figure 3.1: Basic Experimental Setup

3.3 Required Measurements

3.3.1 Generator Phase Voltage and Phase Current

Each generator phase voltage and phase current is measured. While it is expected that the voltages and currents will be balanced (approximately) they are all measured for completeness.

As shown in figure 3.2 below, the output voltage of the variable speed drives has a PWM waveform and is non-sinusoidal in nature. This makes a direct measurement of the voltage difficult as the desired fundamental sinusoid is obscured by the high-frequency switching effects. The high-frequency switching problem is addressed by filtering the switching frequencies from the fundamental voltage and current components for comparison with the corresponding simulation waveforms (which assume a sinusoidal electrical excitation). The effect of the PWM nature of the drive output is assumed to be negligible. This is verified in chapter 5 where the simulation and experimental results for SCIG model evaluation are presented.

The measured phase voltages are reproduced as a model input in the corresponding generator simulation. Measured and simulated current waveforms are compared for model evaluation.

Knowledge of the generator excitation frequency is also required. The SCIG is excited by a power converter which functions to produce a balanced three-phase excitation. Therefore, it is assumed that the excitation frequency is common to all three machine phases. As such, only a single frequency measurement is anticipated. If a common frequency were not the case, the air-gap magnetic-field velocity (as defined in appendix A) would be ill-defined.

The measured generator excitation frequency also serves as a model input in the corresponding generator simulation. Furthermore, in simulating the equivalent dynamic circuit model, the stator excitation frequency is required if the synchronously rotating reference frame is the chosen reference frame.

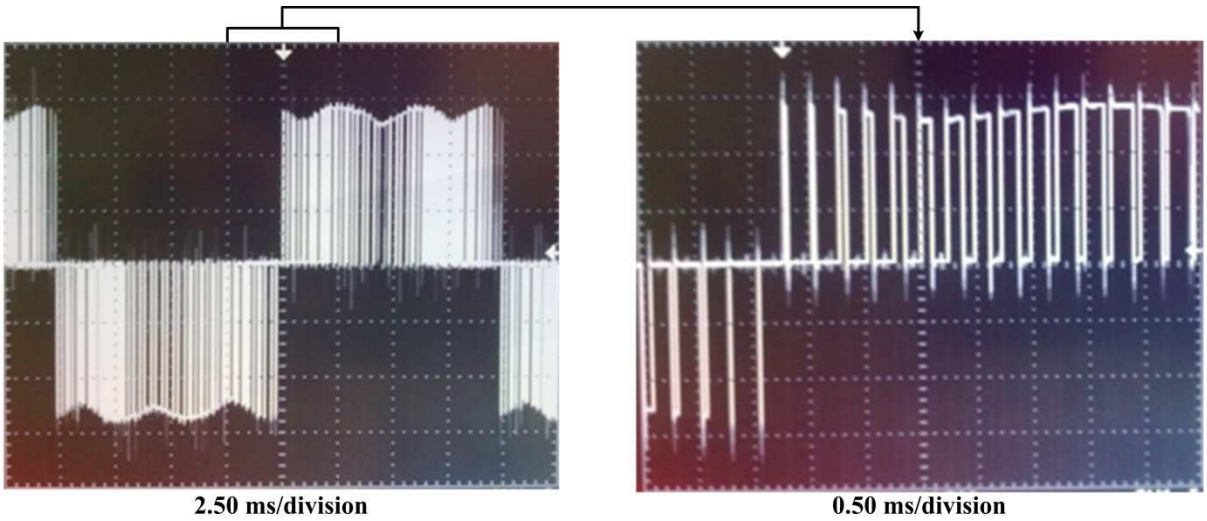

Figure 3.2: Power Converter Output Line Voltage – PWM Equivalent of a Sinusoid

3.3.2 Prime-Mover Torque and Rotor Speed

In order to quantify the mechanical performance of the SCIG, two measurements are required. These are the rotor speed measurement as well as the prime-mover-torque measurement. Since the rotor will only turn in one direction, rotor direction is not a measurement requirement.

The input prime-mover torque serves as an input to the corresponding model simulation. The induction motor may be controlled so as to produce a particular torque trajectory and this measured trajectory is used in the generator simulation.

Rotor speed measurement is used for comparison with the simulated rotor speed which allows for model evaluation.

3.3.3 Prime-Mover (Induction Motor) Measurements

The induction-motor excitation is quantified through measurement of a single phase voltage and corresponding excitation frequency as described for the SCIG. This is included for experiment repeatability if required.

3.3.4 General Measurement Requirements

It is required for all measurements to be carried out on an instantaneous basis and to be synchronised so as to allow for easy comparison/calculation. Data storage and plotting are additional measurement requirements. All of this should occur automatically once a particular experiment has been initiated. The input ranges to be accommodated by the various measurements include:

- Generator phase voltage – all three phases ($0\ V_{RMS} - 231\ V_{RMS}$)
- Generator phase current – all three phases ($0\ A_{RMS} - 4.89\ A_{RMS}$)
- Generator excitation frequency ($0\ Hz - 70\ Hz$)

- Prime-mover torque ($0\ \text{Nm} - 14.8\ \text{N.m}$)
- Generator shaft speed ($0\ \text{rpm} - 2100\ \text{rpm}$)
- Prime-mover phase voltage – one phase ($0\ V_{RMS} - 231\ V_{RMS}$)
- Prime-mover excitation frequency ($0\ \text{Hz} - 70\ \text{Hz}$)

From the required measurements, secondary variables may be derived for a different perspective in model evaluation. This includes both output electrical power and input mechanical power of the SCIG.

3.4 Measurement System Configuration

Figure 3.3 illustrates the general layout and functionality of the implemented measurement system relative to the experimental setup of figure 3.1. The actual signal processing is carried out by a measurement circuit implemented on veroboard. The outputs of the measurement circuit are captured by an oscilloscope. Torque measurement is the exception where the output of the torque transducer is measured directly with an oscilloscope. All of the terminals interfacing the measurement devices and the measurement circuit/oscilloscope are guarded by Common-Mode-Current (CMC) chokes.

3.4.1 Generator Phase Voltage and Phase Current

The generator stator windings are connected in a star configuration [**1**]. This allows the stator phase currents to be measured directly since they are equivalent to the corresponding line currents. Phase voltage measurement requires access to the neutral point of the stator-winding star connection.

Generator phase currents are measured using Current Transformers (CTs) with their secondary circuits completed by a $1\ \Omega$ resistor. The phase currents are scaled down by a factor of 10 and read as a voltage drop across the $1\ \Omega$ resistor. Each generator phase voltage is measured using a Differential Voltage Probe (DVP) which scales the voltage down by a factor of 1000.

Phase-voltage and phase-current measurements are passed on to Low-Pass Filter (LPF) circuits by intermediate buffer circuits. Buffer circuits are used to prevent any loading effect of the measurement circuit on the measurement devices. The purpose of the LPFs is to filter out the higher frequencies present as a result of the power-converter switching. The filtered phase voltages and currents are then captured by an oscilloscope. The fundamental frequency of the generator's electrical excitation (based on the filtered equivalent) is also captured as a DC-equivalent value produced by the corresponding frequency-to-voltage converter.

3.4.2 Prime-Mover Torque and Rotor Speed

An inline torque sensor measures the prime-mover input torque while an incremental shaft encoder is used to measure the generator rotor speed. As previously mentioned, the torque

transducer output is measured by an oscilloscope as a voltage which is proportional to the prime-mover input torque.

The shaft encoder output signal is not isolated by a buffer circuit since the amplitude of this signal is not important; only its frequency is of importance. The only requirement is that the load as seen by the shaft encoder be large enough to produce the voltage input required to trigger the frequency divider. The shaft encoder draws power from the measurement circuit and outputs a pulse train with a frequency proportional to the generator shaft speed. This frequency is scaled down by a factor of 16 using a frequency divider before being represented as a DC-equivalent voltage by the corresponding frequency-to-voltage converter.

3.4.3 Prime-Mover (Induction Motor) Measurements

The prime-mover induction motor also has its stator windings arranged in a star configuration. A single prime-mover phase voltage is measured using a Voltage Transformer (VT) which scales the voltage down by a factor of 40. The measurement-circuit signal processing for voltage and frequency measurement is as discussed for the generator excitation.

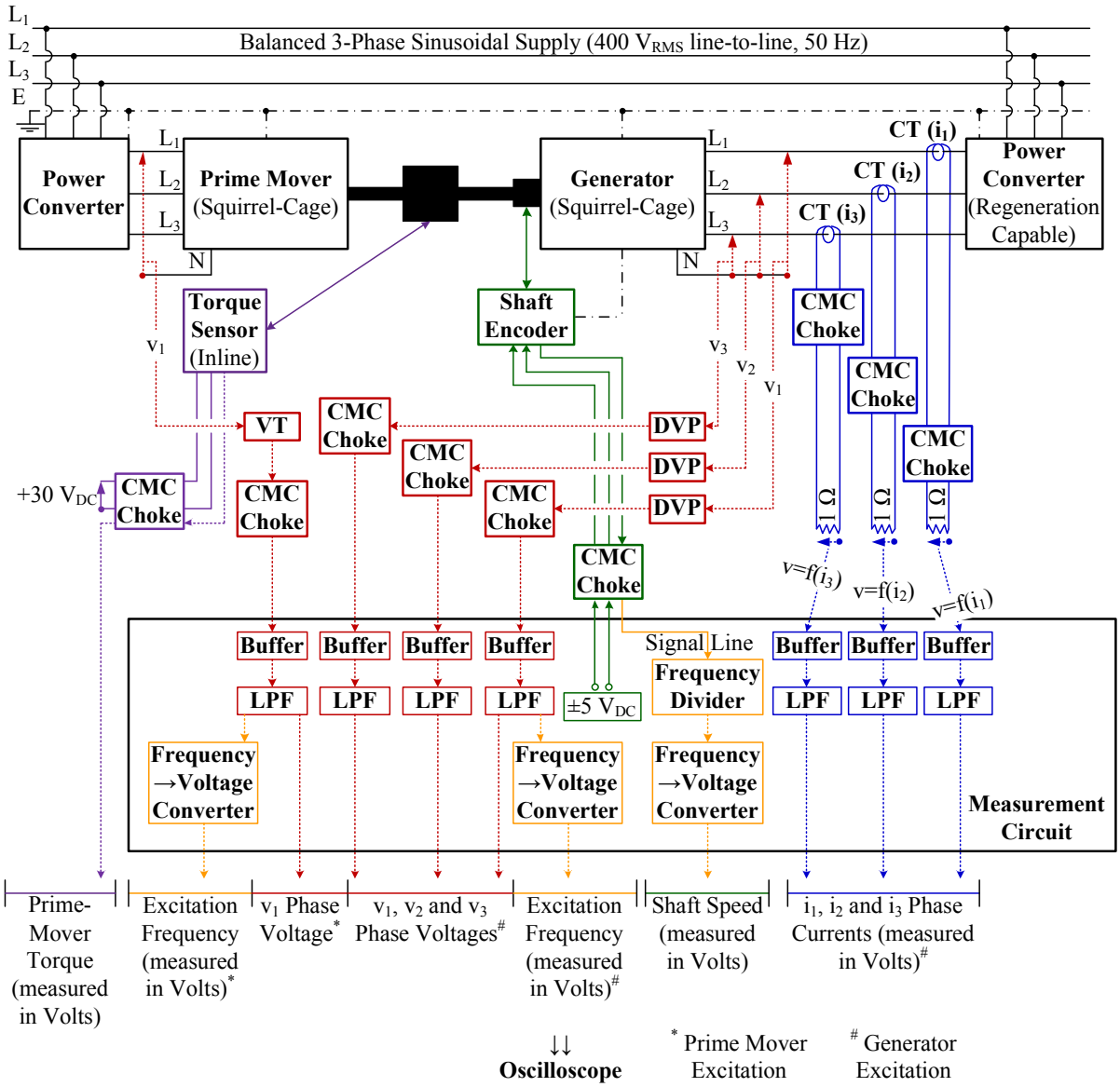

– – – – = Protective Earth (Ground)

..... = Differential Signal (between a signal line and a zero-reference line)

——— = Voltage Measurement
——— = Current Measurement
——— = Frequency Measurement
——— = Speed Measurement
——— = Torque Measurement

DVP Ratio of 1000:1

VT Ratio of 40:1

CT Ratio of 10:1

Figure 3.3: Experimental and Measurement Setup – General Layout and Functionality

3.5 Complete Experimental/Measurement Setup

The experimental setup and measurement system used in the practical testing of a SCIG for model evaluation is presented in figures 3.4-3.7.

As shown in figure 3.4, a waveform generator may be used to provide a speed reference to the control unit of the generator or prime-mover power converter. If the speed reference is applied to the prime-mover converter, the prime-mover induction machine may be controlled so as to reproduce a particular torque input to the SCIG. If, however, the speed reference is fed to the generator converter, a particular generator electrical dynamic may be tested. This approach is used to achieve the mechanical and electrical dynamic tests for the SCIG as described in chapter 1. The actual tests are described in more detail in chapter 5 together with the experimental results.

Figure 3.7 shows the torque transducer CMC choke together with the associated transducer supply and oscilloscope measurement. The other bench-supply output is used to provide a $+5\ V_{DC}$ voltage used to trigger the oscilloscopes.

As previously mentioned, oscilloscopes are used for data acquisition. Real-time plotting facilitates the experimental process while data storage allows for appropriate data analysis and presentation. It is desired for all the oscilloscope measurements to be synchronised. This is achieved by the external trigger functionality in combination with the $+5\ V_{DC}$ system. The measurements are triggered by closing the trigger circuit as shown in figure 3.7.

As shown in chapter 5, the measurement system performs well and is sufficiently protected from CMC effects. However, it is observed that the CMC effects on the measurement system are also function of the experimental layout. This is not unexpected [**2**,**3**,**4**,**5**]. Therefore, in order to obtain interference-free measurements, the measurement system components should not be placed near possible contamination sources such as inverter and induction-machine supply lines. The placement of oscilloscope probe cables is also important.

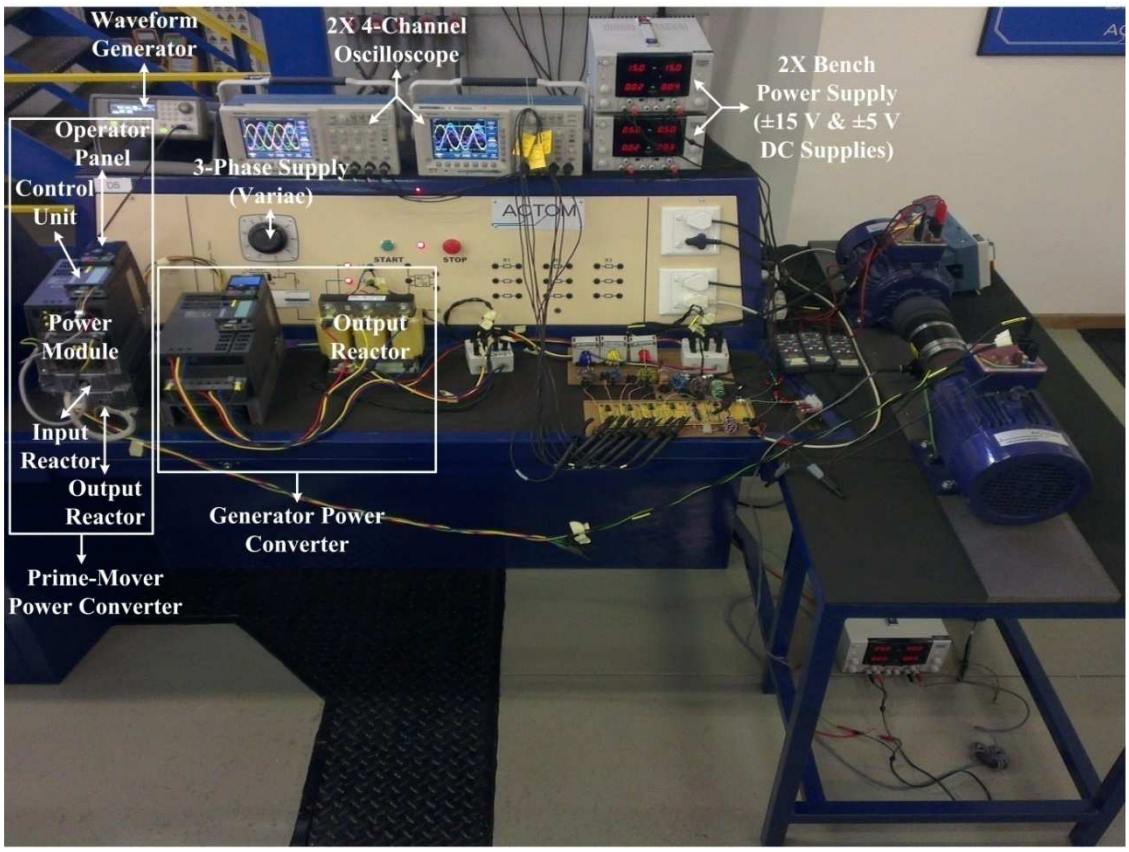

Figure 3.4: Complete Experimental and Measurement Setup

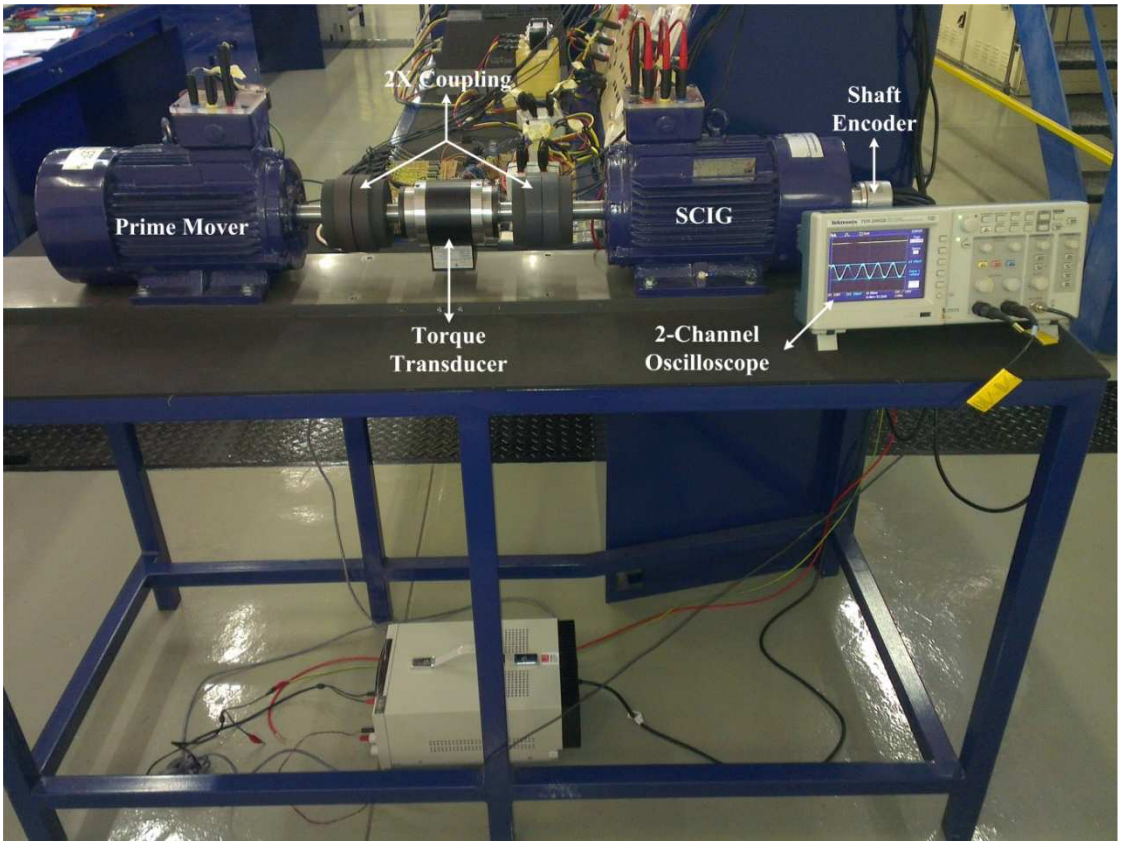

Figure 3.5: Complete Experimental and Measurement Setup

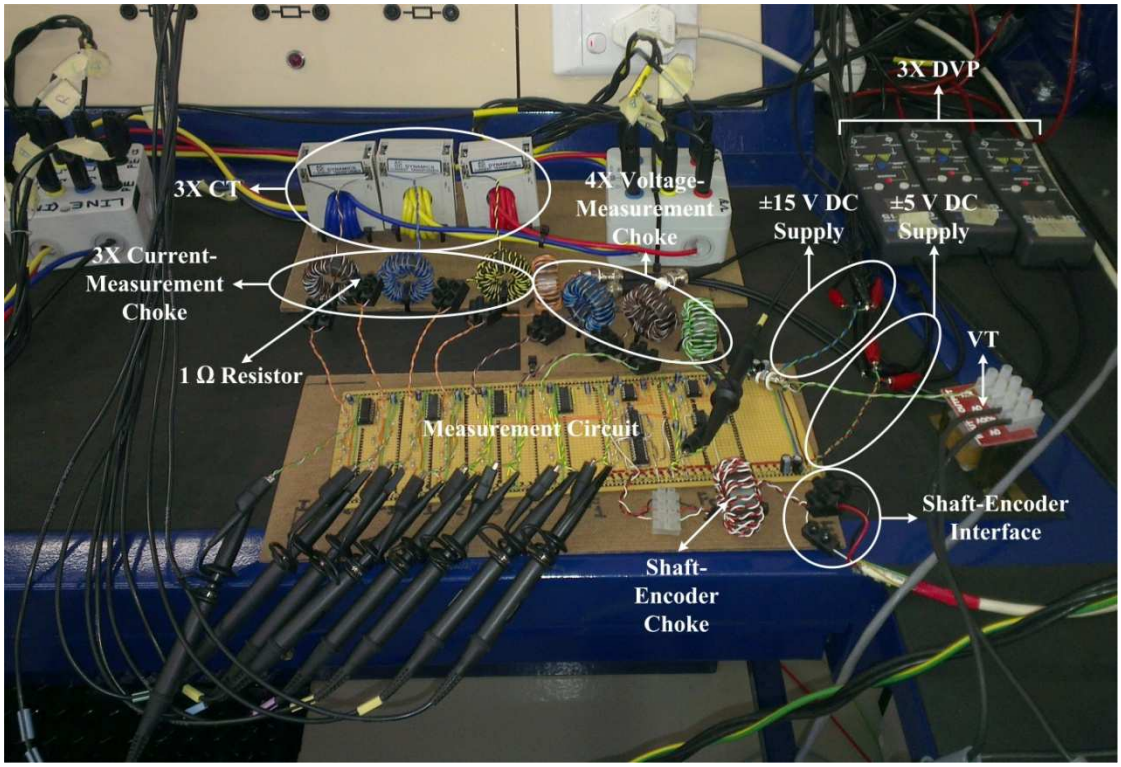

Figure 3.6: Complete Experimental and Measurement Setup – Measurement Circuit

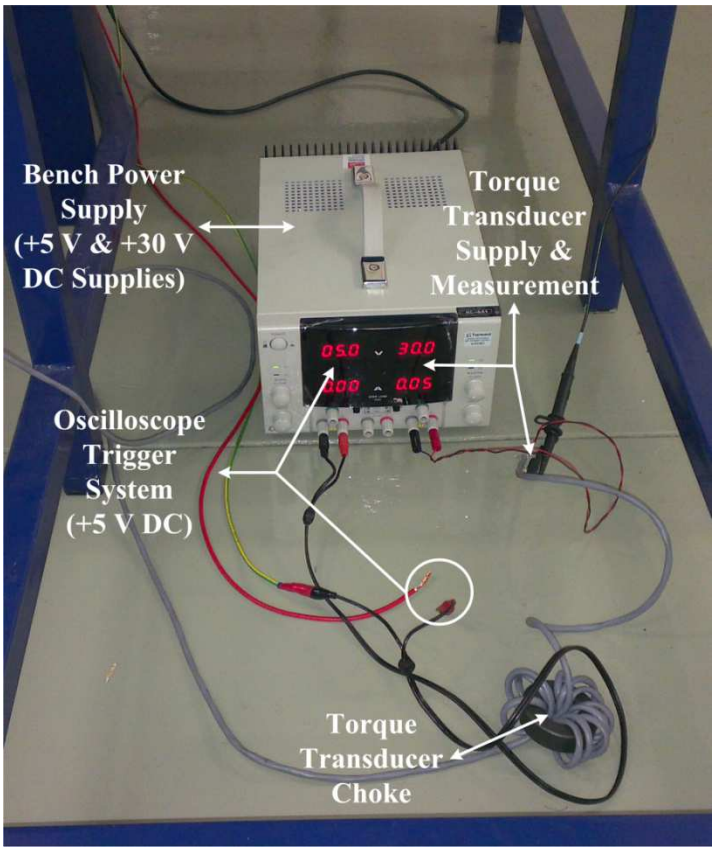

Figure 3.7: Complete Experimental and Measurement Setup

3.5.1 Use/Interpretation of Measurement Outputs

In order to recover the actual quantities from the measurement system outputs as measured by an oscilloscope, the following equations should be used (no phase corrections are made):

$$generator\ phase\ voltage\ (\mathrm{V}) = 1000 \times measurement\ output\ (\mathrm{V}) \tag{3.1}$$

$$generator\ phase\ current\ (\mathrm{A}) = 10 \times measurement\ output\ (\mathrm{V}) \tag{3.2}$$

$$generator\ excitation\ frequency\ (\mathrm{Hz}) = 9 \times measurement\ output(\mathrm{V}) \tag{3.3}$$

$$generator\ rotor\ speed\ (\mathrm{rpm}) = 237.12 \times measurement\ output(\mathrm{V}) \tag{3.4}$$

$$prime\ mover\ torque\ (\mathrm{N.m}) = \frac{1}{0.025} \times measurement\ output(\mathrm{V}) \tag{3.5}$$

$$prime\ mover\ phase\ voltage\ (\mathrm{V}) = 40 \times measurement\ output(\mathrm{V}) \tag{3.6}$$

$$prime\ mover\ excitation\ frequency\ (\mathrm{Hz}) = 9 \times measurement\ output\ (\mathrm{V}) \tag{3.7}$$

The measurement-system testing and calibration corresponding to the above equations are given in appendix D.

The above equations assume that measurement dynamics (detailed in appendix D) are obeyed. Excitation-frequency and rotor-speed measurement require attention in this regard. For a dynamic (sinusoidal) rotor-speed or excitation frequency, the corresponding measurements have a first-order low-pass filtering effect with -3 dB cut-off frequencies of:

- 0.34 Hz (3 s) for rotor-speed measurement
- 0.147 Hz (7 s) for generator excitation-frequency measurement
- 0.153 Hz (7 s) for prime-mover excitation-frequency measurement

As stated in chapter 1, typical prime-mover torque dynamics have a sinusoidal period of $4\ \mathrm{s} - 5\ \mathrm{s}$ for a constant sea state. Therefore, correction of a dynamic rotor speed and/or excitation frequency may be required depending on the dynamics tested. Improvement in rotor-speed/excitation-frequency measurement regarding dynamic performance is left for future development.

As shown in appendix D, error in current measurement (amplitude and phase) by the corresponding CTs is a possible source of measurement error. Mitigation of these errors is left for further development.

Another possible source of measurement error involves torque measurement for low prime-mover input torque (refer to appendix D). This is a consequence of the oscilloscope resolution where the resolution error becomes comparable to the measured torque. This is unavoidable and is a limitation of the measurement implementation. Improvement in reducing this error is left for future development.

For the purpose of model evaluation as presented in chapter 5, the errors involve in the phase-current and prime-mover-torque measurement are considered as acceptable. Cases where measurement error becomes observable are mentioned as/when appropriate.

3.5.2 Experimental Scaling

The experimental setup makes use of a 2.2 kW SCIG which is significantly smaller than demonstrated OWC WEC systems which lie in the range of $60 - 500$ kW as stated in chapter 1 [**6**]. An important consideration is whether the practically large OWC WEC systems are suitably represented by the smaller experimental setup with reduced power rating. In other words, what scale considerations are important in reducing the practical SCIG used in WEC systems to that used in the experimental setup? This is important as it affects how the experimental/simulation conclusions apply to real-life systems.

It is important to note that system dynamics vary with different implementations as they depend on the various system parameters. A good example is turbine/generator moment of inertia. Therefore, the approach should be to test generator dynamics that act as a boundary condition to all possible dynamics for the given application. As previously mentioned, this is a challenge for the case of varying sea state owing to the desired simplicity of the analysis. For the case of a constant sea state, the dynamics have been suitably quantified. What remains is to consider the difference in generator parameters as a result of a down-scaled experimental setup.

3.5.2.1 *Mechanical Considerations*

The actual WEC structure and associated turbine damping response to a particular sea state is not considered [**7**]. Since the hydrodynamics and aerodynamics of the system are not considered, scaling laws such as Froude scaling do not apply to the experimental system [**7**,**8**]. This is a benefit of only considering the generator in the research analysis by reproducing expected dynamic generator inputs.

From a generator perspective, two important quantities are the generator rotor moment of inertia as well as the generator frictional/windage torque. Machine friction and windage are often negligible components [**9**]; therefore, their scaling is not important. Generator moment of inertia is much larger for larger machines. The associated energy storage as a result of the flywheel effect is beneficial owing to the smoothing of generator speed/torque/power oscillations – smaller systems are likely to experience larger oscillations in this regard. Therefore, the experimental use of a smaller generator is appropriate as it is likely to test the worst-case fluctuation in generator power.

3.5.2.2 *Electrical Considerations*

Regarding generator electrical parameters, there is no general scaling between large and small induction machines. The parameters are also dependent on machine construction including rotor construction for example [**1**]. In light of this, any difference in the electrical

parameters of large and small SCIGs is not considered. Even though the exact generator response to dynamic inputs would differ, this is not considered important as the fundamental generator operation is unchanged.

The experimental power level is reduced when compared with practical WEC systems. This is of no concern since typical generator operating conditions (deep generation and light motoring for example) are experimentally reproduced as far as possible.

3.5.2.3 *Final Remarks*

The fundamental difference between the corresponding experimental and practical SCIGs is the reduced power rating. In both cases, the generator rated speed is comparable depending largely on the pole-count of the machine [**1**]. This would be based on the optimal operating speed of the WEC as a whole.

Based on the above-mentioned mechanical and electrical considerations, the conclusions on SCIG modelling (model performance) for the given application should be applicable for both large and small generators. The exact response of the generators will be different but this is not important as machine optimisation is not part of the research focus.

3.6 Conclusion

An experimental setup to be used in establishing the practical operation of a SCIG in an OWC WEC is proposed. For practical purposes, the prime mover is another squirrel-cage induction motor. The measurements required together with the appropriate ranges to be accommodated include:

- Generator phase voltage – all three phases ($0\ \mathrm{V_{RMS}} - 231\ \mathrm{V_{RMS}}$)
- Generator phase current – all three phases ($0\ \mathrm{A_{RMS}} - 4.89\ \mathrm{A_{RMS}}$)
- Generator excitation frequency ($0\ \mathrm{Hz} - 70\ \mathrm{Hz}$)
- Prime-mover torque ($0\ \mathrm{Nm} - 14.8\ \mathrm{N.m}$)
- Generator shaft speed ($0\ \mathrm{rpm} - 2100\ \mathrm{rpm}$)
- Prime-mover phase voltage – one phase ($0\ \mathrm{V_{RMS}} - 231\ \mathrm{V_{RMS}}$)
- Prime-mover excitation frequency ($0\ \mathrm{Hz} - 70\ \mathrm{Hz}$)

The induction machines are excited by power converters where the output voltages are not truly sinusoidal but rather PWM-equivalents thereof. The proposed measurement system makes use of low-pass filters to obtain the fundamental components of the electrical excitation. The design and implementation of the measurement system is detailed in appendix C with the measurement calibration given in appendix D. Important measurement limitations and possible sources of measurement error are discussed here.

All measurements are carried out on an instantaneous basis using oscilloscopes which are triggered for synchronisation. The oscilloscopes also provide data plotting and storage functionality.

The use of a down-scaled experimental SCIG compared with larger generators used in practical OWC WECs is not expected to have any effect on conclusions regarding the modelling of a SCIG for the chosen application.

3.7 References

[1] Sen P. C., *Principles of Electric Machines and Power Electronics*, 2nd ed. Hoboken, United States of America: John Wiley & Sons, Inc., 1997.

[2] Ott H. W., *Electromagnetic Compatability Engineering*. Hoboken, United States of America: John Wiley & Sons, 2009.

[3] Mardiguian M., *EMI Troubleshooting Techniques*. United States of America: McGraw-Hill, 2000.

[4] Shih F. Y., Chen D. Y., Wu Y. P., and Chen Y. T., "A Procedure for Designing EMI Filters for AC Line Applications," *IEEE Transactions on Power Electronics*, vol. 11, no. 1, pp. 170-181, January 1996.

[5] Serrao V., Lidozzi A., Solero L., and Di Napoli A., "Common and Differential Mode EMI Filters for Power Electronics," in *International Symposium on Power Electronics, Electrical Drives, Automation and Motion*, 2008, pp. 918-923.

[6] de O. Falcão A. F., "Wave energy utilization: A review of the technologies," *Renewable and Sustainable Energy Reviews*, vol. 14, no. 3, pp. 899-918, April 2010.

[7] O'Sullivan D. L. and Lewis A.W., "Generator Selection and Comparative Performance in Offshore Oscillating Water Column Ocean Wave Energy Converters," *IEEE Transactions on Energy Conversion*, vol. 26, no. 2, pp. 603-614, June 2011.

[8] Chakrabarti S. K., "Modeling of Offshore Structures," in *Applications in Coastal Modeling*, Lakhan V. C. and Trenhaile A. S., Eds. Amsterdam, Netherlands: Elsevier Science Publishers B. V., 1989, ch. 3, pp. 43-74.

[9] Krause P. C., Wasynczuk O., and Sudhoff S. D., *Analysis of Electric Machinery and Drive Systems*, 2nd ed., El-Hawary M. E., Ed. Hoboken, United States of America: John Wiley & Sons, Inc., 2002.

4 SCIG Parameterisation

4.1 Introduction

The objective of parameterising the experimental SCIG is to obtain the various machine parameters required for model simulation. Induction machine parameterisation is broken down into a characterisation of electrical and mechanical parameters. The parameters are common to both equivalent steady-state and dynamic models as presented in chapter 2.

Electrical parameter characterisation is achieved through two steady-state-excitation tests as well as a DC-resistance measurement [**1**,**2**]. From the steady-state tests, machine parameters are derived from a phasor-based analysis of the equivalent steady-state circuit model [**1**,**2**].

Mechanical parameterisation is focused on characterising the friction and windage loss of the induction machine. This involves quantifying the loss as a function of rotor speed. An unexcited run-down test is used to characterise this loss where any frictional and windage forces are responsible for bringing the rotor to a stop.

This chapter highlights the parameterisation of an induction machine and concludes with the parameters of the given SCIG in the experimental setup of chapter 3.

4.2 Electrical Parameters

DC resistance measurements together with steady-state tests are carried out in order to determine the electrical parameters of an induction machine. Regarding the steady-state tests, a phasor-based derivation of parameter values is possible by considering the per-phase steady-state circuit model. A summary of the DC-measurement, locked-rotor and no-load determination of the induction machine electrical parameters given in [**1**,**2**] is now presented together with the parameters of the tested SCIG. Detailed calculations of parameters are presented in [**1**]. For each steady-state test, required measurements include stator voltage, stator current, average stator power (phase angle between stator voltage and current) and stator frequency.

Steady-state parameterisation of the SCIG used for experimental purposes is achieved by the required sinusoidal three-phase voltage supply as described below. Average values of the measurements across the three-phases are used in the calculation of machine parameters for a symmetrical induction-machine model.

4.2.1 DC Measurement of Stator Winding Resistance

Each stator-winding resistance is found by a DC measurement of the stator windings [**1**]. For the given SCIG, the stator windings have a DC resistance of $2.9\,\Omega, 2.9\,\Omega$ and $2.8\,\Omega$ respectively giving an average per-phase stator winding resistance of $2.87\,\Omega$ to be used in the symmetrical electrical model.

4.2.2 Locked-Rotor Test

The locked-rotor test is carried out with the intention of identifying the stator and rotor leakage inductance values as well as the rotor resistance [**1**]. The rotor is locked while applying a balanced set of stator voltages such that a typical rotor current is present. For rated machine operation, rated stator current should be used. Since operating rotor frequency is desired, a reduced excitation frequency should be used. However, this is only really required for large machines or in cases were rotor resistance and leakage inductance is a function of frequency. Normal small motors can be parameterised using a rated excitation frequency.

The equivalent locked-rotor circuit based on the per-phase steady-state circuit model is presented in figure 4.1 [**1**]. In the case of a locked rotor, the slip is 1 such that the effective rotor impedance is significantly smaller than the stator magnetising impedance; the rotor circuit effectively shorts out the stator magnetising branch.

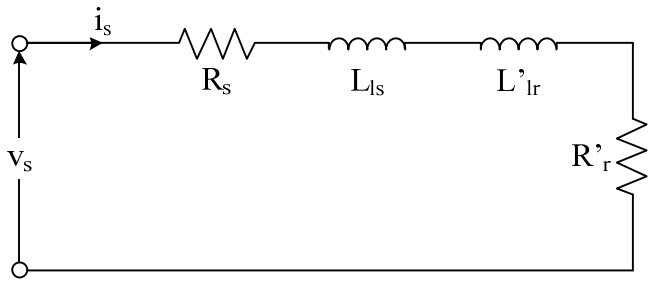

Figure 4.1: Locked-Rotor-Test Equivalent Circuit (Per-Phase) – adapted from [**1**]

The SCIG used for experimental purposes is excited at rated electrical frequency with rated stator currents. With the rotor locked, the per-phase locked-rotor resistance is $R_s + R'_r = 4.8041\ \Omega$. This is found by considering the average stator power. The per-phase stator resistance is found by the previous DC measurement, therefore, $R'_r = 1.9341\ \Omega$. By considering the locked-rotor reactive component, the per-phase locked-rotor inductance is calculated as $L_{ls} + L'_{lr} = 0.022002$ H. Assuming equal stator and rotor leakage inductance values, it is found that $L_{ls} = L'_{lr} = 0.011001$ H [**1**,**2**].

4.2.3 No-Load Test

The aim of the no-load test is to determine the stator magnetising inductance [**1**]. This is achieved by exciting an unloaded induction machine with a balanced stator-voltage supply at rated amplitude and frequency.

The equivalent no-load circuit is given in figure 4.2 [**1**]. Since the slip is approximately zero, the large rotor resistance $\frac{R'_r}{s}$ of figure 2.1 is effectively an open circuit. The no-load loss R_{NL} includes the stator winding loss, magnetic core loss and friction and windage loss.

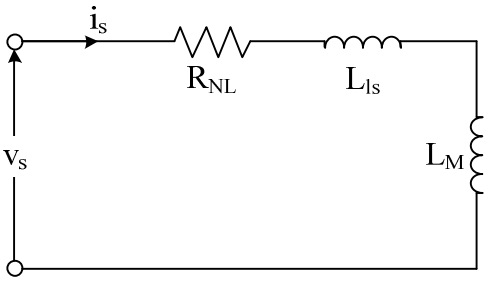

Figure 4.2: No-Load-Test Equivalent Circuit (Per-Phase) – adapted from [**1**]

In parameterising the given SCIG the friction/windage of the coupled (but unexcited) induction machine is assumed to be negligible. From the machine reactive component, the per-phase no-load inductance is $L_{ls} + L_M = 0.27789$ H. Since $L_{ls} = 0.011001$ H from the locked-rotor test, the per-phase stator magnetising inductance is $L_M = 0.26689$ H.

4.2.4 Improved Accuracy of Rotor Resistance

As derived in [**1**], a more accurate rotor resistance $R'_{r,final}$ may be calculated from the initial rotor resistance $R'_{r,initial}$ using

$$R'_{r,final} = R'_{r,initial}\left(\frac{L'_{lr}+L_M}{L_M}\right)^2 \tag{4.1}$$

Based on the previously calculated parameters, the given SCIG has a modelled rotor resistance $R'_r = R'_{r,final} = 2.0969\ \Omega$.

4.3 Mechanical Parameters

4.3.1 Generator Moment of Inertia

The first mechanical parameter that needs to be quantified is the effective rotor Moment Of Inertia (MOI) J_g. The effective MOI includes inertia associated with generator rotor (5.5×10^{-3} kg. m^2 [**3**]), shaft encoder (2×10^{-6} kg. m^2 [**4**]), generator/torque-transducer coupling (4×10^{-3} kg. m^2 [**5**]) and torque transducer (0.485×10^{-3} kg. m^2 [**6**]) giving a total rotor moment of inertia of $J_g = 9.7445 \times 10^{-3}$ kg. m^2. Only half the torque transducer MOI is associated with the generator rotor.

Since the generator's rotor MOI is known, a run-down test may be carried out in order to characterise the friction/windage loss.

4.3.2 Run-Down Test

The run-down test involves the following process:

1. Run the induction machine as a motor at no load with a rated stator voltage supply (amplitude and frequency)
2. Disconnect the stator supply from the induction machine and measure the rotor speed as it comes to a standstill

For the experimental setup in chapter 3, the generator is coupled to another induction machine. Considering that the only torque acting on the coupled rotors is the combined friction/windage torque and assuming that the two induction machines are approximately equivalent in their effective rotor MOI and friction/windage torque, then the system mechanical equation reduces to

$$-2\tau_{f,w} = 2J_g \frac{d\omega_{rsm}}{dt} \tag{4.2}$$

A simple time derivative of the measured rotor angular velocity is used to calculate the instantaneous run-down torque (friction/windage). Then, considering the instantaneous rotor velocity, an expression for the friction/windage torque in terms of rotor angular velocity can be found.

4.3.2.1 Rotor Speed/Acceleration

The measured rotor speed for the run-down test is presented in figure 4.3. The rotor takes approximately 10 s to come to a halt. The measured rotor speed is mathematically approximated for the characterisation of the friction/windage torque. The corresponding acceleration curve is given in figure 4.4. It is observed that there is a non-constant rotor deceleration. The initial positive rotor acceleration is a consequence of the error in approximating the initial rotor speed. Therefore, this region is not considered in the derivation of the rotor friction/windage co-efficient.

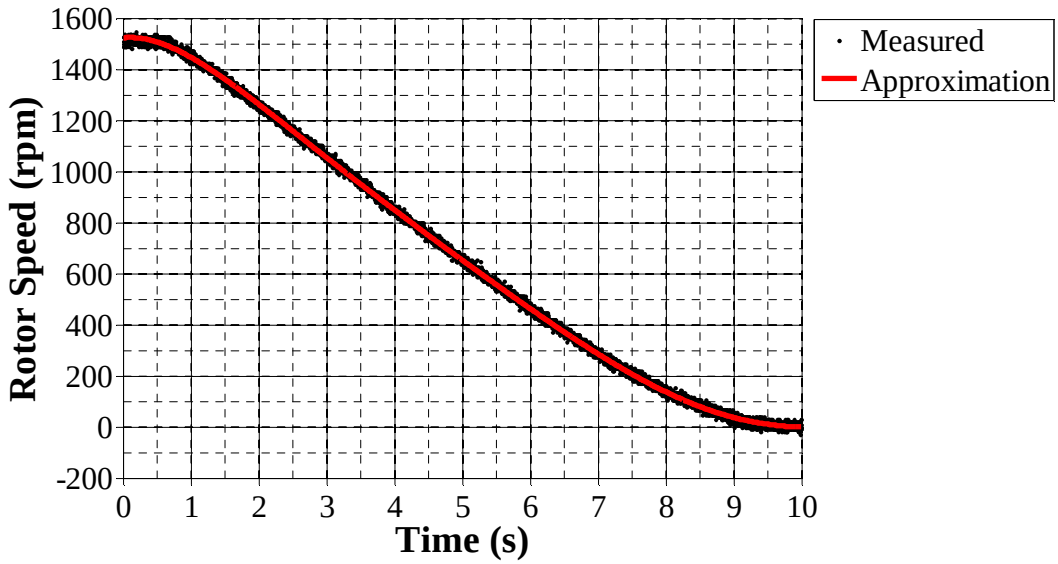

Figure 4.3: Run-Down Rotor Speed

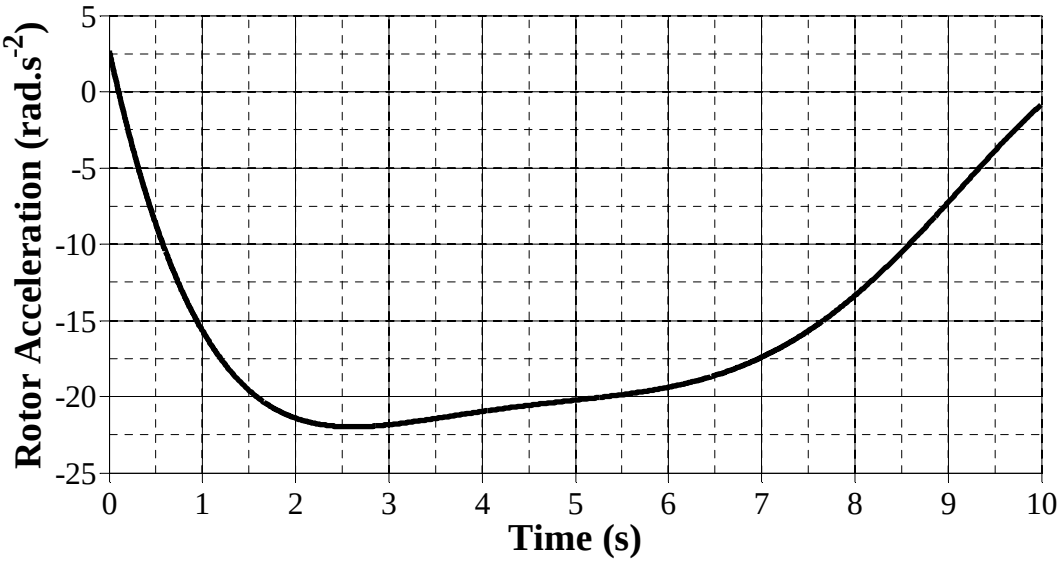

Figure 4.4: Run-Down Rotor Acceleration

4.3.2.2 Friction/Windage Torque as a Function of Rotor Angular Velocity

The friction/windage co-efficient as a function of rotor angular velocity is presented in figures 4.5-4.7 for different friction/windage torque-speed relationships. For square and linear torque-speed relationships, the friction/windage co-efficient varies considerably with rotor speed as shown in figures 4.5-4.6. The relative co-efficient variation decreases with a decrease in the exponent of the rotor angular velocity in the torque-speed relationship. Owing to the variation of the friction/windage co-efficient, the square and linear torque-speed relationships of figures 4.5-4.6 are not considered as appropriate.

As highlighted in section 2.3, the proposed friction/windage torque as a function of rotor angular velocity for the given experimental setup is

$$\tau_{f,w} = C_{f,w}\text{sign}(\omega_{rsm})\sqrt[4]{|\omega_{rsm}|} \tag{4.3}$$

As stated in section 2.3, equation 4.3 is not proposed as a generic friction/windage torque equation but is the most appropriate expression for the given experimental setup. The friction/windage co-efficient based on the torque-speed relationship of equation 4.3 is given in figure 4.7. The co-efficient is relatively constant when compared with figures 4.5 and 4.6 except for the regions where the rotor begins its deceleration and when the rotor comes to a standstill. The spike at zero rotor speed is ignored as it is a result of division by "zero" in calculating the friction/windage co-efficient.

In choosing a constant $C_{f,w}$, for equation 4.3, the outer non-constant regions of figure 4.7 are neglected with a focus on the approximately-constant region. Some inaccuracy may be introduced for the non-constant regions but at least the effect of friction/windage is not understated. Furthermore, friction/windage loss is expected to be small [**2**,**7**]. From figure 4.7, $C_{f,w} = 0.067025\ \text{N.m.s}^{0.25}.\text{rad}^{-0.25}$.

The lower friction co-efficient for high rotor speed (above 1400 rpm) as shown in figure 4.7 is a consequence of the lower initial deceleration shown in figures 4.3-4.4. Perhaps this lower acceleration would be shifted to higher rotor speeds if the run-down test was initiated at a higher speed. The cause of this lower initial acceleration is not known. However, this is of little consequence in the characterisation of the friction/windage loss as previously described where the given region is neglected.

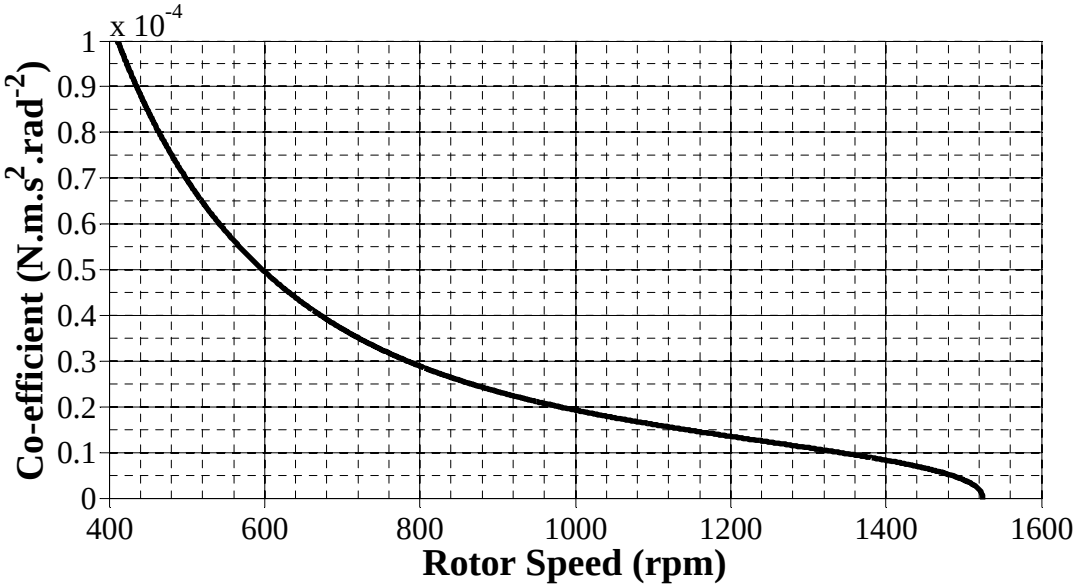

Figure 4.5: Friction and Windage Co-efficient – $\tau_{f,w} = C_{f,w}\text{sign}(\omega_{rsm})\omega_{rsm}{}^2$

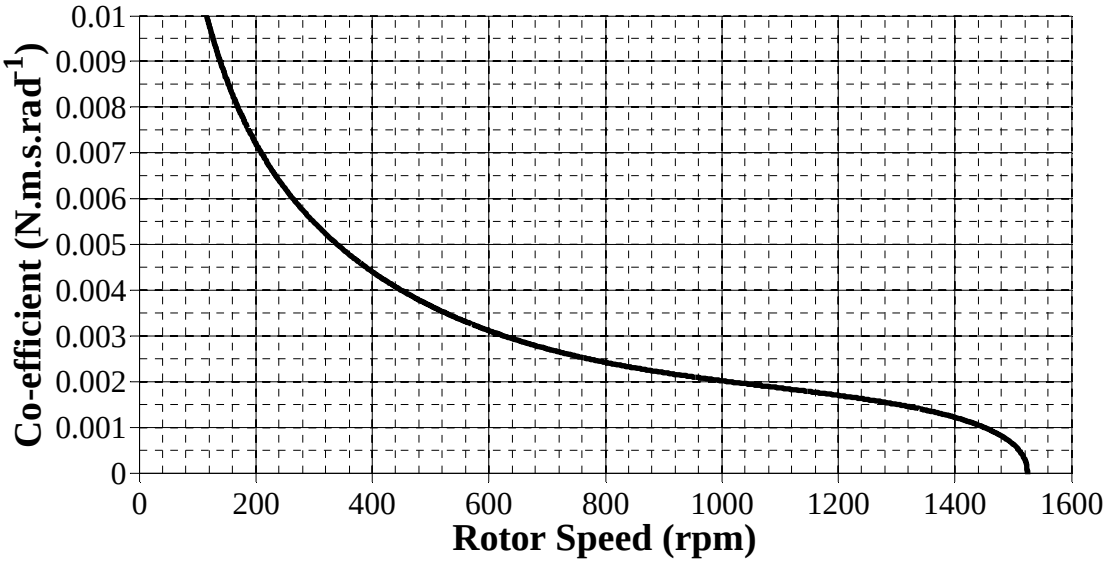

Figure 4.6: Friction and Windage Co-efficient – $\tau_{f,w} = C_{f,w}\omega_{rsm}$

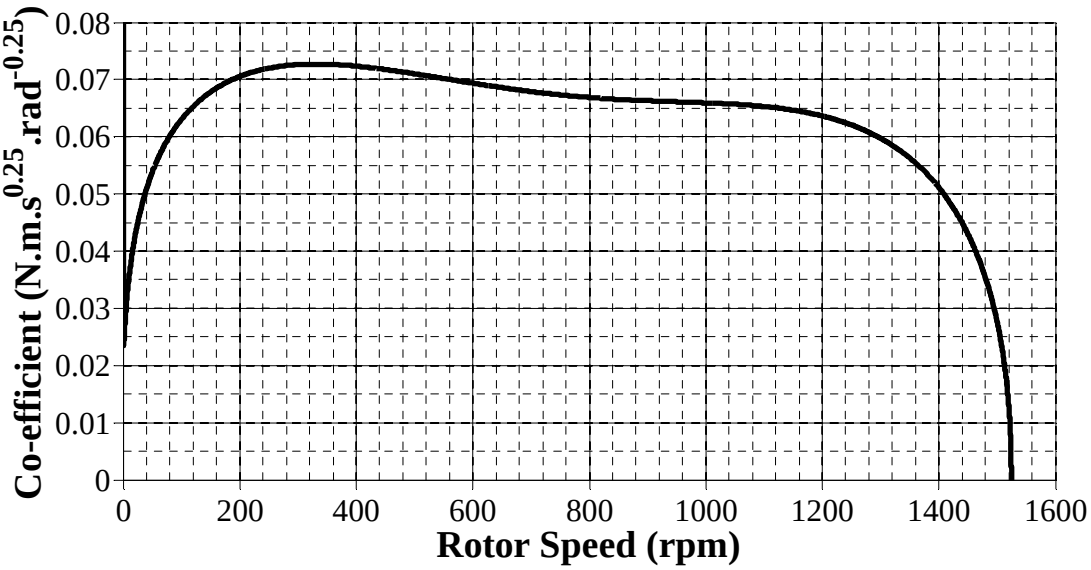

Figure 4.7: Friction and Windage Co-efficient – $\tau_{f,w} = C_{f,w}\text{sign}(\omega_{rsm})\sqrt[4]{|\omega_{rsm}|}$

4.3.2.3 Friction/Windage Power Loss

The associated friction/windage loss is given by

$$p_{f,w} = \tau_{f,w}\omega_{rsm} \tag{4.4}$$

For given friction and windage torque of equation 4.3 with $C_{f,w} = 0.067025\ \text{N.m.s}^{0.25}.\text{rad}^{-0.25}$, the friction and windage loss as a function of rotor speed is illustrated in figure 4.8. For the given squirrel-cage induction machine, the rated mechanical power output is $2.2\ \text{kW}$ at a rated rotor speed of $1420\ \text{rpm}$ (motor operation). The corresponding friction and windage loss as modelled in figure 4.8 is approximately 35 W which is $1.59\ \%$ of the rated power output. This is reasonable as friction and windage loss is typically $1 - 2\ \%$ of the rated power output [**7**].As stated in [**2**], this friction and windage loss is negligibly small; however, it is included in the mechanical model for completeness.

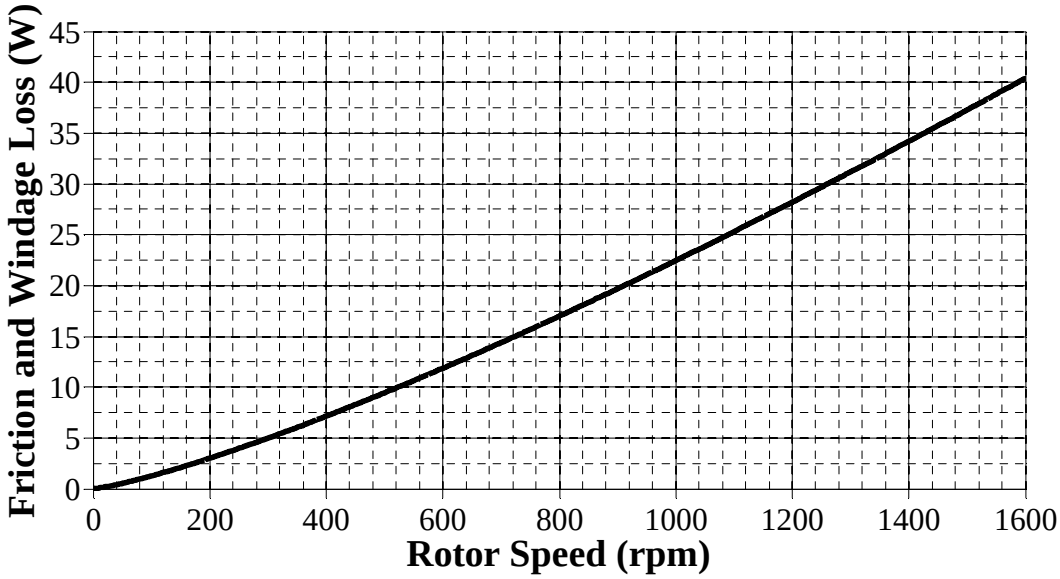

Figure 4.8: Modelled Friction and Windage Power Loss

4.4 Conclusion

The SCIG used for experimental purposes is parameterised through tests/measurements including:

- DC resistance measurement of the stator windings
- Steady-state locked-rotor test
- Steady-state no-load test
- Unexcited run-down test

The unexcited run-down test is used to characterise the rotor friction and windage torque as a function of rotor angular velocity. The electrical model parameters are:

- $R_s = 2.87\ \Omega$
- $L_{ls} = 0.011001$ H
- $L_M = 0.26689$ H
- $L'_{lr} = 0.011001$ H
- $R'_r = 2.0969\ \Omega$

The mechanical model parameters include:

- $J_g = 9.7445 \times 10^{-3}\ \text{kg.m}^2$
- $C_{f,w} = 0.067025\ \text{N.m.s}^{0.25}.\text{rad}^{-0.25}$

4.5 References

[1] Sen P. C., *Principles of Electric Machines and Power Electronics*, 2nd ed. Hoboken, United States of America: John Wiley & Sons, Inc., 1997.

[2] Krause P. C., Wasynczuk O., and Sudhoff S. D., *Analysis of Electric Machinery and Drive Systems*, 2nd ed., El-Hawary M. E., Ed. Hoboken, United States of America: John Wiley & Sons, Inc., 2002.

[3] Actom LS4 Range of Cast Iron LV Motors - Performance Data. [Online]. Available at: http://www.actom.co.za/uploads/LS4%20Performance%20datax.pdf, Last accessed: 13 April 2014

[4] Hengstler. Incremental Shaft Encoder Type RI 58 / RI 59 Installation Instructions. [Online]. Available at: http://www.jdhengstler.co.uk/downloads/RI58%20CONNECTION%20DETAILS.pdf, Last accessed: 13 April 2014

[5] J.H. Fenner & Co. Limited, *Fenner Shaft Couplings*.: Fenner (S.A.) (Pty.) Ltd., 1988.

[6] Magtrol, Inc. (2011, June) TM 300 Series In-Line Torque Transducers - User's Manual. [Online]. Available at: http://www.magtrol.com/manuals/tm300manual.pdf, Last accessed: 13 April 2014

[7] Bartheld R. G. et al., "Motor Selection," in *Handbook of Electric Motors - Second Edition, Revised and Expanded*, Toliyat H. A. and Kliman G. B., Eds. New York, United States of America: Marcel Dekker, Inc., 2004, ch. 3, pp. 167-214.

5 SCIG Model Evaluation

5.1 Introduction

The work presented in this chapter provides an evaluation of the electrical and mechanical equivalent models of chapter 2. Model evaluation is approached from a stability perspective as well as from a comparison of simulation and experimental results. Stability theory reveals the viability of a particular model under dynamic conditions. A comparison of simulation with practical results illustrates model performance and further exposes any particular model limitations.

Verification of the equivalent steady-state model is presented first and is based on evaluating model stability. This analysis is sufficient for concluding on the application of the steady-state model for dynamic generation. Therefore, no comparison of simulation and experimental results is required.

A general conclusion on the stability of the equivalent dynamic model (as presented for the steady-state model) is difficult to achieve. Therefore, model stability is inferred from the behaviour of the simulated generator performance. This is not a generic stability analysis (for all model parameters and operating conditions) but is used as a compromise for the case of testing every combination of generator parameters. A more informative stability analysis is presented in [**1**] with the results summarised in this chapter. Performance of the equivalent dynamic model is presented based on the comparison of simulated and experimental results. The test cases are based on the expected dynamics of an OWC WEC generation case as argued in chapter 1.

The evaluation of the equivalent steady-state model is now presented followed by the evaluation of the equivalent dynamic model. Based on the following results and analysis, any conclusions regarding the modelling of a SCIG driven by a Wells turbine in an OWC WEC are given in chapter 6.

5.2 Equivalent Steady-State Model

In order to evaluate model stability, one should consider the complete SCIG model (electrical and mechanical components). However, if one model component is found to be unstable under certain conditions, this may allow for certain conclusions regarding the overall model stability. Therefore, initially consider only the electrical component regarding model stability.

5.2.1 Model Stability – Electrical Component

The state-space representation of the model illustrated in figure 2.1 is given by equation 2.8 reproduced below for convenience:

$$\begin{bmatrix} \frac{di_s}{dt} \\ \frac{di'_r}{dt} \end{bmatrix} = \begin{bmatrix} -\frac{R_s L'_{lr} + L_M R_s}{D_1} & -\frac{L_M R'_r}{D_1 s} \\ -\frac{L_M R_s}{D_1} & -\frac{L_{ls} R'_r + L_M R'_r}{D_1 s} \end{bmatrix} \begin{bmatrix} i_s \\ i'_r \end{bmatrix} + \begin{bmatrix} \frac{L'_{lr} + L_M}{D_1} \\ \frac{L_M}{D_1} \end{bmatrix} v_s \tag{5.1}$$

where

$$D_1 = L_{ls}L'_{lr} + L_M L'_{lr} + L_M L_{ls} \tag{5.2}$$

$$i_m = i_s - i'_r \tag{5.3}$$

The characteristic equation of a system is used to evaluate the stability of that system [**2**,**3**,**4**]. For a linear time-invariant system expressed in state-space form, the characteristic equation is given as [**2**,**3**]:

$$\det(\mathbb{s}\boldsymbol{I} - \boldsymbol{A}) = 0 \tag{5.4}$$

$\mathbb{s}$ is the Laplace variable; $\boldsymbol{I}$ is the identity matrix with dimensions equal to that of matrix $\boldsymbol{A}$; $\boldsymbol{A}$ is the system matrix which is multiplied to the state vector of the system expressed in state-space form; the function $\det()$ represents the determinant of a matrix. It is important to note that s is used to denote the induction machine operating slip whereas $\mathbb{s}$ denotes the Laplace variable.

The complete steady-state generator model is non-linear and time-varying as discussed in section 2.4.1.1. From the perspective of the electrical subsystem as given by equation 5.1, this is a consequence of the system matrix $\boldsymbol{A}$ and its dependence on the rotor slip s. Comparing equations 5.1 and 2.34, the rotor slip is a function of stator frequency (which may be time-varying) and rotor velocity (which is a state variable). For the sake of evaluating electrical model stability, the mechanical sub-system is ignored. The non-linear nature of equation 5.1 is lost as the rotor velocity no longer features as a state variable. Therefore, from the perspective of the equivalent circuit model, the rotor slip can be varied at will. If the rotor slip is kept constant, the electrical model also becomes time-invariant so that equation 5.4 may be used to evaluate model stability. Assuming a constant rotor slip does not contradict the electrical model and its state variables as given in equation 5.1. The means of achieving this constant slip is not of importance in the following analysis.

All resistance and inductance machine parameters are assumed to be constant. Solving the characteristic equation of the second-order system given by equation 5.1 produces equation:

$$\frac{\left(\mathbb{s}^2(D_1 s) + \mathbb{s}(L_{ls}R'_r + L_M R'_r + R_s L'_{lr} s + L_M R_s s) + (R_s R'_r)\right)}{D_1 s} = 0 \tag{5.5}$$

with $D_1 > 0$ assuming non-zero inductance values. It is important to remember that the model assumes a non-zero rotor slip s. In order to evaluate model stability, the roots/zeros of the characteristic equation need to be evaluated [**2**]. Considering its numerator, equation 5.5 may be written as:

$$(a\mathbb{s}^2 + b\mathbb{s} + c) = 0 \tag{5.6}$$

where

$$a = D_1 s = (L_{ls} L'_{lr} + L_M L'_{lr} + L_M L_{ls}) s \tag{5.7}$$

$$b = L_{ls} R'_r + L_M R'_r + R_s L'_{lr} s + L_M R_s s \tag{5.8}$$

$$c = R_s R'_r \tag{5.9}$$

The roots/zeros of the characteristic equation are, therefore, given as

$$\mathbb{s} = \frac{-b \pm \sqrt{b^2 - 4ac}}{2a} \tag{5.10}$$

In order to qualify the stability of a model, the real parts of the characteristic equation roots/zeros need to be known [**2**]. If $\mathrm{Re}(\mathbb{s}) < 0$ for all roots, then the system is said to be stable. However, if $\mathrm{Re}(\mathbb{s}) > 0$ for any root, then the system is unstable [**2**]. A dynamic/disturbance input will cause the system state variables of an unstable system to follow unbounded trajectories. The model represented by equation 5.1 has the various machine currents as state variables. Practically, it is known that these variables do not follow unbounded trajectories even for dynamic inputs. Therefore, a stable model is desired.

5.2.1.1 Generator Action ($s < 0$)

Consider generation where the rotor slip is negative ($s < 0$):

1. From equation 5.7, $a < 0$ which means that $4ac < 0$ (positive resistance and inductance values are expected).
2. Therefore, $\sqrt{b^2 - 4ac}$ is a positive real number such that $\sqrt{b^2 - 4ac} > |b|$.
3. Equation 5.8 with $s < 0$ is inconclusive regarding the sign of b. Therefore, $b < 0$ or $b > 0$ or $b = 0$.

Whether $b < 0$ or $b > 0$ or $b = 0$ is not important. The fact that $\sqrt{b^2 - 4ac}$ is a positive real number (from point 2 above), that $\sqrt{b^2 - 4ac} > |b|$ (also from point 2 above) and that $\sqrt{b^2 - 4ac}$ is both added to and subtracted from $-b$ in equation 5.10, it means that the numerator of the first non-zero characteristic equation root is real and positive and that of the second root is real and negative.

Therefore, in the case of generation, the second-order state-space model is shown to have a characteristic equation with two non-zero real roots: one negative and one positive. This is illustrated in figure 5.1 which shows the characteristic-equation root placement in the $\mathbb{s}$-plane. As a result, the model is unstable for generation operation as there is always one characteristic equation root with a positive real component. Practically, SCIG operation is known to be stable. Therefore, the second-order state-space model under question is not suitable for simulating dynamic generation.

Having an unstable steady-state model is no contradiction. This is because, as shown in [**1**], the model is derived with the assumption of existing steady-state conditions.

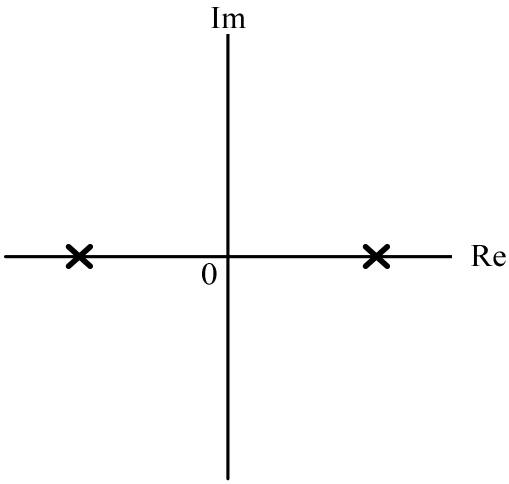

Figure 5.1: Stability of the Steady-State Electrical Model of a SCIG – Position of Characteristic-Equation Roots

5.2.2 Conclusion

The equivalent steady-state circuit model is evaluated regarding its application in the electrical component of a SCIG under dynamic generation. The model validity is considered from a stability perspective.

From equation 5.1, the only influence that the mechanical component has in the electrical sub-system is through the value of the rotor slip s. Therefore, by evaluating the steady-state electrical model according to rotor slip, the mechanical component effects on the electrical sub-system are considered.

Rotor slip is likely to change with dynamic generation which needs to be considered for model stability evaluation. However, the presented stability analysis is generalised for generation ($s < 0$) with instability being consistent over this region of operation. In other words, it doesn't matter what happens in the mechanical sub-system, the generator electrical model response will always be unstable. Therefore, the equivalent circuit model is unstable for generation under dynamic slip conditions. Even though the actual model response is variable and may not be exactly quantified, its nature is sufficiently qualified through stability.

With regards to modelling the generator action of a squirrel-cage induction machine, the steady-state electrical model is unstable for all generating conditions. This instability contradicts the practical operation of a SCIG. Therefore, the steady-state electrical model considered from a time-domain is not suitable for dynamic (or quasi-steady-state) generation.

On examining the steady-state circuit model of figure 2.1, it is observed that the rotor slip s is only present in the variable resistor $\frac{R'_r(1-s)}{s}$. For a negative (generating) rotor slip, the resistance becomes negative and changes characteristic to one of a variable source. This makes sense as the element now models a generating power flow from the mechanical system

to the electrical system. However, the nature of this source is such that there is no direct control over its behaviour. In other words, it is not a model input and is hidden within the model detail. It is suspected that this "hidden" variable source is responsible for the model instability. This may be a consequence of the steady-state simplifying assumptions used in the model derivation as described in [**1**] which results in the incorrect modelling of dynamic generation from a time-domain perspective.

5.3 Equivalent Dynamic Model

The equivalent steady-state circuit model is not applicable for dynamic generation. However, a complete SCIG model for the given application is still desired. As such, the model comprising the equivalent dynamic electrical model and mechanical model of chapter 2 is now considered. Model stability is addressed first after which a performance evaluation based on a comparison of simulation and experimental results is presented.

5.3.1 Model Stability

Stability analysis of the complete SCIG dynamic model is made difficult by its non-linearity and time-varying nature as described in section 2.4.2.1. The matter is further complicated if a general result (general machine parameters and operating conditions) is desired. An analysis providing useful insight into induction machine model stability is presented in [**1**]. Important assumptions and results are highlighted as follows.

Model stability is evaluated based on the roots of the characteristic equation as given by solving equation 5.4. This implies that a linear time-invariant equivalent of the complete induction machine model is used. This is achieved by considering small displacements (and their associated Taylor expansions) from a given steady-state balanced operating condition. The stability analysis is based in the synchronous reference frame and is somewhat generalised by considering a motoring slip ($0 < s < 1$) for three different machine sizes at constant (rated) stator frequency. The dynamics of the three machines are different but an important common result is observed. The dynamic model is generally unstable for high motoring slip values and stable for low motoring slip values [**1**]. Model instability for high slip values does not invalidate the application of the model as machine operation may very well be unstable for such values as the machine approaches a stable operating point (low rotor slip). The model instability/stability is said to correspond to the positive/negative gradient of the steady-state torque speed curve of an induction motor as illustrated in figure A.3 [**1**]. Remember, the equivalent steady-state circuit model is not applicable for generation simulation as it is unstable for all generating slip values ($s < 0$).

The stability analysis presented in [**1**] covers induction machine motoring operation. The work presented here is concerned with generation and requires a stability analysis for such operation. The results from [**1**] indicate that the equivalent dynamic model has regions of stability and instability for motor action and is not generalised for all possible induction machine parameter combinations. If the same applies for generation, then there is no purpose

in reproducing this analysis as there are regions of both stable and unstable operation with the analysis not being generalised for all machine parameters. However, it is required that the model is not unstable for all generation operation – the model must have regions of stable generation as shown by the experimental results which follow. In the following comparison of simulation and experimental results, possible model stability is observed by the good agreement between simulated and measured results.

In other words, model stability must match practical generator stability for the given operating condition. This is easily observed in a comparison of simulation and experimental results. In the generation tests which follow, stable generator behaviour is practically observed.

5.3.2 Model Performance – Simulation versus Experimental Results

The following is presented with the intention of evaluating the equivalent dynamic model of chapter 2. The simulation implementation of the model has been described in sections 2.4.2-2.4.3. The model is evaluated by first considering rated (approximately) steady-state generation followed by dynamic generation. Dynamic generation is considered from the perspective of both mechanical and electrical inputs. All tests are based on a balanced three-phase generator supply.

Each test includes:

- A basic test description with appropriate experimental and simulation settings/parameters
- Reasons for carrying out the given test including desired objectives
- Simulation and experimental results/observations targeted at satisfying the test objectives
- Test summary on important observations and conclusions

As previously mentioned, stator voltage excitation (amplitude and frequency) and prime-mover input torque act as experimental and simulation inputs. Stator current (magnitude and phase relative to stator voltage) and rotor speed are the experimental and simulation outputs which are compared for model verification. Power waveforms (electrical and mechanical) are derived outputs which provide a different perspective for the comparison of experimental and simulation results.

5.3.2.1 Steady-State Generation

5.3.2.1.1 Test Description

The SCIG is excited so as to generate under rated (approximately) steady-state conditions:

- Electrical excitation $\approx 400\ V_{RMS}$ line-to-line @ 50 Hz
- Constant prime-mover torque ≈ 14.8 N. m

For the first steady-state test (sinusoidal supply test), the SCIG is not excited by a power converter as illustrated in figure 3.4. Instead, it is supplied from the preceding three-phase

variac output. The coupled induction motor is excited by a power converter as shown in the same figure. The converter excites the motor based on a linear volts-per-hertz control such that the SCIG is driven above its synchronous velocity of 1500 rpm [**5**].

The second steady-state test (inverter supply test) is a repeat of the first test except that the SCIG is excited by a power converter as illustrated in figure 3.4. The converter is also set to linear volts-per-hertz control.

As previously mentioned in chapter 2, one point in time for induction machine steady-state operation is merely a time-shifted equivalent of any other point in time – voltage and current amplitude and phase, excitation frequency, electromagnetic torque, rotor speed/slip and electrical and mechanical power are all constant [**1**,**5**]. A consequence of this is that the experimental and simulation results do not have to be synchronised in order for them to be compared. As long as magnitudes and relative waveform phases (voltage versus current for example) can be established for each set of measurements, an appropriate comparison of results is possible.

Where constant values are produced by simulation, average values of the corresponding experimental results are used provided that an offset is obvious.

5.3.2.1.2 Test Objectives

The steady-state generation test is the obvious first test that should be carried out for model evaluation. It is a simple test that avoids the more complicated dynamic test should the models fail.

The experimental test is carried out twice: first with a truly-sinusoidal generator supply and then with an inverter-based generator supply. A comparison of the results from the two tests is used to expose the effect of the inverter PWM output (non-sinusoidal) on the operation of the SCIG. More specifically: if the inverter excitation is represented by its fundamental sinusoidal component as measured by the given measurement circuit, how does the operation of the SCIG compare with that of a truly-sinusoidal voltage excitation? In the ideal case, there is no significant difference between truly-sinusoidal and inverter-based supply tests. This is used to evaluate the approach of considering only the fundamental sinusoidal component of the inverter excitation – at least from an operational perspective for symmetrical systems with balanced excitation. Furthermore this implies that sinusoidal-excitation-based simulation results may be compared with inverter-based practical results for model evaluation.

5.3.2.1.3 Experimental/Simulation Results and Observations

5.3.2.1.3.1 Generator Inputs

Figures 5.2-5.3 show the SCIG phase-voltage excitation for the experimental cases of truly-sinusoidal and inverter excitation respectively. As illustrated in these figures the generator electrical supply is approximately balanced in both cases.

Obviously the generator supply as given in figures 5.2-5.3 is not perfectly sinusoidal in both cases with a "wavy" signal super-imposed on the sinusoidal fundamental. This occurs for both the sinusoidal and inverter excitation and is, therefore, not a consequence of the inverter operation. The effect of this non-ideal excitation is observed in the generator power which follows.

The ideal perfectly-balanced equivalent of the generator excitation is given by the simulated generator excitation as shown in figure 5.4.

The stator frequency for the two excitation cases is measured as illustrated in figures 5.5-5.6. There appears to be some variability in the measured frequencies which is further affected by the measurement resolution of the oscilloscope and a multiplication factor as discussed in appendix D. This is observed by the stepped nature of the measured signals. However, the measurements appear to have an average value of 51.35 Hz and 51.99 Hz for figures 5.5 and 5.6 respectively. The maximum measured frequency deviation is no more than 3 % from these average values.

The simulated voltage supply (perfectly balanced) of figure 5.4 is based on the measurements for the truly-sinusoidal excitation case. As such, the stator phase voltage has a peak amplitude of 327 V and frequency of 51.35 Hz.

The experimental and simulation voltage excitations are comparable in frequency and amplitude. A visual inspection of figures 5.2-5.4 also indicates that they are balanced supplies (approximately balanced in the experimental cases). Therefore, all three supplies are comparable. Slight deviations from a balanced supply are easily observed in the total electrical power waveforms presented later.

The inverter-excitation fundamental component is comparable to that of the sinusoidal excitation case. Since the inverter output is set to 100 % (with the appropriate machine data entered into the controller), this implies that the inverter output is a good approximation (from a fundamental perspective) of the sinusoidal excitation it aims to mimic.

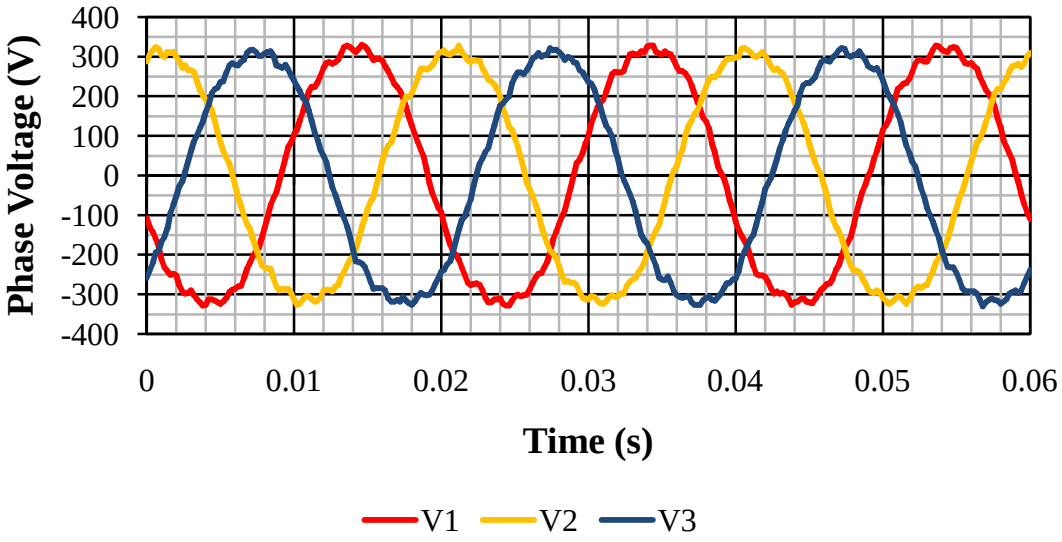

Figure 5.2: SCIG Stator Voltage – Sinusoidal Excitation

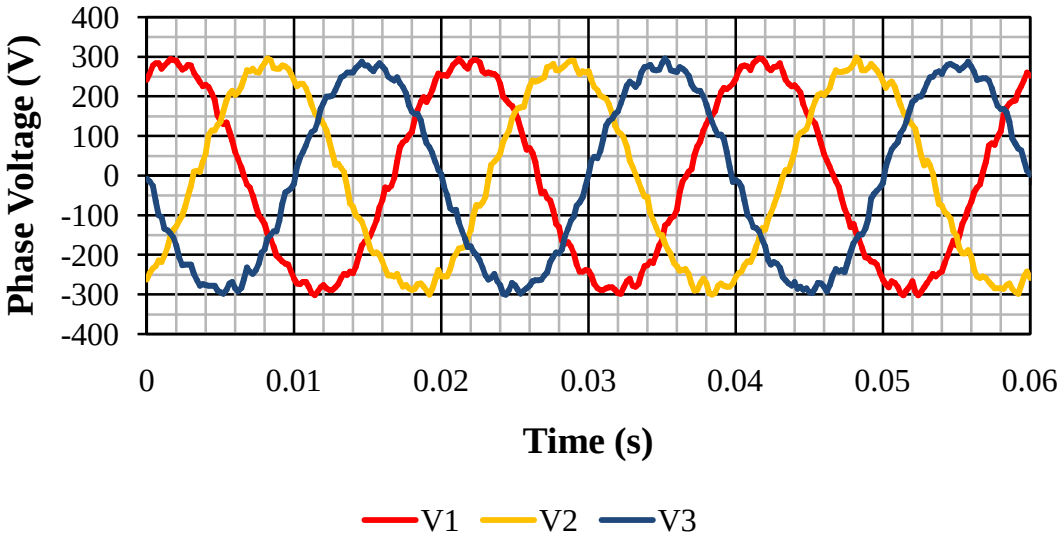

Figure 5.3: SCIG Stator Voltage – Inverter Excitation

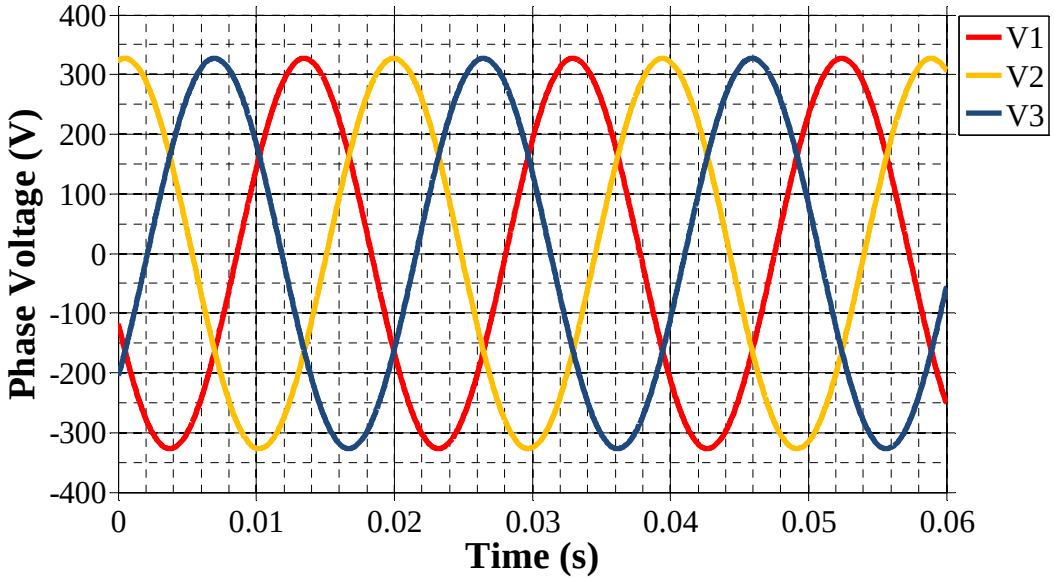

Figure 5.4: SCIG Stator Voltage – Simulation

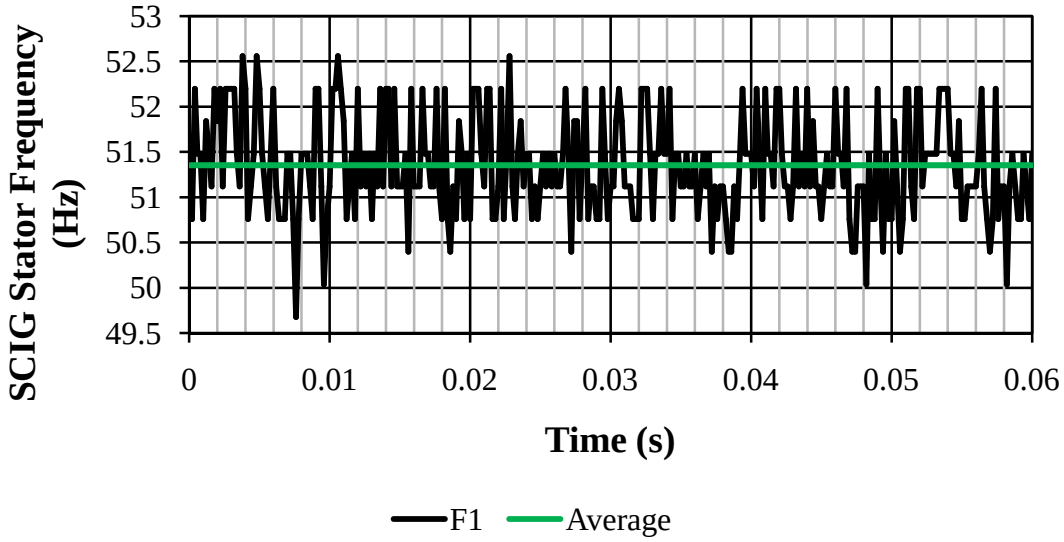

Figure 5.5: SCIG Stator Frequency – Sinusoidal Excitation

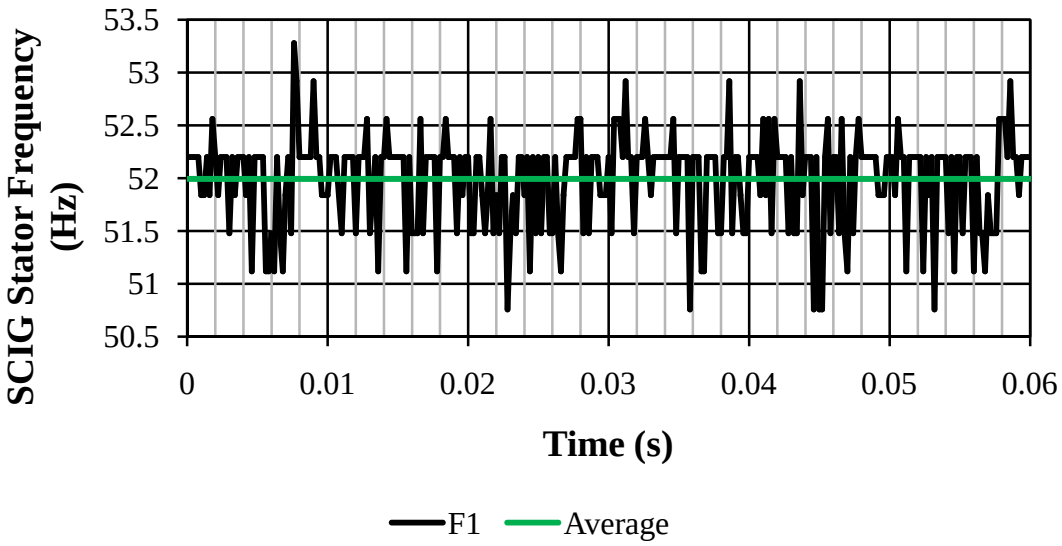

Figure 5.6: SCIG Stator Frequency – Inverter Excitation

The mechanical input to the SCIG is given by the prime-mover input torque. This is measured as shown in figures 5.7 and 5.8 for the truly-sinusoidal and inverter excitation respectively. The torque is only approximately constant with an average value of 14.76 N. m and 14.36 N. m for the truly-sinusoidal and inverter supply cases respectively. From the measured results, the maximum torque deviation from the average torque values is 11 %. Non-ideal machine coupling may be a contributing factor to the non-constant prime-mover torque. For simulation purposes, a constant prime mover torque of 14.76 N. m is used.

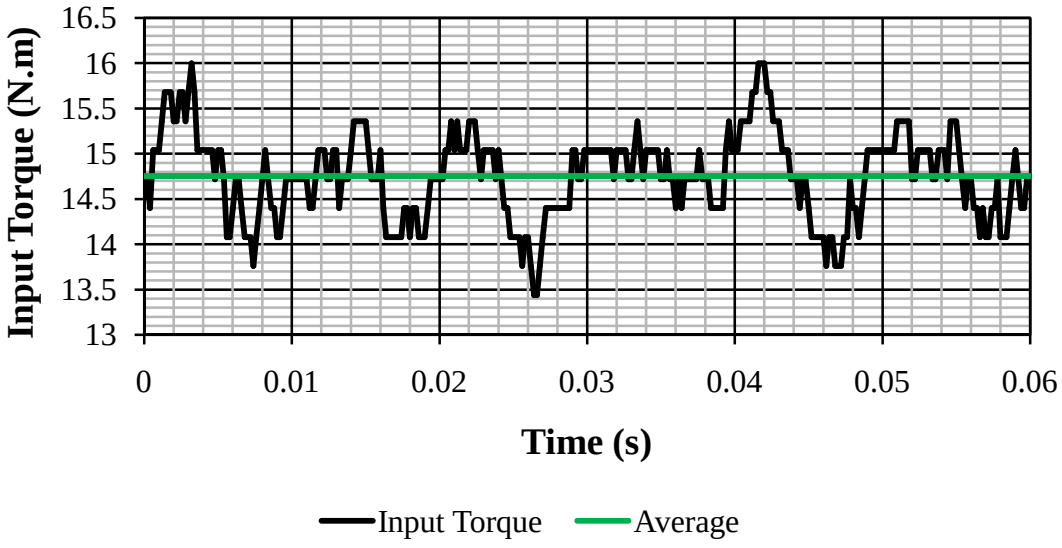

Figure 5.7: Input Prime-Mover Torque – Sinusoidal Excitation

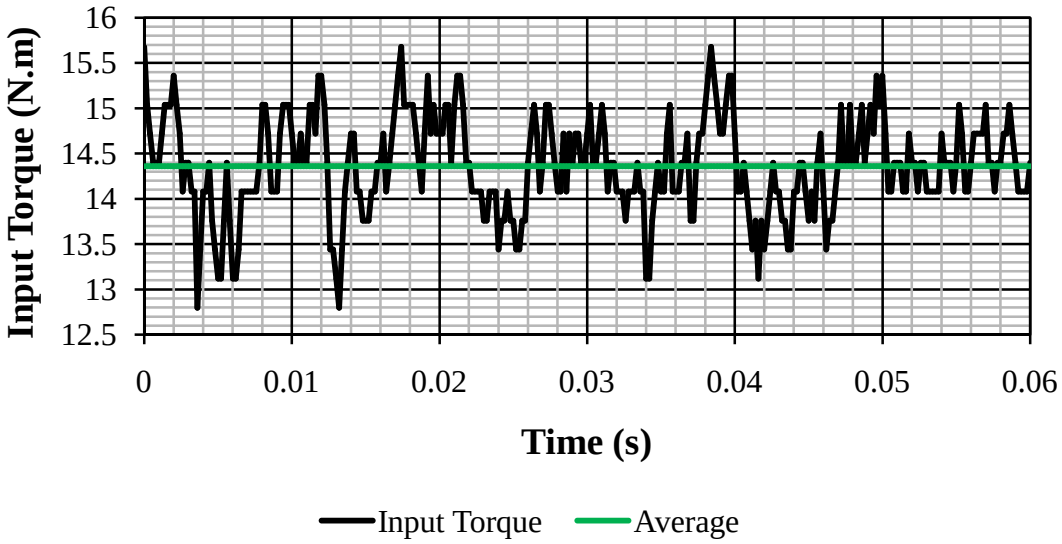

Figure 5.8: Input Prime-Mover Torque – Inverter Excitation

Since both electrical and mechanical inputs to the SCIG are comparable for the truly-sinusoidal and inverter excitation cases, the generator responses may be compared in observing the effect of inverter excitation. This provides insight regarding the reduction of the inverter-based excitation to its fundamental sinusoidal equivalent.

Furthermore, the experimental and simulation generator inputs also show good agreement. Therefore, a comparison involving the measured/simulated generator response is possible and provides insight into model performance at steady-state.

5.3.2.1.3.2 Generator Response

The measured stator phase currents for both experimental cases are given in figures 5.9-5.10. The corresponding simulated phase currents are presented in figure 5.11. Like the corresponding phase voltages, the phase currents are comparable in amplitude, frequency and their balanced nature. Again, any deviation from a balanced excitation is observed in the waveforms of the total electrical power.

What remains is to compare the current phase relative to the corresponding voltage as this affects electrical power. This is possible in figures 5.12-5.14. Since all three cases have approximately balanced electrical excitation, only a single phase needs to be considered. The phase voltage leads the phase current by $135°, 146°$ and $135°$ for the three cases respectively. A lagging power factor together with a phase angle θ where $90° < \theta < 180°$ resulting in a negative (generating) average phase power is expected [5]. The three phase angles are not identical but are comparable – difference is less than $10\ \%$. Furthermore, the wavy non-ideal nature of the of the measured waveforms affects the measured phase angles; any error introduced is magnified in converting a phase angle from $seconds$ to $degrees$.

In conclusion, the phase currents for both experimental cases as well as the simulation are comparable.

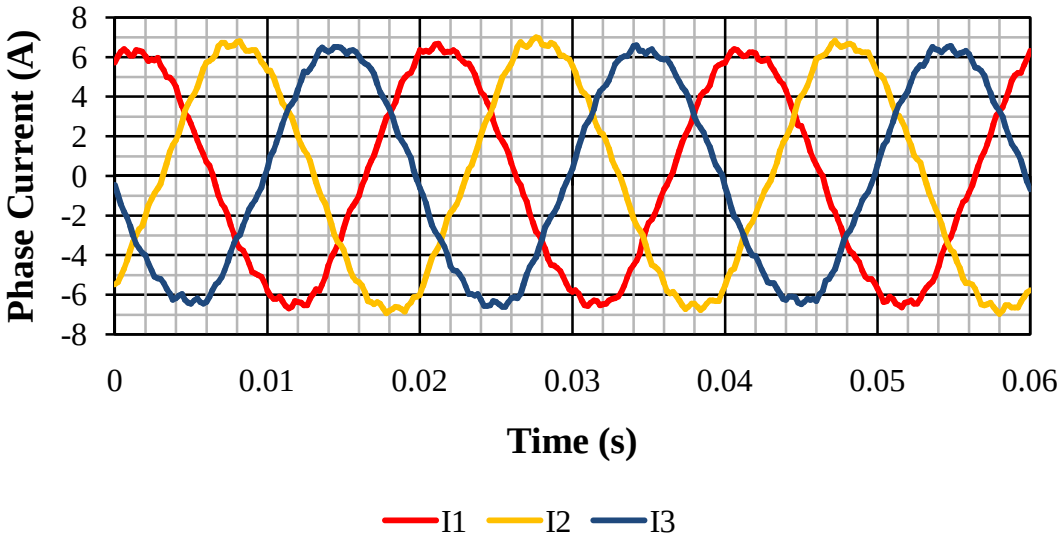

Figure 5.9: SCIG Stator Current – Sinusoidal Excitation

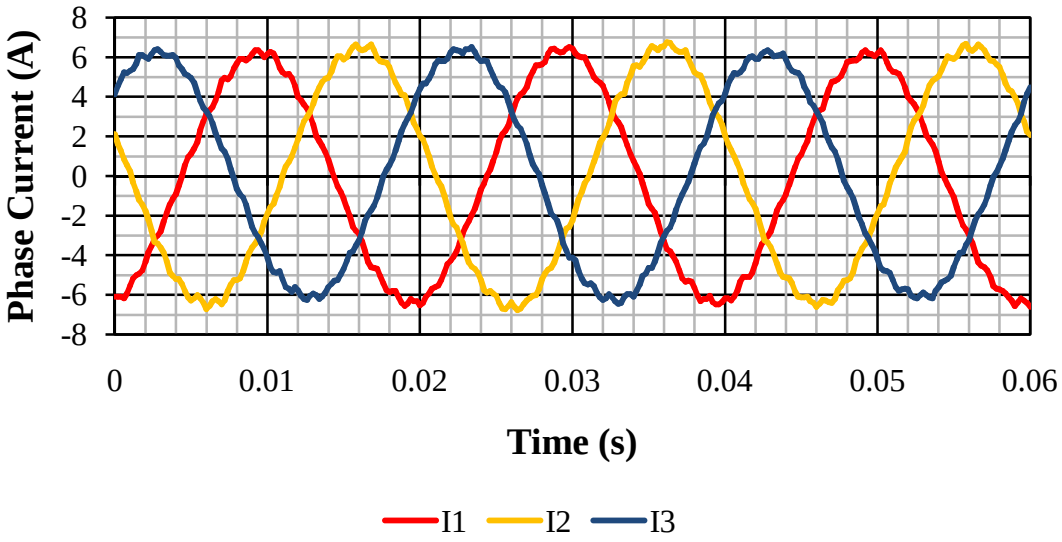

Figure 5.10: SCIG Stator Current – Inverter Excitation

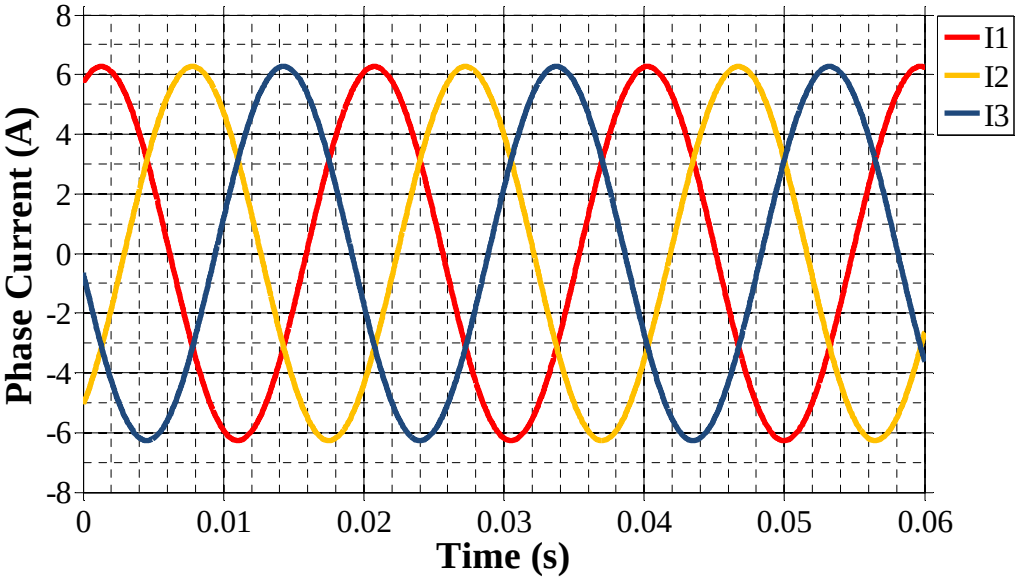

Figure 5.11: SCIG Stator Current – Simulation

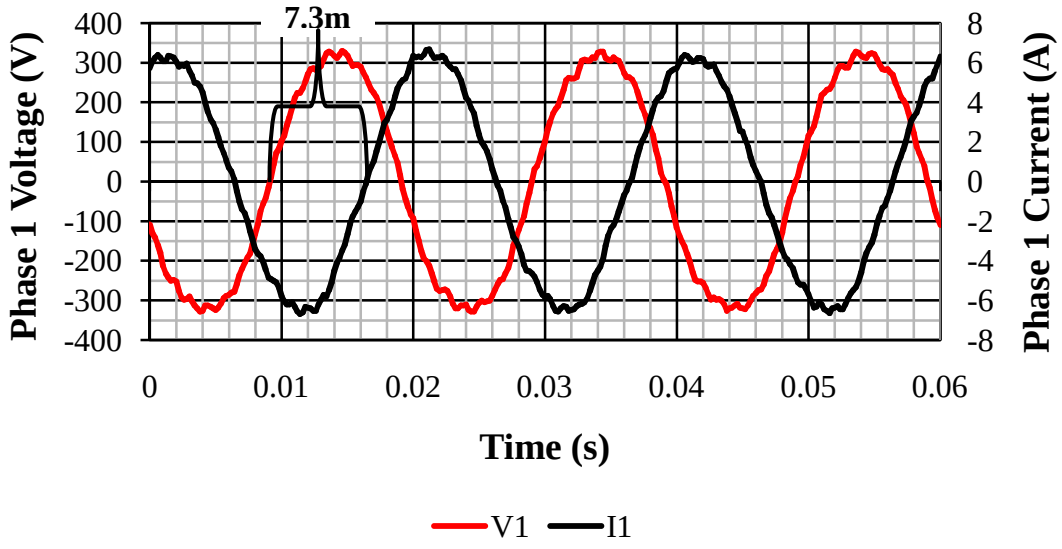

Figure 5.12: SCIG Phase 1 Excitation – Sinusoidal Excitation

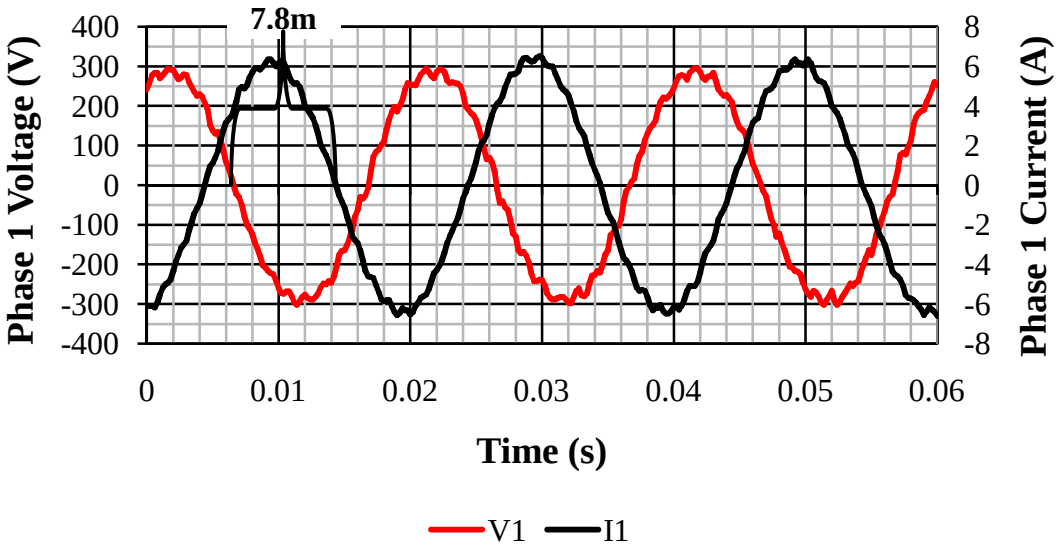

Figure 5.13: SCIG Phase 1 Excitation – Inverter Excitation

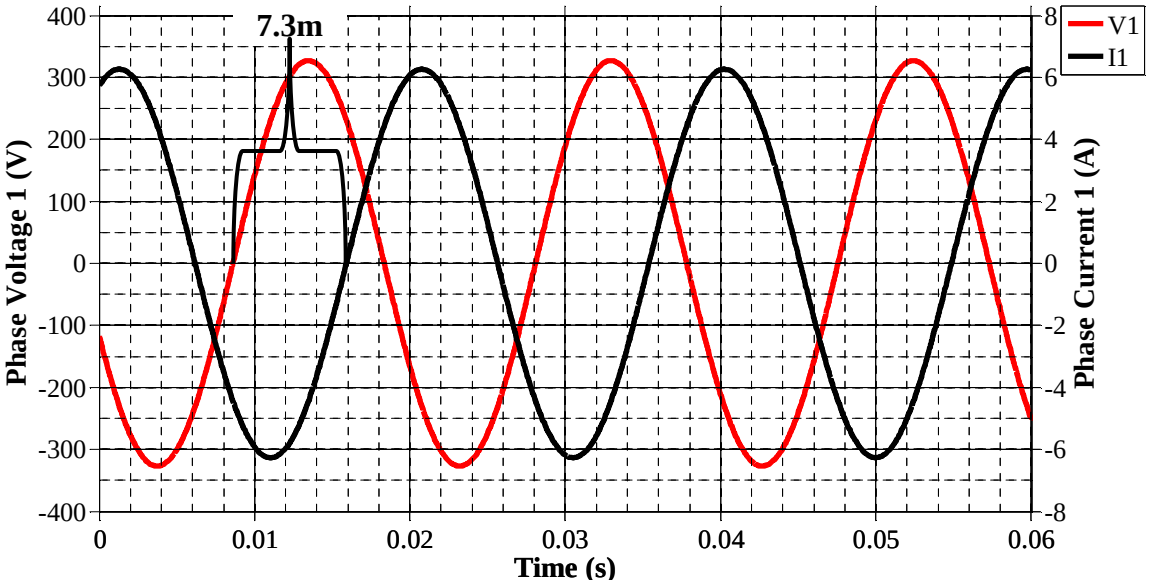

Figure 5.14: SCIG Phase 1 Excitation – Simulation

The next machine output to be considered is the rotor speed as presented in figures 5.15-5.17. The limited oscilloscope resolution is observed in the tiered nature of the measured rotor speeds; measured signals are represented by their average values. The average rotor speed is 1568 rpm and 1576 rpm for the sinusoidal and inverter excitation respectively. Experimentally, the maximum rotor speed deviation from average rotor speed is no more than 2 %. The simulated rotor speed is constant at 1588 rpm. Therefore, the rotor speed is comparable for the experimental and simulated cases.

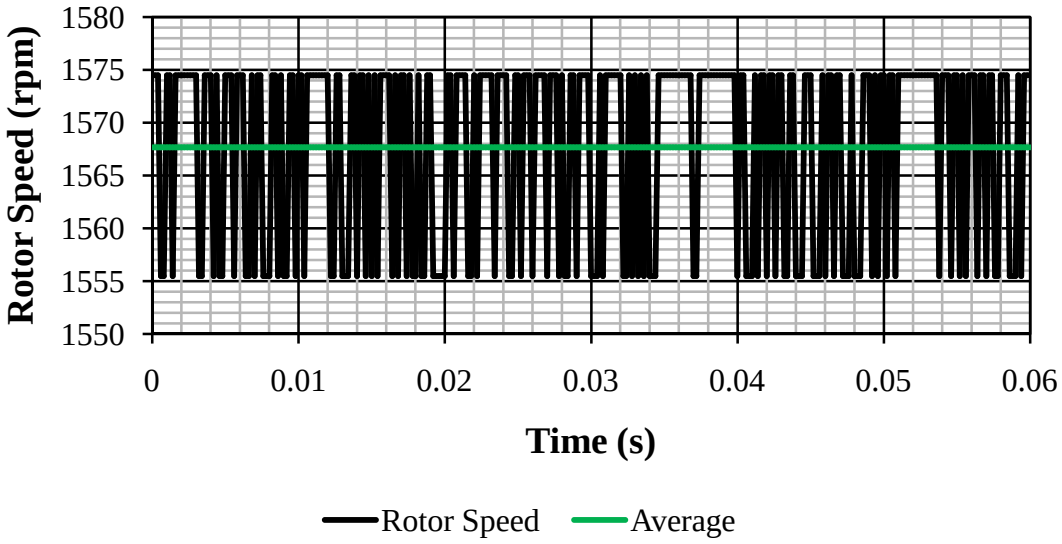

Figure 5.15: Rotor Speed – Sinusoidal Excitation

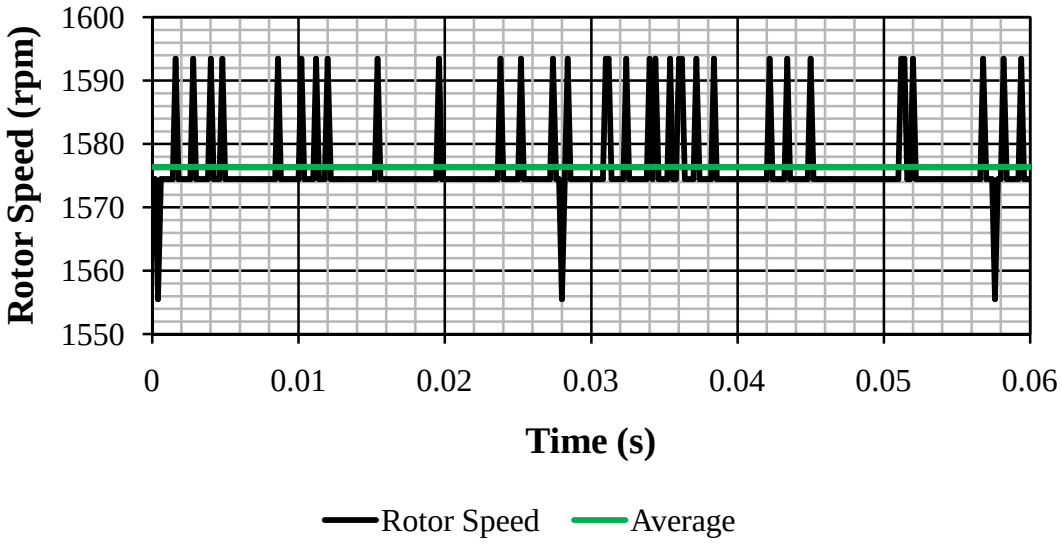

Figure 5.16: Rotor Speed – Inverter Excitation

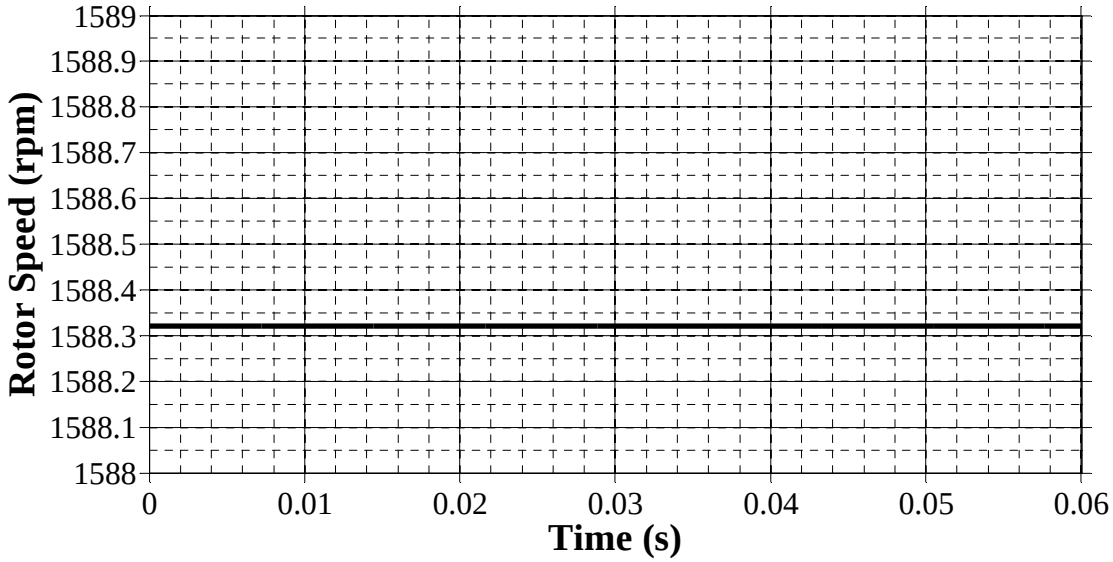

Figure 5.17: Rotor Speed – Simulation

Power and efficiency information are now presented to provide a different perspective on generator and model performance. Ideal generation based on a perfectly balanced machine supply and ideal machine construction is illustrated in the simulation results of figure 5.18. The sinusoidal components of the per-phase powers cancel with the average powers summing to give a constant total power of -2.17 kW (generation) [**5**].

Per-phase powers as well as total stator power for the experimental cases are given in figures 5.19-5.20. The experimental voltage and current measurements are only approximately sinusoidal/balanced as previously mentioned. This is reflected in the corresponding stator powers:

- Per-phase powers are approximately sinusoidal.
- Total stator power is approximately constant.

The approximately balanced/sinusoidal nature of the phase voltages and currents is a consequence of practical system non-idealities which may include:

- A non-ideal voltage supply that:
  - is variable in amplitude and frequency
  - is not perfectly balanced
  - has some source impedance such that the output voltage is current dependent
- A non-ideal generator that:
  - is not perfectly symmetrical across all three phases
  - has windings placed in slots instead of being continuously distributed
- A non-constant prime mover torque

However, a definite average total power of -2.12 kW and -2.11 kW is observed for figures 5.19 and 5.20 respectively. A worst-case deviation of approximately 13 % from the average power is observed in the experimental cases.

There is a noticeable difference in comparing the peak powers of the truly-sinusoidal and inverter supply cases – the reason for this difference is unknown. The simulated peak powers appear to match the inverter-based results more closely. The three average total powers show agreement. Overall, the power results for the three figures are comparable, especially considering the fact that the experimental results are derived from voltage and current measurements of non-ideal systems – slight differences in the voltages and currents between the three cases are magnified by voltage-current multiplication in calculating the electrical power.

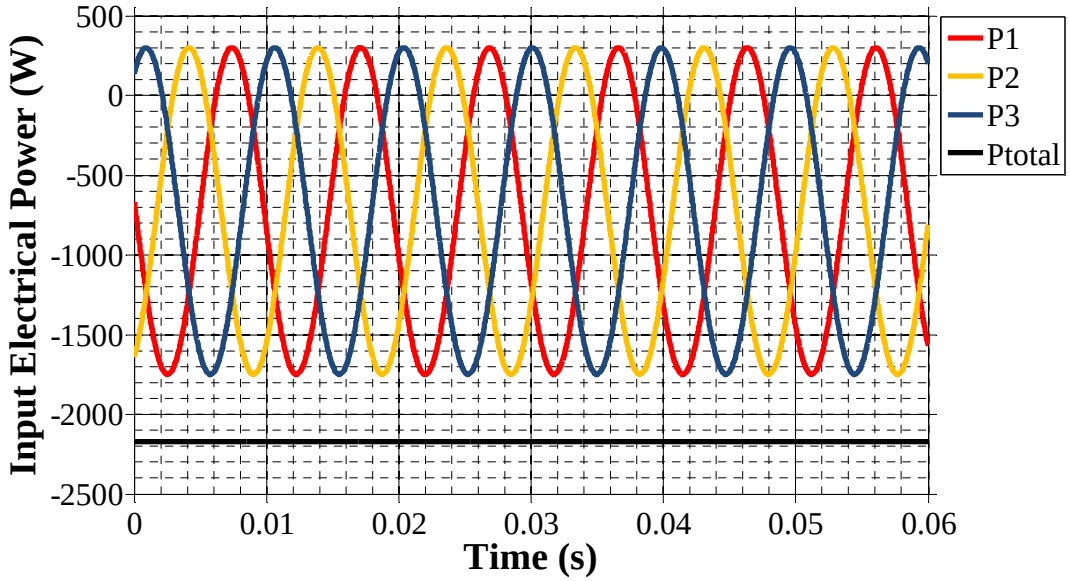

Figure 5.18: Input Electrical Power – Simulation

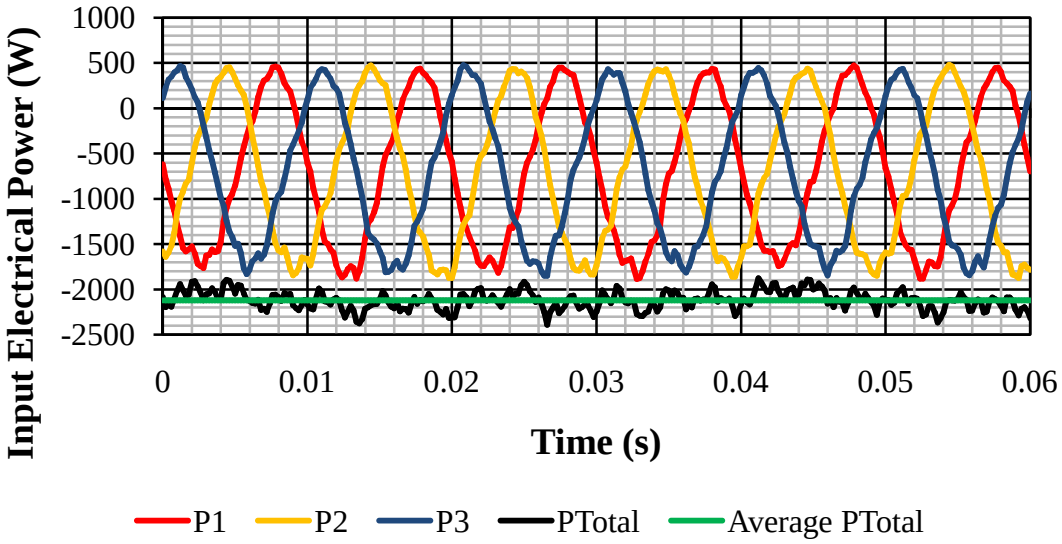

Figure 5.19: Input Electrical Power – Sinusoidal Excitation

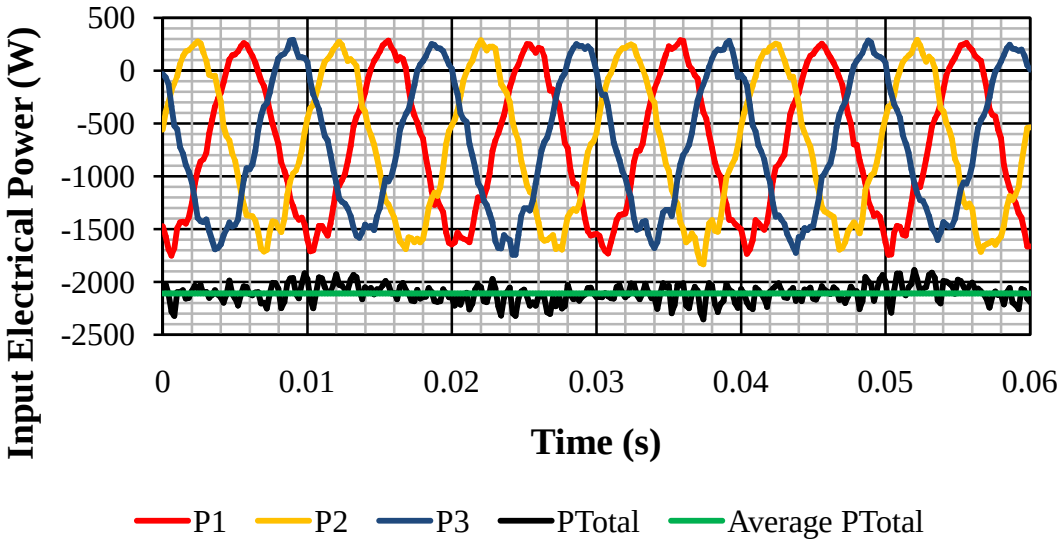

Figure 5.20: Input Electrical Power – Inverter Excitation

The mechanical power input to the SCIG by the prime-mover is presented in figures 5.21-5.22 for the experimental tests. The mechanical power is derived from the rotor speed and prime-mover torque measurements shown earlier. Therefore, the calculated mechanical power suffers from the same variability as the original measurements. However, there is a clear average power of 2.42 kW and 2.37 kW for the truly-sinusoidal and inverter excitation cases respectively. Deviation from these averages is no more than 11 %. The average experimental mechanical powers are comparable to the constant simulated power of 2.46 kW.

The mechanical power loss as a result of friction and windage is simulated at 40 W which is less than 2 % of the average mechanical input. As a result, the power entering the electrical

subsystem from the mechanical subsystem at steady-state (no change in angular momentum) is approximately the same as the prime-mover input power.

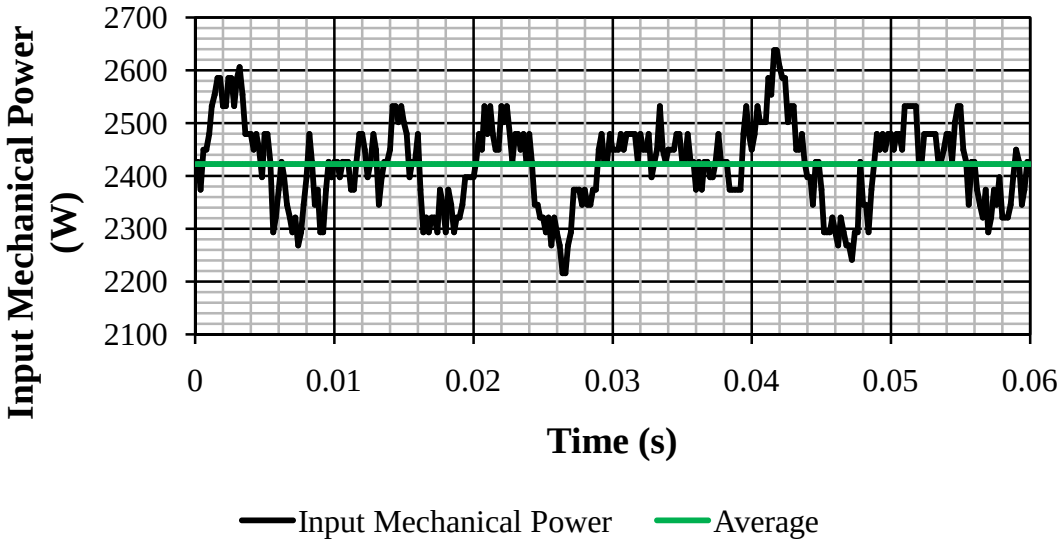

Figure 5.21: Input Mechanical Power – Sinusoidal Excitation

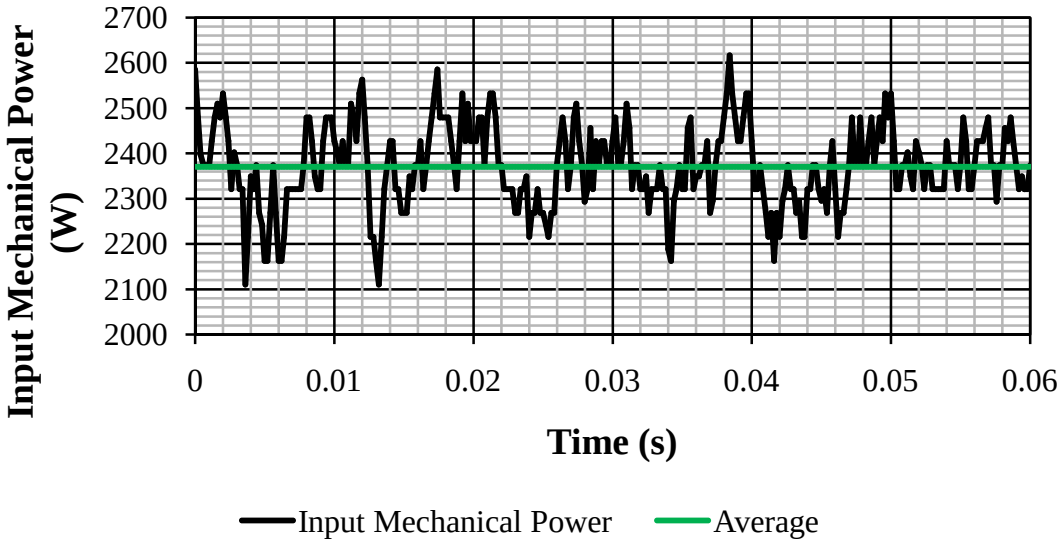

Figure 5.22: Input Mechanical Power – Inverter Excitation

Generation efficiency may be calculated by considering the average electrical/output power as a fraction of the average mechanical/input power. Generation efficiency is 87.60 % and 89.03 % for the sinusoidal- and inverter-based experimental cases respectively; simulated generator efficiency is 88.21 %. The experimental efficiencies are a little high – they should be slightly lower than the simulated efficiency since magnetic core loss is neglected in the theoretical models. However, the measured efficiencies are still acceptable considering that they are derived values from measurements of practically non-ideal systems.

5.3.2.1.4 Conclusion

The experimental electrical excitation is found to be comparable (from a fundamental frequency perspective) for truly-sinusoidal and inverter-based excitation. This gives an indication that the inverter is functioning correctly in approximating a sinusoidal supply.

Stator currents as well as average rotor speed is found to be comparable for the experimental cases of truly-sinusoidal and inverter-based excitation. This implies that the two methods of machine excitation are equivalent when considering the fundamental component of electrical waveforms as a means of comparison. This is supported by the derived electrical and mechanical power waveforms as well as the generation efficiency results. Therefore, inverter-based generator excitation may be used with measured electrical waveforms reduced to their fundamental sinusoidal component.

Since practical and simulated generator responses are comparable, the induction machine model gives a good representation of practical SCIG performance for rated steady-state operation.

5.3.2.2 Dynamic Generation – Mechanical Input Dynamics

The following test deals with a case of constant generator supply (voltage amplitude and frequency) but dynamic prime-mover torque. This test is carried out with the intention of concluding on SCIG model performance in an OWC WEC for the case of a constant sea state as presented in chapter 6.

5.3.2.2.1 Test Description

The experimental setup is the same as that of test 2 (inverter-excitation test) of the previous steady-state-generation analysis with the prime-mover power converter controlled such that a sinusoidal torque is applied to the generator rotor. The prime-mover torque ranges from $0\ \mathrm{N.m}$ to a rated torque of $14.8\ \mathrm{N.m}$ (approximately). The torque period may be varied but is chosen as $0.1\ \mathrm{s}$ ($10\ \mathrm{Hz}$). This accommodates dynamics which are slower while allowing for a convenient analysis of results (electrical excitation frequency is not significantly higher than the torque frequency). The generator voltage excitation is set constant in amplitude and frequency.

The fundamental test characteristic is based on cycling the SCIG from no generation (light motoring) to deep generation and back again about a given synchronous velocity.

5.3.2.2.2 Test Objectives

The objective of the following test is to evaluate the performance of the SCIG dynamic model in the case of a set generator supply with a dynamic prime-mover torque.

Another test objective involves determining whether the steady-state SCIG circuit model may be used to identify the initial generator currents for the dynamic generation in question

(balanced stator supply with constant voltage amplitude and frequency together with a sinusoidal prime-mover torque).

5.3.2.2.3 Experimental/Simulation Results and Observations

5.3.2.2.3.1 Generator Inputs

The measured generator stator supply is given by figure 5.23 and approximates a balanced three-phase supply. The phase voltages are reproduced in the simulations with a peak amplitude of 295.33 V and frequency of 46 Hz such that the simulation voltages are in-phase with their corresponding experimental voltages over the given time series.

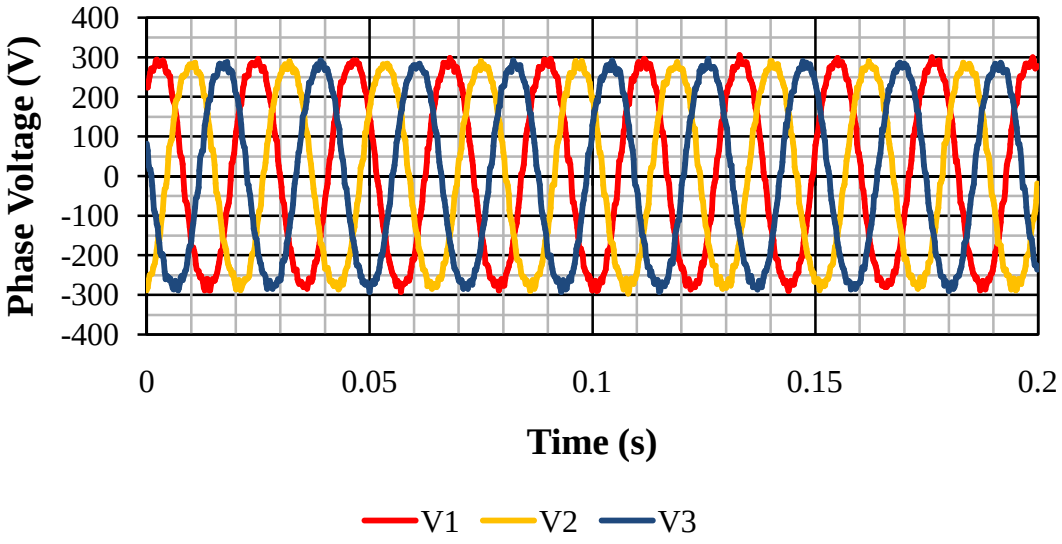

Figure 5.23: SCIG Stator Voltage – Experimental

The generator mechanical input is given by the torque waveforms of figure 5.24. The sinusoidal simulated torque approximates the measured experimental torque as desired.

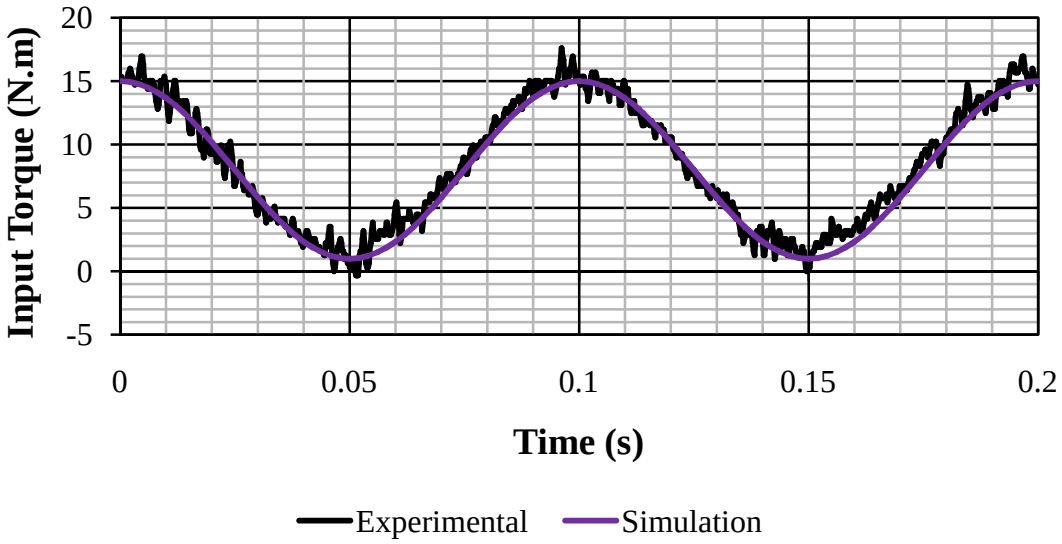

Figure 5.24: Input Prime-Mover Torque

The SCIG inputs are comparable and synchronised for the experimental and simulation tests. Therefore, the practical and theoretical generator responses can be compared on an instantaneous basis.

5.3.2.2.3.2 Generator Response

The generator response may be characterised by first analysing the resulting stator currents. The experimental and simulated currents are given in figures 5.25 and 5.26 respectively. From these figures, it is observed that the practical and theoretical stator currents show good agreement thus confirming generator model performance.

As described in chapter 2, the SCIG steady-state circuit model has been used to identify the generator initial currents based on a phasor approach. From the current waveforms presented, it is concluded that the initial conditions are derived approximately but sufficiently.

As shown in figures 5.25-5.26, the stator currents appear to be sinusoidal in nature with instantaneously varying amplitude and frequency. The variable frequency is apparent when considering the "sinusoidal" half-periods. This is not possible according to a phasor analysis of the SCIG steady-state circuit model where the stator-current frequency would be determined by the stator-voltage frequency (constant in this case). Therefore, if the test had started at some other point in the generation operation it is possible that the calculated initial conditions would have been less accurate. Therefore, it should be concluded that the SCIG steady-state circuit model cannot be used to exactly identify the initial generator currents but may give a good approximation of them. In other words, the given dynamic generation is not exactly a series of different steady-state conditions.

Since the voltages and currents of the experimental and simulation tests have been compared on an instantaneous basis, there is no need to verify the phase shift of the phase currents relative to their corresponding phase voltages.

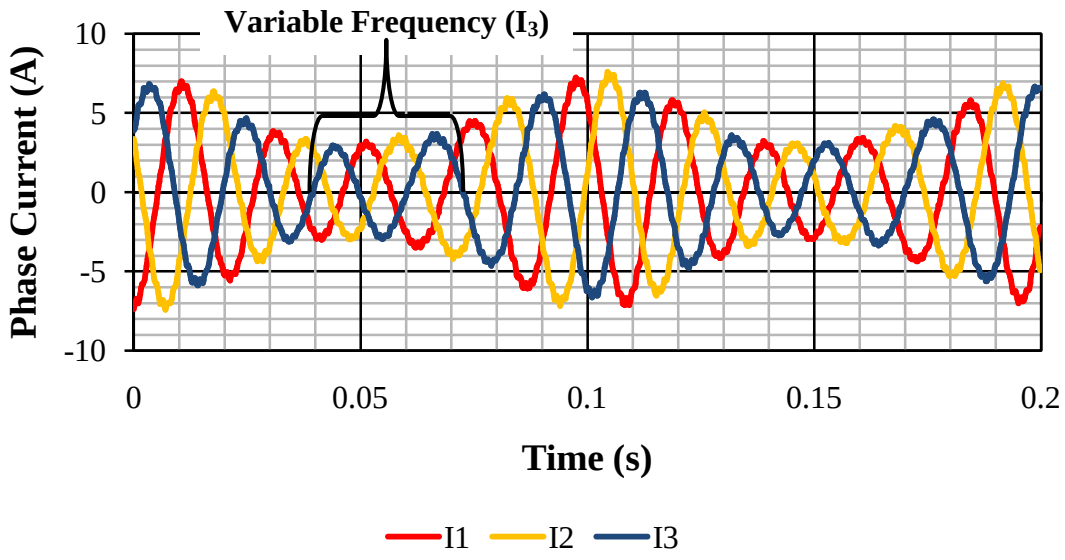

Figure 5.25: SCIG Stator Current – Experimental

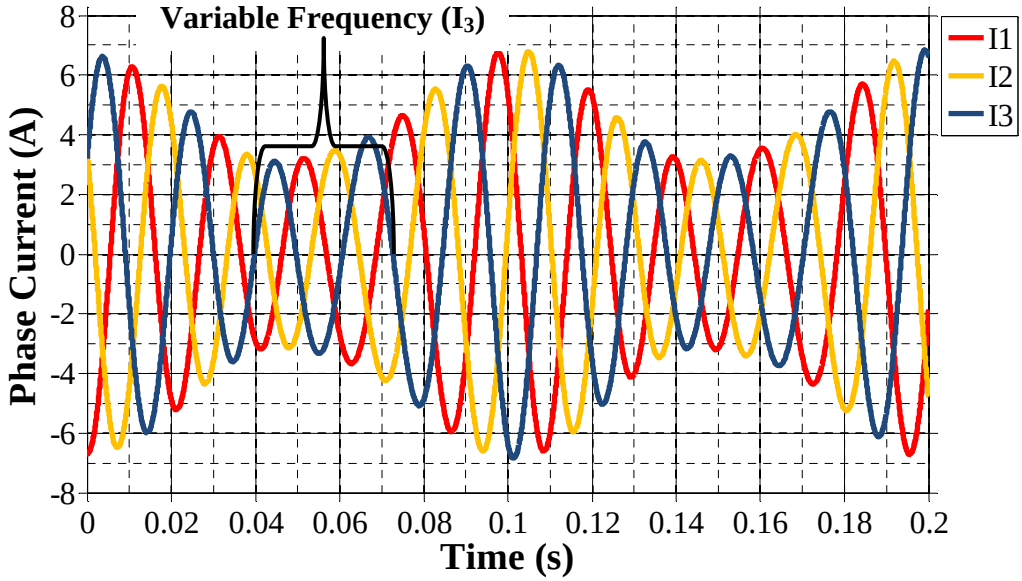

Figure 5.26: SCIG Stator Current – Simulation

The practical and theoretical rotor speed is presented in figures 5.27 and 5.28 respectively. A speed variation with variable driving torque is expected based on the torque-speed relationship of an induction machine [**5**]. This is clearly shown in the simulated rotor speed which is sinusoidal with a frequency of 10 Hz. Such a sinusoidal variation is not observed in the measured rotor speed. This is a consequence of the first-order low-pass filtering effect of the rotor speed measurement as mentioned in section 3.5.1 and quantified in section D.5.2. For a given frequency of rotor speed variation, the speed measurement has a -3 dB bandwidth of 0.34 Hz. Therefore, a 10 Hz simulated speed variation of 60 rpm will be measured as 2.04 rpm. This speed variation is lost in the measurement resolution as shown in

figure 5.27. The average measured speed is 1433 rpm which corresponds to the average simulated speed of 1405 rpm.

The generator model cannot be evaluated from a speed comparison; however, the previous comparison of stator currents is sufficient. The machine rotor and stator windings are magnetically coupled and, for argument purposes, may be considered as some sort of rotating transformer. In this way, the stator currents are dependent on the rotor currents. According to Faraday's and Lenz's laws of electromagnetic induction, the voltage induced in the rotor windings is dependent on the rotor velocity relative to the air-gap magnetic field. This implies that the rotor current and, therefore, stator current is dependent on the rotor speed. If there is good agreement between measured and simulated stator currents, then there will be good agreement between the corresponding rotor speeds. From a steady-state perspective, the dependence of the stator current on rotor speed/slip is observed in the circuit model of figure 2.1 where the effective rotor resistance is dependent on the rotor slip.

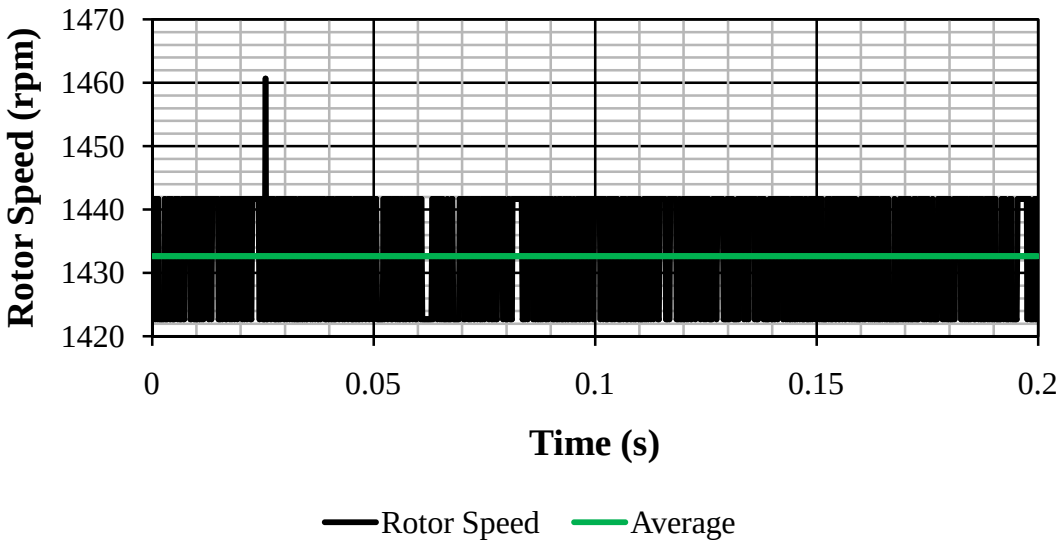

Figure 5.27: Rotor Speed – Experimental

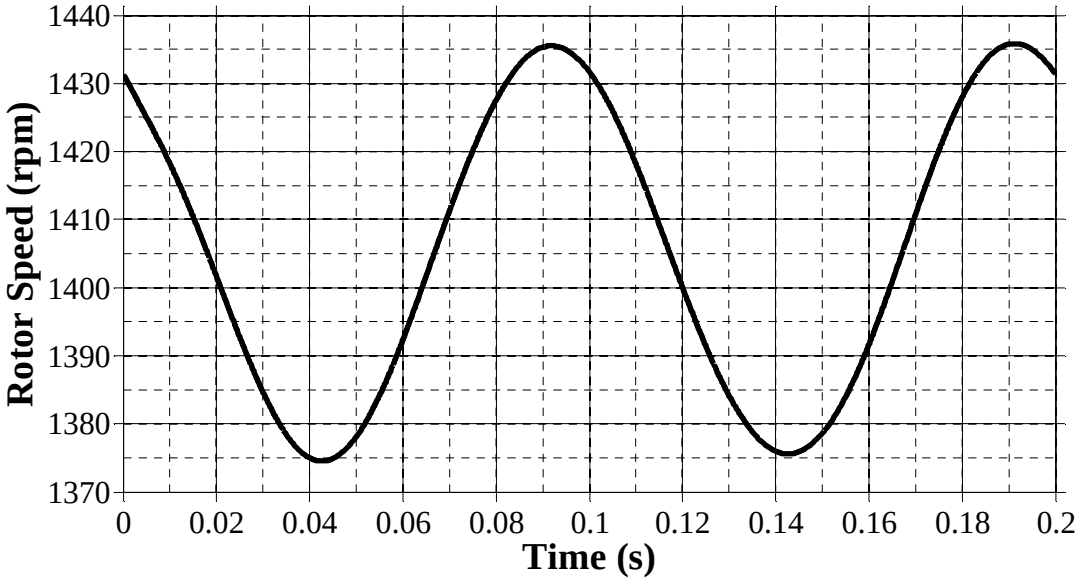

Figure 5.28: Rotor Speed – Simulation

Experimental and simulated power waveforms are now presented providing further insight into model performance.

The per-phase and total electrical input power is given in figures 5.29 and 5.30 for the experimental and simulated results respectively. Considering possible system non-idealities, the power waveforms show good agreement. The machine operation oscillates between deep generation and light motoring. The change in per-phase power and its effect on the total electrical power developed is obvious. It appears as though the machine operation is a sort of variable steady-state operation comprising a series of different steady-state conditions. Such an analogy is not exactly true based on the varying current frequency evident in figures 5.25-5.26.

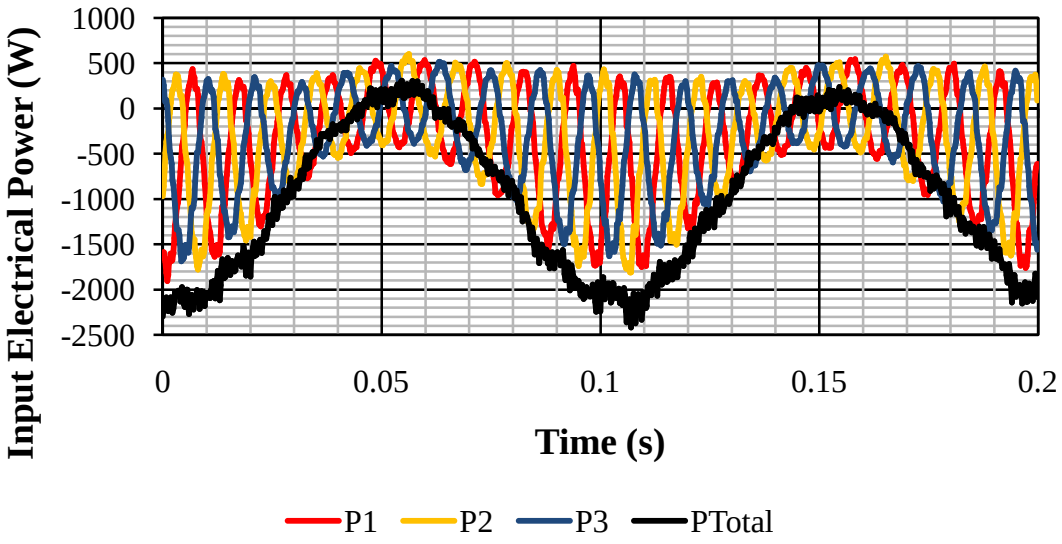

Figure 5.29: Input Electrical Power – Experimental

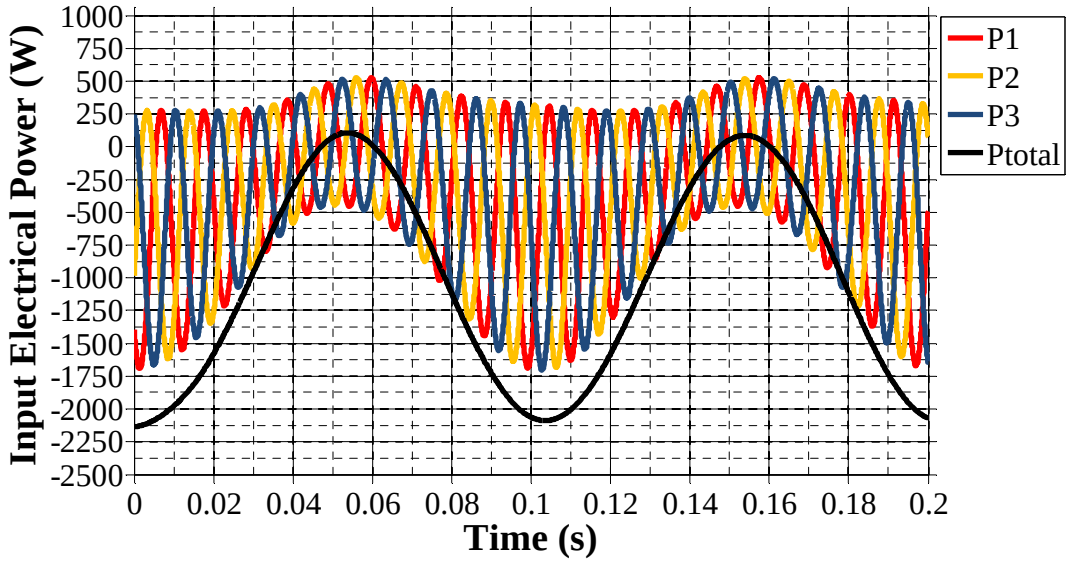

Figure 5.30: Input Electrical Power – Simulation

The simulated speed deviation from its average value is 2.14 %. For the purpose of determining mechanical power, the speed can be considered as being approximately constant. Therefore, the measured speed of figure 5.27 can be used in the experimental power calculation to obtain approximate values.

The experimental generator electrical power and prime-mover mechanical power are illustrated in figure 5.31. The corresponding simulation results are also given in figure 5.31. Despite the inaccuracy in the speed measurement, there is good agreement between measured and simulated mechanical powers.

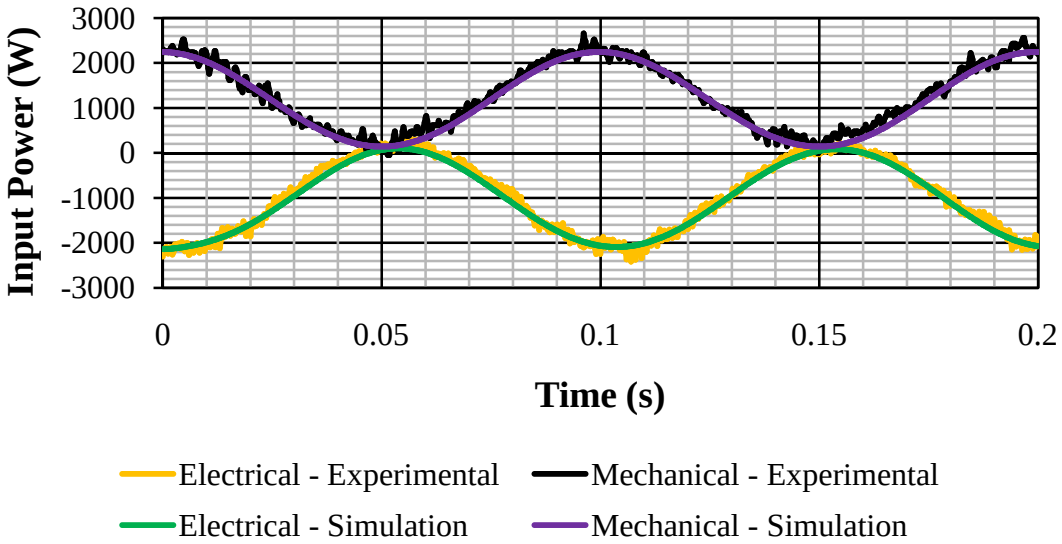

Figure 5.31: Prime-Mover Mechanical Power versus SCIG Electrical Power

5.3.2.2.4 Conclusion

The dynamic model is evaluated by comparing simulation and experimental results in the case of a dynamic prime-mover torque. The considered dynamic involves a sinusoidally-varying input torque driving the SCIG between light motoring and deep generation.

Even though there is a good agreement between the average values of the measured and simulated rotor speed, a comparison of rotor speed cannot be used to conclusively evaluate model performance. This is because the rotor speed dynamics are not accommodated by the measurement system bandwidth. However, the good agreement based on the stator currents is sufficient to conclude that the dynamic model is applicable for the given case of a dynamic prime-mover torque. This is supported by the agreement in simulation/experimental power waveforms.

The tested generation condition involves a balanced stator supply with constant voltage amplitude and frequency together with a sinusoidal prime-mover torque. It is concluded that the considered dynamic generation is not exactly a series of steady-state operating conditions. This is apparent in the stator-current frequency variation. As a result, a phasor-based analysis of the equivalent steady-state circuit model is only able to approximate the initial stator/rotor current conditions for the given dynamic generation.

5.3.2.3 Dynamic Generation – Electrical Input Dynamics

The test in question involves model performance with dynamics in generator electrical supply. The intention of carrying out the following test is to conclude on SCIG model performance in an OWC WEC for the case of a change in sea state as discussed in chapter 6.

5.3.2.3.1 Test Description

The dynamic considered involves a sinusoidal variation of the stator supply frequency. The sinusoidal variation has a frequency of 4 Hz where the generator operation is continuously cycled between light generation and deep generation.

The prime-mover induction machine electrical excitation is kept constant – there is no intentional variation in generator mechanical excitation. Owing to the coupled nature of induction-machine torque to its rotor speed/slip there will be a prime-mover torque response [**5**]. The measured prime-mover torque is simply reproduced in the simulations.

As is the case for the previous dynamic generation based on a dynamic prime-mover torque, the generator and prime-mover induction machines are electrically supplied by power converters.

5.3.2.3.2 Test Objectives

The test objective is to evaluate the performance of the SCIG dynamic model in the case of a variable generator supply; the dynamic considered is a sinusoidal variation of the stator frequency.

The results are presented for one cycle of supply variation; however, generator operation is merely repeated with following cycles.

A secondary objective involves investigating whether the equivalent steady-state circuit model may be used in determining the initial stator and rotor currents for the given repetitive generation condition.

5.3.2.3.3 Experimental/Simulation Results and Observations

5.3.2.3.3.1 Generator Inputs

The measured stator voltage supply of the SCIG is given by figure 5.32. The three-phase supply appears to be approximately balanced in nature. Any variation of the supply amplitude and frequency is not immediately obvious from figure 5.32 but will become apparent on the establishing a mathematical equivalent for simulation purposes. However, no periodic variation in voltage amplitude (especially one that matches the periodic frequency variation) can be identified. Therefore, the voltage amplitude is assumed to be constant for simulation purposes.

The stator voltage supply and its variable frequency nature reduce to a simple case of frequency modulation where a phase voltage may be expressed as [**6**]

$$v_{phase} = V_{peak} \cos\left(2\pi \int_0^t f_v(\tau) d\tau + \theta_v\right) \tag{5.11}$$

$V_{peak} = 294.67$ V is the constant peak value of the phase-voltage; θ_v is the phase of the given phase voltage: $\theta_v = \frac{19}{60}\pi$ rad for phase one with phase two and three delayed by a further $\frac{2}{3}\pi$ rad and $\frac{4}{3}\pi$ rad respectively; τ is a dummy variable for time t; $f_v(\tau)$ is the instantaneous frequency of the phase voltages expressed as

$$f_v(\tau) = F_{peak} \cos\left(2\pi f_f \tau + \theta_f\right) + F_{average} \tag{5.12}$$

$F_{peak} = 2$ Hz is the maximum deviation from an average frequency of $F_{average} = 48.025$ Hz; the frequency at which the instantaneous frequency $f_v(\tau)$ varies from its average value $F_{average}$ is $f_f = 4$ Hz; the phase of the sinusoidal frequency variation is found to be $\theta_f = \frac{7}{72}\pi$ rad. Substituting equation 5.12 into equation 5.11 gives a phase voltage of

$$v_{phase} = V_{peak} \cos\left(\frac{F_{peak}}{f_f} \sin\left(2\pi f_f t + \theta_f\right) + 2\pi F_{average} t - \frac{F_{peak}}{f_f} \sin\left(\theta_f\right) + \theta_v\right) \tag{5.13}$$

In summary, the three-phase supply is similar to a balanced supply with a peak voltage of 294.67 V and relative phase delays of 120° between the phases. The only difference is the instantaneous frequency which has a peak sinusoidal deviation of 2 Hz from an average frequency of 48.025 Hz. The sinusoidal frequency deviation has a period of 0.25 s.

A comparison of the measured and modelled phase-one voltage supply is presented in figure 5.33. The instantaneous electrical frequency is also given in this figure. The frequency variation is observable in the voltage supply and there is also a good agreement between measured and simulated phase-one voltages. This agreement is also true for the other phase voltages.

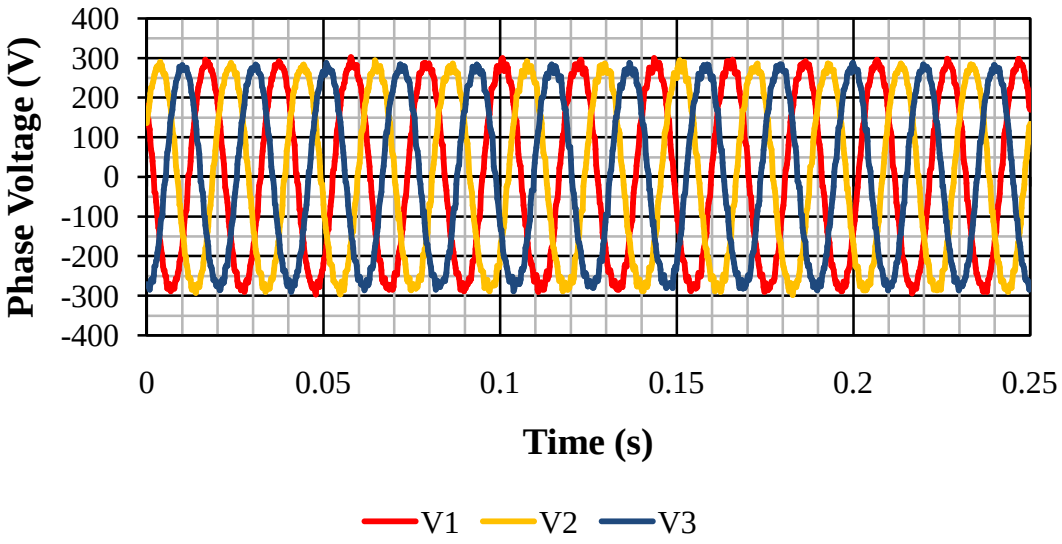

Figure 5.32: SCIG Stator Voltage – Experimental

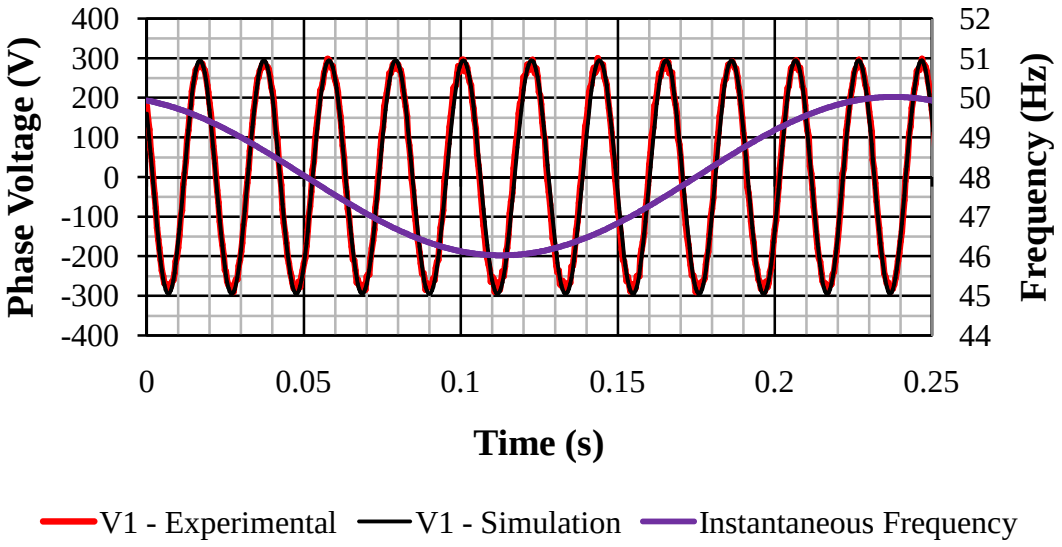

Figure 5.33: SCIG Stator Voltage – Experimental versus Simulation

The stator frequency as measured by the measurement circuit is given in figure 5.34. This frequency measurement has a first-order low-pass filter characteristic with a -3 dB bandwidth of approximately 0.147 Hz. As a result, any sinusoidal frequency variation is significantly attenuated. However, the average frequency of 48 Hz shows good agreement with the modelled value of 48.025 Hz.

A practical indication of the instantaneous supply frequency can still be achieved if one considers the speed-reference signal input to the control unit of the generator power converter. Through a series of steady-state tests (where the measurement circuit frequency measurement is applicable), it is found that the speed reference voltage is directly proportional to the inverter output frequency. Based on the speed reference signal, the associated generator supply frequency is presented in figure 5.35. The simulated supply frequency is also shown and supported by this figure. It is observed that the power converter introduces a negligible attenuation and delay of the actual supply frequency versus the desired supply frequency.

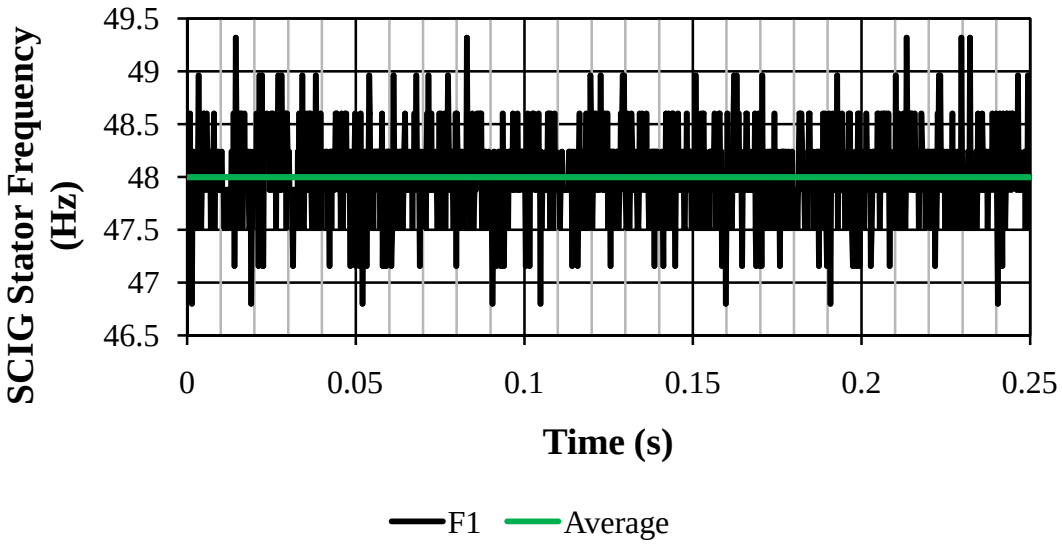

Figure 5.34: SCIG Stator Frequency – Experimental (Measurement Circuit)

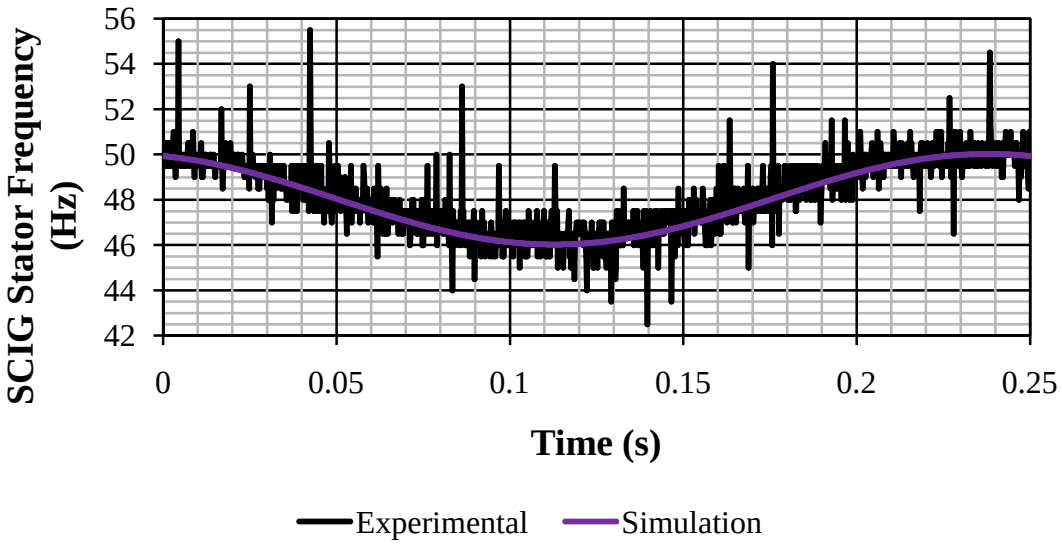

Figure 5.35: SCIG Stator Frequency – Experimental (Inverter Control Reference) versus Simulation

The measured prime-mover torque and its simulation equivalent are presented in figure 5.36. The torque is sinusoidal with a frequency of 4 Hz and an average of 8.25 N. m.

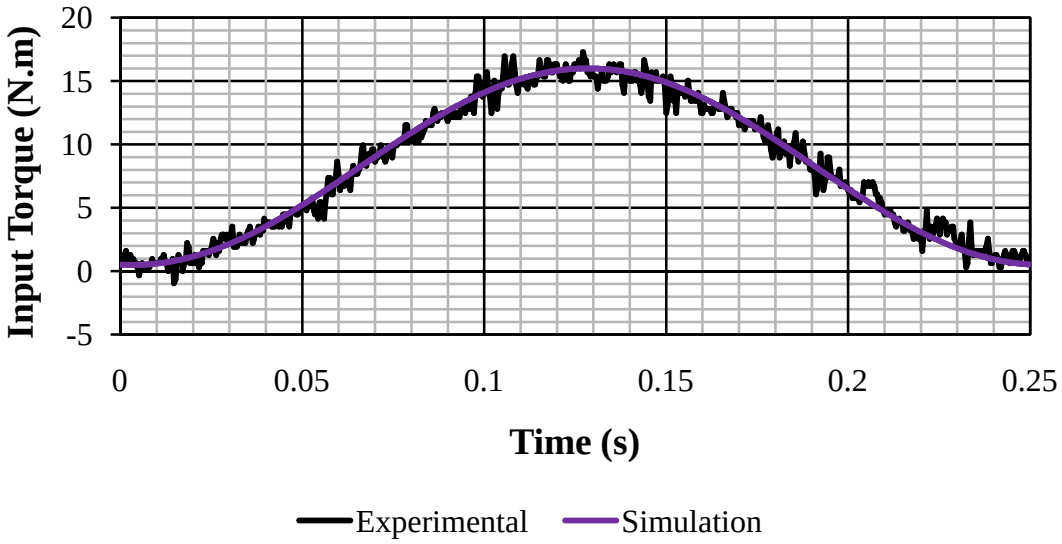

Figure 5.36: Input Prime-Mover Torque

Since all experimental and simulation inputs for the SCIG are comparable and synchronised, the practical and modelled generator responses can now be compared on an instantaneous basis.

5.3.2.3.3.2 Generator Response

The experimental and simulated generator currents are presented in figures 5.37 and 5.38 respectively. The corresponding currents are comparable in phase and magnitude thus confirming the performance and application of the dynamic generator model. The slight difference in the current amplitudes is acceptable when considering supply and generator non-idealities as previously mentioned.

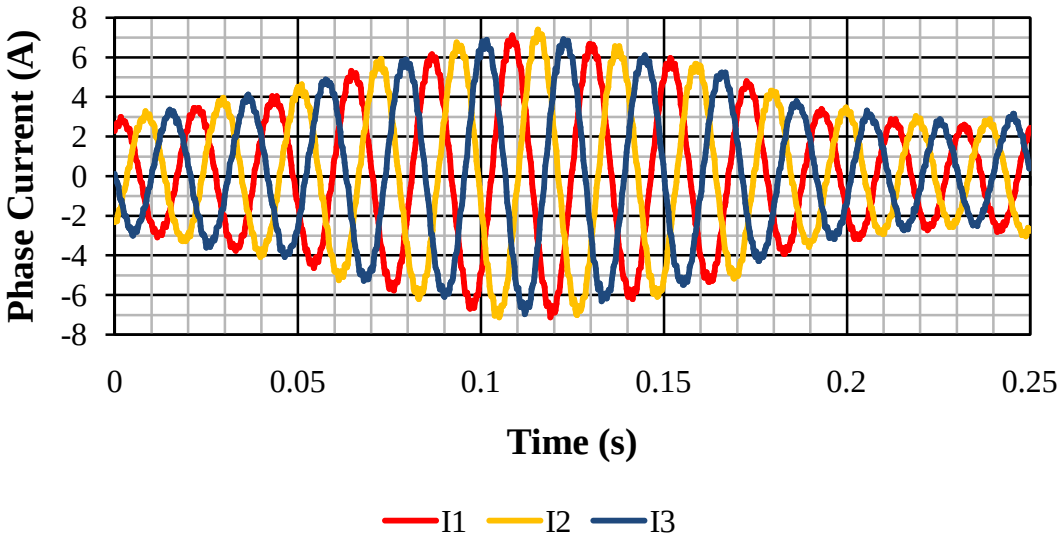

Figure 5.37: SCIG Stator Current – Experimental

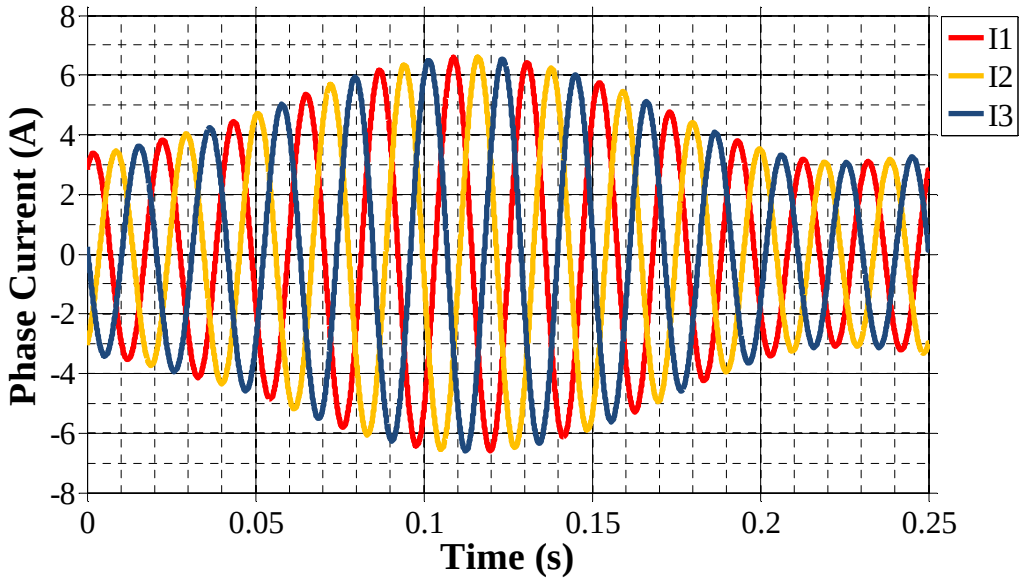

Figure 5.38: SCIG Stator Current – Simulation

The experimental and simulated rotor speed is illustrated in figures 5.39 and 5.40 respectively. Based on the simulation result, the experimental rotor speed would be significantly attenuated by the measurement implementation as discussed in the case of mechanical input dynamics. Hence, the sinusoidal speed profile is not observed in figure 5.39. However, the average measured rotor speed (not affected by the measurement low-pass filter characteristic) of 1485 rpm is comparable with the simulated value of 1466 rpm. As discussed in the rotor speed analysis for the case of mechanical input dynamics, a good agreement between measured and simulated stator currents is sufficient to prove model performance in the case of deficient rotor speed measurement.

The beginning of figure 5.40 shows that the simulation initial conditions are not perfect. However, the results still allow for the evaluation of generator model performance. Therefore, the equivalent steady-state circuit model may be used to derive approximate initial stator/rotor current conditions for the given repetitive generation condition.

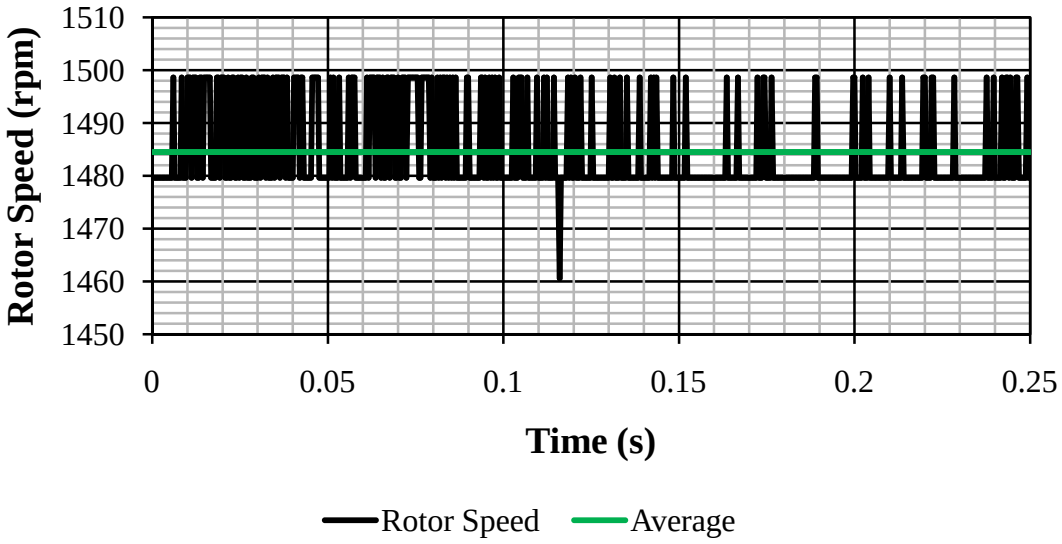

Figure 5.39: Rotor Speed – Experimental

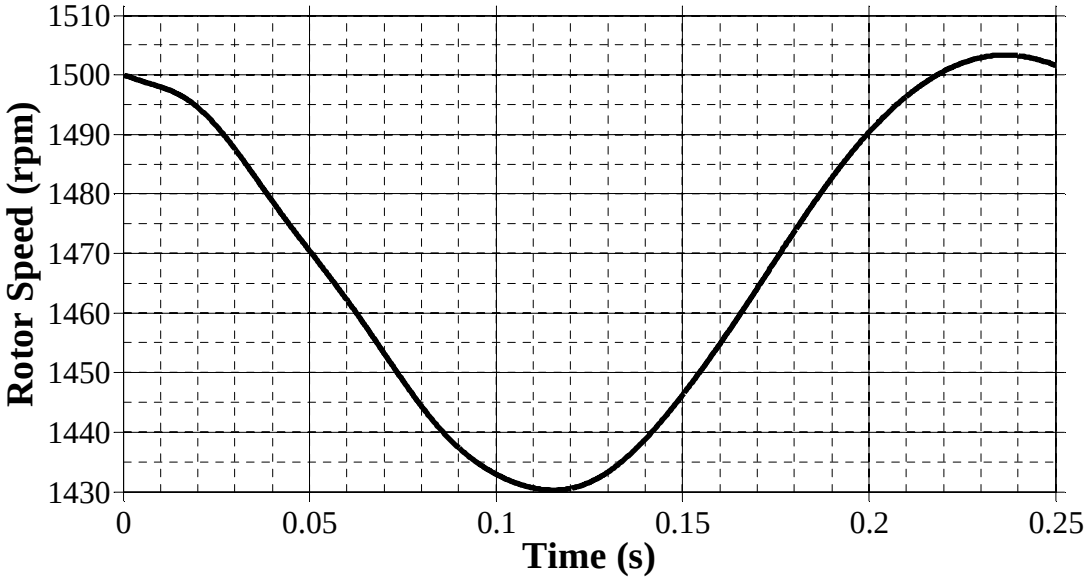

Figure 5.40: Rotor Speed – Simulation

Based on the agreement between the practical and simulated stator currents, the SCIG model performance has been verified for the given generation condition. Power curves are now presented and analysed to further support this claim from a different perspective.

The per-phase and total electrical power are presented in figures 5.41 and 5.42 for the measured and simulated cases respectively. The total power is not as smooth for the measured results as for the simulated results. This is a consequence of the non-ideal practical

system. However, the profile and general magnitude of the corresponding powers are comparable. This is also illustrated in figure 5.43 which shows the measured and simulated total electrical power on the same set of axes.

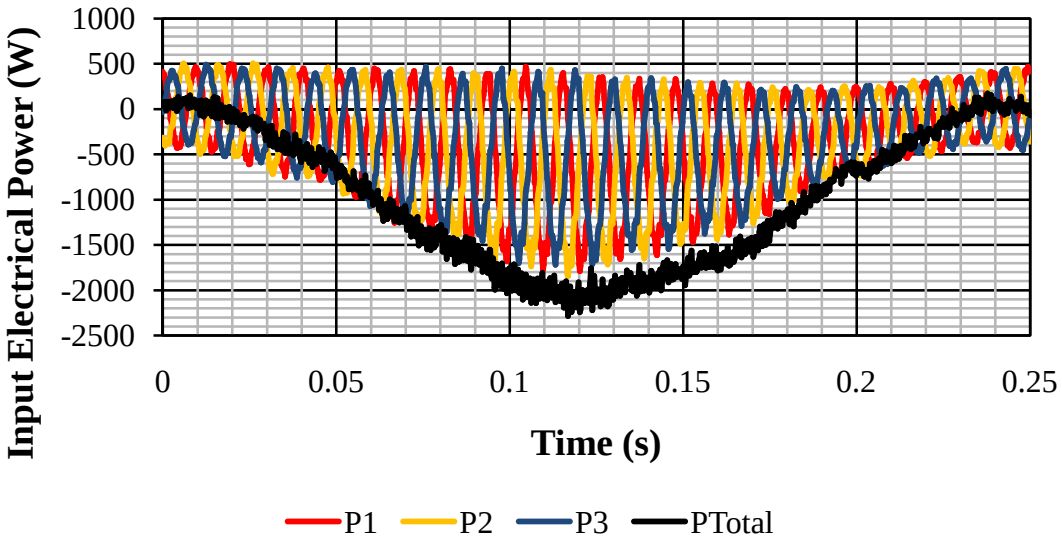

Figure 5.41: Input Electrical Power – Experimental

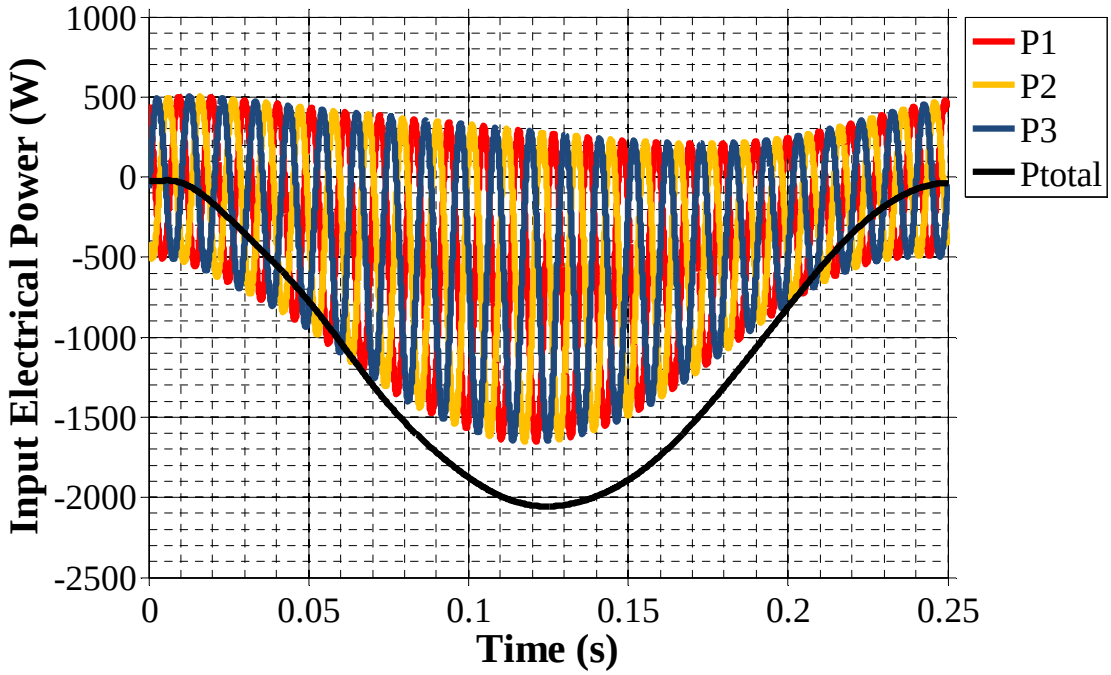

Figure 5.42: Input Electrical Power – Simulation

According to figure 5.40 the maximum rotor speed deviation is 2.5 % from its average value. As a result the rotor speed may be considered as being approximately constant for the purpose of evaluating mechanical input power. In other words, the sinusoidal speed component is considered negligible. Therefore, the measured rotor speed of figure 5.39 is used in the calculating the practical mechanical power input to the SCIG.

The mechanical input power to the generator is presented in figure 5.43 for both the experimental and simulation results. There is good agreement despite the deficiency in rotor speed measurement.

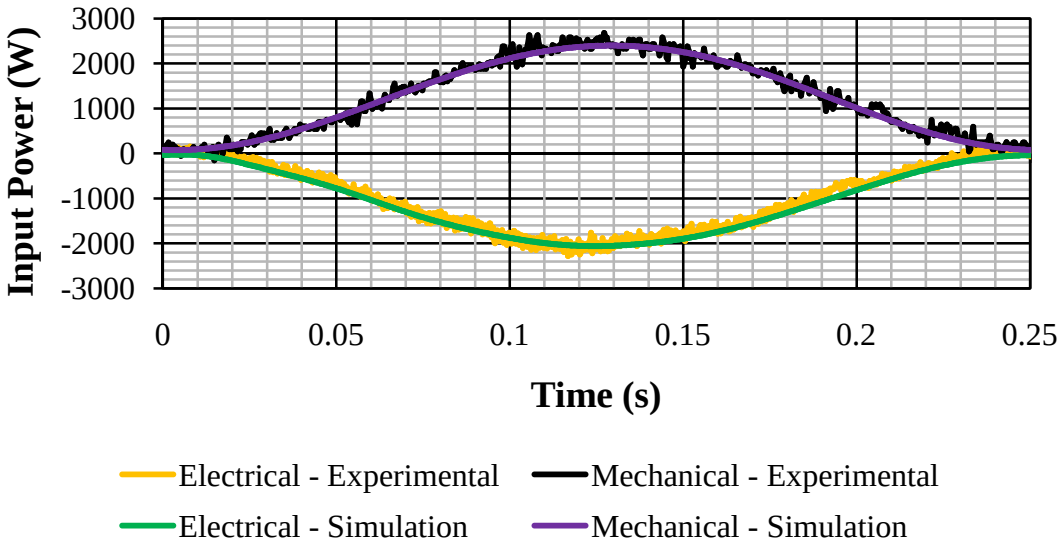

Figure 5.43: Prime-Mover Mechanical Power versus SCIG Electrical Power

5.3.2.3.4 Conclusion

The equivalent dynamic model is evaluated by considering dynamics in electrical excitation. Model evaluation is achieved by comparing simulation results with experimental results. The particular dynamic involves a sinusoidally-varying electrical frequency.

There is good agreement between the average values of the measured and simulated rotor speed. However, the bandwidth of the rotor speed measurement is insufficient and does not cater for the tested dynamics. This is also the case for the model verification based on a dynamic torque input. Again, a comparison of simulated and measured rotor speed cannot be used for conclusive model evaluation.

However, the simulated and measured stator currents show good agreement. As mentioned before, this is sufficient for a positive model evaluation. The application of the dynamic SCIG model for the given dynamics is also supported by the generator electrical and mechanical power waveforms.

Therefore, the dynamic SCIG model is applicable for the tested electrical-excitation dynamics.

It is also shown that the equivalent steady-state circuit model may be used to derive approximate initial stator/rotor current conditions for the given generation condition.

5.4 Conclusion

An equivalent steady-state model and dynamic model for a SCIG are evaluated for the case of dynamic generation. The steady-state model is evaluated from a stability perspective whereas the dynamic model is evaluated through a comparison of simulation and experimental results.

The steady-state model is found to be unstable for all generating conditions (negative slip). In practice, the SCIG has regions of stable generation operation. Therefore, the steady-state model considered from a time-domain perspective is not applicable for dynamic generation.

The dynamic model is evaluated by considering three operating conditions:

- Rated steady-state generation
- Dynamic generation involving a dynamic torque input and steady-state voltage excitation
- Dynamic generation involving a dynamic voltage excitation and a dynamic prime-mover torque

Based on the agreement between simulation and experimental results, the dynamic model is found to be applicable for the given dynamic generation conditions.

It is also observed that the use of a phasor analysis of the steady-state equivalent circuit model at $t = 0$ s sufficiently approximates the initial machine currents for the given steady-state and dynamic generation tests. It is important to note that the steady-state circuit model instability is irrelevant in a phasor-based analysis.

5.5 References

[1] Krause P. C., Wasynczuk O., and Sudhoff S. D., *Analysis of Electric Machinery and Drive Systems*, 2nd ed., El-Hawary M. E., Ed. Hoboken, United States of America: John Wiley & Sons, Inc., 2002.

[2] Burns R. S., *Advanced Control Engineering*. Oxford, United Kingdom: Butterworth-Heinemann, 2001.

[3] Rowell D. (2002, October) State-Space Representation of LTI Systems. [Online]. Available at: http://web.mit.edu/2.14/www/Handouts/StateSpace.pdf, Last accessed: 13 April 2014

[4] University of Illinois. (2008) Pole-Zero Cancellations and Stability. [Online]. Available at: http://courses.engr.illinois.edu/ece486/documents/lecture_notes/pole_zero_canc.pdf, Last accessed: 13 April 2014

[5] Sen P. C., *Principles of Electric Machines and Power Electronics*, 2nd ed. Hoboken, United States of America: John Wiley & Sons, Inc., 1997.

[6] Poddar A. Supplementary notes on select topics in physics and electronics – Theory of frequency modulation and phase modulation. [Online]. http://www.abhipod.bravehost.com/teachingpage/notes/FMtheory/note_FMtheory.html, Last accessed: 13 April 2014

6 Conclusion

6.1 Research Problem

The fundamental research question involves the modelling of a three-phase symmetrical SCIG in generating electrical energy from ocean-wave energy. The chosen application involves a generator driven by a Wells turbine in an OWC WEC. The modelling approach involves the evaluation of existing generator models; it is important for these models to correctly reproduce the practical generator response for the given application.

Considering the dynamic nature of ocean-wave energy and the chosen WEC setup, the generating condition is dynamic. However, the input dynamics are relatively slow compared to the generator electrical response such that generator operation may be considered as quasi-steady-state. Owing to the quasi-steady-state, yet dynamic, generator operation, two SCIG models are considered:

- The equivalent steady-state model
- The equivalent dynamic model

Both models are considered from a time-domain perspective (time-based differential equations). Before implementing and testing the SCIG models, their stability is considered which is important given the dynamic generating application.

Generator function is broken down into two modes of operation for the purpose of model evaluation:

- Generation for a constant sea state

  This involves the typical system operation where the WEC operating point has been set for a particular sea state. The generator speed and, therefore, electrical excitation is set with a dynamic prime-mover torque that oscillates with the wave power. Expected torque oscillations are sinusoidal with a period of $4\ \mathrm{s} - 5\ \mathrm{s}$.

- Generation during a change in sea state

  This mode of operation involves the WEC response to a change in sea state so as to optimise system efficiency. The system response involves establishing a new turbine/generator speed which corresponds to the new sea state so as to avoid poor turbine efficiency. The expected generator dynamics are not easily quantified since they depend on the system control implementation possibly including the use of an air-flow valve as well as various system parameters such as rotor MOI. Some electrical input dynamic (voltage amplitude and frequency) is used to bring about a change in generator/turbine speed while causing some sort of system mechanical response in terms of a turbine torque applied to the generator rotor. Once the system reaches the new

operating point, the WEC functioning is described by the operating mode for a constant sea state.

The SCIG models are evaluated by reproducing the dynamic electrical and mechanical generator inputs (voltage amplitude and frequency and prime-mover torque) for a particular generation mode while comparing the simulated and experimental generator response (stator current and rotor speed). In this way, the generator models are evaluated without explicitly including the rest of the WEC system in the analysis. Agreement between simulated and measured stator current is sufficient to conclude on model performance; however, rotor speed as well as electrical and mechanical power are also used providing a different perspective.

6.2 Equivalent Steady-State Model

The steady-state model is evaluated for dynamic generation by considering the stability of the electrical subsystem circuit model as a function of rotor slip. It is shown that the model is unstable for all negative slip values and, therefore, all generation conditions. Since a SCIG has regions of stable generation in practice (as shown by the test cases of chapter 5), the equivalent steady-state model as considered from a time-domain perspective is not suitable for the given generation application. Quasi-steady-state generation is still classified as dynamic generation, just with slow input dynamics.

6.3 Equivalent Dynamic Model

6.3.1 Generation for a Constant Sea State

The first dynamic generation test presented in chapter 5 involves a dynamic mechanical input to a SCIG. This test is used to evaluate the dynamic model for generation in the case of a constant sea state. The stator voltage excitation is constant in amplitude and frequency (near rated in this case) corresponding to some system operating speed. A sinusoidal prime-mover (turbine) torque drives the induction machine between light motoring and deep generation. This is the worst-case generation dynamic for a constant sea state as described in chapter 1. The tested dynamic involves a prime-mover torque oscillation with a period of $0.1\ \mathrm{s}$ ($10\ \mathrm{Hz}$) which is faster than the typical dynamic of $4\ \mathrm{s} - 5\ \mathrm{s}$. Furthermore, the tested torque dynamic is rather fast considering that it is a mechanical dynamic. It is unlikely that a faster realistic dynamic should occur in practice.

Based on the agreement between simulated and measured generator response in terms of stator current, the model is found to be applicable for the tested dynamic generation. The agreement in corresponding electrical and mechanical power further supports this conclusion. Therefore, the model is applicable for typical SCIG operation as driven by a Wells turbine in an OWC WEC for a constant sea state with a dynamic torque oscillation up to a frequency of $10\ \mathrm{Hz}$. This is provided magnetic saturation and parameter variability (as discussed in chapter 2) are not present. Otherwise, model parameters become a function of the generator operating point.

6.3.2 Generation for a Change in Sea State

As previously mentioned, quantification of the generator input dynamics in the case of the system response to a change in sea state is difficult to achieve. This is especially true for the simplistic approach adopted where the rest of the WEC system is not explicitly modelled. What is known is that some change in generator electrical excitation is used to move the generator to a new operating speed while experiencing some turbine torque response. In light of this, an informative dynamic test is carried out in chapter 5 ("Dynamic Generation – Electrical Input Dynamics") which provides an indication of the model performance.

The tested dynamic involves a sinusoidal variation in stator excitation frequency. This mimics the case of an oscillating desired system speed. The prime-mover torque is also sinusoidal in nature and is simply the response of the experimentally coupled induction motor excited with a steady-state voltage. For experimental purposes the induction generator oscillates between light generation and deep generation. Obviously the exact WEC system response has not been considered. However, the objective is to observe model performance for a dynamic electrical excitation with some dynamic prime-mover torque.

The electrical-frequency and torque oscillations have a sinusoidal period of $0.25\ \mathrm{s}$ ($4\ \mathrm{Hz}$). Such a dynamic is expected to be much faster than any typical dynamic for the given application. For perspective, consider the typical wave period of $8\ \mathrm{s} - 10\ \mathrm{s}$. This is much slower than the tested dynamic. Furthermore, changes between sea states are not expected to occur at anywhere close to the typical wave period.

Since there is good agreement between the simulated and experimental generator response (given by the stator current and electrical and mechanical power), the model is applicable for the tested dynamic. Owing to the nature of the tested dynamic (sinusoidal electrical frequency and prime-mover torque with a relatively fast oscillation), it is suspected that the dynamic model would also be applicable for actual generator operation as a result of a change in sea state. Again, cases involving magnetic saturation and parameter variation still require further consideration.

6.4 Research Context

As discussed in chapter 1, the work in [**1**] is focused on reducing the fluctuation in generated power in the case of an OWC WEC fitted with an induction generator. The work is based on a phasor analysis (frequency domain) of the per-phase steady-state circuit model. The research question answered by the work presented in this dissertation is whether the same model may be considered from a differential-equation (time-domain) perspective.

The work presented in [**2**] is concerned with improving the Wells turbine efficiency in an OWC WEC by avoiding aerodynamic stalling. The work assumes a DFIG and makes use of the equivalent dynamic model. The research presented in this dissertation is based on proving/supporting the use of the same model in the case of a SCIG.

6.5 Final Remarks and Future Work

In modelling the SCIG for the given test cases, magnetic core loss is neglected and magnetic saturation and parameter variability are not considered/included. Based on the good agreement between simulated and experimental results, these assumptions are justified. As previously mentioned, cases involving magnetic saturation and parameter variability are left for future development.

System starting and shutdown are not considered. Such operation would require the incorporation of the entire WEC model. This is left for future development. Based on the model performance for the given dynamic test cases, one might expect the generator model to perform suitably for starting and shutdown conditions. However, it is important to note that the tested dynamics have relied on a balanced, albeit dynamic, stator voltage supply. Cases involving some strange electrical-supply transient such as an electrical fault or phase-switching have not been considered. Again, model evaluation of such cases requires further research.

As discussed in chapter 1, experimental scaling has no bearing on the research results/conclusions. In evaluating the SCIG dynamic model, the experimental and simulated results show good agreement – especially considering possible system non-idealities:

- Stator voltage supply which is not perfectly balanced with some source impedance
- Generator which is not perfectly symmetrical across all three phases and where windings are not continuously distributed
- Non-ideal generator/prime-mover mechanical coupling

The inclusion of system non-idealities in the generator model is not considered part of the research scope and is left for future development.

The SCIG models considered are focussed on providing information regarding the electrical and mechanical variables of the generator including terminal voltages and currents, mechanical torque and rotor velocity. Important power flow and energy loss between the mechanical and electrical systems can also be obtained from the model simulation while giving an indication of the machine mode of operation. Thermal considerations including heat dissipation and ventilation as well as mechanical wearing and vibration are not solved in the given models.

6.6 References

[1] Muthukumar S. et al., "On Minimizing the Fluctuations in the Power Generated from a Wave Energy Plant," in *2005 IEEE International Conference on Electric Machines and Drives*, San Antonio, 2005, pp. 178-185.

[2] Amundarain M., Alberdi M., Garrido A. J., and Garrido I., "Modeling and Simulation of Wave Energy Generation Plants: Output Power Control," *IEEE Transactions on Industrial Electronics*, vol. 58, no. 1, pp. 105-117, January 2011.

Appendix

A. Basic Induction-Machine Construction and Operation

A.1 Introduction

The purpose of this note is to establish a basic understanding in induction machine construction and operation. Important concepts include:

- Air-gap magnetic field
- Electrical versus mechanical units of space and time
- Basic winding arrangement
- Rotor slip
- The steady-state torque-speed curve showing different modes of induction-machine operation

A.2 Air-Gap Magnetic Field

Operating as a motor, the induction machine stator windings are excited by some three-phase power supply (ideally balanced [**1**,**2**]). A three-phase voltage supply is said to be balanced if the voltages of each phase are sinusoidal with equal amplitudes and frequencies and respective phase shifts of $\frac{2\pi}{3}$ radians in time [**1**,**2**].

The currents developed in the stator windings produce a magnetic field in the air gap between the rotor and the stator [**1**,**2**]. Owing to the winding distribution of each phase, a pulsating sinusoidal magnetic field is developed by each phase winding with the number of pole pairs (one pole pair consists of two "magnetic poles": a "north pole" and a "south pole") determined by each phase winding configuration. This is illustrated for phase "a" in figure A.1 which shows the winding configuration of a three-phase, four-pole induction machine [**1**,**2**,**3**]. It is important to note that a wound rotor is illustrated for explanation purposes as a squirrel-cage rotor can be represented by its wound rotor equivalent [**1**]. Figure A.1 shows that the rotor windings merely mirror their corresponding stator windings [**1**].

The sinusoidal magnetic field for each phase is a consequence of the per-phase winding distribution and not the power supply [**1**]. This is discussed in section A.4.2 for a three-phase, two-pole induction machine – figure A.1 illustrates a concentrated winding arrangement for explanation purposes. As shown in figure A.1, all three phase windings are identical but relatively displaced around the stator. Owing to the fact that there are three identical phases which are mechanically displaced, that each phase supply is sinusoidally time varying and that the excitation voltage of each phase is equal but electrically displaced by $\frac{2\pi}{3}$ radians in time (balanced three-phase electrical grid supply), the superposition of all three phases produces a sinusoidal time-varying magnetic field that rotates in the air gap [**1**].

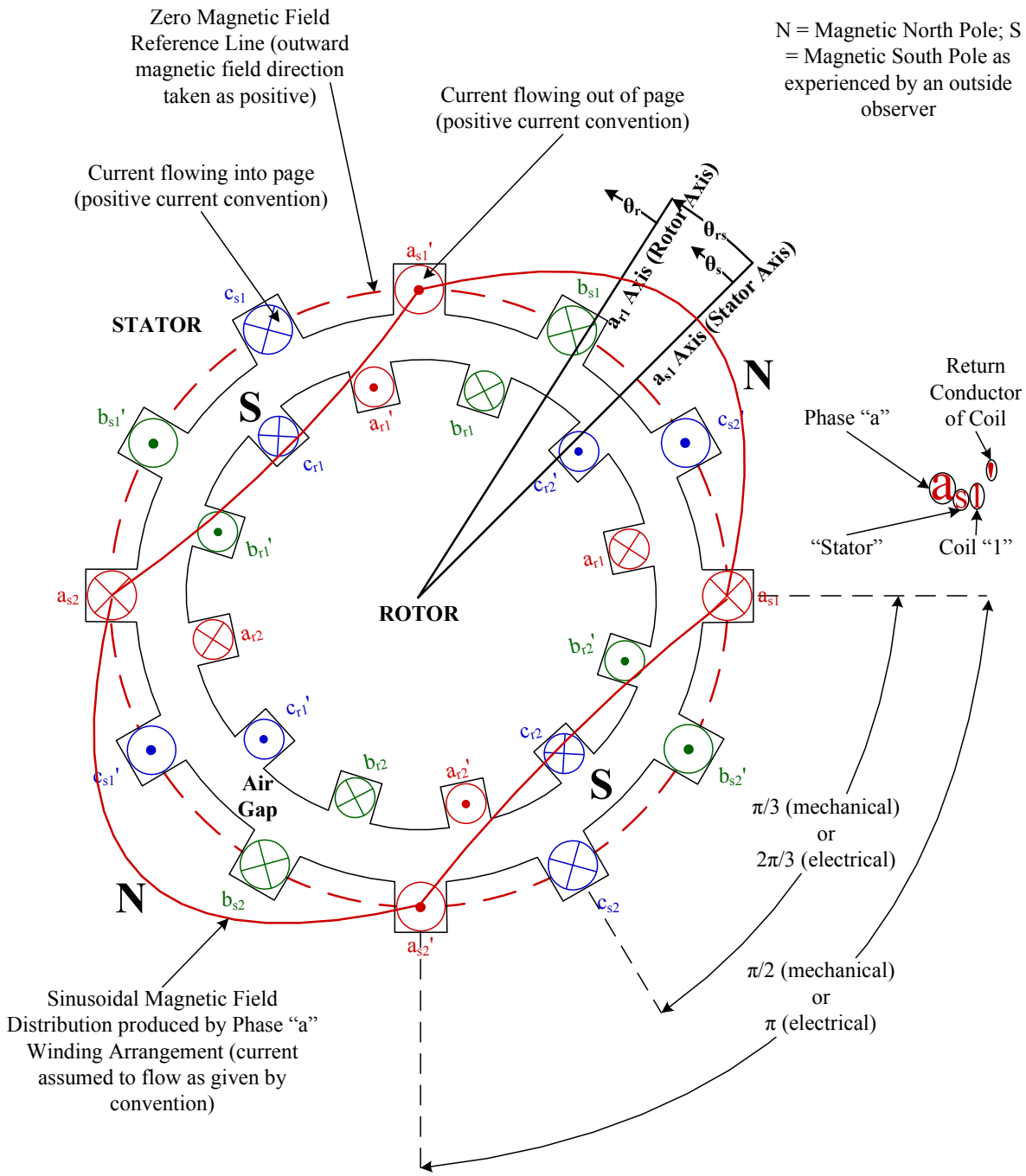

Figure A.1: Concentrated Equivalent of the Winding Configuration of a Three-Phase, Four-Pole Induction Machine (Wound Rotor) – Cross Section adapted from [**1**,**2**,**3**]

The resultant rotating stator magnetic field consists of two pole pairs. This magnetic field varies relative to the windings of the rotor. According to Faraday's and Lenz's law of induction, a three-phase sinusoidal voltage and current is induced in the rotor windings. The induced three-phase current produces a rotor magnetic field of its own. The stator magnetic field "pulls on" the rotor magnetic field so that the two are aligned and rotate synchronously [**1**]. As a result, a torque is produced on the rotor which causes it to rotate. According to Lenz's law, the rotor will rotate in the same direction as the magnetic fields so as to reduce the change in magnetic field observed by the rotor windings [**1**]. However, in order for a

voltage to be induced in the rotor, the stator magnetic field must be varying relative to the rotor (Faraday's law of induction). This implies that rotor must rotate slower than the stator and rotor magnetic fields (which form the resultant magnetic field) [**1**].

A.3 Electrical and Mechanical Units of Space and Time

It is important to differentiate between electrical and mechanical units of position and, therefore, displacement and velocity (spacial quantities). This can be explained with the aid of figure A.1. For a four-pole machine, a full rotor rotation represents 2π mechanical radians. However, since two sinusoidal wave periods of the rotating resultant magnetic field fit along the air gap, one full rotor rotation represents 4π electrical radians (one wave period is 2π electrical radians). For a P-pole machine, the relationship between a physical angle measured in electrical radians θ and mechanical radians θ_m is [**1**,**2**,**3**]

$$\theta = \frac{P}{2}\theta_m \tag{A.1}$$

For a balanced three-phase power supply, the phase voltages are relatively phase-shifted by $\frac{2\pi}{3}$ electrical radians [**1**,**2**]. This is a time-base displacement or shift and not a spacial or physical displacement like the relative displacements of the stator windings.

In an induction machine, both time-based and physical displacements occur, which can be expressed in units of electrical or mechanical radians. Time-based shifts are conventionally expressed in terms of electrical radians.

A.4 Winding Arrangement of a Three-Phase Four-Pole Induction Machine

A.4.1 Concentrated Winding Representation

The winding configuration of figure A.1 is derived as follows [**1**,**2**,**3**]. Each phase winding is required to produce a sinusoidal magnetic field such that two magnetic pole pairs are present in the air gap. Therefore, two coils (connected in series) are required per phase winding with each coil comprising a conductor carrying current into the page and a conductor carrying current out of the page [**2**,**3**]. As shown in figure A.1 the coils do not cross. Furthermore, the current direction (into or out of the page) of the conductors of each phase winding alternates around the stator. This results in constructive superposition of the magnetic fields produced by any two adjacent conductors as given by the right hand rule. A magnetic pole is, thus, produced between two adjacent conductors. Each magnetic pole occupies π electrical radians and this translates into $\frac{\pi}{2}$ mechanical radians as given by equation A.1. This angle is shown in figure A.1.

A balanced three-phase system has phase voltages (and currents) which are relatively phase shifted in time by $\frac{2\pi}{3}$ electrical radians. In order to produce the desired resultant magnetic field, the phase windings must be physically displaced by $\frac{2\pi}{3}$ electrical radians [**1**]. This

translates into $\frac{\pi}{3}$ mechanical radians as shown in figure A.1. The winding displacements are anticlockwise and, thus, produce a positive rotor rotation in the anticlockwise direction.

As shown in figure A.1, angles can be measured relative to the stator circuit or rotor circuit [**2**]. The reference points of these circuits are given by the axis of the (a_{s1}, a_{s1}') and (a_{r1}, a_{r1}') coils respectively. Angles (in electrical radians) measured relative to these axes are given by θ_s and θ_r respectively. The rotor circuit position relative to the stator circuit (in electrical radians) is given as θ_{rs}. Where angles are given in mechanical radians, the subscript m is be included, for example, θ_{sm}, θ_{rm} and θ_{rsm}. The same applies to angular velocities in rad.s^{-1}.

A.4.2 Practical versus Ideal Winding Arrangement

Figure A.1 represents the concentrated equivalent of the various windings for explanation purposes. However, in order to achieve a sinusoidal magnetic field distribution from each phase winding, the coil turns should be arranged in a continuous sinusoidal distribution as shown in figure A.2 for a single-phase stator winding of a two-pole induction machine [**1**]. In figure A.2, the size of the corresponding conductor circles indicates the relative "turn" density of the winding.

In reality, the coil "turns" cannot be continuously distributed and are placed in a physically-limited number of slots [**1**]. Furthermore, it is practically convenient to have an equal number of "turns" in each slot [**1**]. As a result, the practical distributed winding produces a stepped magnetic field that approximates a sinusoidal magnetic field [**1**].

The stepped magnetic field can be represented by its Fourier series which includes a fundamental sinusoid together with a number of higher-frequency harmonic sinusoids (unwanted). The magnetic field harmonics produce undesirable effects on the torque-speed relationship of the machine [**1**]. Therefore, complicated winding techniques such as short-chording exist to suppress/eliminate problematic harmonic signals [**1**].

For the purposes of the work presented in this dissertation, a sinusoidal air-gap magnetic field is assumed. From the above winding descriptions, the stator winding of an induction machine may be broken down into its various components as:

$$conductors\ carrying\ current\ into\ and\ out\ of\ the\ page \rightarrow$$

$$\text{turns}(concentrated\ or\ distributed) \rightarrow$$

$$coils\ (determines\ the\ number\ of\ magnetic\ pole\ pairs) \rightarrow$$

$$phase\ windings\ (stator\ or\ rotor)$$

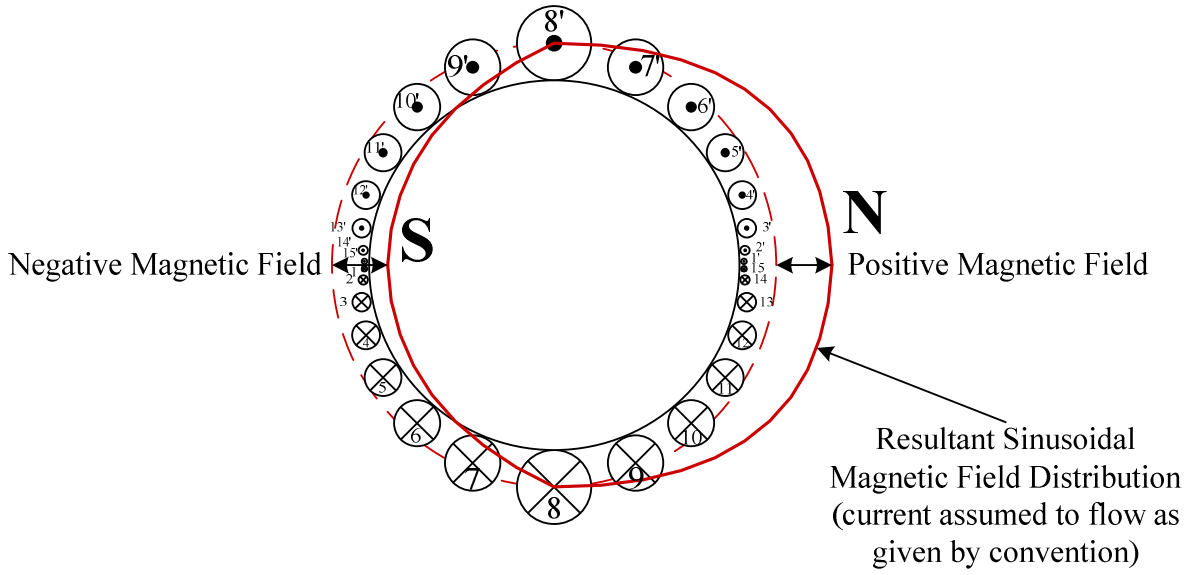

Figure A.2: Ideal Distribution of a Single-Phase Stator Winding in a Three-Phase, Two-Pole Induction Machine for a Sinusoidal Air-Gap Magnetic Field – Cross Section

A.5 Rotor Slip

The difference between the resultant magnetic field's rotational velocity (referred to as the synchronous velocity) and the rotor rotational velocity is known as slip and is given as [**1**]

$$s = \frac{n_{syn} - n_{rs}}{n_{syn}} \tag{A.2}$$

where n_{syn} (rpm) is the synchronous velocity and n_{rs} (rpm) is the rotor velocity both relative to the stator. The synchronous speed of an induction machine is dependent on the stator electrical frequency f_s and the number of magnetic poles P such that [**1**]

$$n_{syn} = \frac{120 f_s}{P} \tag{A.3}$$

It is assumed that the direction of positive mechanical rotation is given by the rotation of the air-gap magnetic field [**1**].

Since the resultant magnetic field rotates slower relative to the rotor as compared to the stator, the frequency of the induced rotor voltage and current f_r must also be lower when compared with f_s [**1**]. This is evident from equation A.3 by replacing the stator variables with their corresponding rotor equivalents. Therefore, the relationship between the stator and rotor frequency is given as [**1**]

$$f_r = s f_s \tag{A.4}$$

For generation $n_{syn} < n_{rs}$ in equation A.2 and, therefore, $s < 0$. This implies a negative rotor frequency in equation A.4. To get the actual rotor frequency, the modulus of the negative frequency may be taken. However, the negative sign of the frequency implies an air-

gap magnetic field which rotates in the opposite direction to the rotor as observed by the rotor. This is because the rotor is rotating faster than the resultant magnetic field even though both rotate in the same direction relative to the stator. For this reason, equation A.4 is presented without taking the modulus of the slip.

A.5.1 Negative Rotor Frequency for Generation

For balanced, steady-state operation, the rotor variables are of the form [**2**]

$$g_{ar} = G_r \cos\left(\omega_{er} t + \theta_{gr}(0)\right) \tag{A.5}$$

$$g_{br} = G_r \cos\left(\omega_{er} t + \theta_{gr}(0) - \frac{2\pi}{3}\right) \tag{A.6}$$

$$g_{cr} = G_r \cos\left(\omega_{er} t + \theta_{gr}(0) + \frac{2\pi}{3}\right) \tag{A.7}$$

where g is a placeholder for the variable in question, G_r is the rotor-variable amplitude and $\theta_{gr}(0)$ is the initial phase shift. Subscripts a, b and c refer to the different rotor phases. $\omega_{er} = 2\pi f_r$ is the electrical angular velocity of the rotor excitation.

During generation operation, the rotor is rotating faster than the air-gap magnetic field relative to the stator. Relative to the rotor, the air-gap appears to be rotating in the opposite direction (negative direction of rotation). This opposite direction-of-rotation is observed in the negative rotor frequency as follows. For generation, equations A.5-A.7 can be written as

$$g_{ar} = G_r \cos\left(-|\omega_{er}| t + \theta_{gr}(0)\right) = G_r \cos\left(|\omega_{er}| t - \theta_{gr}(0)\right) \tag{A.8}$$

$$g_{br} = G_r \cos\left(-|\omega_{er}| t + \theta_{gr}(0) - \frac{2\pi}{3}\right) = G_r \cos\left(|\omega_{er}| t - \theta_{gr}(0) + \frac{2\pi}{3}\right) \tag{A.9}$$

$$g_{cr} = G_r \cos\left(-|\omega_{er}| t + \theta_{gr}(0) + \frac{2\pi}{3}\right) = G_r \cos\left(|\omega_{er}| t - \theta_{gr}(0) - \frac{2\pi}{3}\right) \tag{A.10}$$

If any two phases on the stator are switched, then the air-gap magnetic field rotates in the opposite direction to that indicated in figure A.1. Applying this logic to the rotor, the rotation of the resultant magnetic field in the negative direction relative to the rotor implies that two of the rotor phases have been switched. This is clearly evident in comparing equations A.5-A.7 with equations A.8-A.10 where rotor phases b and c have been switched. The effect of switching rotor phases is achieved by a negative rotor frequency for machine generation.

A.6 Steady-State Torque-Speed Curve

The induction machine may operate as a motor, generator and plug. [**1**]. The regions of operation can be explained by considering the electromagnetic torque exerted on the rotor τ_e as a function of rotor velocity (or slip) as given by figure A.3 [**1**].

For motoring operation the rotor speed is less than synchronous speed. τ_e is positive (in the same direction as positive rotor rotation) as electrical energy is converted to mechanical energy required to drive a mechanical load. However, if the rotor begins to rotate faster than the air-gap magnetic field, then τ_e becomes negative by Lenz's law as a reduction of the rotor speed relative to the magnetic field is desired [**1**]. The induction machine is said to generate electrical energy from mechanical energy. In dynamic systems, the induction machine can be kept in generator mode by adjusting the stator frequency so as to keep the synchronous speed below the rotor speed [**1**].

During plugging operation the rotor velocity is negative and the rotor rotates in the opposite direction to the air gap magnetic field. τ_e is positive and attempts to bring the rotor to a standstill before driving the rotor during motor action. Plugging is, thus, used to bring the rotor to a rapid halt by switching any two supply phases [**1**].

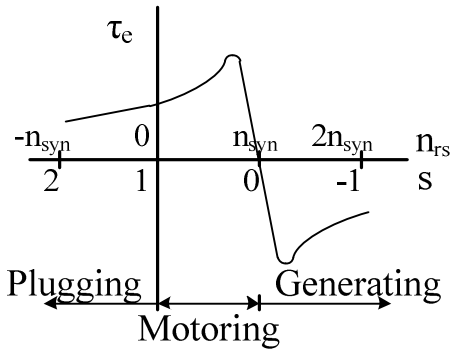

Figure A.3: Steady-State Torque-Speed Curve of an Induction Machine showing the Different Regions of Operation – adapted from [**1**]

A.7 Conclusion

Important induction-machine concepts have been highlighted. These include:

- The air-gap magnetic field
- Electrical versus mechanical units of space and time
- Basic winding arrangement
- Rotor slip
- The steady-state torque-speed curve showing different modes of induction-machine operation

A.8 References

[1] Sen P. C., *Principles of Electric Machines and Power Electronics*, 2nd ed. Hoboken, United States of America: John Wiley & Sons, Inc., 1997.

[2] Krause P. C., Wasynczuk O., and Sudhoff S. D., *Analysis of Electric Machinery and Drive Systems*, 2nd ed., El-Hawary M. E., Ed. Hoboken, United States of America: John Wiley & Sons, Inc., 2002.

[3] Cronje W. A., Power Engineering - Lesson 7, 2010, School of Electrical and Information Engineering, University of the Witwatersrand, Johannesburg, South Africa.

B. DEVELOPMENT OF THE EQUIVALENT DYNAMIC CIRCUIT MODEL _B-1

B. Development of the Equivalent Dynamic Circuit Model

B.1 Introduction

The machine-variable-based dynamic circuit model as well as its development into an arbitrary-reference-frame-based circuit model using general reference-frame theory is detailed in [**1**]. A summary of this work is presented in this note for convenience.

The equivalent dynamic circuit model is first presented in terms of its machine variables (such as the stator phase voltages and currents) [**1**]. The stator circuit is expressed in terms of the stator excitation frequency whereas the rotor circuit is expressed in terms of the rotor excitation frequency. However, for simplified control and analysis, the complete circuit model may expressed relative to some other reference frame such as the synchronous reference frame (rotates synchronously with the rotating magnetic field) [**1**]. The appropriate reference frame depends on the operation of the induction machine. The arbitrary-reference-frame-based circuit model is then presented where substitution of the corresponding angular velocity determines the chosen frame of reference [**1**].

B.2 Dynamic Circuit Model expressed in terms of Machine Variables

B.2.1 Voltage Equations expressed in terms of Currents and Flux Linkages

In order to effectively model an induction machine from a circuit perspective the model must account for each phase of both the stator and the rotor circuits. Furthermore, the voltage equation of each phase must account for an external excitation voltage, a voltage associated with winding loss as well as a voltage resulting from electromagnetic induction or varying flux linkage. Physical symmetry between the phases of an induction machine (such as winding resistance) will translate into symmetry of the resulting voltage equations [**1**]. The voltage equations of a three-phase induction machine are [**1**]

$$\boldsymbol{v}_{abcs} = \boldsymbol{R}_s \boldsymbol{i}_{abcs} + \frac{d}{dt}\boldsymbol{\lambda}_{abcs} \tag{B.1}$$

$$\boldsymbol{v'}_{abcr} = \boldsymbol{R'}_r \boldsymbol{i'}_{abcr} + \frac{d}{dt}\boldsymbol{\lambda'}_{abcr} \tag{B.2}$$

where

$$(\boldsymbol{g}_{abcs})^T = [g_{as} \quad g_{bs} \quad g_{cs}] \tag{B.3}$$

$$(\boldsymbol{g'}_{abcr})^T = [g'_{ar} \quad g'_{br} \quad g'_{cr}] \tag{B.4}$$

The voltage equations involve derivatives with respect to time. T refers to the transpose of a matrix/vector and g is a placeholder for the terminal voltages v, terminal currents i and flux linkages λ (Wb. turns) of equations B.1-B.2. The subscripts a, b and c refer to the three phases of the induction machine while s and r refer to stator and rotor quantities respectively. $\boldsymbol{v'}_{abcr}$ is not the magnetically-induced rotor voltage but represents the rotor windings'

terminal voltages (in the case of a wound rotor). The diagonal matrices $\boldsymbol{R}_s$ and $\boldsymbol{R'}_r$ account for the stator and rotor phase-winding resistances respectively. A symmetrical induction machine implies equal diagonal values.

B.2.2 Rotor Quantities Referred to the Stator

Equations B.2 and B.4 involve rotor quantities already referred to the stator (in terms of magnitude) via the stator-rotor turns ratio a [**1**]:

$$\boldsymbol{v'}_{abcr} = a\boldsymbol{v}_{abcr};\ \boldsymbol{R'}_r = a^2\boldsymbol{R}_r;\boldsymbol{i'}_{abcr} = \frac{1}{a}\boldsymbol{i}_{abcr};\ \boldsymbol{\lambda'}_{abcr} = a\boldsymbol{\lambda}_{abcr} \tag{B.5}$$

After being referred to the stator, the rotor variables are still functions of rotor frequency f_r and have not been converted to stator frequency f_s. As a result of different frequencies, the stator and rotor equations cannot be graphically represented on the same circuit diagram [**2**]. Only once both circuits have been referred to a common reference frame with a single frequency, can the rotor and stator equations be represented on the same circuit diagram [**1**].

B.2.3 Flux Linkage Equations

λ is the flux linkage of a particular phase winding such that [**1**]

$$\begin{bmatrix}\boldsymbol{\lambda}_{abcs}\\ \boldsymbol{\lambda'}_{abcr}\end{bmatrix} = \begin{bmatrix}\boldsymbol{L}_s & \boldsymbol{L'}_{sr}\\ (\boldsymbol{L'}_{sr})^T & \boldsymbol{L'}_r\end{bmatrix}\begin{bmatrix}\boldsymbol{i}_{abcs}\\ \boldsymbol{i'}_{abcr}\end{bmatrix} \tag{B.6}$$

Expressing the various flux linkages in terms of current variables and constant inductance values assumes the use of a magnetically-linear induction machine (no magnetic saturation) [**1**].

A uniform air gap is also assumed in deriving the expressions for the various machine inductance values [**1**]. These inductance values are expressed as self and mutual inductance which may be further reduced to leakage and magnetising inductance. The stator-winding inductance matrix accounting for the stator windings' self inductance as well as the mutual inductance between the stator windings is given as [**1**]

$$\boldsymbol{L}_s = \begin{bmatrix} L_{ls}+L_{ms} & -\frac{1}{2}L_{ms} & -\frac{1}{2}L_{ms}\\ -\frac{1}{2}L_{ms} & L_{ls}+L_{ms} & -\frac{1}{2}L_{ms}\\ -\frac{1}{2}L_{ms} & -\frac{1}{2}L_{ms} & L_{ls}+L_{ms}\end{bmatrix} \tag{B.7}$$

L_{ls} and L_{ms} are the leakage and magnetising inductance of each stator winding respectively (constants). The corresponding rotor inductance matrix accounting for the rotor windings' self inductance as well as the mutual inductance between the rotor windings is given as [**1**]

$$\boldsymbol{L'}_r = a^2\boldsymbol{L}_r = \begin{bmatrix} L'_{lr} + L_{ms} & -\frac{1}{2}L_{ms} & -\frac{1}{2}L_{ms} \\ -\frac{1}{2}L_{ms} & L'_{lr} + L_{ms} & -\frac{1}{2}L_{ms} \\ -\frac{1}{2}L_{ms} & -\frac{1}{2}L_{ms} & L'_{lr} + L_{ms} \end{bmatrix} \tag{B.8}$$

where

$$L'_{lr} = a^2 L_{lr} \tag{B.9}$$

$$L_{ms} = a^2 L_{mr} \tag{B.10}$$

L_{lr} and L_{mr} are the leakage and magnetising inductance of each rotor winding respectively (constants). The stator-rotor coupling matrix accounting for the mutual inductance between the stator and rotor windings is of the form [**1**]

$$\boldsymbol{L'}_{sr} = a\boldsymbol{L}_{sr} = L_{ms}\begin{bmatrix} \cos\theta_{rs} & \cos\left(\theta_{rs} + \frac{2\pi}{3}\right) & \cos\left(\theta_{rs} - \frac{2\pi}{3}\right) \\ \cos\left(\theta_{rs} - \frac{2\pi}{3}\right) & \cos\theta_{rs} & \cos\left(\theta_{rs} + \frac{2\pi}{3}\right) \\ \cos\left(\theta_{rs} + \frac{2\pi}{3}\right) & \cos\left(\theta_{rs} - \frac{2\pi}{3}\right) & \cos\theta_{rs} \end{bmatrix} \tag{B.11}$$

where

$$L_{ms} = aL_{sr} \tag{B.12}$$

L_{sr} is the amplitude of the mutual inductance between the stator and rotor windings (constant) and θ_{rs} is the rotor position relative to the stator (in electrical radians).

In equation B.6 stator (rotor) flux linkages are a function of rotor (stator) currents. The appropriate transformation of rotor (stator) to stator (rotor) frequency is achieved by the $\boldsymbol{L'}_{sr}$ matrix containing sinusoidal terms which are functions of the respective rotor-stator displacement.

B.2.4 Voltage and Torque Equations expressed in terms of Currents

Using equation B.6 the voltage equations B.1-B.2 may be expressed solely in terms of stator and rotor currents [**1**]:

$$\begin{bmatrix} \boldsymbol{v}_{abcs} \\ \boldsymbol{v'}_{abcr} \end{bmatrix} = \begin{bmatrix} \boldsymbol{R}_s + \frac{d}{dt}\boldsymbol{L}_s & \frac{d}{dt}\boldsymbol{L'}_{sr} \\ \frac{d}{dt}(\boldsymbol{L'}_{sr})^T & \boldsymbol{R'}_r + \frac{d}{dt}\boldsymbol{L'}_r \end{bmatrix} \begin{bmatrix} \boldsymbol{i}_{abcs} \\ \boldsymbol{i'}_{abcr} \end{bmatrix} \tag{B.13}$$

The total torque equation (for all three phases) linking the electrical and mechanical systems is derived as [**1**]

$$\tau_e = \frac{P}{2}(\boldsymbol{i}_{abcs})^T\left(\frac{d}{d\theta_{rs}}\boldsymbol{L'}_{sr}\right)\boldsymbol{i'}_{abcr} \tag{B.14}$$

where P is the machine magnetic-pole count.

B.2.5 Induction Machine Winding Connections

The equations B.1-B.2 are based on per-phase stator and rotor circuits. Therefore, the stator and rotor voltage excitation must be reduced to its per-phase equivalent. Under balanced operating conditions, per-phase voltages and currents are easily derived regardless of the three-phase connections used. For unbalanced conditions per-phase voltages and currents are easily obtained from a Y-Y-connected system with a neutral line present. This is because the system is inherently connected in a per-phase configuration. Otherwise, per-phase voltages and currents need to be measured directly which is not always convenient. Basic three-phase circuit theory is presented in [**2**].

B.3 Dynamic Circuit Model expressed in terms of the Arbitrary Reference Frame

The inductance matrix of equation B.11 defines the mutual inductance between the stator and rotor windings in terms of the rotor angular displacement relative to the stator (θ_{rs}). This means that the voltage equations given by equation B.13 have coefficients which are functions of rotor position (θ_{rs}) and rotor angular velocity ω_{rs} relative to the stator. However, some of the terms involving θ_{rs} and ω_{rs} can be eliminated by selecting a particular frame of reference and expressing the stator and rotor voltage equations relative to this frame of reference [**1**].

The reference frame is chosen for effect based on the expected nature of operation of the induction machine [**1**]. Popular reference frames include the stationary reference frame, synchronous reference frame and the reference frame synchronous with the rotor.

The dynamic circuit model is now presented relative to an arbitrary reference frame [**1**]. From this reference frame, the dynamic model in terms of any other reference frame can be derived by substitution of the corresponding reference-frame angular velocity relative to the stator ($\omega_{refs.}$).

B.3.1 Arbitrary Reference Frame in Relation to the Stator and Rotor Circuits

Before the dynamic circuit model can be expressed relative to some reference frame, the relationship between the machine variables of the stator and rotor circuits with the variables of the arbitrary reference frame needs to be established. This relationship is shown in figure B.1 [**1**].

Figure B.1 shows the reference frame and machine circuits on a 2π electrical radians Cartesian plane. In a multiple pole-pair induction machine, each phase winding has appropriately repeated and distributed coil sets in the physically constrained 2π mechanical radians. Since the repeated coils of each phase winding are identical and

physically displaced by 2π electrical radians, the analysis reduces to that of a two-pole machine as shown in figure B.1.

The three components of the stator circuit (corresponding to the three phases which are physically displaced by $\frac{2\pi}{3}$ electrical radians) are reduced to two orthogonal arbitrary-reference-frame components ($g_{as}, g_{bs}, g_{cs} \rightarrow g_{qs}, g_{ds}$). The same applies to the rotor circuit ($g'_{ar}, g'_{br}, g'_{cr} \rightarrow g'_{qr}, g'_{dr}$). As shown in figure B.1, the stator and rotor machine variables are trigonometrically related to the arbitrary reference frame components by

- θ_{refs} which is the arbitrary reference frame angular displacement relative to the stator circuit
- θ_{refr} which is the arbitrary reference frame angular displacement relative to the rotor circuit

To complete the transformation, there is a third component known as the "zero" component (g_{0s} or g'_{0r}) which is numerically related to the rotor and stator circuit components [**1**]. Since this component is independent of the relative reference frame displacements (θ_{refs} and θ_{refr}) it is not included in figure B.1.

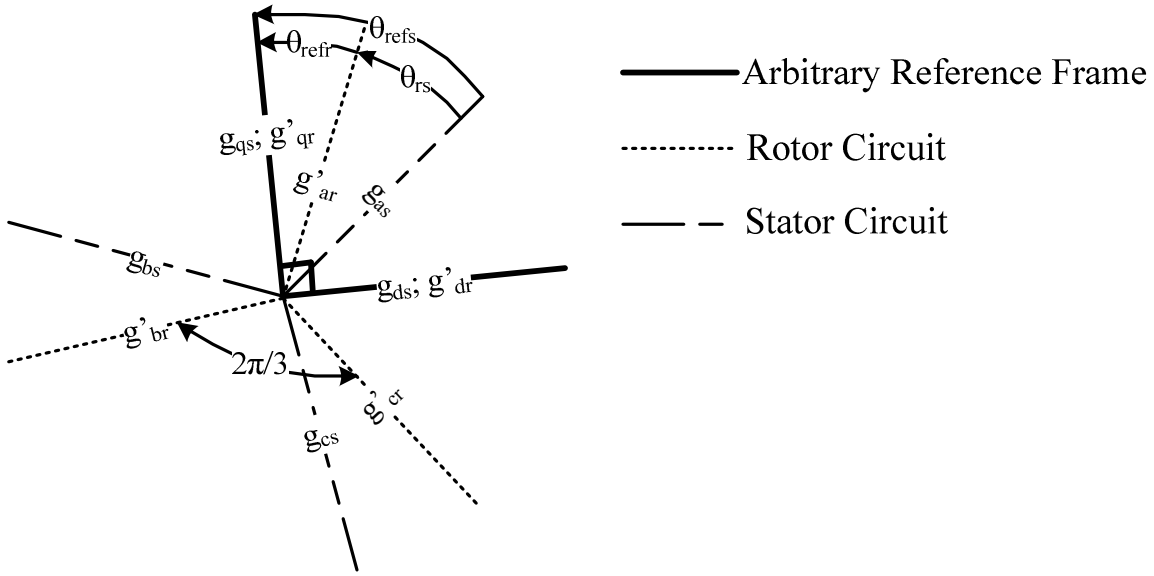

Figure B.1: Transformation of Machine Variables to the Arbitrary Reference Frame (angles are in electrical radians) – adapted from [**1**]

B.3.2 Transformation Equations

The stator machine variables are transformed from the stator circuit to the arbitrary reference frame using the transformation [**1**]

$$\boldsymbol{g}_{qd0s} = \boldsymbol{K}_s \boldsymbol{g}_{abcs} \tag{B.15}$$

where

$$\left(\boldsymbol{g}_{qd0s}\right)^T = [g_{qs} \quad g_{ds} \quad g_{0s}] \tag{B.16}$$

$$\boldsymbol{K}_s = \frac{2}{3}\begin{bmatrix} \cos(\theta_{refs}) & \cos\left(\theta_{refs} - \frac{2\pi}{3}\right) & \cos\left(\theta_{refs} + \frac{2\pi}{3}\right) \\ \sin(\theta_{refs}) & \sin\left(\theta_{refs} - \frac{2\pi}{3}\right) & \sin\left(\theta_{refs} + \frac{2\pi}{3}\right) \\ \frac{1}{2} & \frac{1}{2} & \frac{1}{2} \end{bmatrix} \tag{B.17}$$

The appropriate transformation of the machine-variable frequency is achieved through multiplication with the sinusoidal terms containing the relative reference-frame angular displacement (θ_{refs}). The same effect is achieved by the $\boldsymbol{L'}_{sr}$ matrix (equation B.11) in the flux linkage equations (equation B.6) where $\boldsymbol{\lambda}_{abcs}$ is at stator frequency f_s and $\boldsymbol{\lambda'}_{abcr}$ is at rotor frequency f_r.

The stator variables may be transformed back to machine-variable form using the inverse transformation [**1**]

$$\boldsymbol{g}_{abcs} = (\boldsymbol{K}_s)^{-1}\boldsymbol{g}_{qd0s} \tag{B.18}$$

where

$$(\boldsymbol{K}_s)^{-1} = \begin{bmatrix} \cos(\theta_{refs}) & \sin(\theta_{refs}) & 1 \\ \cos\left(\theta_{refs} - \frac{2\pi}{3}\right) & \sin\left(\theta_{refs} - \frac{2\pi}{3}\right) & 1 \\ \cos\left(\theta_{refs} + \frac{2\pi}{3}\right) & \sin\left(\theta_{refs} + \frac{2\pi}{3}\right) & 1 \end{bmatrix} \tag{B.19}$$

Similar transformations and inverse transformations exist for the rotor variables involving transformation matrix $\boldsymbol{K_r}$ [**1**]. $\boldsymbol{K_r}$ and $(\boldsymbol{K}_r)^{-1}$ are the same as their corresponding stator matrices with θ_{refs} replaced by θ_{refr}. From figure B.1, θ_{refr} is found from

$$\theta_{refr} = \theta_{refs} - \theta_{rs} \tag{B.20}$$

B.3.3 Voltage and Torque Equations in the Arbitrary Reference Frame

After completing the necessary transformations and simplifications as given in [**1**], the induction machine dynamic circuit model relative to the arbitrary reference frame is given by the voltage equations [**1**]

$$\boldsymbol{v}_{qd0s} = \boldsymbol{R}_s\boldsymbol{i}_{qd0s} + \omega_{refs}\boldsymbol{\lambda}_{dqs} + \frac{d}{dt}\boldsymbol{\lambda}_{qd0s} \tag{B.21}$$

$$\boldsymbol{v'}_{qd0r} = \boldsymbol{R'}_r\boldsymbol{i'}_{qd0r} + \left(\omega_{refs} - \omega_{rs}\right)\boldsymbol{\lambda'}_{dqr} + \frac{d}{dt}\boldsymbol{\lambda'}_{qd0r} \tag{B.22}$$

where

$$\left(\boldsymbol{\lambda}_{dqs}\right)^T = [\lambda_{ds} \quad -\lambda_{qs} \quad 0] \tag{B.23}$$

$$\left(\boldsymbol{\lambda}'_{dqr}\right)^T = [\lambda'_{dr} \quad -\lambda'_{qr} \quad 0] \tag{B.24}$$

$$\omega_{refs} = \frac{d}{dt}\theta_{refs} \tag{B.25}$$

$$\omega_{rs} = \frac{d}{dt}\theta_{rs} \tag{B.26}$$

The induction machine flux linkages are expressed in terms of stator and rotor currents by [**1**]

$$\begin{bmatrix} \boldsymbol{\lambda}_{qd0s} \\ \boldsymbol{\lambda}'_{qd0r} \end{bmatrix} = \begin{bmatrix} \begin{bmatrix} L_{ls}+L_M & 0 & 0 \\ 0 & L_{ls}+L_M & 0 \\ 0 & 0 & L_{ls} \end{bmatrix} & \begin{bmatrix} L_M & 0 & 0 \\ 0 & L_M & 0 \\ 0 & 0 & 0 \end{bmatrix} \\ \begin{bmatrix} L_M & 0 & 0 \\ 0 & L_M & 0 \\ 0 & 0 & 0 \end{bmatrix} & \begin{bmatrix} L'_{lr}+L_M & 0 & 0 \\ 0 & L'_{lr}+L_M & 0 \\ 0 & 0 & L'_{lr} \end{bmatrix} \end{bmatrix} \begin{bmatrix} \boldsymbol{i}_{qd0s} \\ \boldsymbol{i}'_{qd0r} \end{bmatrix} \tag{B.27}$$

where

$$L_M = \frac{3}{2}L_{ms} \tag{B.28}$$

Equations B.21-B24 and B27 imply an induction machine dynamic circuit model as shown in figure B.2 [**1**].

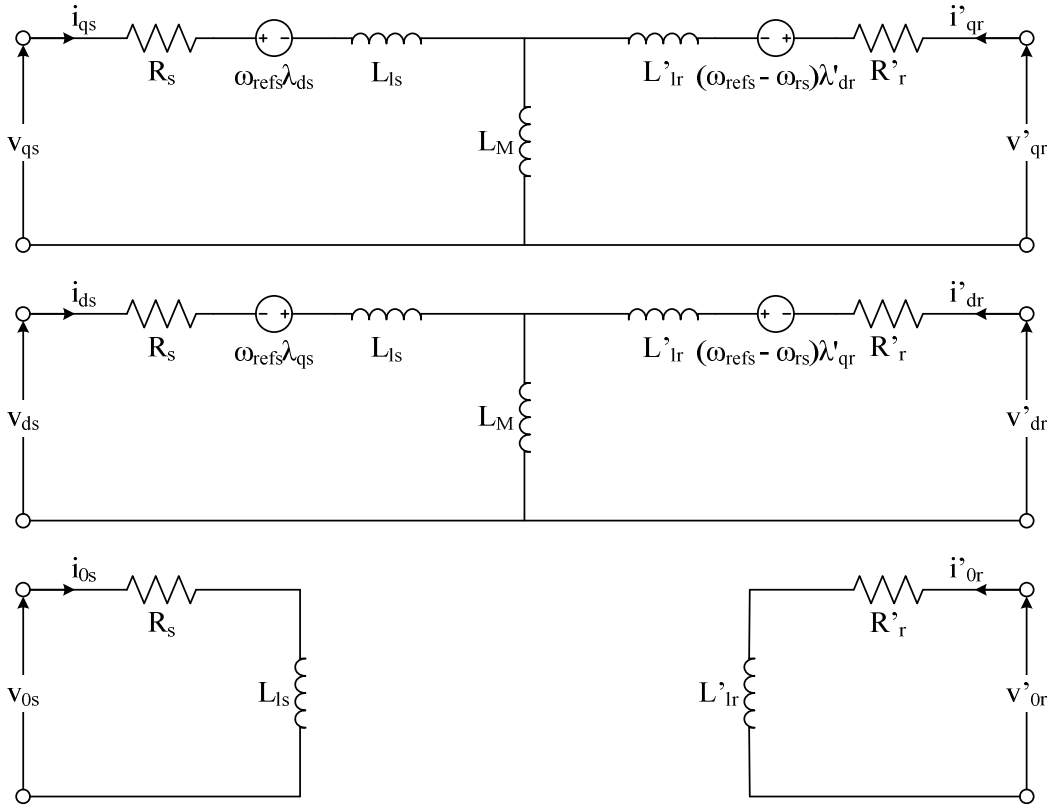

Figure B.2: Induction Machine Dynamic Circuit Model expressed in terms of an Arbitrary Reference Frame – adapted from [**1**]

The electromagnetic torque (positive for motoring) expressed in terms of arbitrary-reference-frame current components is given as [**1**]

$$\tau_e = \frac{3PL_M}{4}\left(i_{qs}i'_{dr} - i_{ds}i'_{qr}\right) \tag{B.29}$$

The resulting electromagnetic torque plotted as a function of time is independent of the choice of reference frame [**1**]. This is not immediately obvious from equation B.29.

B.3.4 Rotor Terminal Voltages in a Squirrel-Cage Induction Machine

The dynamic circuit model presented is a generic model accommodating all three-phase induction machines. Since a SCIG is the chosen induction machine, a decision needs to be made regarding the treatment of the rotor terminal voltages ($v'_{ar}, v'_{br}, v'_{cr}, v'_{qr}, v'_{dr}, v'_{0r}$).

The rotor cage consists of rotor bars arrange in a cylindrical fashion short-circuited at both ends by conducting rings [**2**]. The assumption is that the three-phase rotor currents arrange themselves spatially in the rotor cage such that they can be thought of as leaving one end of the squirrel cage via a particular rotor bar and then returning via another rotor bar. This is a simplistic view as current is likely to be distributed over a number of spatially-appropriate rotor bars.

Regarding three-phase electricity distribution, three-phase circuits are either connected in star or delta arrangements as described in [**2**]. The rotor current distribution described above can be thought of as a three-phase system with star connections (including a neutral connection) at each end. Obviously, each phase is short-circuited at both ends as the rotor bars and rings are assumed to be good conductors. This type of connection implies that

$$v'_{ar} = v'_{br} = v'_{cr} = 0\ \text{V} \rightarrow v'_{qr} = v'_{dr} = v'_{0r} = 0\ \text{V} \tag{B.30}$$

B.4 Conclusion

The dynamic electrical model of an induction machine is presented in terms of machine variables. The development/transformation of this model to one expressed in terms of an arbitrary reference frame is also given as a summary of [**1**]. The selection of a particular reference frame is achieved through the substitution of the reference frame angular velocity.

The dynamic circuit model transformed to the arbitrary reference frame has voltage equations expressed in terms of stator and rotor currents and flux linkages. These voltage equations may be further expressed solely in terms of current or flux-linkage state variables for effect [**1**].

B.5 References

[1] Krause P. C., Wasynczuk O., and Sudhoff S. D., *Analysis of Electric Machinery and Drive Systems*, 2nd ed., El-Hawary M. E., Ed. Hoboken, United States of America: John Wiley & Sons, Inc., 2002.

[2] Sen P. C., *Principles of Electric Machines and Power Electronics*, 2nd ed. Hoboken, United States of America: John Wiley & Sons, Inc., 1997.

C. Measurement System Design and Implementation

C.1 Introduction

This note describes the theory, design and implementation of the measurement system adopted in the experimental setup of chapter 3. This includes:

- The buffer and LFP circuitry for voltage and current measurement
- The frequency-to-voltage converters for excitation-frequency measurement
- The shaft encoder, frequency divider and frequency-to-voltage for rotor speed measurement
- The inline torque sensor for input prime-mover torque measurement
- CMC-interference mitigation through choke implementation

The veroboard layout of the measurement circuit proposed in chapter 3 is also given together with the experimental equipment list. Measurement system calibration is detailed in appendix D.

C.2 Circuit Diagram Conventions and Parameters

Component values for the circuit diagrams are given in table C.1. In these circuit diagrams, red and blue indicate circuitry associated with positive and negative supplies respectively (± 5 V_{DC}, ± 15 V_{DC} and $+30$ V_{DC}) whereas green indicates signals to be measured by an oscilloscope. Furthermore, $V_{s1} = 15$ V_{DC}, $V_{s2} = 5$ V_{DC} and $V_{s3} = 30$ V_{DC} in these figures.

Table C.1: Circuit-Diagram Component Values

Component	Value
C_1	10 µF
C_2	47 nF
C_3	100 nF
C_4	$5\ \mu F = 2 \times 10\ \mu F$ in series
C_5	1 µF
C_6	680 pF
R_1	$2.257\ k\Omega = 2.2\ k\Omega + 56\ \Omega + 1\ \Omega$
R_2	$3.327\ k\Omega = 3.3\ k\Omega + 27\ \Omega$
R_3	$202.6\ k\Omega = 180\ k\Omega + 22\ k\Omega + 330\ \Omega + 270\ \Omega$
R_4	$10\ k\Omega$
R_5	$1\ k\Omega$
R_6	$89.1\ k\Omega = 56\ k\Omega + 33\ k\Omega + 100\ \Omega$
D_1	PH4148

C.3 Buffer and LPF Circuitry

The circuit diagram for the measurement of the generator phase voltage is given in figure C.1. In this case, the phase-one voltage measurement is illustrated. Description of the CMC choke is given later but is included for completeness. The triangular reference represents the

zero-reference conductor of the measurement circuit. This reference is the same as the oscilloscope-measurement zero-reference which is common to the oscilloscope grounding reference. The relationship between this zero-reference and the protective earth reference of the experimental setup in figure 3.3 is revealed later. The buffer and filter are implemented through the use of TL084CN quad-operational-amplifier packages.

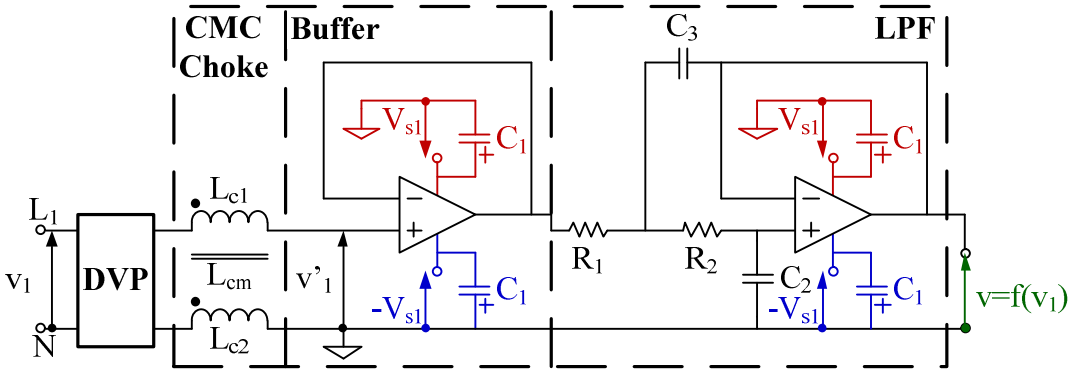

Figure C.1: Generator Phase-Voltage Measurement – Circuit Diagram

The buffer circuit is a typical operational-amplifier voltage follower with its input v'_1 scaled down from v_1 by the DVP such that:

$$v'_1 = \frac{v_1}{1000} \tag{C.1}$$

The buffer output is passed on to a second-order active low-pass filter. The chosen filter is a Butterworth filter in a Sallen-Key Topology with a unity gain as presented in [**1**]. The filtered output is a function (scaled-down filtered version) of the phase-voltage v_1.

An active filter (using an operational amplifier) is chosen over a passive filter so that a second-order filter can be achieved without the use of an inductor [**1**]. A Butterworth filter is chosen so as to achieve maximum pass-band flatness [**1**]. Furthermore, a second-order filter is chosen as a first-order filter has a lower attenuation for higher frequencies. Even though higher-order Butterworth filters produce a flatter pass-band they introduce larger phase shifts over the pass-band which is undesirable in the given measurement application [**1**].

In selecting the bandwidth of the filter, one needs to consider the range of the fundamental frequency to be measured as well as the attenuation and time delay (phase shift) introduced by the filter. If a maximum generator synchronous speed of 2000 rpm is chosen, this translates into an excitation frequency of 67 Hz for a four-pole machine (equation A.3). Therefore, the measured-signal fundamental bandwidth is approximately 70 Hz. In order to accommodate filter attenuation and time delay, a filter -3 dB bandwidth of 800 Hz is chosen.

The buffer and LPF circuitry for the generator phase-current measurement as well as the prime-mover phase-voltage measurement is identical to that of figure C.1. The only

difference being the input to the corresponding buffer circuit. This is illustrated in figures C.2-C.3 for the generator current and prime-mover voltage measurement respectively. The CT and VT ratios in these figures are scaling ratios.

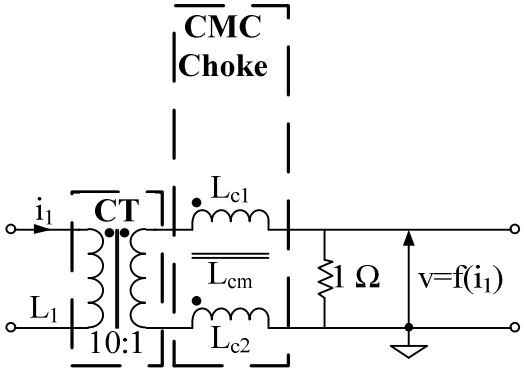

Figure C.2: Generator Phase-Current Measurement – Input to Buffer Circuit

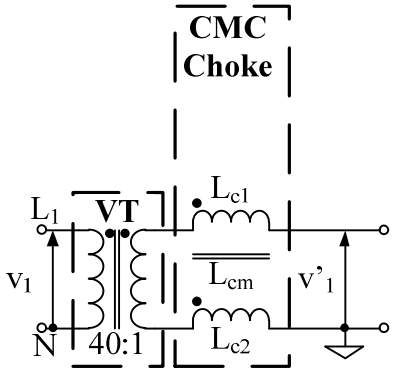

Figure C.3: Prime-Mover Phase-Voltage Measurement – Input to Buffer Circuit

C.3.1 Filter Design

Based on an ideal operational-amplifier analysis with the use of Fourier transforms, the transfer function of the LPF in figure C.1 may be written as

$$B(j\omega) = \frac{v_{out}(j\omega)}{v_{in}(j\omega)} = \frac{1}{(1-R_1R_2C_2C_3\omega^2)+jC_2(R_1+R_2)\omega} \tag{C.2}$$

Active filter design is presented in [**1**] which explains the procedure used in selecting the filter component values. The process is highlighted here for convenience. From [**1**], equation C.2 may be expressed as

$$\frac{v_{out}(\mathbb{s})}{v_{in}(\mathbb{s})} = \frac{1}{1+\omega_c C_2(R_1+R_2)\mathbb{s}+\omega_c{}^2 R_1R_2C_2C_3\mathbb{s}^2} \tag{C.3}$$

such that

$$\mathbb{s} = \frac{j\omega}{\omega_c} \tag{C.4}$$

$$\omega_c = 2\pi f_c \tag{C.5}$$

$$a_1 = \omega_c C_2 (R_1 + R_2) \tag{C.6}$$

$$b_1 = {\omega_c}^2 R_1 R_2 C_2 C_3 \tag{C.7}$$

f_c is known as the corner frequency or -3dB frequency of the filter. The parameter selection is carried out as follows [**1**]:

1. $a_1 = 1.4142$ and $b_1 = 1$ are obtained from a table of values for a second-order low-pass Butterworth filter.
2. C_2 is chosen for convenience.
3. C_3 is chosen such that [**1**]

$$C_3 \geq \frac{4b_1}{{a_1}^2} C_2 \tag{C.8}$$

4. R_1 and R_2 are chosen such that [**1**]

$$R_{1,2} = \frac{a_1 C_3 \mp \sqrt{{a_1}^2 {C_3}^2 - 4 b_1 C_2 C_3}}{4\pi f_c C_2 C_3} \tag{C.9}$$

It is recommended that $1\ \text{k}\Omega \leq R_{1,2} \leq 100\ \text{k}\Omega$ and $1\ \text{nF} \leq C_{2,3} \leq$ several μF [**1**]. Based on this procedure and practically available capacitor values, the recommended component values are $C_2 = 47\ \text{nF}$; $C_3 = 100\ \text{nF}$; $R_1 = 2.26\ \text{k}\Omega$ and $R_2 = 3.726\ \text{k}\Omega$ ($f_c = 800\ \text{Hz}$). The resistors are implemented practically as (nominal values not considering tolerance) $R_1 = 2.257\ \text{k}\Omega = 2.2\ \text{k}\Omega + 56\ \Omega + 1\ \Omega$ and $R_2 = 3.327\ \text{k}\Omega = 3.3\ \text{k}\Omega + 27\ \Omega$.

C.3.2 Theoretical Filter Response

Based on the implemented component values, the theoretical filter frequency response is given by figures C.4-C.5. The $-40\ \text{dB/dec}$ filter response for high frequencies is clearly visible in figure C.4. The phase shift introduced in the $0\ \text{Hz} - 70\ \text{Hz}$ band is addressed in the calibration process of appendix D.

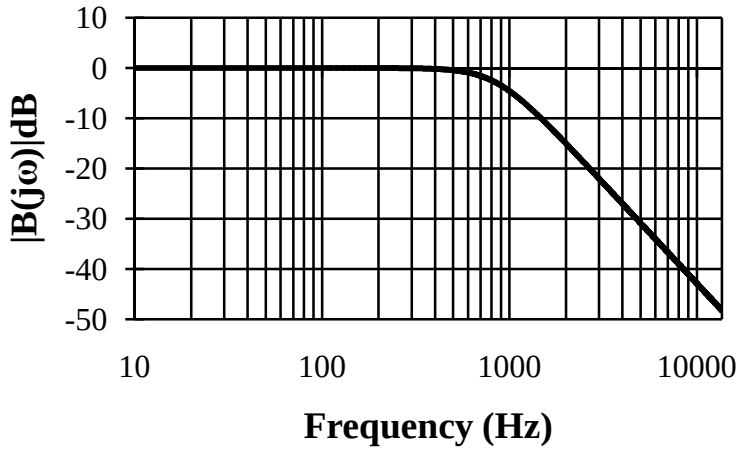

Figure C.4: Filter Frequency Response (Theoretical) – Bode Modulus

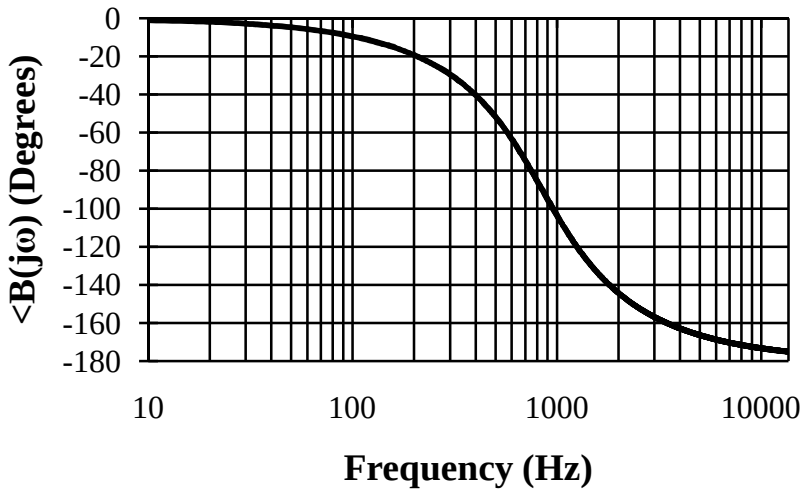

Figure C.5: Filter Frequency Response (Theoretical) – Bode Phase

The theoretical filter attenuation and phase shift at 70 Hz and 800 Hz is given in table C.2. It is observed that the ideal attenuation and phase shift of -3 dB and $-90°$ respectively is not achieved at 800 Hz. This is because the chosen resistor values are not identical to the recommended resistor values. Furthermore, it is observed that the filter amplifies the signal (negligibly) at 70 Hz as opposed to attenuating it. This is a result of the filter transfer function being under-damped causing amplification (negligible) rather than attenuation (negligible) of the lower bandwidth frequencies.

Table C.2: Theoretical Filter Frequency Response at 70 Hz and 800 Hz

Frequency (Hz)	Attenuation (dB)	Phase Shift (Degrees)
70	0.0012	-6.629
800	-2.435	-85.31

C.4 Frequency-to-Voltage Converter – Excitation-Frequency Measurement

The frequency-to-voltage converter circuit for both generator and prime-mover excitation-frequency measurement is presented in figure C.6 [**2**,**3**]. Each converter has the corresponding scaled-down/filtered phase-voltage as its input and outputs a DC-voltage which is directly proportional to the input frequency. Converter functionality, design and parameter selection is obtained from the LM2907N − 8 datasheet and application note [**2**,**3**]. The packages are supplied by a single +15 V_{DC} supply with the passive circuit parameters chosen so as to consider:

1. Input frequency to output voltage relationship including linearity
2. Output voltage ripple
3. Frequency-to-voltage converter response time

The chosen component values include $C_2 = 47$ nF, $R_3 = 202.6\,\text{k}\Omega = 180\,\text{k}\Omega + 22\,\text{k}\Omega + 330\,\Omega + 270\,\Omega$, $C_4 = 5\,\mu\text{F} = 2 \times 10\,\mu\text{F}$ in series. $R_4 = 10\,\text{k}\Omega$ is chosen to be the same as that prescribed in [**2**,**3**]. The frequency-voltage relationship is established in the calibration process (appendix D).

The generator and prime-mover phase voltages should larger than $\pm 40\ V_{peak}$ and $\pm 1.6\ V_{peak}$ respectively in order to trigger the corresponding frequency-to-voltage converters (worst-case input thresholds) [**3**]. This considers all the scaling ratios before frequency measurement is actually achieved. This requirement is of no consequence as experiments will not be conducted at such low excitation levels.

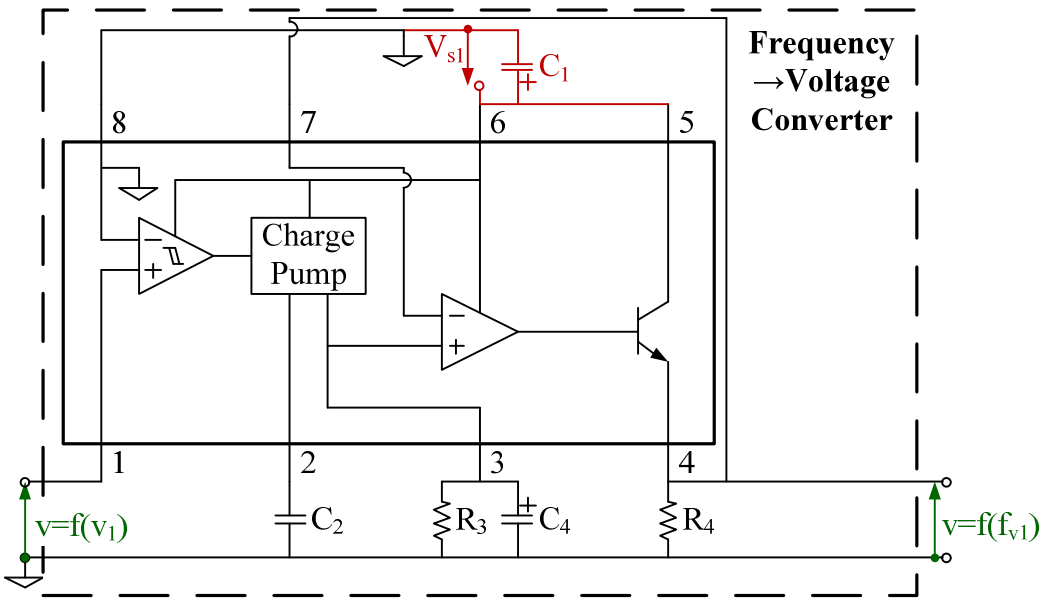

Figure C.6: Frequency-to-Voltage Converter – Excitation-Frequency Measurement (adapted from [**2**,**3**])

C.5 Shaft Encoder with Frequency Divider and Frequency-to-Voltage Converter – Generator Speed Measurement

The shaft encoder is rated at 5000 ppr (pulses-per-revolution). The synchronous speed of a four-pole induction machine excited at 70 Hz is 2100 rpm (equation A.3). Therefore, the maximum shaft encoder output frequency to be accommodated is 175 kHz. In order to obey advised component limits of the frequency-to-voltage converter as presented in [**2**,**3**], it is necessary for this frequency to be stepped down. This is the purpose of the frequency divider which reduces the shaft encoder output frequency by a factor of 16. The drawback of this scaling is that any measurement errors may be multiplied when calculating the generator speed.

The rotor-speed-measurement circuit diagram is presented in figure C.7 (frequency-to-voltage converter adapted from [**2**,**3**]). Conventionally, the shaft encoder has a positive DC supply voltage applied at the red terminal relative to the black terminal (zero-reference), with a pulse-train output at the white terminal relative to the black terminal. However, in order to limit the number of voltage supplies required by the measurement system as well as considering a maximum input voltage of 7 V for the MB74LS73A flip-flop package used in the following frequency divider, a different encoder interface is proposed.

The veroboard circuit has a $\pm 5\ V_{DC}$ supply with the positive supply being required for the flip-flop package. The negative supply is included to provide a voltage supply of $10\ V_{DC}$ required by the shaft encoder. This is achieved by connecting the positive supply to the red terminal and the negative supply to the black terminal. As a result, the zero-reference of the shaft encoder is actually at $-5\ V_{DC}$ relative to the measurement circuit zero-reference. Therefore, the $0\ V, 10\ V$ pulse-train output of the shaft encoder (relative to its black terminal) is actually $-5\ V, +5\ V$ relative to the measurement circuit zero-reference. The PH4148 diode (D_1) is used to block the negative half-cycle of shaft encoder pulse train applied to the input of the flip-flop package and a $1\ k\Omega$ resistor (R_5) acts as a pull-down resistor during this period. Therefore, the first flip-flop sees a $0\ V, 5\ V$ pulse train. Direction of rotation is not required as the generator will only ever turn in one direction. The other shaft-encoder outputs are not used.

The frequency divider consists of four-stages of J-K flip-flops which are set as toggle switches [**4**,**5**]. The flip-flops toggle on a high-to-low transition such that each flip-flop halves its incoming frequency. The "clear" inputs of the flip-flops are always inactive, even on system initialisation. This is because the actual state of each flip-flop output is not important, just the frequency at which it changes. Of course there is a delay generated by the frequency divider when the frequency changes, however, this is considered negligible in comparison to the delay created by the following frequency-to-voltage converter which needs to balance output-voltage ripple and response time. The output of the frequency divider sees a

DC-blocking 1 µF capacitor (C_5) before activating the frequency-to-voltage converter. This is to generate a bipolar pulse train from a unipolar train which is required to switch the converter comparator.

The frequency-to-voltage converter topology in figure C.7 is the same as before except for the component values: $C_6 = 680$ pF and $R_6 = 89.1\ \text{k}\Omega = 56\ \text{k}\Omega + 33\ \text{k}\Omega + 100\ \Omega$.

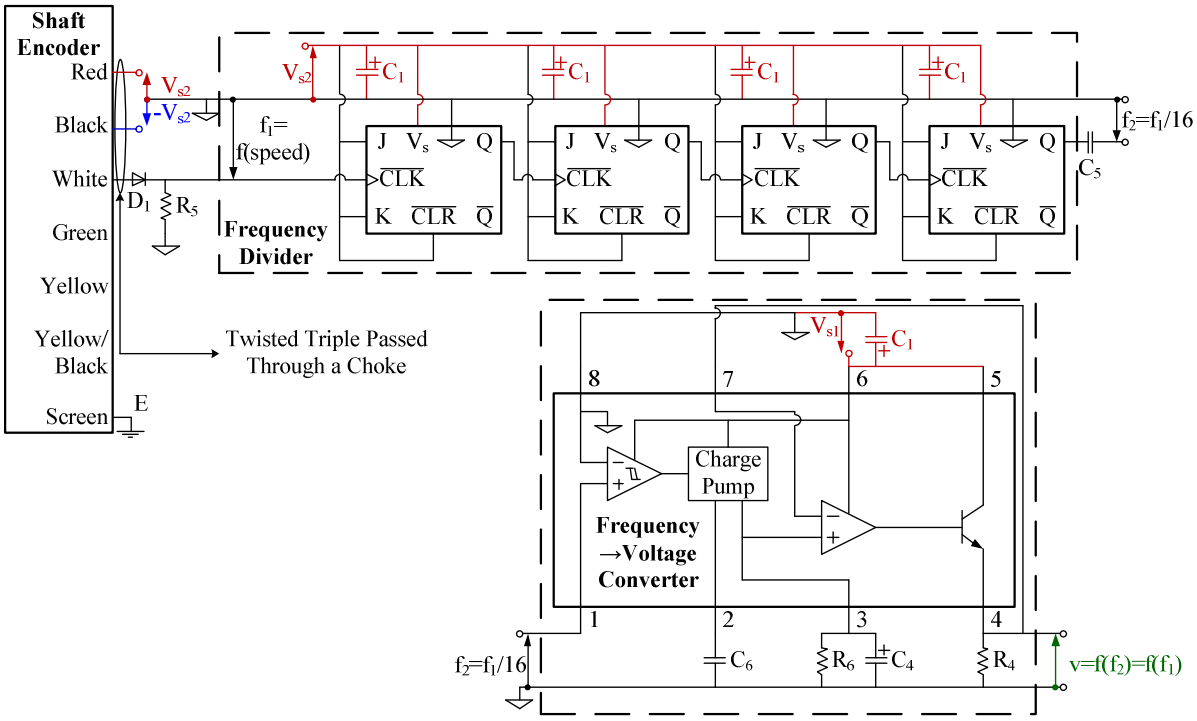

Figure C.7: Rotor Speed Measurement – Circuit Diagram (frequency-to-voltage converter adapted from [**2**,**3**])

C.6 Inline Torque Transducer

The basic electrical setup for the torque transducer is presented in figure C.8. The transducer wiring consists of a supply loop and a measurement loop – each with separate zero-reference lines [**6**]. The bench-supply provides an isolated $+30\ \text{V}_{\text{DC}}$ voltage and an oscilloscope measures the prime-mover torque τ_{pm} as an output voltage from the transducer. The conductors of the two loops are arranged as twisted pairs to reduce possible magnetic interference [**6**]. The use of CMC chokes in the suppression of CMC interference is discussed in the following section.

Proper shielding of the measurement against electric-field coupling is difficult to achieve owing to the use of a separate supply and measurement interface on the right of figure C.8 [**6**,**7**,**8**]. Therefore, it is important to minimise any coupling after the CMC choke which may result in noticeable CMCs. The placement of the choke, supply and oscilloscope away from possible sources of electric-field coupling should be considered.

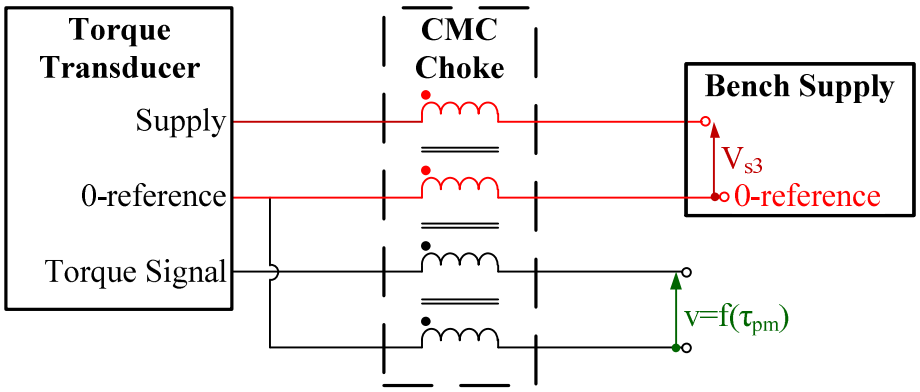

Figure C.8: Torque Transducer Electrical Connections

C.7 CMC Interference Mitigation through Choke Implementation

The concept of electromagnetic compatibility is well established and involves the generation, coupling and reception of various forms of ElectroMagnetic Interference (EMI) [**7**]. Various interference mitigation techniques targeted at these three areas of EMI are also well developed [**7**,**9**,**8**]. The purpose of this section is to highlight the application of existing knowledge to the measurement problem as previously defined including:

- Differential- and common-mode interference signals together with the corresponding circuit model [**7**,**9**,**10**].
- General power line filters and ideal CMC choke operation [**7**,**8**,**9**,**11**,**12**].
- CMC interference associated with PWM power converters [**7**].

These topics are applied specifically to the measurement problem with the aim of producing "cleaner" and more reliable measurements. The CMC choke is used as the primary means of reducing circuit susceptibility to EMI. The operation and ideal performance of a multi-conductor choke (shaft-encoder and torque-transducer chokes) is stated as an extension of the simpler twin-conductor case [**8**,**9**].

C.7.1 Differential-Mode and Common-Mode Interference – Equivalent Circuit Model

In order appreciate the nature of EMI and, therefore, develop techniques targeted at interference mitigation, appropriate models need to be used. Figure C.9 is a circuit diagram developed in [**9**] which models a source of interference such that emission occurs via conduction. The source circuit is given by the solid lines with the load circuit elements given by the broken lines. In order to make sense of this circuit model, consider loop "A12" to be the differential (main) circuit loop with conductor 1 as the "go-to" conductor and conductor 2 as the "return" conductor. In this loop the differential-mode interference source is given by the combination of $v_{1,DMI}$ and $v_{2,DMI}$. $Z_{1,diff}$ and $Z_{2,diff}$ represent some differential-mode impedances with Z_{L12} loading the given loop. Conductor 3 represents some reference conductor (protective earth is a good example) with its associated common-mode interference source v_{CMI} and conductor impedance Z_{com}. v_{CMI} is defined as a common-mode voltage source as it attempts to drive a common-mode current i_{CMI} through conductors 1 and 2 in the

same direction (i.e. conductors 1 and 2 form a parallel branch) with conductor 3 as the return conductor. Z_{L13} and Z_{L23} are load impedances. The $v_{1,DMI}$, $v_{2,DMI}$ and v_{CMI} sources together form the general source of EMI. This model is not concerned with how these sources are generated, but rather on how a source of interference may be defined together with the effect that this source has on a load.

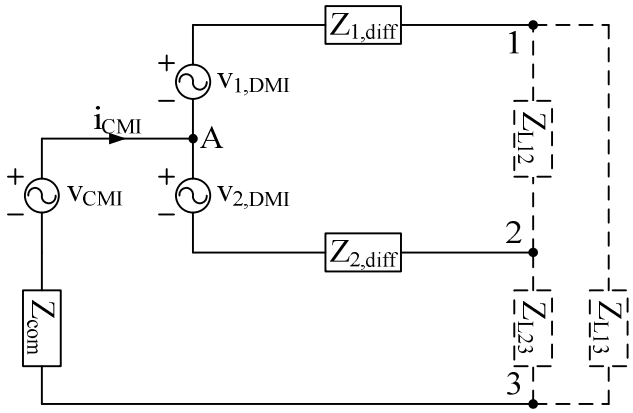

Figure C.9: General Circuit Model for an Interference Source and its Corresponding Load Circuit – adapted from [**9**]

Since PWM power converters are used, common-mode interference is the primary source of interference to the measurement circuit [**7**]. If $v_{1,DMI}$ and $v_{2,DMI}$ are neglected such the entire circuit is balanced with $Z_{1,diff} = Z_{2,diff}$ and $Z_{L13} = Z_{L23}$, the voltage produced across Z_{L12} as a result of the common-mode voltage source is zero [**7**,**10**]. This is obvious if one considers that $v_{12} = v_{13} - v_{23}$ where v_{13} and v_{23} are derived from loops "A13" and "A23" respectively.

Forcing a circuit to be balanced in this way provides a technique that reduces the common-mode to differential-mode interference conversion from v_{CMI} to v_{12} [**7**,**10**]. If, however, an unbalanced condition is assumed with $Z_{1,diff} \neq Z_{2,diff}$ and $Z_{L23} \neq Z_{L13} = \infty\,\Omega$ and $v_{1,DMI}, v_{2,DMI}$ are neglected, figure C.9 may be further modified into that of "Common-Mode Circuit" of figure C.13 [**4**]. This circuit model is the interference model assumed for the purpose of the measurement system and includes the placement of a choke for common-mode interference mitigation.

From figure C.9, a CMC may be defined as a current that flows in the reference conductor [**9**].

C.7.2 General Power-Line Filters

A typical power-line filter, illustrated in figure C.10, is used to mitigate both differential-mode and common-mode interference [**7**,**9**]. Such a filter circuit may be used at the input and/or output of switch-mode power supplies depending on the nature and origin of EMI [**7**,**9**]. Placement and physical construction of the filter also influences the effectiveness of the filter [**7**,**8**]:

- The incoming and outgoing wire ends of the choke should be separated as far as possible so as to minimise any parasitic capacitance between them that would effectively short-circuit the choke at high frequencies.
- The power line filter should be fitted as close to the entry/exit point of a protective (to EMI) enclosure. This hinders any short-circuiting across the choke as the high-frequency currents are intercepted by the enclosure and make their way to the protective earth connection of the enclosure.

Consider figure C.10 with the source of differential- and common-mode interference to the left and some susceptible load to the right. The differential- and common-mode currents are represented by i_{diff} and $i_{com} = i_{1,com} + i_{2,com}$ respectively with the differential- and common-mode filtering elements being presented in blue and red respectively.

The differential-mode filter assumes a low source impedance with a corresponding high load impedance [**7**]. The uncoupled inductors L_1 and L_2 together with the capacitor C_X develop a low-pass filtering effect to differential-mode signals.

Regarding common-mode interference, the filter components are arranged assuming a high source impedance with a corresponding low load impedance [**7**]. An ideal CMC choke is one which has no effect on the differential current (acts as a short circuit) but presents a large impedance to CMCs (as a result of the mutual coupling between coupled inductors) [**7**,**9**,**11**,**12**]. This is because a differential-mode current produces cancelling magnetic fields for the two windings whereas a common-mode current produces additive fields for the two windings [**7**,**9**,**11**]. L_{c1} and L_{c2} represent the choke self-inductance values whereas L_{cm} represents the mutual inductance between the choke windings. Ideal choke-inductance relationships are discussed later. The presence of "Y" capacitors C_{Y1} and C_{Y2} provide an alternative (easier) path for CMCs to flow when faced by a large choke impedance. From a practical perspective, L_1 and L_2 may be achieved as choke leakage inductances [**8**,**9**].

Considering the proposed measurement circuit, only the choke is implemented regarding common-mode interference. An active filter is used to filter the actual measured signal in order to extract the signal fundamental. This filter also serves for differential-mode-interference filtering.

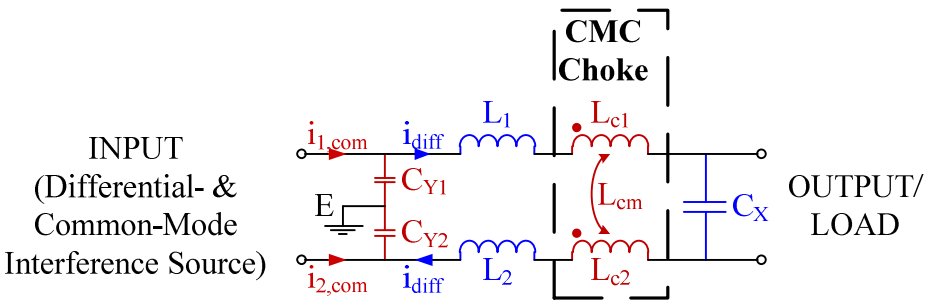

Figure C.10: Typical Power-Line Filter – adapted from [**7**]

C.7.3 PWM-based Power Converters and their associated CMC Interference

In order to appreciate and mitigate the interference problem faced by the measurement system, one needs to have an understanding of the source of this interference. In this case, the high $\frac{dv}{dt}$ of the switch-mode power converter is the source of the common-mode interference [**7**]. This is easily observed in the PWM nature of the power converter output as illustrated in figure 3.2. The interference problem is illustrated in figure C.11 with the typical common-mode interference path indicated in purple [**7**].

In figure C.11, a typical 400 V_{RMS} (line-to-line), 50 Hz three-phase supply excites a three-phase variac which outputs the same voltage supply. This supply excites a power converter which drives a SCIG. Considering a single phase, there is high $\frac{dv}{dt}$ at point "F" with respect to the protective earth reference "E" as a result of the converter switching action [**7**]. These high frequencies develop a current path in the protective earth conductor as a result of parasitic capacitance [**7**]. Part of this capacitance is situated between windings of the induction machine and its metal enclosure (C_b) which is connected to protective earth. The current path is completed by capacitance between protective earth and the switching circuitry as indicated by C_a. Since the neutral point of the variac is also connected to protective earth, an alternative current path exists via the variac and rectifier circuitry. The problem is repeated for the power-converter/squirrel-cage-induction-motor combination.

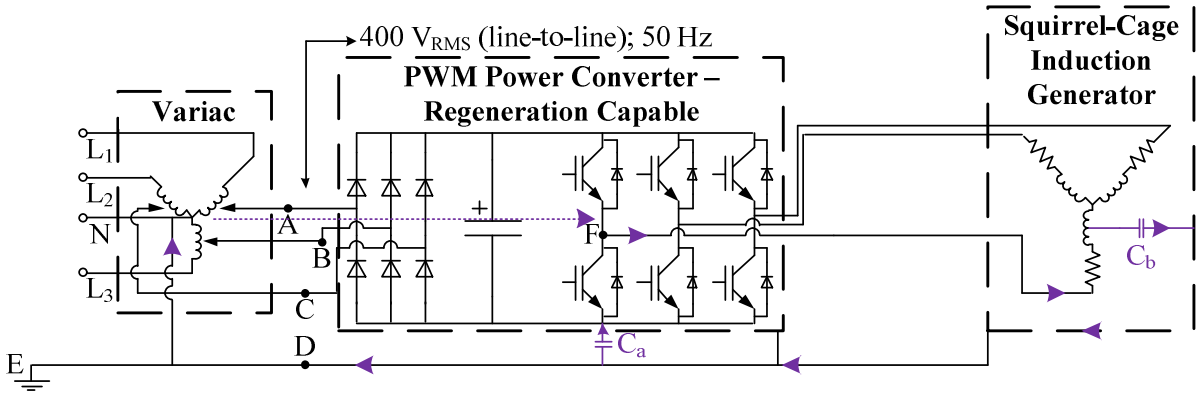

Figure C.11: PWM-Based Power Converter CMC Interference – adapted from [**7**]

The interference problem as observed by the measurement system is indicated in orange in figure C.12. The common-mode interference is passed on to the measurement circuit via the parasitic inter-winding capacitance of the current and voltage transformers [**7**]. It is assumed that the DVPs are immune to CMCs but the voltage measurements are protected with chokes anyway. The common-mode current in the measurement circuit zero-reference conductor has a path to the protective earth conductor via the oscilloscope zero-reference line which is directly connected to the protective earth – the common-mode current loop is thus complete. The common-mode current component in the signal lines may make their way to the circuit

zero-reference either by direct conduction (via the 1 Ω resistors across the output of the CT's) or via parasitic capacitance.

A possible alternative path for common-mode currents in the measurement circuit to return to the protective earth conductor is via the bench power supplies [**4**]. The reference terminal of the supply voltages are directly connected to the circuit zero-reference and, therefore, provide a conduction path. Interference current may present itself on the other supply lines as discussed before. From the bench supply terminals, the common-mode currents may make their way to the protective earth conductor via parasitic capacitance such as wire-to-casing capacitance where the casing is connected to protective earth.

All the voltage and current measurements are achieved after a buffer circuit which presents an open circuit to the signal line and, therefore, the corresponding CMC component. However, the presence of non-negligible parasitic capacitance and inductance at high frequencies make it difficult to predict the behaviour of the measurement circuit as a result of CMCs [**13**,**14**]. Two points on the same conductor may have a potential difference as a result of parasitic inductance [**4**]. As a result zero-reference or protective earth connections may not always be as expected. The situation is made worse in that the parasitic elements are largely a function of circuit layout and construction [**13**,**14**]. As shown later in figure C.13, an open-circuit load (buffered load for example) remains susceptible to common-mode to differential-mode interference conversion, even though the current component flowing though the load is zero. Therefore, the best approach is to prevent the common-mode interference from entering the circuit.

Another measurement circuit input susceptible to common-mode interference is the shaft encoder interface. A three-wire choke is used to reduce this susceptibility. The supply and signal wires from the encoder have a shield which is connected to the encoder enclosure. The enclosure and shield are grounded (connected to protective earth) via the generator chassis to direct any capacitive/common-mode interference to the protective earth away from the encoder wires [**8**]. If possible, the shield should be grounded at both ends [**15**]. Furthermore, the measurement circuit should be located in a grounded enclosure which is connected to the shield so that the encoder wires are completely enclosed and protected [**15**]. This is not the case and the encoder wires protrude from their shielding, thus, providing another entry point of interference. However, the measurement circuit performs suitably with the CMC choke for interference mitigation in the absence of a protective enclosure.

Possible interference in the torque measurement is indicated in figure C.12 and is similar to that discussed above.

An additional means of mitigating the CMC interference introduced into the measurement circuit as a result of inverter operation involves the use of a Faraday shield [**7**]. This technique aims to reduce the inter-winding capacitance of the measurement transformers. A

Faraday shield is simply a grounded shield between the primary and secondary windings of the transformers where any CMCs originating from the primary winding are intercepted and passed directly to protective earth. The given measurement transformers do not include this shielding.

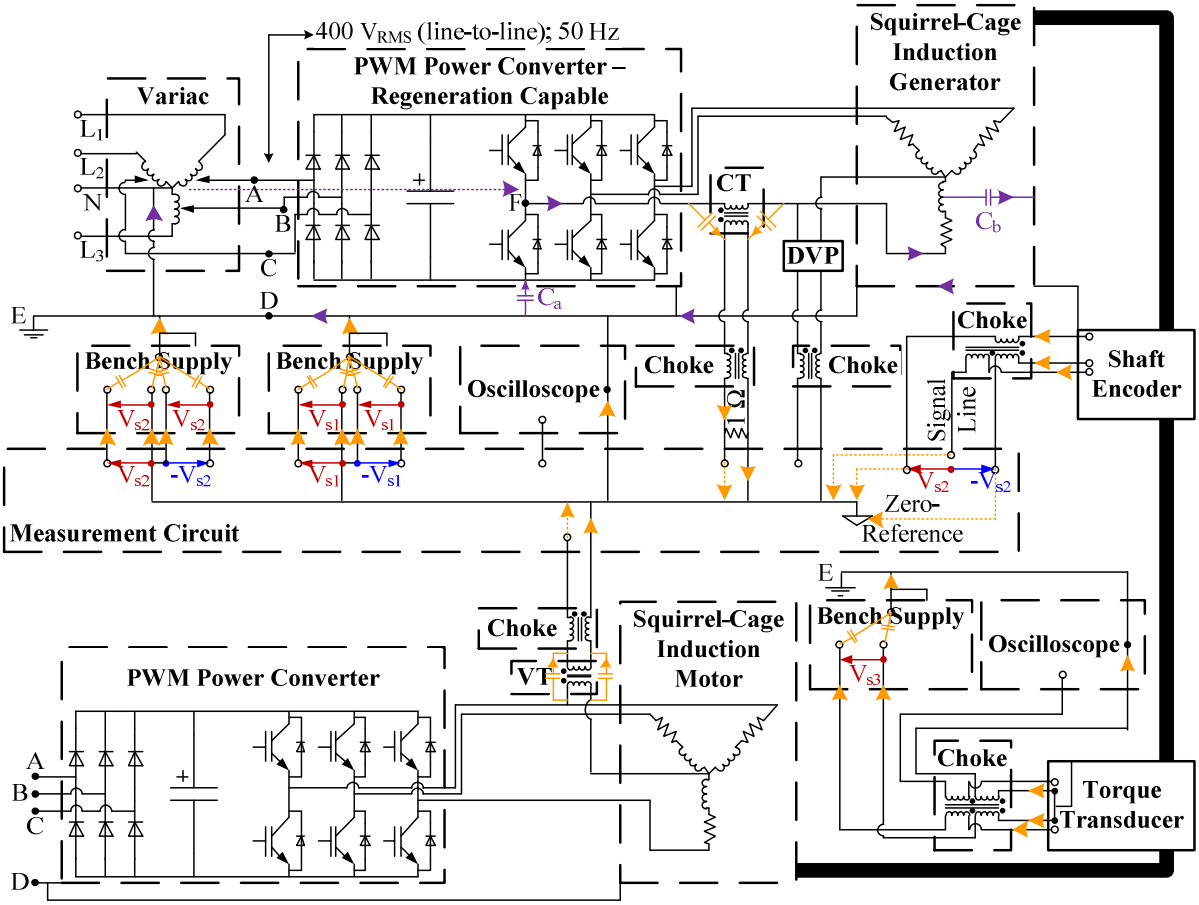

Figure C.12: Measurement-Circuit CMC-Interference Consideration

C.7.4 Measurement-Circuit Chokes – Desired Performance, Design and Construction

C.7.4.1 *Equivalent Differential-Mode and Common-Mode Circuit Models for a CMC Choke*

Figure C.13 is a circuit diagram showing the placement of a CMC choke in a typical (differential-mode) circuit together with its corresponding common-mode circuit equivalent. As previously mentioned, the common-mode circuit is based on figure C.9 assuming an unbalanced case [**4**,**7**,**9**,**10**]. Figure C.13 is concerned with analysing and reducing CMCs introduced into a "receiver" circuit and not on a circuit producing CMCs. The aim is to reduce the effects of CMCs on the load Z_L.

The differential-mode circuit comprises a desired voltage source v_{diff} (with source impedance $Z_{s,diff}$) that drives a current i_{diff} through the load Z_L. The zero-reference of the differential-mode circuit is separated from general (protective) earth E by impedance Z_E

which may be zero. A two-winding choke with self inductance L_{c1}, L_{c2} and mutual inductance L_{cm} has voltage and current conventions as depicted in blue.

The common-mode circuit comprises a high-frequency voltage source v_{com} (high-frequency switching components of a PWM-based power converter for example) which drives a common-mode current i_{com} through the differential-mode circuit. The voltage source has a "source impedance" $Z_{s,com}$ such that the total common-mode impedance external to the original differential-mode circuit is given as $Z_E + Z_{s,com}$. This impedance is split so as to account for a non-zero total external impedance even if the differential-mode circuit zero-reference and general earth E are connected. Each parallel branch now has an additional common-mode impedance $Z_{1,com}$ or $Z_{2,com}$ which accounts for additional impedances as a result of the high-frequency current paths. These impedances include intra- and inter-winding capacitances of transformers as well as parasitic inductance as previously described. If $Z_{1,com}$ and $Z_{2,com}$ are neglected, then without a CMC choke, the branch with L_{c2} becomes a short circuit and the upper branch has a load Z_L. Theoretically, the common-mode current would be confined to the lower loop and, thus, would not affect the differential-mode circuit i.e. no common-mode current problem. Since this is not the case experimentally, $Z_{1,com}$ and $Z_{2,com}$ are included.

The choke model used in figure C.13 is that of two coupled inductors and, therefore, is incomplete for high frequencies where parasitic effects such as intra- and inter-winding capacitance is not negligible [**13**,**14**,**16**]. For the purpose of desired choke performance, design and construction presented here, these parasitic effects are not considered.

The location of the differential-mode source and source impedance relative to the common-mode-interference source and common-mode impedance is not explicitly defined. This is of no importance to the analysis presented as the focus is on the load Z_L.

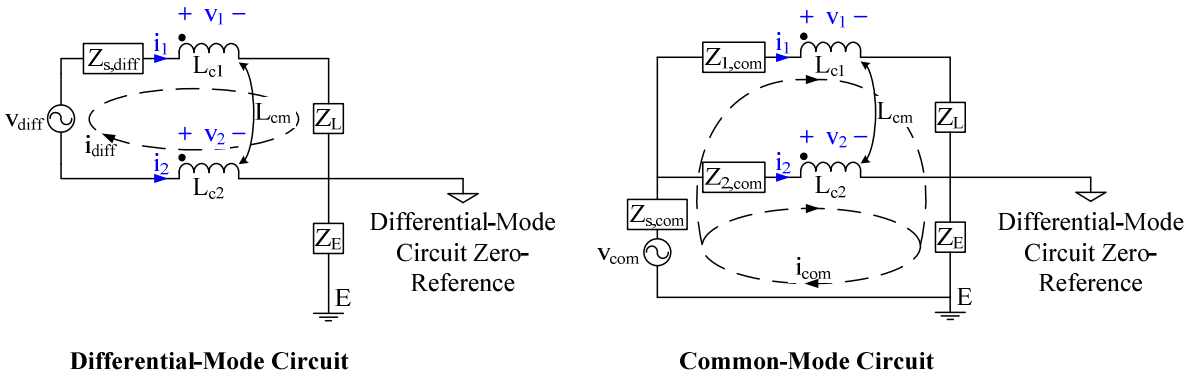

Figure C.13: Receiver-Based Differential-Mode and Common-Mode Circuit Models including a CMC Choke

C.7.4.2 ***First Design/Construction Requirement – Minimise CMCs***

In the proposed measurement circuit, it is difficult to quantify the magnitude/nature of the common-mode voltage source and, therefore, the magnitude/nature of the common-mode current to be attenuated. Faraday's law for the mutually coupled inductors of figure C.13 may be written as

$$v_1 = N_1 \frac{d\phi_1}{dt} = L_{c1} \frac{di_1}{dt} + L_{cm} \frac{di_2}{dt} \tag{C.10}$$

$$v_2 = N_2 \frac{d\phi_2}{dt} = L_{c2} \frac{di_2}{dt} + L_{cm} \frac{di_1}{dt} \tag{C.11}$$

where N is the inductor turn count and ϕ is the linking-flux of the given inductor. Equations C.10-C.11 assume a linear choke (no magnetic saturation). The mutual inductance is related to the self inductance by the coupling factor K as

$$L_{cm} = K\sqrt{L_{c1}L_{c2}} \tag{C.12}$$

Furthermore, the self inductance may be expressed as

$$L_{c1} = \frac{{N_1}^2}{\mathcal{R}_1} \text{ and } L_{c2} = \frac{{N_2}^2}{\mathcal{R}_2} \tag{C.13}$$

where $\mathcal{R}$ is the reluctance of the magnetic field path of the given inductor. If a symmetrical choke with 100 % coupling is assumed ($\mathcal{R}_1 = \mathcal{R}_2 = \mathcal{R};\ N_1 = N_2 = N;\ K = 1$) then from equations C.12-C.13)

$$L_{c1} = L_{c2} = L_{cm} = \frac{N^2}{\mathcal{R}} \tag{C.14}$$

A symmetrical choke with 100 % coupling produces an ideal choke as defined in section C.7.2 [**12**]. This is shown in the following section. Equations C.10-C.11 may then be written as ($\phi_1 = \phi_2 = \phi$)

$$v_1 = v_2 = N\frac{d\phi}{dt} = \frac{N^2}{\mathcal{R}}\frac{di_1}{dt} + \frac{N^2}{\mathcal{R}}\frac{di_2}{dt} \tag{C.15}$$

In the common-mode circuit of figure C.13, equation C.15 shows that in order to attenuate the CMC ($i_{com} = i_1 + i_2$) as much as possible where the coupled inductors dominate the common-mode impedance such that $v_1 \approx v_2 \approx v_{com}$, the inductors should be made with as many turns as practically possible. Considering another perspective, v_{com} determines the core magnetisation as given in equation C.15. In order to avoid saturation, as many winding turns as possible should be applied. This is the first of two design/construction requirements of the implemented chokes.

C.7.4.3 ***Ideal (Desired) CMC Choke Operation and Performance***

The ideal choke operation and performance is analysed from a differential-mode as well as a common-mode circuit perspective.

C.7.4.3.1 Differential-Mode Circuit Perspective

From a differential-mode circuit perspective, the coupled inductors are connected in anti-series such that $i_{diff} = i_1 = -i_2$ (figure C.13). Assuming an ideal choke given by equation C.14, the choke equations C.10-C.11 reduce to

$$v_1 = v_2 = 0\,\frac{di_{diff}}{dt} \tag{C.16}$$

In other words, the coupled inductors can be modelled as short-circuits. However, this assumes a symmetrical choke with 100 % coupling as given in equation C.14. If this is not the case, the coupled inductors don't cancel out completely and introduce a voltage v_{choke} in the differential-mode circuit given as

$$v_{choke} = v_1 - v_2 = \left(L_{c1}\frac{di_1}{dt} + L_{cm}\frac{di_2}{dt}\right) - \left(L_{c2}\frac{di_2}{dt} + L_{cm}\frac{di_1}{dt}\right) = (L_{c1} + L_{c2} - 2L_{cm})\frac{di_{diff}}{dt} \tag{C.17}$$

Furthermore, if the choke is non-ideal, the negative terminal of the differential-mode source v_{diff} is no longer at the same potential as the circuit zero-reference. The inductance $L_{c1} + L_{c2} - 2L_{cm}$ accounts for the differential-mode filtering of the choke as previously described.

C.7.4.3.2 Common-Mode Circuit Perspective

The purpose of a choke is to minimise any CMC so as to reduce its effect on a load. Therefore, consider the choke impedance to dominate the common-mode circuit of figure C.13 such that all other impedances are neglected. It is assumed that the choke impedance is such that any possible series resonance with the existing circuit impedance is easily compensated for by the choke impedance. The circuit reduces to coupled inductors in parallel with each other and a common-mode voltage source v_{com} as shown in figure C.14. From figure C.14 and assuming an ideal choke such that $L_{c1} = L_{c2} = L_{cm} = L$, equations C.10-C.11 reduce to

$$v_{com} = L\,\frac{di_{com}}{dt} \tag{C.18}$$

If the inductors are decoupled such that $L_{c1} = L_{c2} = L;\ L_{cm} = 0$, equation C.18 would become

$$v_{com} = \frac{L}{2}\frac{di_{com}}{dt} \tag{C.19}$$

Equations C.18-C.19 show that a CMC choke with 100 % coupling produces double the effective CMC impedance than two separate inductors [**8**,**11**,**12**].

The individual voltages v_1 and v_2 as a result of CMC i_{com} are non-zero. As a result, the negative terminal of the differential-mode source v_{diff} is no longer at the same potential as the circuit zero-reference.

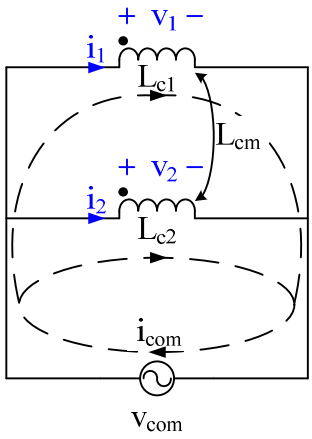

Figure C.14: Assumed CMC Choke Performance

Practically, it is impossible to develop an infinite common-mode impedance. Therefore, it is expected that an element of CMC interference will always be present (may be insignificant).

C.7.4.4 *CMC Interference Considering an Open-Circuit Load*

If Z_L is an open circuit, a CMC-induced voltage may still appear across it as a result of $Z_{2,com}$. This is shown in figure C.13 if the choke is removed. If $Z_{2,com}$ can be removed/reduced, the problem will be solved. If this is not possible, the current flowing through $Z_{2,com}$ should be reduced. Introducing an inductor in series with $Z_{2,com}$ will reduce the current; however, it will not solve the problem as the CMC-induced voltage now appears across the inductor which is in parallel with Z_L.

The problem is better solved by introducing an ideal choke as shown in figure C.13. Considering equations C.10-C.11 and that $i_1 = 0$, it can be shown that the L_{c2} component is effective in reducing i_2 as desired. Furthermore, the coupling between the two windings (L_{cm}) will induce a voltage in the upper winding equal to the voltage produced across the lower winding L_{c2} inductance by i_2. These voltages cancel in the upper loop and, therefore, only a reduced $Z_{2,com}$ voltage appears across Z_L as a result of CMC i_{com}.

C.7.4.5 *Second Design/Construction Requirement – Ideal CMC Choke Characteristic*

From a differential-mode circuit perspective, no choke filtering is desired as this is carried out by the active LPFs where required. If the chokes are ideal, they can be neglected when considering the differential-mode circuit.

From a common-mode circuit perspective, it has also been shown that an ideal choke is desired for minimising a CMC.

In conclusion, the proposed measurement system requires a choke with as close to an ideal characteristic as possible ($L_{c1} = L_{c2} = L_{cm}$). Such a choke is achieved by having two identical windings with 100 % coupling. To facilitate this from a construction perspective, the two windings are wound bifilar around a toroidal core which helps to minimise any leakage flux between the windings [**8**,**12**].

C.7.4.6 *Magnetic Saturation*

In order for the choke to be effective in blocking CMCs, it is important that the magnetic core does not saturate. This is the reason for applying as many winding turns as possible – the common-mode voltage source of figure C.13 does not saturate the magnetic core. In this way, the CMCs are also reduced.

The differential-mode current also requires consideration regarding possible core saturation. For an ideal choke (desired case) having two identical windings with 100 % coupling, the net magnetic field produced by the two windings is zero as the individual magnetic fields cancel completely. This is a consequence of the coupled inductors being connected in anti-series for a differential current as illustrated in figure C.13. As a result, the core is not saturated by a differential-mode current.

In conclusion, the proposed choke implementation should not suffer from magnetic saturation.

C.8 Measurement Circuit – Veroboard Layout

The veroboard implementation of the measurement circuit is presented in figure C.15. The lower section of the veroboard comprises the various buffer and filter circuits whereas the upper section of the board holds the frequency divider, frequency-to-voltage converters and circuit supply inputs.

Each half of a TL084CN package forms the buffer-LPF pair of a particular voltage or current measurement. The filter inputs enter the board on the left hand side with their filtered equivalents exiting to the right.

The two LM2907N − 8 frequency-to-voltage converter packages on the left are responsible for frequency-excitation measurement. The LM2907N − 8 and MB74LS73A packages on the right are involved in rotor-speed measurement.

The outer-most veroboard strips are used for the ± 15 V_{DC} and ± 5 V_{DC} supply tracks as well as the measurement circuit zero-reference. The supply voltages are re-enforced with 100 μF DC-bus capacitors with local package supplies stabilised using 10 μF capacitors.

The various input/output interfaces to/from the measurement circuit are arranged as twisted pairs/triples so as to reduce any loop self and mutual inductance [**4**,**7**]. Mutual inductance provides a possible means of magnetic interference. These twisted pairs and triples are also

connected reasonably close to their ideal connection points in order to further reduce any inductance [**4**].

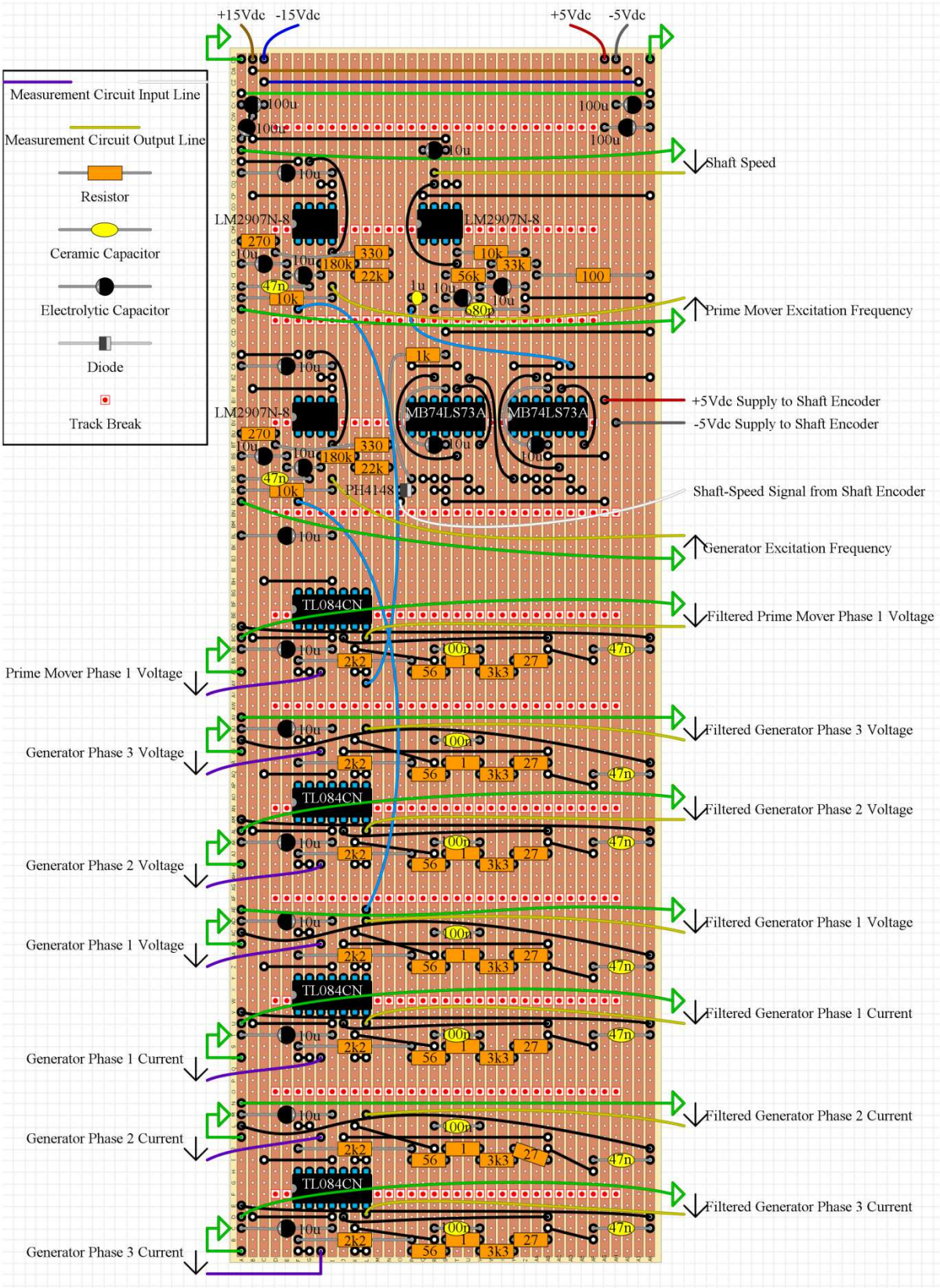

Figure C.15: Measurement Circuit – Veroboard Implementation

C.9 Equipment List

The list of required equipment is presented in table C.3:

Table C.3: Equipment List

Equipment	Additional Information
Siemens Sinamics G120 Power Converter (Prime Mover)	
Power Module (PM240)	2.2 kW; input = 3-phase AC @ 380-480 V, 50/60 Hz; FSB type; order number = 6SL3224-0BE22-2UA0
Control Unit (CU240E-2 DP)	order number = 6SL3244-0BB12-1PA1
Input Reactor	FSB type; order number = 6SL3203-0CD21-0AA0
Output Reactor	FSB type; order number = 6SL3202-0AE21-0CA0
Intelligent Operator Panel	order number = 6SL3255-0AA00-4JA0
Siemens Sinamics G120 Power Converter (Generator)	
Power Module (PM250)	5.5/7.5 kW; input = 3-phase AC @ 380-480 V, 50/60 Hz; FSC type; order number = 6SL3225-0BE25-5AA1
Control Unit (CU240E-2 DP)	order number = 6SL3244-0BB12-1PA1
Output Reactor	FSD type; order number = 6SE6400-3TC05-4DD0
Intelligent Operator Panel	order number = 6SL3255-0AA00-4JA0
2X Four-Pole Squirrel-Cage Induction Machine (Actom Low Voltage Motor)	2.2 kW; input = 3-phase AC @ 400 V, 4.89 A, 50 Hz, power factor = 0.79; 1420 rpm; y-connected; type = LS4101-4AU
Hengstler Shaft Encoder (RS58-O/5000EK.42KB)	Supply = 10-30 V_{DC}; 5000 ppr
Magtrol In-Line Torque Transducer – TMB 212	Rated torque = 200 N.m; rated speed = 4000 rpm; torque sensitivity = 25 $mV.N^{-1}.m^{-1}$; supply = 20-32 V_{DC}
3X Topward Dual-Tracking DC Power Supply (6303D)	
Agilent 20MHz Function / Arbitrary Waveform Generator (33220A)	
2X Tektronix TDS 3034B – Four Channel Color Digital Phosphor Oscilloscope	300 MHz; 2.5 GS/s
4X Tektronix P2221 Voltage Probe	(200 MHz, 10 MΩ, 16 pF, 10X / 6 MHz, 1 MΩ, 95 pF, 1X)
4X Tektronix P2220 Voltage Probe	(200 MHz, 10 MΩ, 16 pF, 10X / 6 MHz, 1 MΩ, 95 pF, 1X)

Tektronix TDS 2002B – Two Channel Digital Storage Oscilloscope	60 MHz; 1 GS/s
2X Tektronix P2220 Voltage Probe	(200 MHz, 10 MΩ, 16 pF, 10X / 6 MHz, 1 MΩ, 95 pF, 1X)
3X Elditest Electronic Differential Probe (GE8115)	30 MHz Bandwidth; > 50 dB CMRR (1 MHz)
3X AC/DC Dynamics Current Transformer (DS101 10T)	2.5 VA, 660 V, 50/60 Hz; ratio = 10:1 A; class = 1; 20 mm ring
Voltage Transformer	

C.10 Conclusion

The design and implementation of the measurement system for the experimental testing of a SCIG as proposed in chapters 1 and 3 is presented. Of particular focus is:

- The buffer and LFP circuitry for voltage and current measurement
- The frequency-to-voltage converters for excitation-frequency measurement
- The shaft encoder, frequency divider and frequency-to-voltage for rotor speed measurement
- The inline torque sensor for input prime-mover torque measurement

Care is taken to reduce the effects of EMI on the measurement system. Of particular importance is the CMC interference produced by the power converters. CMC chokes constitute the main form of protection against this interference.

The measurement circuit layout (veroboard) is presented together with the experimental equipment list.

C.11 References

[1] Kugelstadt T., "Active Filter Design Techniques," in *Op Amps For Everyone - Design Reference*, Mancini R., Ed.: Texas Instruments, 2002, ch. 16, pp. 16.1-16.64.

[2] National Semiconductor. (1976, June) LM2907 Tachometer/Speed Switch Building Block Applications - Application Note 162. [Online]. Available at: http://www.ti.com/lit/an/snaa088/snaa088.pdf, Last accessed: 3 May 2014

[3] National Semiconductor. (2003, May) LM2907/LM2917 Frequency to Voltage Converter. [Online]. Available at: http://pdf.datasheetcatalog.com/datasheet2/0/01gcjjplyzka2uqqx3846g9ri17y.pdf, Last accessed: 3 May 2014

[4] Hofsajer I., Personal Communication.

[5] Jain R. P., *Modern Digital Electronics*, 1st ed. New York, United States of America: McGraw-Hill, 2008.

[6] Magtrol, Inc. (2011, June) TM 300 Series In-Line Torque Transducers - User's Manual. [Online]. Available at: http://www.magtrol.com/manuals/tm300manual.pdf, Last accessed: 13 April 2014

[7] Ott H. W., *Electromagnetic Compatability Engineering*. Hoboken, United States of America: John Wiley & Sons, 2009.

[8] Mardiguian M., *EMI Troubleshooting Techniques*. United States of America: McGraw-Hill, 2000.

[9] Goedbloed J. J., *Electromagnetic Compatability*. Hertfordshire, England: Prentice Hall, 1992.

[10] Vasilescu G., *Electronic Noise and Interfering Signals: Principles and Applications*. Berlin, Germany: Springer, 2005.

[11] Murata Manufacturing Co., Ltd. Other Filters - Differential and Common Mode Noise. [Online]. Available at: http://www.murata.com/products/emc/knowhow/pdf/26to30.pdf, Last accessed: 5 May 2014

[12] Paul C. R., *Introduction to Electromagnetic Compatability*, 2nd ed., Chang K., Ed. Hoboken, New Jersey: John Wiley & Sons, 2006.

[13] Shih F. Y., Chen D. Y., Wu Y. P., and Chen Y. T., "A Procedure for Designing EMI Filters for AC Line Applications," *IEEE Transactions on Power Electronics*, vol. 11, no. 1, pp. 170-181, January 1996.

[14] Serrao V., Lidozzi A., Solero L., and Di Napoli A., "Common and Differential Mode EMI Filters for Power Electronics," in *International Symposium on Power Electronics, Electrical Drives, Automation and Motion*, 2008, pp. 918-923.

[15] Hengstler. Incremental Shaft Encoder Type RI 58 / RI 59 Installation Instructions. [Online]. Available at: http://www.jdhengstler.co.uk/downloads/RI58%20CONNECTION%20DETAILS.pdf, Last accessed: 13 April 2014

[16] Roc'h A. and Leferink F., "In Situ Performances of Common Mode Chokes," in *10th International Symposium on Electromagnetic Compatability*, York, 2011, pp. 494-499.

D. Measurement System Calibration

D.1 Introduction

This note details the unit testing and calibration of the measurement system adopted in chapter 3 and appendix C. The testing and calibration includes:

- CTs, VT and DVPs – magnitude and phase error
- Buffer and LPF circuits – frequency response and output offsets
- Frequency divider – frequency division
- Frequency-to-voltage converters – linearity and dynamic response
- Inline torque sensor – frequency response
- CMC chokes – differential-mode and common-mode impedance to low and high frequencies
- Oscilloscope resolution

The purpose of calibrating the measurement circuit is to quantify any difference between the actual quantity and its measured equivalent as a result of measurement errors/non-idealities. In this process, any differences can be reversed when the measured results of various tests are analysed.

D.2 CT, VT and DVP

The CTs, VT and DVPs are calibrated using a single-phase system where a $165\ V_{RMS}, 50\ Hz$ sinusoidal source excites a $402.8\ \Omega$ resistive load. The DVP is assumed to be the reference measurement device from which the CTs and VT can be assessed. Each CT-Choke-$1\ \Omega$-resistor combination is tested with a DVP load-voltage measurement for comparison. A VT voltage measurement is then taken simultaneously with a DVP voltage measurement for VT evaluation.

D.2.1 CT Calibration Results

All three CT combinations produced a leading current waveform relative to the voltage waveform measured by the DVP. The leading times are given in table D.1 below together with their angle equivalents. This implies a capacitive load which is unexpected. If anything, a slightly inductive load could be expected. The leading current angle is seen to be affected by the mechanical connections to the transformer secondary winding; the values in table D.1 are stated as worst-case approximations.

Table D.1 also includes the actual current amplitudes measured by the different CT combinations. For the given single-phase system, a current of $410\ mA_{RMS}$ is expected. The results of table 3.3 are close enough for the purpose of the measurement system (maximum error of $9\ \%$). Slight measurement inaccuracies are expected as a result of system non-idealities including the $1\ \Omega$ resistor tolerance ($5\ \%$).

Current measurement is taken directly across the $1\ \Omega$ resistor and not across the CT output so as to not include the voltage drop across choke winding resistance.

Table D.1: CT Sinusoidal Performance

	CT 1 (I1)	**CT 2 (I2)**	**CT 3 (I3)**
Leading Phase Introduced in Current Measurement (μs)	128	220	200
Leading Phase Introduced in Current Measurement (Deg)	2.3	3.96	3.6
Current Amplitude (mA_{RMS})	438	451	436

D.2.2 VT Calibration Results

VT-measurement is evaluated by comparing the single-phase load voltage as measured by both the VT and DVP. It is found that the VT voltage waveform lags the DVP voltage waveform by $40\ \mu s$ or $0.72°$. The VT output voltage has an amplitude of $4.10\ V_{RMS}$; considering the scaling ratio of $40:1$, this translates into a measured voltage of $164\ V_{RMS}$. Therefore, there is a good agreement between VT and DVP sinusoidal-voltage measurement.

D.2.3 Final Remarks

The CTs and VTs are not able to measure DC excitation components. This is no limitation to the measurement system as DC components are not expected.

For the purpose of the measurements required in this dissertation, $100\ \%$ accuracy is not a necessity. The CTs, VT and DVPs are assumed to be ideal with their outputs related to their inputs by scaling ratios of $10:1, 40:1$ and $1000:1$ respectively. However, there is room for improvement in the CT current measurement.

D.3 Buffer and LPF Circuits

D.3.1 Frequency Response

The active filters are calibrated by applying a sinusoidal voltage to each filter input via the corresponding buffer circuit and measuring both input and output signals for attenuation and phase difference. This is done for frequencies of $70\ Hz, 800\ Hz$ and $4\ kHz$. The results are given in table D.2 and compared to their theoretical design equivalents. V_4 represents the filter corresponding to the prime-mover phase-voltage measurement.

From the table of results it is observed that all active filters perform similarly and close to the designed characteristic for a frequency of $70\ Hz$. There is no amplitude attenuation for frequencies around $70\ Hz$ which are the frequencies of interest. Since the introduced phase delay is common to all filters at $70\ Hz$, voltage and current can be multiplied without adjustment when calculating electrical power. A phase delay of $6.5°$ at a frequency of $70\ Hz$ is equivalent to a time delay of $0.3\ ms$. Since the system mechanical dynamics are expected

to be relatively slow, this time delay is neglected. The frequency measurements will include this delay as they rely on voltage measurement, however, a time delay of 0.3 ms is insignificant when compared with that inherent in the frequency measurement.

For the higher frequencies of 800 Hz and 4 kHz, the filter performance is generally common to all filters and similar to the theoretical performance. Difference in attenuation and phase between filters for higher frequencies is not serious as these undesired frequencies are filtered from the desired signal.

Table D.2: Active Filter Performance – Attenuation and Phase

Filter		**I1**	**I2**	**I3**	**V1**	**V2**	**V3**	**V4**	**Designed Filter**
70 Hz	**Attenuation (dB)**	0	0	0	0	0	0	0	0.0012
	Phase (Deg)	-6.4	-6.3	-6.5	-6.5	-6.4	-6.4	-6.4	-6.629
800 Hz	**Attenuation (dB)**	-2.3	-2.7	-2.3	-2.3	-2.3	-2.1	-2.3	-2.435
	Phase (Deg)	-81.8	-83.5	-85.3	-82.9	-76	-77.2	-78.9	-85.31
4 KHz	**Attenuation (dB)**	-25.5	-26.2	-26.3	-26	-24.6	-25.1	-25.2	-
	Phase (Deg)	-159.8	-146.9	-161.3	-162.7	-158.4	-161.3	-159.8	-

An example of the filter input/output attenuation for a logarithmic frequency sweep of 50 Hz – 4 kHz (with a sweep time of 50 ms) is presented in figure D.1. This figure illustrates the low-pass nature of the filter.

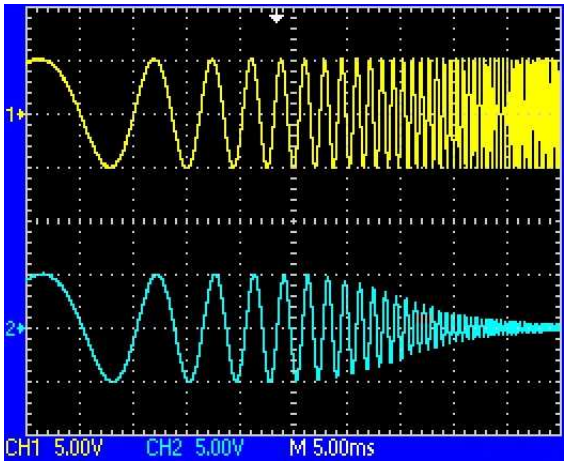

Figure D.1: Active Filter Low-Pass Characteristic

D.3.2 DC Offset

In order to quantify a possible DC offset introduced into the measurements by the active filters, each filter output is measured with the input (to the corresponding buffer circuit) short-circuited. The results are presented in table D.3. Considering the scaling ratios of the CTs, VT and DVPs, the effect of the introduced offset on the measurement is also given in table D.3. Comparing these effects to the rated induction machine line values of $4.89\ A_{RMS}$ and $400\ V_{RMS}$, they may be neglected.

Table D.3: Active Filter Performance – DC Offset Introduced

Filter		**I1**	**I2**	**I3**	**V1**	**V2**	**V3**	**V4**
Short-Circuit Test	**Input (mV_{DC})**	0	0	0	0	0	0	0
	Output i.e. Offset (mV_{DC})	6	6	6	2	2	-6	2
	Offset Affect on Measurement (Scaling Ratio)	0.06 A	0.06 A	0.06 A	2 V	2 V	-6 V	0.08 V

D.3.3 Final Remarks

From the results and analysis presented thus far, it can be concluded that the buffers and active filters have no significant undesired effect on the measurements that they facilitate. Therefore, their measurements are used without correction.

D.4 Frequency Divider for Rotor Speed Measurement (Shaft-Encoder Interface)

Performance of the frequency divider implementation is verified by driving it with a $\pm 5\ V$, $175\ kHz$ square wave. The diode D_1 included in figure C.7 is effective in blocking the negative half-cycle of the input signal as required. The $1\ \mu F$ capacitor C_5 following the flip-flop Integrated Circuits (ICs) also shown in figure C.7 is effective in blocking DC before the corresponding frequency-to-voltage converter.

Channel 1 and 2 of figure D.2 show the waveforms before the diode and after the capacitor respectively. The frequency of $175\ kHz$ is reduced by a factor of 16 for an output frequency of $10937.5\ Hz$. Any voltage level reduction is irrelevant as the signal frequency is what contains information about the rotor speed – provided that the voltage levels are sufficient to trigger the following frequency-to-voltage converter. The voltage levels given in figure D.2 are expected for all rotor speed values as they are only dependent on the various supply voltages.

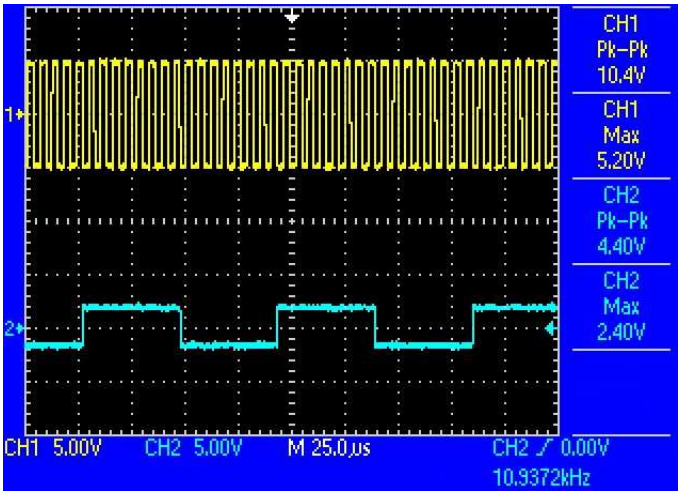

Figure D.2: Frequency Divider – Output versus Input

D.5 Frequency-to-Voltage Converters

Calibration of the frequency-to-voltage converters is important in order to establish input/output linearity and, in so doing, develop equations relating the output voltage to the input frequency. The converter dynamic response to a varying input frequency is also desired.

D.5.1 Input/Output Relationship (Linearity)

In order to establish linearity and frequency-to-voltage equations, the converters measuring excitation frequency are excited with sinusoidal frequencies of $0\ \text{Hz}, 10\ \text{Hz}, 70\ \text{Hz}$ and a frequency for which the converter output voltage is $10\ V_{DC}$. The converter associated with the shaft encoder undergoes the same analysis except for frequencies of $0\ \text{Hz}, 5.5\ \text{kHz}, 11\ \text{kHz}$ and a frequency for which the output voltage is $10\ V_{DC}$. The results are presented in figures D.3 and D.4 respectively. The figures include the equations for the best-fit linear approximations of the measured results. For practical purposes, the converters of figure D.3 are assumed to be identical.

Assuming that non-zero y-intercepts are negligible, the excitation frequency and rotor speed (in rpm) can be recovered from the output voltage of the corresponding converters using equations D.1 and D.2 respectively:

$$excitation\ frequency = 9 \times measurement\ output \tag{D.1}$$

$$rotor\ speed = 237.12 \times measurement\ output \tag{D.2}$$

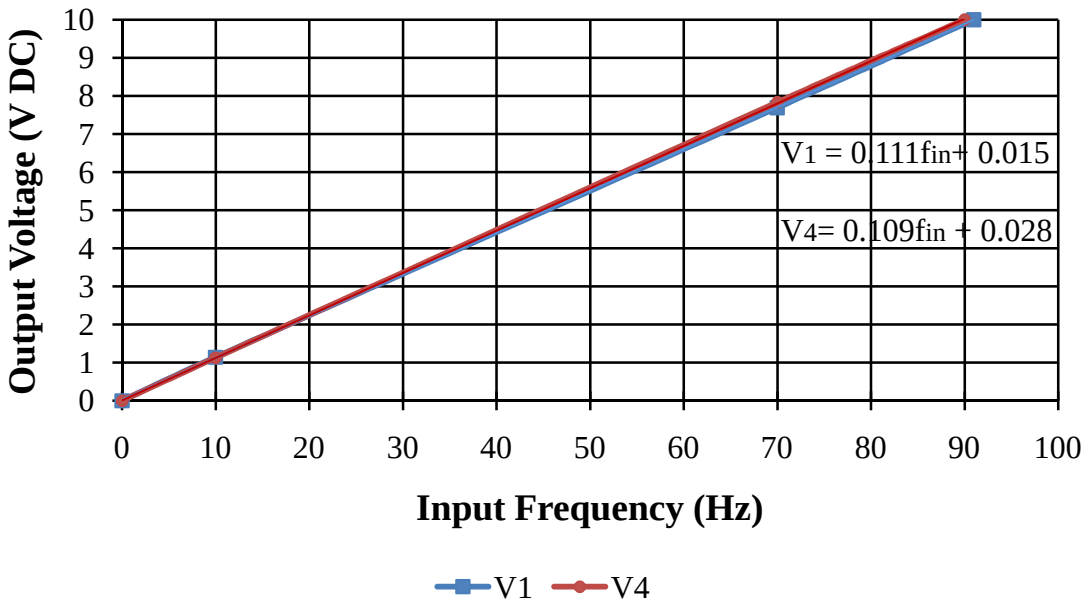

Figure D.3: V_1 (Generator) and V_4 (Prime-Mover) Frequency-to-Voltage Converters – Input/Output Relationship

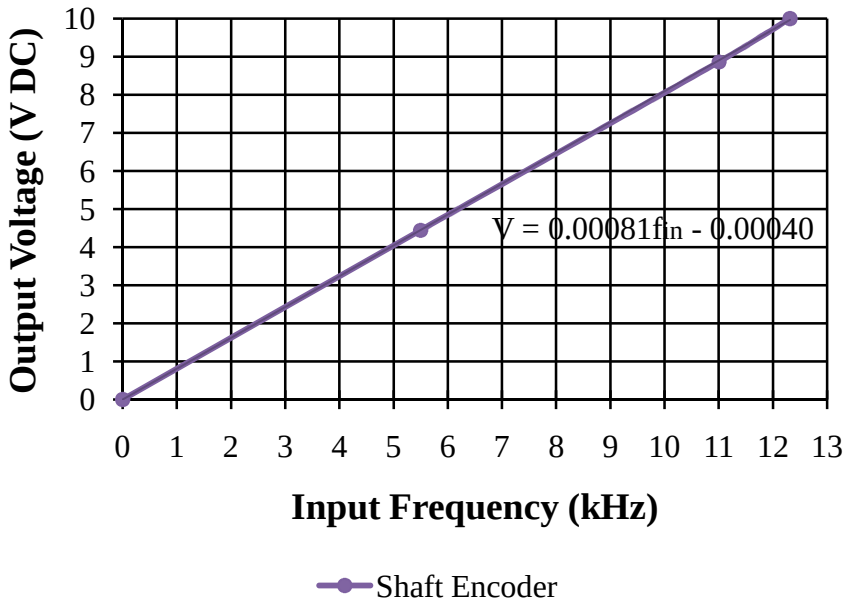

Figure D.4: Shaft-Encoder Frequency-to-Voltage Converter – Input/Output Relationship

D.5.2 Converter Dynamic Response

The measurement response to a varying rotor speed and generator/prime-mover excitation frequency is now considered. This is achieved by considering the attenuation and delay introduced in the measurement [**1**]. Rotor-speed and excitation-frequency measurement is achieved by means of a frequency measurement with a corresponding output voltage. The attenuation for a given oscillating (sinusoidal variation) rotor speed or excitation frequency (in dB) is given by considering the actual sinusoidal voltage output from the frequency-to-voltage converter as a fraction of the un-attenuated sinusoidal voltage output as given by the

steady-state equations D.1-D.2. This is repeated for different oscillation frequencies to produce the measured results of figure D.5.

The delay introduced for a given oscillating rotor speed or excitation frequency is obtained by considering the phase difference between the sinusoidally-varying input rotor speed or excitation frequency and the sinusoidal output voltage. The delay introduced for different oscillation frequencies is given by the measured results of figure D.6.

The speed-measurement results of figures D.5-D.6 include the dynamics of the frequency divider before the frequency-to-voltage converter of figure C.7. This is done because the previous calibration of the frequency-divider is a steady-state/constant rotor-speed calibration.

The frequency responses of figures D.5-D.6 approximate that of a first-order low-pass filter. The corresponding theoretical responses are also given in these figures. The rotor-speed, generator excitation-frequency and prime-mover excitation-frequency measurements have -3 dB cut-off frequencies of 0.34 Hz, 0.147 Hz and 0.153 Hz respectively. These cut-off frequencies translate into sinusoids with periods of 3 s, 7 s and 7 s respectively. As expected, the frequency-measurement converters have a similar dynamic response.

From the frequency-response results of figures D.5-D.6, the speed and excitation-frequency measurement may require amplitude/phase correction depending on the dynamics tested.

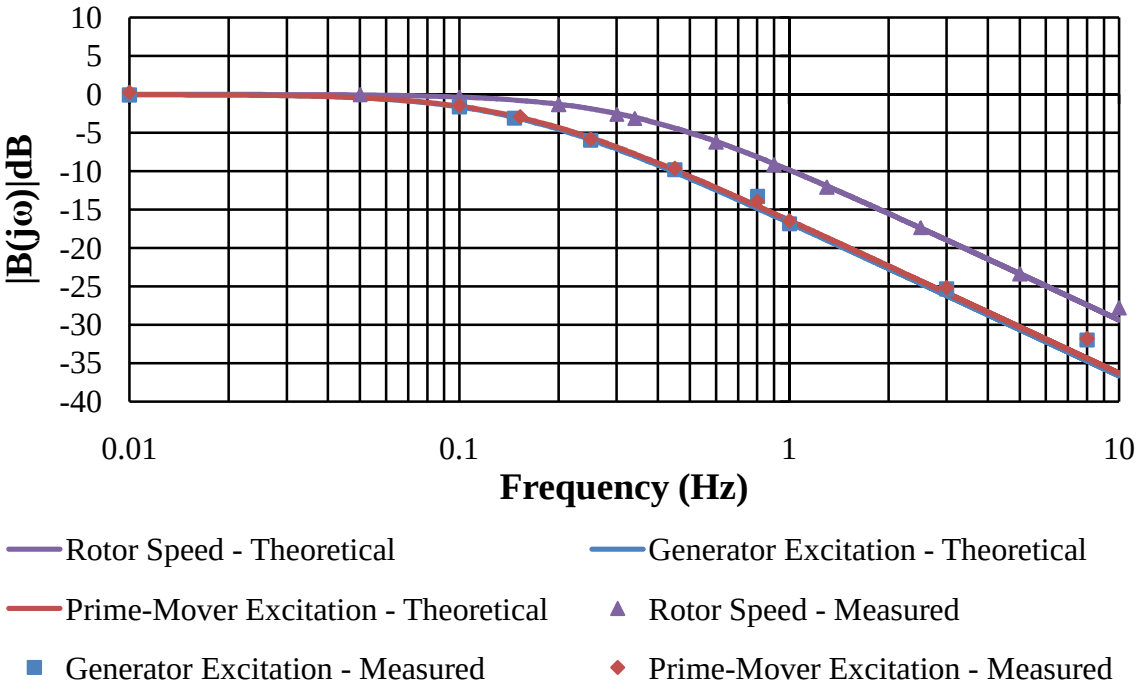

Figure D.5: Frequency-to-Voltage Converter Frequency Response – Bode Modulus

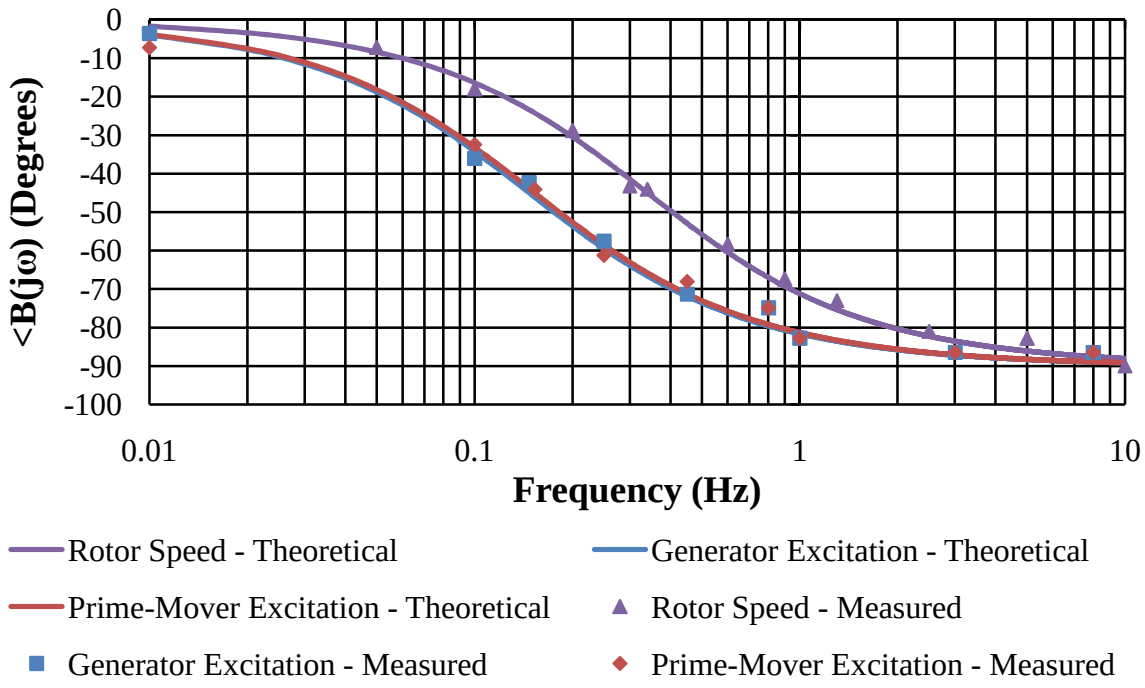

Figure D.6: Frequency-to-Voltage Converter Frequency Response – Bode Phase

D.6 Inline Torque Transducer

The torque transducer has a built-in filter based on a second-order low-pass Butterworth characteristic [**2**]. 1 kHz is the chosen −3 dB cut-off frequency for the experimental testing. Based on this selection, the frequency-phase response is as presented in figures D.7 below – the attenuation is negligible over the considered frequency range. As shown in this figure, the phase delay introduced is also negligible. Therefore, the torque measurement requires no correction after measurement.

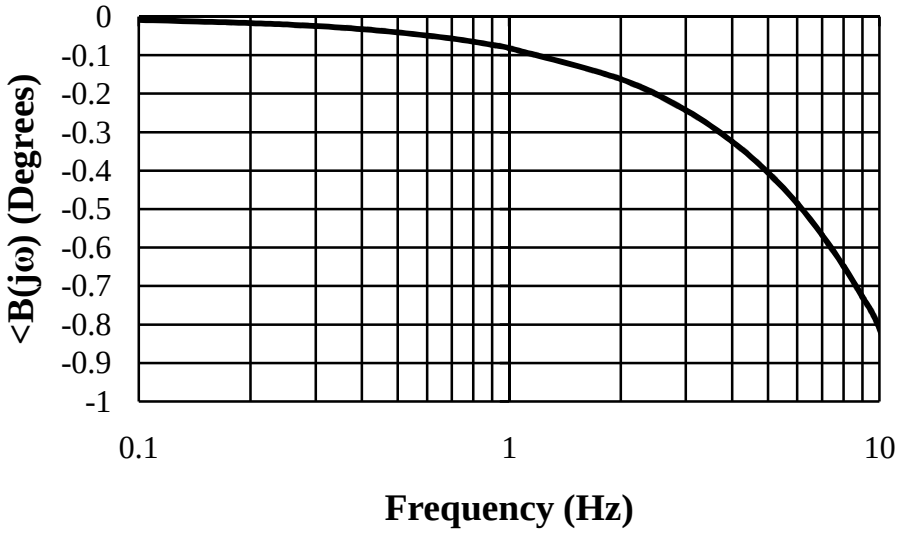

Figure D.7: Torque Measurement Frequency Response – Bode Phase

Based on the transducer sensitivity of $0.025\,\mathrm{V.N^{-1}.m^{-1}}$, the prime-mover torque is recovered from the transducer output voltage using equation

$$\tau_{pm} = prime\ mover\ torque = \frac{1}{0.025} \times measurement\ output \quad \text{(D.3)}$$

D.7 CMC Choke Characterisation

As mentioned in appendix C, it is desired that the CMC chokes operate as close to their ideal characteristic as possible. This involves having a negligible effect on the differential-mode current but producing a high inductive impedance to CMCs [**3**,**4**,**5**,**6**]. Tests regarding choke operation are focused at evaluating such performance characteristics. The following analysis involves the two-conductor chokes used in the voltage and current measurements where the load is either an open circuit (buffer input) or a $1\,\Omega$ resistor.

Choke characterisation is based on a frequency-dependent measurement and analysis. This involves effective differential-mode and common-mode impedance measurements for a frequency sweep of $20\,\mathrm{Hz} - 2\mathrm{MHz}$. In this way, the effects of parasitic capacitance, hysteresis and eddy-current losses are considered [**3**,**4**,**6**,**7**,**8**]. The high-frequency range considers the fact that the large common-mode inductive impedance is being shunted by a lower impedance path produced by the parasitic intra-winding capacitance [**3**]. This choke evaluation merely provides an indication of the expected performance as the choke/system interaction is not considered [**8**,**9**,**10**]. The interaction of the choke with the external system may result in poor CMC filtering over a certain frequency range. An example of this is a series resonance of a choke inductance with a system capacitance (parasitic or not) [**8**,**10**]. Therefore, final choke testing must involve checking for the effects of CMCs in the outputs of the measurement circuit.

Various choke impedances are measured with an Agilent E4980A Precision LCR Meter fitted with a 16047E test fixture. Any inductance-resistance (impedance) measurements are taken as a series inductor-resistor equivalent. A discussion regarding the appropriate equivalent circuit model for a given impedance measurement is presented in [**11**].

D.7.1 Differential-Mode Impedance

The differential-mode choke impedance magnitude and angle as a function of frequency is presented in figures D.8 and D.9 respectively. This impedance is measured by connecting the choke windings in anti-series for different differential-mode current values.

The following analysis assumes a differential-mode current is present as is the case for phase-current measurements where the measurement circuit load is effectively a $1\,\Omega$ resistor. However, load presented in the case of phase-voltage measurement is the open-circuit buffer input impedance. No differential-mode current is expected and the following analysis is unnecessary.

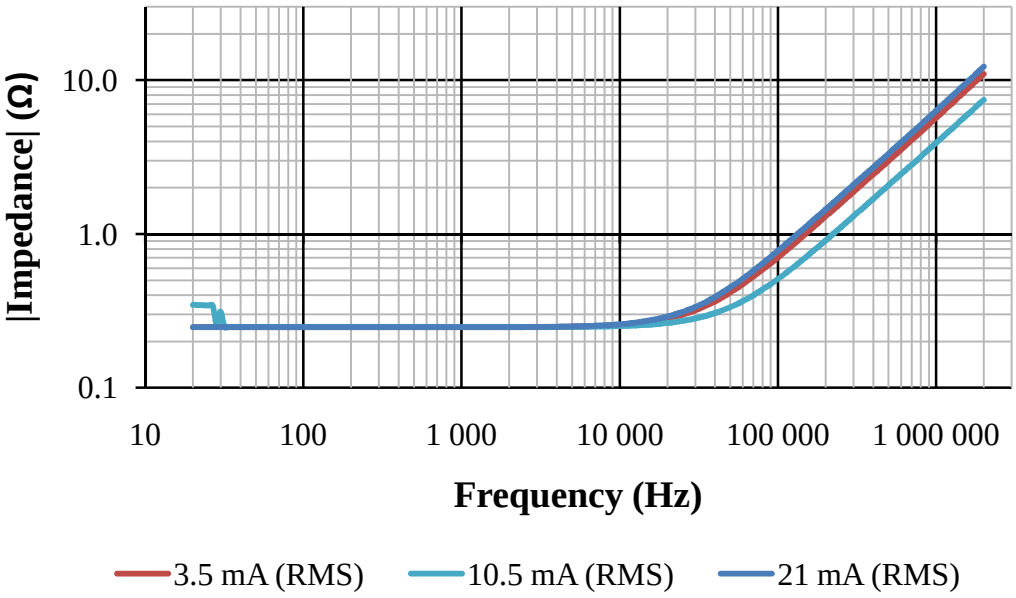

Figure D.8: Differential-Mode Choke Impedance (Magnitude) versus Frequency

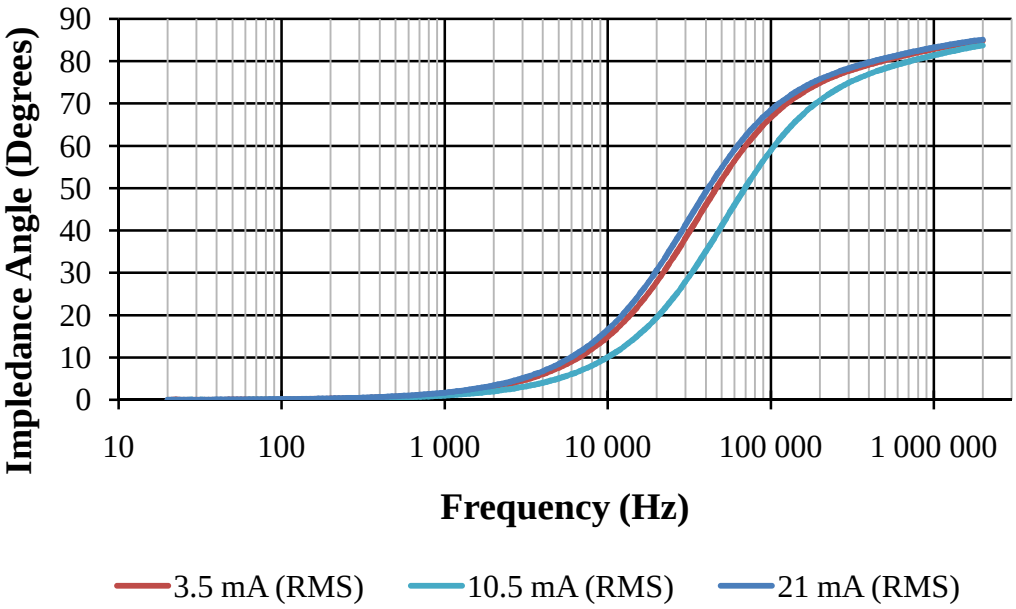

Figure D.9: Differential-Mode Choke Impedance (Angle) versus Frequency

D.7.1.1 ***Low Frequencies***

For low frequencies, the differential-mode impedance is low and is attributed to the DC winding resistance as shown by a zero impedance angle in figure D.9. The impedance is constant with a zero reactive component as a function of current excitation. These two observations support the notion of an ideal choke with no core magnetisation as a result of a differential-mode current (zero differential-mode inductance since there is a zero net magnetic field). The effective differential-mode resistance is constant versus frequency and current which implies that core losses such as hysteresis are not present. This further supports the notion that the core is not being magnetised.

These results are as expected. As already mentioned, the two windings have the same turn count and are wound bifilar around the toroidal magnetic core [**6**,**12**]. Based on this geometry, two identical windings with $\approx 100\,\%$ coupling are expected as both windings occupy the same point in space [**6**].

D.7.1.2 *High Frequencies*

In the case of high frequencies, parasitic effects such as intra-winding capacitance provide alternative current paths such that a net differential-mode flux is produced. This net flux is associated with the inductive impedance for frequencies above 10 KHz as shown in figures D.8-D.9.

Figure D.8 shows an impedance magnitude that varies linearly with frequency for high frequencies. This may indicate that the net magnetic flux is produced in air where the core frequency-based non-linearity doesn't affect the effective differential-mode impedance [**8**]. Either this is the case or the core non-linearity as a function of frequency is negligible. This is especially true for frequencies above 100 KHz in figures D.8-D.9 where the impedance angle is approaching 90° and the impedance is almost exactly a function of effective inductance and frequency. A mostly reactive impedance with a relatively small resistive component supports the notion of any generated flux being contained in an "air-core" and not in the magnetic core. Otherwise hysteresis loss would develop a noticeable resistive component.

One observation that does question the proposed location of the magnetic flux is the impedance dependence on current excitation where slight core non-linearity has an effect. Perhaps there is a combination of core-based and air-based magnetic flux.

Non-negligible inductive impedance for high frequencies implies that the choke is not ideal for these frequencies. However, this is actually beneficial as these filtered differential-mode frequencies are undesirable and are also filtered by the following active LPF anyway. The choke low-pass impedance profile is desirable and qualitatively matches the profile of the following active filter.

One question that remains is whether the high-frequency differential-mode currents saturate the core in the case of phase-current measurement, thus, reducing choke effectiveness against CMCs. Such core saturation is unlikely:

- As previously mentioned, it is likely that magnetic flux produced by high-frequency differential-mode currents is distributed between the choke's core and the surrounding air.
- High-frequency differential-mode currents are not expected as high-frequency components in SCIG phase currents are not present. This is a consequence of the inductive nature of an induction machine.

D.7.1.3 ***Final Remarks***

In summary, the two-conductor chokes used in phase-voltage and phase-current measurement are expected to perform suitably from a differential-mode perspective.

D.7.2 Common-Mode Impedance

The effective common-mode impedance as measured by connecting the choke windings in parallel (dot-terminals connected together) is given in figures D.10-D.11. From figure D.10, the common-mode impedance increases with frequency as desired. A small impedance for low frequencies is not a concern as the CMCs are expected to be high-frequency in nature.

The effective inductance and resistance components of the measured impedance are given in figures D.12 and D.13 respectively. These figures do not represent modelled components at high frequencies, since they do not consider the complete model including parasitic capacitance which is not negligible at these frequencies [**10**].

The CMC is expected to be relatively small after choke inclusion. Therefore, the impedance measurements of figures D.10-D.13 are carried out for a low CMC ($i_{com} = 3.5\ \mathrm{mA_{RMS}}$).

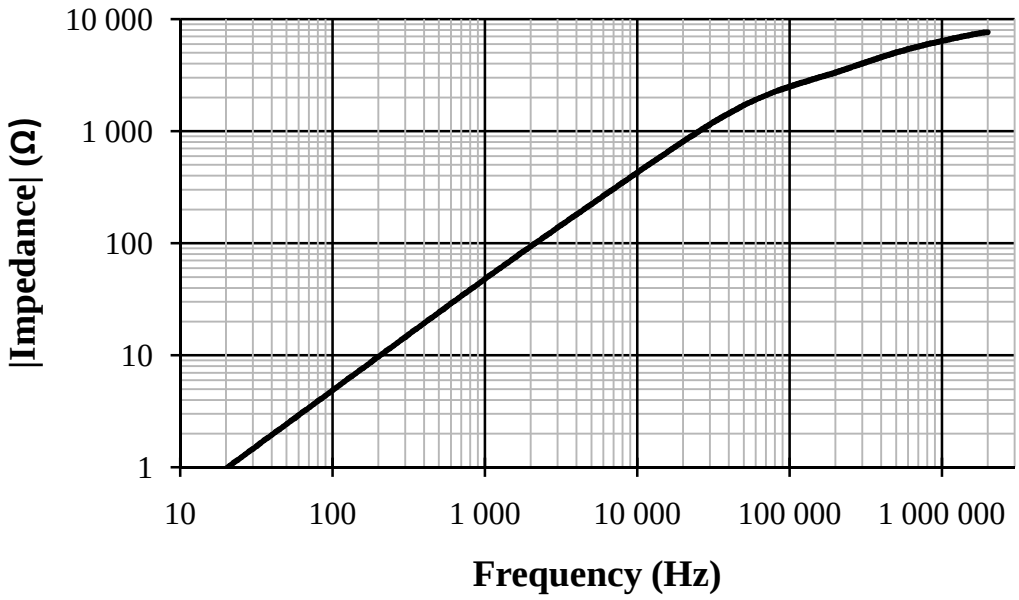

Figure D.10: Common-Mode Choke Impedance (Magnitude) versus Frequency

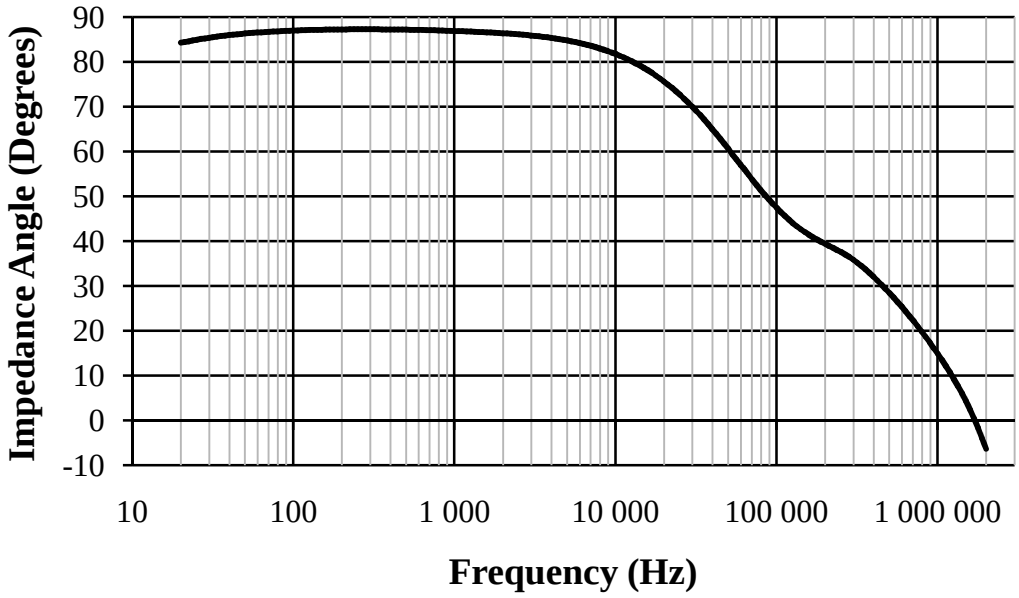

Figure D.11: Common-Mode Choke Impedance (Angle) versus Frequency

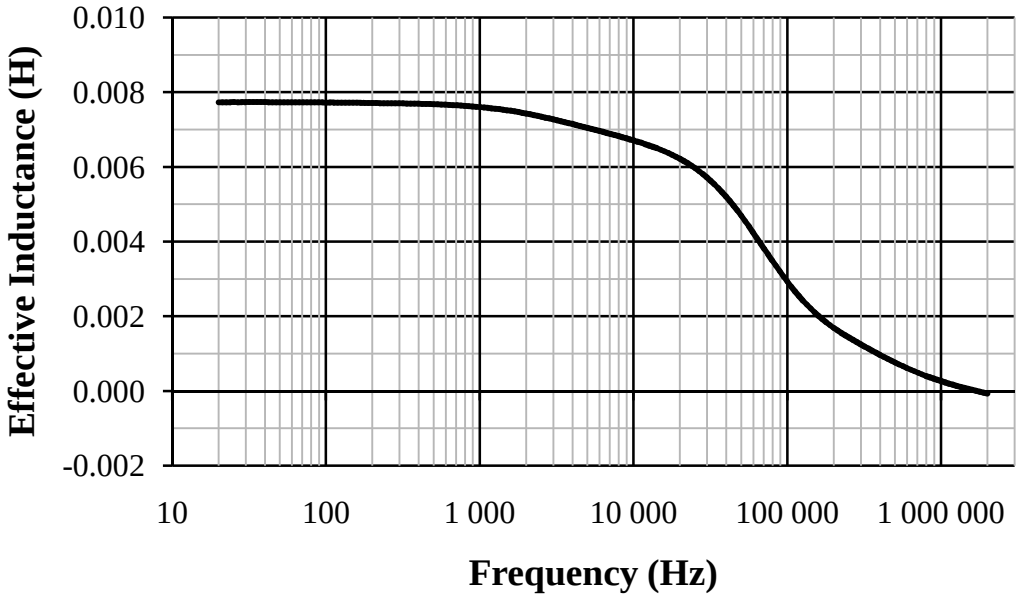

Figure D.12: Effective Common-Mode Choke Inductance versus Frequency

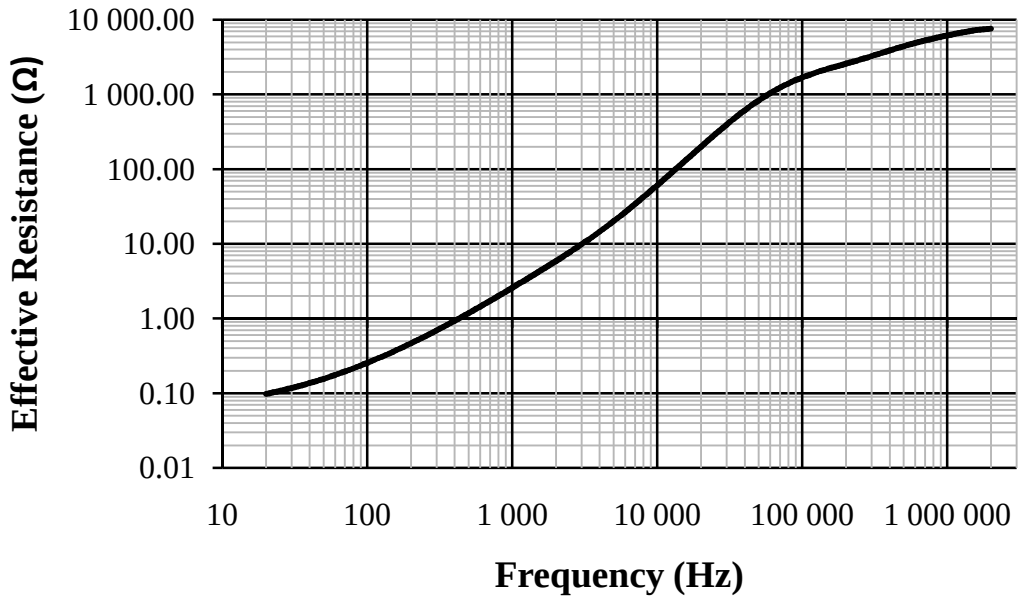

Figure D.13: Effective Common-Mode Choke Resistance versus Frequency

D.7.2.1 ***Low Frequencies***

From figure D.11, it is observed that the choke is effectively an inductor for low frequencies. This is desired according to the analysis in section C.7.4.3.2. The effective inductance is also approximately constant as shown in figure D.12. This implies that the parasitic intra-winding capacitance is negligible for these frequencies as expected. The effective resistance (relatively small compared to the effective reactance) increases with increasing frequency over the low-frequency region. This is expected and is a consequence of increasing choke loss as a result of magnetic hysteresis.

If the upper-limit of the low-frequency region is defined as the point where choke behaviour deviates from that expected/desired, then, from figures D.11-D.12, the low-frequency upper limit is approximately $10\,\text{kHz}$. This corresponds to the low-frequency region of the differential-mode impedance analysis. Based on this comparison, the increase in effective resistance of figure D.13 over the low-frequency region is probably not a consequence of the skin effect in the choke windings. Otherwise, this increasing resistance would be observed in the impedance profile of figure D.8. Therefore, the increasing resistance of figure D.13 is a consequence of magnetic hysteresis which is not present in figure D.8 since the magnetic core is not magnetised.

The choke behaves as desired over the low-frequency range; it is effectively an inductor. This analysis is based on a load $Z_L \neq \infty\,\Omega$ in figure C.13. Since the low-frequency differential-mode performance shows a symmetrical choke with $\approx 100\,\%$ coupling, the desired common-mode choke behaviour is also expected for low frequencies where $Z_L = \infty\,\Omega$ as discussed in section C.7.4.4.

D.7.2.2 *High Frequencies*

It is important to note that there is no distinctive inductive-capacitive resonance observable in figure D.10 which is typical of an inductor at high frequencies [**11**]. This is strange since there is definitely a shift from an inductive characteristic to a capacitive characteristic as given by the change in phase angle in figure D.11 between 1 MHz and 2 MHz [**11**]. The changing impedance angle is also observed in the decreasing effective inductance profile of figure D.12 which eventually becomes negative [**11**].

Resonance is not observed in figure D.10 because the resistive component is dominating the impedance as shown in figure D.13. Furthermore, the impedance angle doesn't instantaneously transition from 90° lagging to 90° leading. The resistive component is maintaining a desirable impedance profile for high frequencies with their energy being dissipated as heat [**4**,**10**]. The reason for this resistive component is not known exactly and could be a result of magnetic hysteresis and/or increased winding resistance due to the skin effect.

For phase-current measurement the choke load is a 1 Ω resistor. The large resistive choke impedance at high frequencies reduces the CMC i_{com} and, therefore, its voltage drop across the 1 Ω resistor also decreases as desired.

The effect of a common-mode voltage source on an open-circuit load is discussed in section C.7.4.4. This is applicable in the case of phase-voltage measurement where the choke load is given by the buffer input impedance. Based on the analysis of section C.7.4.4 a choke which functions more like a resistor than a set of coupled inductors may not be effective in decreasing the effect of the common-mode voltage source on the open-circuit load. Since the frequencies (and their magnitudes) produced by the common-mode voltage source have not been quantified, it is difficult to anticipate the choke common-mode performance for an open-circuit load. In this case, choke performance is evaluated by the presence/absence of CMC effects in the measurement circuit outputs.

D.7.3 Overall CMC Choke Performance

The investigation into choke performance must include a complete measurement-circuit evaluation with the chokes included. This is required as the choke/system interaction needs to be considered [**8**,**9**,**10**]. Such an evaluation also proves whether the choke common-mode impedance is sufficient while qualifying the high-frequency common-mode performance with an open-circuit load. Based on the measured results produced by the measurement circuit, the chokes perform suitably – negligible CMC effects are observed. According to this evaluation, the other multi-conductor chokes used in the measurement system also perform as required.

D.8 Oscilloscope Resolution as a Source of Measurement Error

An important source of measurement error is the digital measurement of an analogue signal by an oscilloscope. The Tektronix TDS 2002B and Tektronix TDS 3034B oscilloscopes have

a vertical resolution of 8 bits and 9 bits respectively [**13**,**14**]. Approximate measurement errors are given in tables D.4 and D.5 respectively while showing which variables are measured on which oscilloscopes. The errors are approximate since:

- It is assumed that the each oscilloscope uses the entire decimal range of its digitizers.
- The equivalent voltage resolution of a given measurement is dependent on the voltage range accommodated by the oscilloscope. This is variable by adjusting the "volts-per-division" setting for each oscilloscope channel. The resolution errors of tables D.4-D.5 are based on the "volts-per-division" settings used in the experimental measurements of chapter 5 (all probes always have an attenuation of 1 ×).

Measurement error as a result of oscilloscope resolution is amplified by the various scaling factors converting a voltage measurement into the required speed (rpm) etc. measurement. The error amplification is also given in these tables.

Table D.4: Tektronix TDS 2002B Oscilloscope – Measurement Resolution

Measurement	V/Division	Resolution (V)	Resolution (Correct Units)
Prime-Mover Stator Frequency	2	0.0627	0.5647 Hz
Rotor Speed	2	0.0627	14.8781 rpm
Prime-Mover Torque	0.2	0.0063	0.2510 N.m

Table D.5: Tektronix TDS 3034B Oscilloscope – Measurement Resolution

Measurement	V/Division	Resolution (V)	Resolution (Correct Units)
SCIG Voltage	0.1	0.0016	1.5656 V
SCIG Current	0.2	0.0031	0.0313 A
Prime-Mover Voltage	5	0.0783	3.1311 V
SCIG Stator Frequency	2	0.0313	0.2818 Hz

The oscilloscope resolution errors are assumed to be negligible relative to the expected magnitudes of the corresponding measurements as shown in chapter 5. The only real concern is when the SCIG is operating at low load with an associated low prime-mover torque. In this case the torque resolution error is more comparable to the measured torque. This is a challenge of the measurement system.

D.9 Conclusion

The unit testing and calibration is shown for the measurement system discussed in chapter 3 and designed in appendix C. The unit testing and calibration focuses on:

- The magnitude and phase error of the CTs, VT and DVPs
- The frequency response and output offset of the buffer and LPF circuits

- The frequency division accuracy of the frequency divider
- The linearity and frequency response of the frequency-to-voltage converters
- The frequency response of the inline torque sensor
- The differential-mode and common-mode performance of the various CMC chokes
- The oscilloscope resolution

A possible source of measurement error is the phase-current measurement using the various CTs. This involves the current amplitude and phase as previously described. However, the measurements are still appropriate for SCIG model evaluation – measurement-error effects are noted when appropriate.

The rotor-speed and excitation-frequency measurements have room for improvement in terms of the dynamics accommodated. The frequency-to-voltage converters have a first-order low-pass filtering effect regarding dynamics in measured speed and excitation frequency. The corresponding -3 dB cut-off frequencies are:

- 0.34 Hz for rotor-speed measurement
- 0.147 Hz for generator excitation-frequency measurement
- 0.153 Hz for prime-mover excitation-frequency measurement

The steady-state input-output relationships of the rotor-speed and excitation-frequency measurements are linear as desired.

Special attention is given to CMCs produced by the PWM power converters and the mitigation thereof using chokes. Based on the equivalent differential-mode and common-mode impedance for a range of frequencies, the implemented chokes are expected to perform suitably in the measurement application.

Oscilloscope resolution errors are neglected for the purpose of SCIG model verification. However, for conditions of low generator load and the corresponding low prime-mover torque, the oscilloscope resolution error may be comparable to the measured torque. This is unavoidable and is a limitation of the measurement system.

D.10 References

[1] Hofsajer I., Personal Communication.

[2] Magtrol, Inc. (2011, June) TM 300 Series In-Line Torque Transducers - User's Manual. [Online]. Available at: http://www.magtrol.com/manuals/tm300manual.pdf, Last accessed: 13 April 2014

[3] Ott H. W., *Electromagnetic Compatability Engineering*. Hoboken, United States of America: John Wiley & Sons, 2009.

[4] Goedbloed J. J., *Electromagnetic Compatability*. Hertfordshire, England: Prentice Hall, 1992.

[5] Murata Manufacturing Co., Ltd. Other Filters - Differential and Common Mode Noise. [Online]. Available at: http://www.murata.com/products/emc/knowhow/pdf/26to30.pdf, Last accessed: 5 May 2014

[6] Paul C. R., *Introduction to Electromagnetic Compatability*, 2nd ed., Chang K., Ed. Hoboken, New Jersey: John Wiley & Sons, 2006.

[7] Sen P. C., *Principles of Electric Machines and Power Electronics*, 2nd ed. Hoboken, United States of America: John Wiley & Sons, Inc., 1997.

[8] Shih F. Y., Chen D. Y., Wu Y. P., and Chen Y. T., "A Procedure for Designing EMI Filters for AC Line Applications," *IEEE Transactions on Power Electronics*, vol. 11, no. 1, pp. 170-181, January 1996.

[9] Serrao V., Lidozzi A., Solero L., and Di Napoli A., "Common and Differential Mode EMI Filters for Power Electronics," in *International Symposium on Power Electronics, Electrical Drives, Automation and Motion*, 2008, pp. 918-923.

[10] Roc'h A. and Leferink F., "In Situ Performances of Common Mode Chokes," in *10th International Symposium on Electromagnetic Compatability*, York, 2011, pp. 494-499.

[11] Agilent Technologies. (2009, June) Agilent Impedance Measurement Handbook - A guide to measurement technology and techniques (4th Edition). [Online]. Available at: http://cp.literature.agilent.com/litweb/pdf/5950-3000.pdf, Last accessed: 3 May 2014

[12] Mardiguian M., *EMI Troubleshooting Techniques*. United States of America: McGraw-Hill, 2000.

[13] Tektronix. TDS 1000B and TDS2000B Series Digital Storage Oscilloscopes - User Manual. [Online]. Available at: http://www.testunlimited.com/pdf/an/071181702web_2009.10.27.15.37.08_16272_EN.pdf, Last accessed: 2 May 2014

[14] Tektronix. TDS3000B Series Digital Phosphor Oscilloscopes - User Manual. [Online]. Available at: http://physics.ucsd.edu/neurophysics/Manuals/Tektronix/TDS%203000B%20Manual.pdf, Last accessed: 2 May 2014